Understanding the Processes that Controlled Rifting of the Tyrrhenian Basin

Montserrat Guzman Vendrell

Advisors: César Rodríguez Ranero
Valentí Sallarès Casas

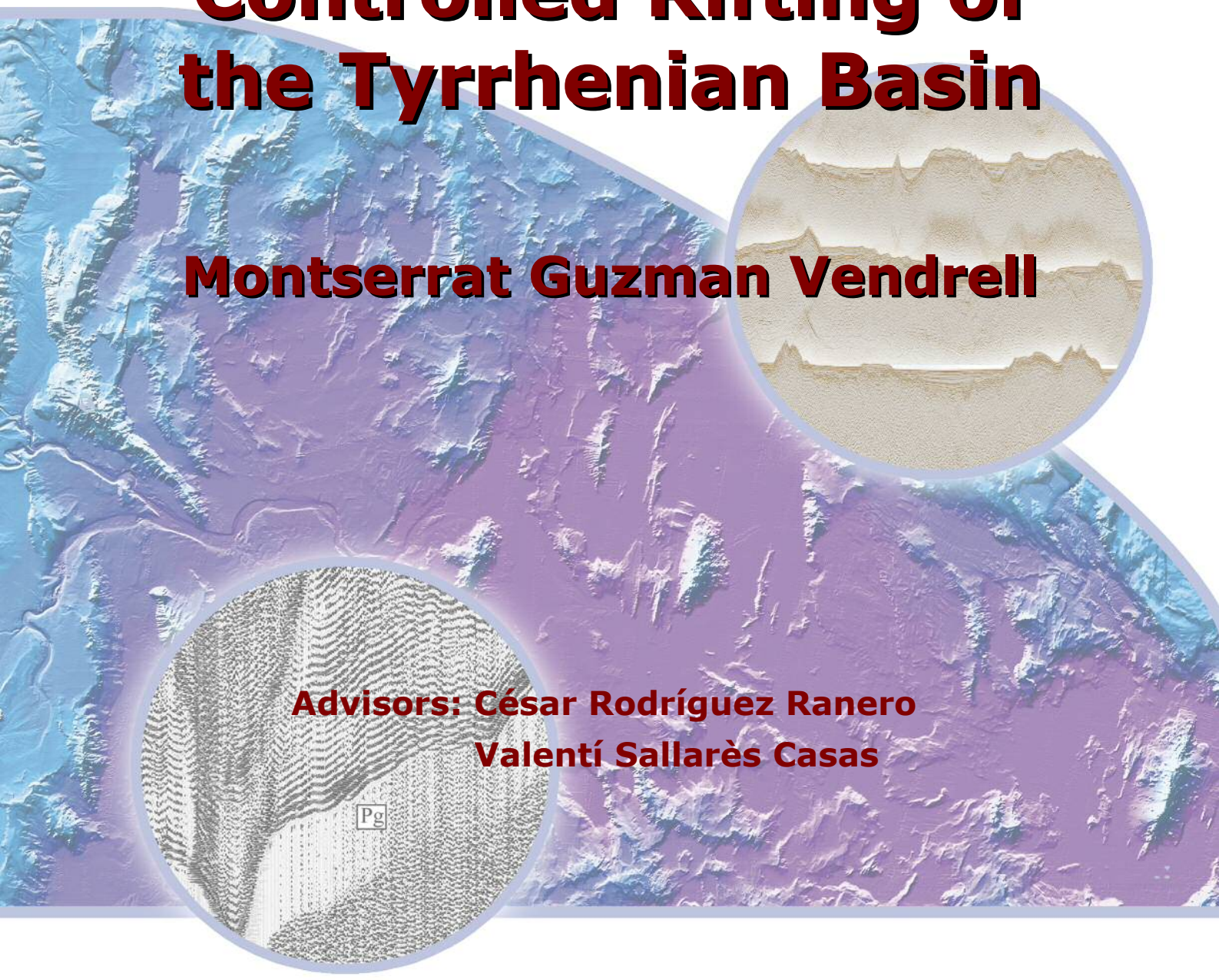

Institut de Ciències del Mar

CSIC
Consejo Superior de Investigaciones Científicas

Barcelona CSI
Center for Subsurface Imaging

Doctorat en Ciéncies de la Terra, 2015, at Universitat de Barcelona

"Tot està per fer,

i tot es possible."

Miquel Martí i Pol

A mi,

per la paciència que m'he tingut mentre escrivia la tesis.

Al Dídac,

perquè ha tingut més paciència que jo. I això no ho sabeu, però té molt de mèrit.

A la Judit,

per la paciència que ha tingut mentre la mama escrivia la tesis.

I als meus pares,

perquè m'han tingut més paciència que nosaltres tres junts.

I la paciència es la mare de la ciència, que diuen, oi?

Agraïments:

Hi ha molta gent sense el suport dels quals aquests anys de treball no haurien arribat enlloc.

Per començar m'agradaria donar les gracies als meus dos directors de tesis: al César i al Valentí, per donar-me la oportunitat de treballar amb ells i poder aprendre tot el que he aprés. A César, sobre tot per confiar en mi i oferir-me les dades de la campanya per a poder realitzar la tesi. També pels seus ànims que m'ha donat aquests últims temps, quan jo ho veia tot massa negre. Però sobretot, per ser un bon mestre i pels seus consells directes i sincers. I al Valentí també per haver confiat amb mi, i haver-me donat la oportunitat de descobrir el món de la sísmica de gran angle.

A en Nevio Zitellini i la Gabriela Carrara per acollir-me a l'Ismar de Bologna y donar-me totes les facilitats que em van durant la meva estada allí. Tot i que en aquell moment era una pipiola en el món de la ciència que literalment no feia ni una setmana que havia començat a treballar en la meva tesis, em van ajudar en tot el que vaig necessitar sense posar-me cap impediment. Els estic molt agraïda per la paciència que em van tenir. Grazie mille!

A l'Stefano Carluccio també per ajudar-me durant aquella estada a Bologna. Per fer-me de guia a l'institut i per els bons moments passats. Però sobretot per descobrir-me la botiga de còmics i pels consells culinaris.

A tots els companys del CMIMA, que m'han aguantat durant tots aquests anys. A l'Adrià, per aguantar-me des de l'inici dels temps... bé, des de l'inici del màster. Per les partides de póker i les filosofades al despatx. Al Manel, per les partides de póker, pel seu suport i els seus ànims, per aguantar-me durant les guàrdies de la campanya, però sobretot per ajudar-me amb tot el tema del gran-angle. Sense ell, aquesta tesi no estaria escrita. A la Sara, pels seus consells i el seu caràcter directe. Fan falta mes persones com ella al món. A l'Alejandra, per les partides de pòker i per l'optimisme que rulava al despatx. Però sobretot perquè tot i que he estat molt desapareguda aquest últim any, ha estat disposada en tot moment a donar-me un cop de mà. A l'Agnès, companya de despatx, per tot el suport i la juerga, tan en les campanyes, com a l'hora de treballar (ehem...). A l'Alsi per tot el que m'ha ensenyat de la sísmica de reflexió. De fet, gairebé tot el que sé de sísmica li dec a ella... Però també pel seu suport, el seu humor i el seu optimisme. A la Clàudia, per ajudar-me a re-localitzar els OBS de la meva línia de refracció. I en Jean, l'Hector, en Josep, la Berta, el Rafa, la Laura, la Marina, en Jon, ... i segur que me n'estic deixant uns quants.

Moltes gràcies a tots per haver-me donat un cop de mà sempre que ho he necessitat.

Als meus sogres, cangurs incondicionals i proveïdors de tuppers deliciosos. No sé que hauria fet (i menjat) sense ells.

Als meus germans, pel seu suport. A l'Andreu pel seu humor i per creure en mi... encara que no entenc gaire bé perquè. I a la Mercè, pel seu suport que ha creuat fronteres, pels seus ànims, la seva empatia, i agafar un avió i venir-me a donar un cop de mà. Moltíssimes gràcies!!

A les nenes, que tot i que fa tant de temps que em coneixen, continuen aguantant-me.

Als de Can Corki, pels bons moments, per tot el que hem viscut, i pel que ens queda. Però sobretot, Lluís, per les festes de l'1 d'agost.

Al Raúl Lovera, perque encara que haguem perdut totalment el contacte, sense el seu avís no hauria descobert a temps aquella oferta per a realitzar un doctorat.

Al "John-Wheel" per la seva ajuda incondicional en el format de la tesis.

I segur que m'estic deixat algú...

Moltes gràcies a tots!

Index

Summary....11
1.INTRODUCTION AND OBJECTIVES....16
1.1.Introduction....17
1.2.Basics about back-arc basins....18
1.3.Geological context and tectonic evolution....21
1.4.Objectives of this work....26
2.METHODOLOGY....28
2.1.Introduction....29
2.2.Seismic waves....31
2.2.1.Snell's law and Huygens principle....32
2.2.2.The convolution....34
2.3.Multichannel seismic reflection....35
2.3.1.Data acquisition....35
2.3.2.Processing flow....39
Quality control....40
Spherical Divergence correction....43
Geometry....44
Deconvolution....46
Velocity analysis....48
Radon analysis....52
Internal and external mutes....54
Stack....55
F-K filtering....56
Post-stack time migration....56
2.3.3.Seismic interpretation....60
2.4.Wide-angle seismic data modelling....61
2.4.1.WAS acquisition system....62
Processing....66
2.4.2.Identification of seismic phases....67
2.4.3.Modelling....68
Layer stripping method....71
Uncertainty analysis....71
3.CORTICAL DOMAINS....74
3.1.Introduction....75
3.2.Methodology....77
3.2.1.Seismic phase identification....77
3.2.2.Travel-time tomography....78
Uncertainty analysis....79
3.2.3.Gravity modelling....81
3.3.Seismic structure of the crust and the uppermost mantle....81
3.3.1.Petrological interpretation....83
3.3.2.Tectonic structure....84
3.4.Discussion....87
3.4.1.Formation of the the Sardinia - NW Sicily conjugated margins....87
3.4.2.Along-axis variations of magmatic crustal accretion on the Cornaglia Terrace....89
3.5.Crustal variability across the section....90
4.BASIN-SCALE STRATIGRAPHY....92
4.1.Introduction....93
4.2.Basin stratigraphy....93
4.2.1.Seismic basement....93

4.2.2.Tortonian....96
Corsica-Sardinia margin....97
North Tyrrhenian region....100
Sechi-Farfalle region....103
North Sicily Margin....109
4.2.3.Messinian....109
Corsica-Sardinia margin....110
North Tyrrhenian region....111
Cornaglia Terrace and Campania Terraces....112
Sechi-Farfalle region....118
Italian Margin....119
North Sicily Margin....120
4.2.4.Pliocene....121
Corsica-Sardinia margin....122
North Tyrrhenian region....122
Cornaglia Terrace and Campania Terrace....125
Sechi-Farfalle region....126
Vavilov and Magnaghi Basins....126
Italian Margin....130
North Sicily Margin....133
4.2.5.Pleistocene....133
4.2.6.Volcanics....134
4.3.Discussion....135
Seismic Basement....136
Tortonian....137
Messinian....139
Pliocene....141
Pleistocene....143
Volcanics....144
4.4.Stratigraphic evolution interpretation....147
5.TECTONIC SETTING....152
5.1.Introduction....153
5.2.Corsica-Sardinia Margin domain....153
5.3.North Tyrrhenian region....158
5.4.Cornaglia Terrace domain....162
5.5.Vavilov and Magnaghi Basins region....165
5.6.Campania Terrace region....170
5.7.Italian Margin region....172
5.8.North Sicily Margin domain....175
5.9.Discussion....178
5.9.1.Corsica-Sardinia Margin domain....179
5.9.2.North Tyrrhenian region....179
5.9.3.Cornaglia Terrace domain....181
5.9.4.Vavilov and Magnaghi Basins region....182
5.9.5.Campania Terrace region....183
5.9.6.Italian Margin region....183
5.9.7.North Sicily Margin domain....185
5.10.Kinematic evolution....185
6.CONCLUSIONS AND OUTLOOK....190
6.1.Crustal domains from the Sardinia to the NW Sicily margins....191
6.2.Basin-scale stratigraphy....191
6.3.Tectonic framework....193

6.4.Summary of basin formation evolution....195
6.5.Outlook....198
Drilling and dredging....198
Seismic sections....201
Bibliography....204
Annexes....214
Figure index....214
Acquisition parameters of the multichannel profiles....220
Wide-angle seismic record sections....221

Summary

Work carried out in this thesis has the purpose to trace the tectonic and stratigraphic features of the Tyrrhenia Sea, and from these characteristics, to define the processes that get involved into the basin formation.

The Tyrrhenian is a back-arc basin belonging to the Western Mediterranean realm. Its formation is directly related with the subduction system of the Ionian slab (African plate) below the Mediterranean domain (European plate). The slab retreat causes an stretching of the overriding plate and triggered the opening of the Liguro-Provençal basin, and later on the Tyrrhenian basin (Faccenna et al., 2001; 2007).

Traditionally has been considered that the opening in the Tyrrhenian Sea started with continental rifting which subsequently leads to oceanic crust formation at the central region of the Vavilov and Magnaghi Basins. But MEDOC survey results provided new data suggesting a more complex evolution that involves total crustal break up, and the consequent mantle exhumation.

Data analysed in the thesis are seismic profiles acquired during the MEDOC survey, that was carried out in spring 2010 within the frame of the MEDOC ("MEDiterraneo Occidental") project. These data consist in a profile set including multichannel seismic and wide-angle sections shot across the basin. This dataset covers the most part of the northern and central parts of the basin as well as the western margin. So it spans both conjugated margins of the basin, providing quality data to understand their relations (symmetry/asymmetry relations), as well as the Tyrrhenian evolution.

Multichannel seismic profiles image the subsoil providing information about the stratigraphy and the geometric relations between the strata as well as with the tectonic structures. Meanwhile the wide-angle data brings the Moho geometry and velocity models of the crust which unravel the nature of the basement. These sections were acquired with an east-west direction with the purpose to cut perpendiculary the tectonic structures and provide a realistic imaging for them. At last, the wide-angle sections were shot coincident with some of the multichannel sections to get complementary information about the subsoil and allow a better understanding.

Also complementary data has been used to aid the MEDOC data interpretation. They consist in a high-resolution multibeam bathymetry (Marani & Gamberi, 2004), or sampling data from ODP (Kastens & Mascle, 1990) and DSDP surveys (Ryan et al., 1973; Hsü et al, 1978), and dredging data (Colantoni et al., 1981).

The sedimentary record described in the Tyrrhenian Basin spans from early-Miocene to the most recent Pleistocene deposits. The distribution of these sediments, their geometry and their relations with the tectonic structures reflects the basin evolution throughout the time.

Oldest sediments are located at the Corsica and Sardinia basins. They consist in pre-Trotonian materials deposited during the formation of these basins, in the early Miocene. Thus this region may have been opened previously to the Tortonian times. In fact, these basins formed as episutural basins during the early Miocene (Sartori et al., 2001; 2004; Mauffret et al., 1999; Mauffret & Contrucci, 1999).

The overlying Tortonian unit has only been identified at the continental areas of Corsica and Sardinia Basins, the North Tyrrhenian domain and the North Sicily Margin. Theoretically, it also should be present at the Italian Margin, but it has not been identified there.

The rifting onset took place during the Tortonian, as suggested by the sedimentary discontinuity described within this unit. This discontinuity marks the base of the syn-rift wedges, and it is known at the literature as the "L" discontinuity.

Meanwhile the Messinian unit has been described almost everywhere with the exception of the Magnaghi and Vavilov Basins. Its presence at the Campania and Cornaglia Terraces, where no Tortonian has been found suggest that these areas were formed in some moment during the early Messinian. But, in fact, Messinian strata show a clear post-rift character in these areas. Thus both terraces can be formed during the Tortonian, concurrently to the rifting processes of the rest of the Tyrrhenian.

Thus, during the Tortonian extension started at the Tyrrhenian as suggested by the lowermost sediments of the syn-rift wedges. In the North Tyrrhenian area extension occurred through rifting processes, leading to rotated blocks that can be well appreciated at the bathymetry. North-south trend of these blocks suggest that extension direction during this extensional stage was mainly east-west.

While at the same time, southwards, at the Cornagla and Campania Terraces, extensional processes become more complex. Continental extension took place in the southern Cornaglia, while at the center, at the north and at the Campania Terrace back-arc magmatic crustal accretion took place. Instead, in the southern Cornaglia Terrace a limited amount of magmatic crustal accretion might have happened according to velocity models obtained. This north-south variability of the extensional processes has been related with the interaction of landmasses with the subduction front, reducing the width of subducting slab. This fact triggered in variations on the style of back arc extension and consequently in spatial variations of back-arc magmatism. According to sedimentary syn-rift geometries, extension continued in these areas during the Messinian, although extensional processes become attenuated.

Apart from this, three Messinian sub-units have been identified. The lower one (M1) has a discrete presence along the Tyrrhenian, but broadly, it is present at every place where Messinian has been described. The second sub-unit are evaporitic layers deposited during the Messinian Salinity crisis, that can only be found at the Campania and Cornaglia Terraces. Since these deposits have only been observed in these areas, we can suppose that during the Messinian crisis these areas were flooded while the rest of the Tyrrhenian terrains could be exposed. Eroded – flattened – ridges observed on MEDOC 1 and MEDOC 2 sections also support this theory. At last, the third sub-unit has been found everywhere where the Messinian is present. It is a well-layered unit easy to identify everywhere, aiding to mark the Messinian top.

The Pliocene deposits are the first unit that can be found everywhere, including the deepest areas of the Vavilov and Magnaghi Basins. This unit has been divide into two sub-units. The lower one has a clear syn-rift character almost everywhere, while the upper sub-unit has a parallel disposition of the strata suggesting post-rift sedimentation. Discontinuity between both sub-units in known as the "X" discontinuity, and marks the end of this extensional stage.

In fact, this discontinuity is related with a jump of the extensional locus towards the east, which took place during the uppermost Messinian – lower Pliocene, and leads to the formation of the Magnaghi and Vavilov Basins. This change has been related with the tearing of the subducting plate below the Sicily Channel region, which triggered a sudden retreat of the slab towards the east (Faccenna et al., 2007). This fact produces a migration of the trench and a crustal break-up of the overriding plate, which triggered to mantle exhumation at the Vavilov and Magnaghi Basins domains.

The Magnaghi Basin may have opened during the uppermost Messinian, as suggested by the pre-rift Messinian evaporites observed at the western half of this basin. Then, in a short time lapse, extensional locus continues its migration towards the east and the Vavilov basin opened at the lower Pliocene. Opening of these two basisn may have occurred during a short period as suggested by the absence of syn-rift deposits in the area.

At the same time, extensional processes at the continental and back-arc regions ceased completely, as suggested by the intra-Pliocene unconformity. It implies that the former magmatic extensional regime changed to an essentially amagmatic extension.

Finally, at the boundary between the Pliocene-Pleistocene a slab tearing below the Italian peninsula leads to a new tectonic setting in the basin. This change caused a fast retreat of the slab and a new jump in the extensional locus of extension. As in the former case, a new basin opened: the Marsili Basin.

In this episode, the direction of extension changed from E-W to fairly NW-SE related with this slab tearing. Therefore, it become more parallel to the slab subduction direction and thus roll-back fastened. Like in the former cases, this evolution is recorded by a stratigraphic discontinuity across the basin, which is fairly coincident with the contact between the Pliocene and the Pleistocene units.

Concurrently, in a certain moment during the upper Pliocene, transpression-transtensional tectonics started along the Italian Margin region related with this trench migration towards the south-east, and reactivated the former extensional faults.

1.INTRODUCTION AND OBJECTIVES

1.1. Introduction

The goal of this thesis is to advance in our understanding of the processes that controlled the formation and shaped the crustal and tectonic structure of the Tyrrhenian Sea Basin.

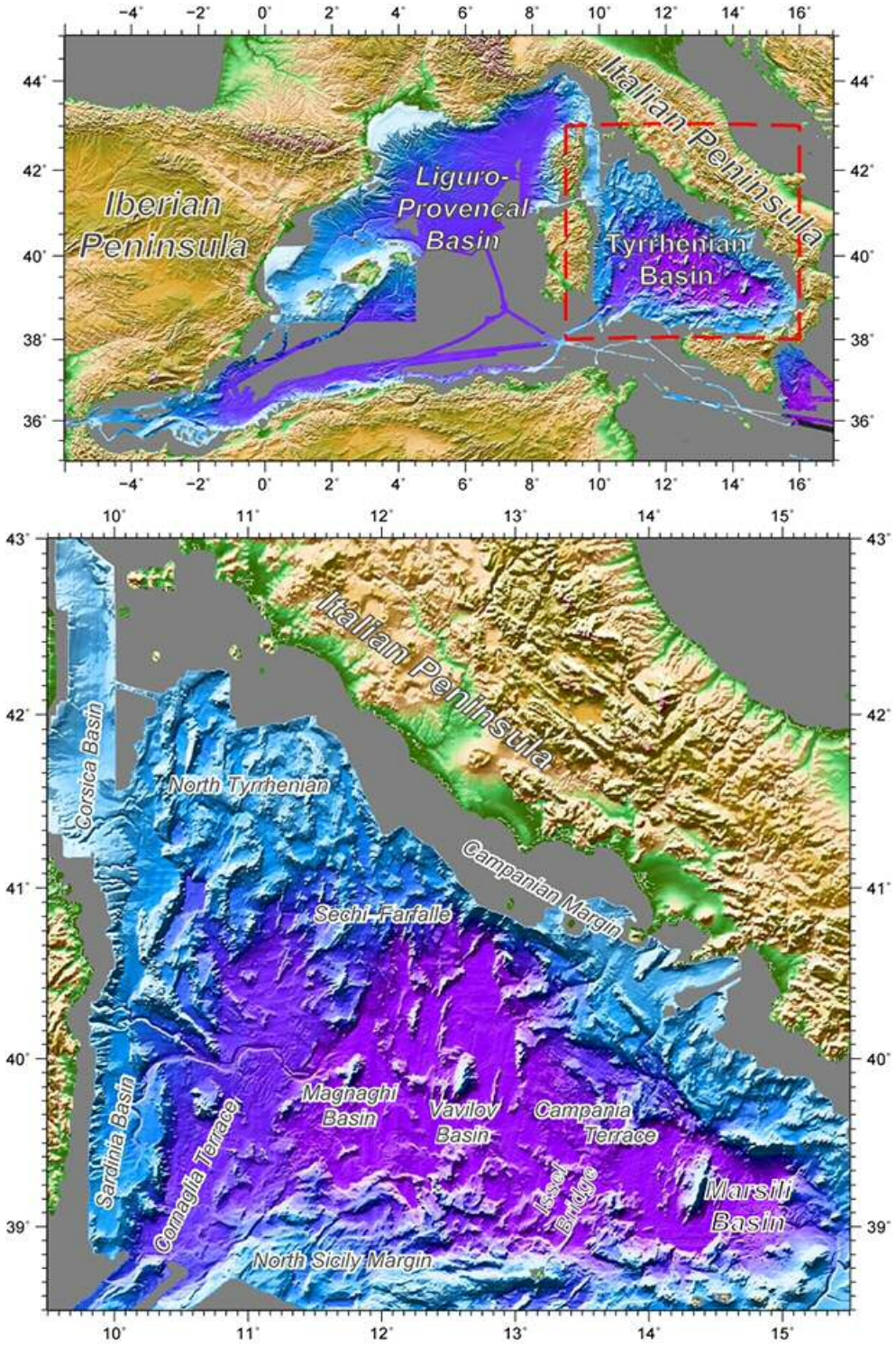

Figure 1.1: Regional bathymetric map of the Western Mediterranean domain, with the working area – the Tyrrhenian Sea – framed in the red rectangle, and enlarged next. Also the major topographic features mentioned at the text have been labelled.

Like all of the other basins within the western Mediterranean Sea realm, it is a back-arc basin related to the Alpine subduction system. All of them were formed in an extensional system within the context of the Africa and European plates convergence (e.g. Gueguen et al., 1998; Faccenna et al., 2004; Viti et al., 2009).

The Tyrrhenian basin developed in a rear position of a compressional region with a thick continental crust, and developed on the site formerly occupied by the Alpine-Apenninic orogenic belt (Sartori et al., 2004). And like in a typical back-arc basin setting, the extensional processes are simultaneous to the compression in the circum-Tyrrhenian area.

Broadly speaking, the basin history started during the early Miocene (perhaps locally during the latemost Oligocene) with the continental lithosphere being stretched and thinned by rifting processes. The opening evolved from continental crust stretching, trough oceanic crust generation, and finally to a complete crustal break up with mantle exhumation (Prada et al., 2014; 2015). The opening processes lasted until recent times days. That is the reason why it can be considered a Neogene stratigraphic type locality. Although the first extensional processes may have started near the Oligocene-Miocene boundary, across most of the basin, the onset of the major rifting phase probably started around 9 Ma ago – during the late Tortonian -, probably coinciding with a change in the direction of the Africa-Europe convergence. This change in the motion direction probably resulted in a decrease in obliquity of the subduction direction with respect of the plate convergence direction, so that it favoured the back-arc extension in the Tyrrhenian basin location (Faccenna et al., 2004; Kastens & Mascle, 1990).

1.2. Basics about back-arc basins

By definition, back-arc basins involve both convergent and divergent type plate boundaries. Back-arc basins develop behind subduction zones. These systems may occur in an setting where the two plates are oceanic, and were typically extension focus on volcanic arcs, so that the rifting process lead to the formation of spreading centers and produce new oceanic seafloor. But back-arc settings may also occur in a system in which the overriding plate is continental and here extension shares similarities with continental rifting processes (e.g. Taylor et al., 1995). This is the case for most western Mediterranean basins.

According to Martinez et al. (2007), growing and evolution of these basins can be explained with two plate convergence kinematic contexts. Although both cases develop in convergence contexts, the relative motion between the plates results in a divergent setting. In the first case (fig. 1.2, left-hand column), the subducting slab sinks into the mantle faster than the convergence rate between the plates. This fact causes a retreat of the underlying plate wile the overriding plate remains motionless, resulting in a stretching of this last. Second case (fig.

1.2, right-hand column) occurs when the second case occurs when the overriding plate moves away from the trench, but the subducting slab acts as a sea anchor in the mantle resisting the migration of the trench.

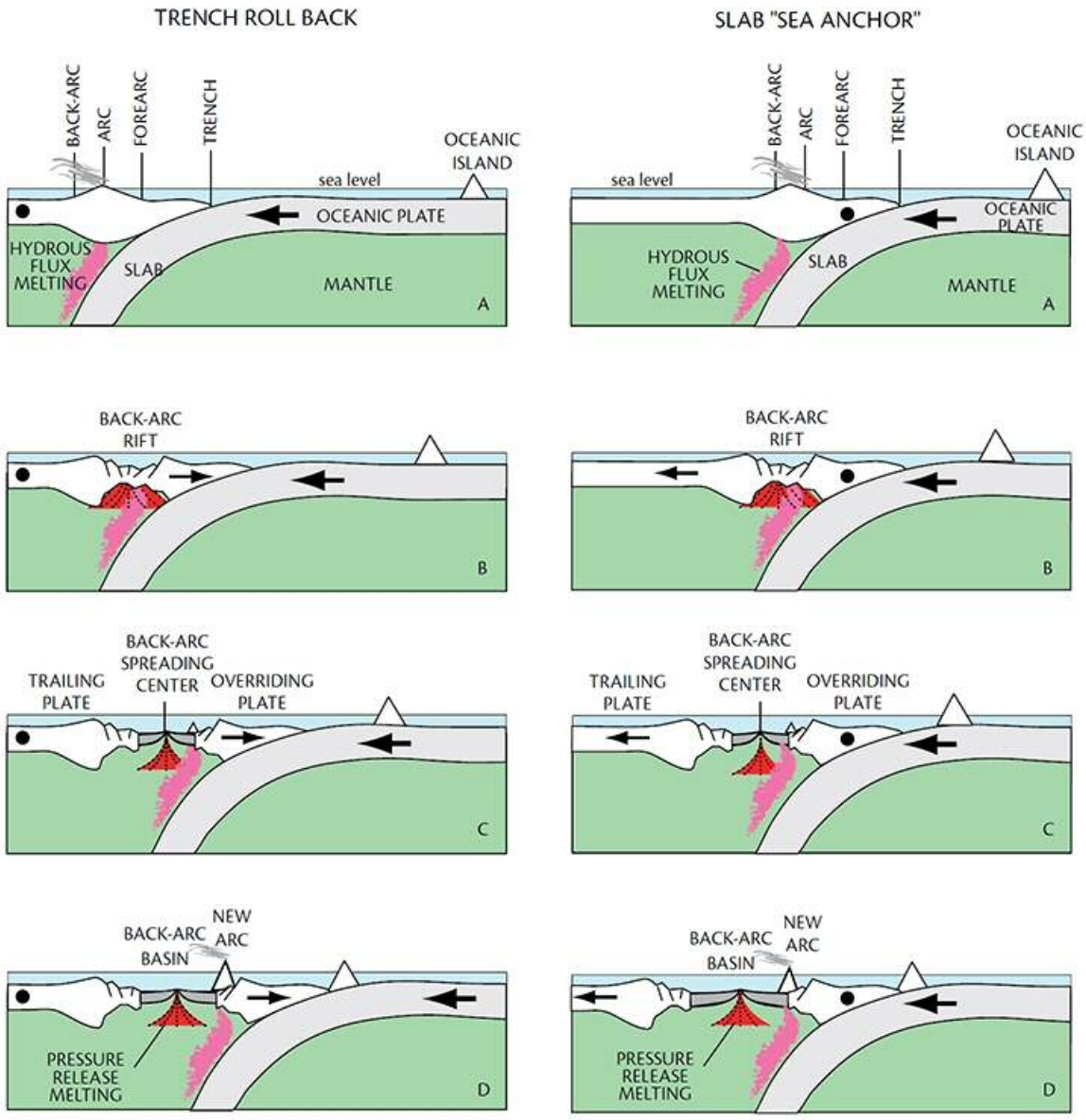

Figure 1.2: Models for back arc basin opening. Left panels show the evolution of a basin with a slab roll-back as a dredging mechanism, while right panels show the evolution of a basin with the slab acting as a mantle anchor (from Martinez et al., 2007).

Associated to the subduction front there is usually a volcanic arc, and the rifting processes usually start in their vicinities. Some rifting systems starts behind the arc while in the other cases start in the forearc. It depends on several factors, for example, the local weakness of the overriding plate. The motion and the geometry of the subducting slab also affect the result. And at last the coupling of the slab with the mantle wedge might also control the process (Martinez et al., 2007).

In general, the evolution of these basins usually shows an episodic behaviour throughout the time. Their formation and development occurs for periods of up to tens of millions of years, and then come to an standstill, only to begin a new cycle of arc rifting and spreading a few million years later (Faccenna et al., 2004; Martinez et al., 2007). At the same time, the extensional axis of these basins jumps towards the trench episodically. This behaviour may lead to asymmetric distribution of stresses, with one of the conjugated margins suffering compression related to the subduction, while the other is an extending margin.

Broadly speaking, the conjugate margins of a normal rift system can be compensated and restored back together by a simple rotation of one plate with respect to the other. But by contrast the reconstruction of the margins of a back-arc basin system often does not fit well when the two margins are brought back together, indicating a non-rigid behaviour of the lithosphere at basin scale (Martinez et al., 2007).

At the beginning, magmatism in back-arc basins starts close to the volcanic front and geochemical analysis show a strong influence by hydrous flux melting from the underlying slab. But as the rifting evolves and the extensional locus separates from the arc with time, melting contribution from the slab decreases and magma production changes progressively towards mainly pressure-release melting. Therefore, crustal composition evolves from felsic composition (andesites and dacites) with strong slab chemical influence, toward mafic mid-ocean ridge basalts MORB that characterize seafloor spreading in the open oceans.

Instead of the classical magnetic lineations related to oceanic floor generation at mid-ocean ridges, the only magnetic anomalies found at the Tyrrhenian sea appear related to volcanic constructions, rather than the spreading-type magnetic lineations, as can be well (Sartori et al., 2004).

Being a back-arc basin, the Tyrrhenian shows some classical characteristics. First there is the Aeolian arc at the southeast part of the basin. It is an active volcanic arc generated by the subduction processes of the Ionian oceanic plate below the Tyrrhenian. Besides the volcanic arc, there is also volcanism at the central part of the basin with a characteristic tholeitic compostion (Kastens et al., 1988). Also, existing data indicates a shoaling of the Moho that occurs approaching the central part of the basin (Sartori et al., 2004, Prada et al., 2014; 2015) reaching the 10 km. depth at its shallower part (Sartori et al., 2004). Locally the presence of exhumed serpentinized peridotites, which directly expose mantle at the seafloor trough faulting, has been documented by drilling (Kastens and Mascle, 1990; Bonatti et al., 1990). Exhumed mantle windows at back-arc contexts have been documented in several places, for example at the Philippine Sea (Martinez et al., 2007). And finally, a high heat flow (up to 200 mW/m^2) has been measured in the area (Kastens et al., 1988; Bonatti et al., 1990).

1.3. Geological context and tectonic evolution

Oldest materials described in the Tyrrhenian Basin are some outcrops that currently can be found at the Sardinia, Corsica and Sicily Islands. They consist in materials ranging from pre-Cambrian to early Paleozoic that were affected by the Variscan Orogeny during mid Paleozoic times. Some of them were reactivated during the Alpine Orogen, like the calabrian-peloritanian-kalabide units in Sicily, while other materials remained unaffected (Sartori et al., 2001).

At the beginning of the Mesozoic the region of study belonged to the Pangea supercontinent. But during the middle to late Triassic, rifting began to split the European and African plates. This activity gave way to seafloor spreading from Jurassic to early Cretaceous and formed the Piemont-Ligurian Ocean, also know as Alpine Tethys, that was a sub-basin belonging to the Tethys Ocean.

Lately, during the upper Cretaceous the kinematic setting changed, and the African and the European plates started to converge again, leading to the subduction of the Tethys ocean. This process lasted until the collision between the two continental plates during the Cretaceous-Eocene, producing the closure of the Piemont-Ligurian Ocean and the formation of the Alps. As a result of this collision, the Corsican Alps overthrusted over Variscan Corsica, and at the same time, the Calabrian block run onto Sardinia and Corsica (Mauffret & Contrucci, 1999). In the Eocene a fragment of this Mesozoic oceanic crust still persisted east and northeast of Calabria. The subduction zone gradually consumed this remnant during the last compression event (37 Ma) at the end of Eocene (Mauffret & Contrucci, 1999). Nevertheless, several authors disagree with a complete subduction of the oceanic crust, and argue that some remnants of this old ocean may still be found at northwest of the Corsica Island (Sartori et al., 2001).

Once the Tethys Ocean became extinct with the closure of the Jurassic Tethys during the upper Cretaceous, subduction in the central Mediterranean started (Faccenna et. al., 2001; Finetti et al., 2001). As it is typical for the back-arc basin systems, the Mediterranean sub-basins formation evolved episodically within the geological context of the European and African plates convergence. Probably, throughout the first 20 – 30 Ma velocity did not reach the centimeter per year (Faccenna, et. al., 2001). Therefore, during the first stages of the convergence the new subduction processes were slow, although the convergence between the African and European plates was important.

The first rifting episode can be considered to start during the early Oligocene, when the lower plate had penetrated enough into the mantle to increase the slab-pull so that it fact accelerated the subduction progressively (Faccenna et al., 2001). At this point, the African

plate started a roll-back process towards the east leading to the opening of a back-arc basin that would become the Liguro-Provençal Basin (Mauffret & Contrucci, 1999).

These incipient rifting processes gave way to seafloor spreading. The onset of this oceanic crust formation is dated by a middle Aquitanian (22 Ma.) break-up unconformity (Mauffret & Contrucci, 1999). Because of this rifting, a continental fragment including Corsica, Sardinia and Calabria split from the continent by back-arc extension and migrated towards the east by a 30º counterclockwise rotation (Mauffret & Contrucci, 1999).

The subduction front migration lasted until early Miocene (Mauffret & Contrucci, 1999), when the slab reached the 660 km deep mantle discontinuity, and then trench migration blocked (Faccenna et al., 2001).

Evidences of the volcanic activity related with the subduction processes during this period have been found. They consist in late Oligocene calc-alcali volcanics that can be found intruding Sardinia terrains (Kastens and Mascle, 1990). This volcanism continued its activity on Sardinia for a longer time and vanished at about 13 Ma, during the Serravalian, suggesting that subduction continued beneath the splited continental fragment for a longer time, although the trench migration ended earlier (Kastens and Mascle, 1990; Sartori et al., 2001).

Concurrently the Corsica terrains underwent a first extensional event along interpreted east-dipping detachment faults. This extension resulted in an epi-sutural basin formed on the top of a collisional prism (Mauffret & Contrucci, 1999; Mauffret et al., 1999). This extensional process has been related with the extensional processes occurred at the forearc of the Alpine orogen, which gave way to the European Oligocene Rift System. Subsequently, during late Oligocene - early Miocene, left-lateral transpressive motion reactivated Variscan faults in this island. This could explain the rhomboidal shape of the Corsica basin that suggests a pull-apart basin (Mauffret & Contrucci, 1999). Drilling in the area give at least, a Burdigalian age for the 5 km thick syn-rift. But could be Oligocene according to industrial wells (Mauffret & Contrucci, 1999).

From early Miocene until Tortonian times, compressional processes became widespread around the area that would become the north, east, and southeast margins of the actual Tyrrhenian basin (Kastens and Mascle, 1990). During this time interval, subduction stopped and the trench remained motionless, although plate convergence continued. There are also indefinite evidences for pre-Tortonian rifting at the Sardinia and Corsica margins (Kastens and Mascle,1990). In addition, Sartori et al. (2001) suggest that compression ended at some point during the Serravalian, at least in the Sardinia margin area, and during the time interval from Serravalian to Tortonian post-tectonic sedimentation occurred in a shallow epi-sutural basin that would become the actual Sardinia basin (Sartori et al., 2001).

During all this time interval, the slab rearranged its shape at the base of the upper mantle and changed its configuration to a steeper dip during the Tortonian (around 10-6 Ma). This fact triggered that the subduction front shifted some tens of kilometers eastwards, and subduction resumed its activity. Therefore, the rifting axis also migrated towards the east and the whole Tyrrhenian basin underwent a new rifting episode. This is the point when the second rifting episode starts (Mauffret & Contrucci, 1999; Faccenna, 2004) (fig.1.3).

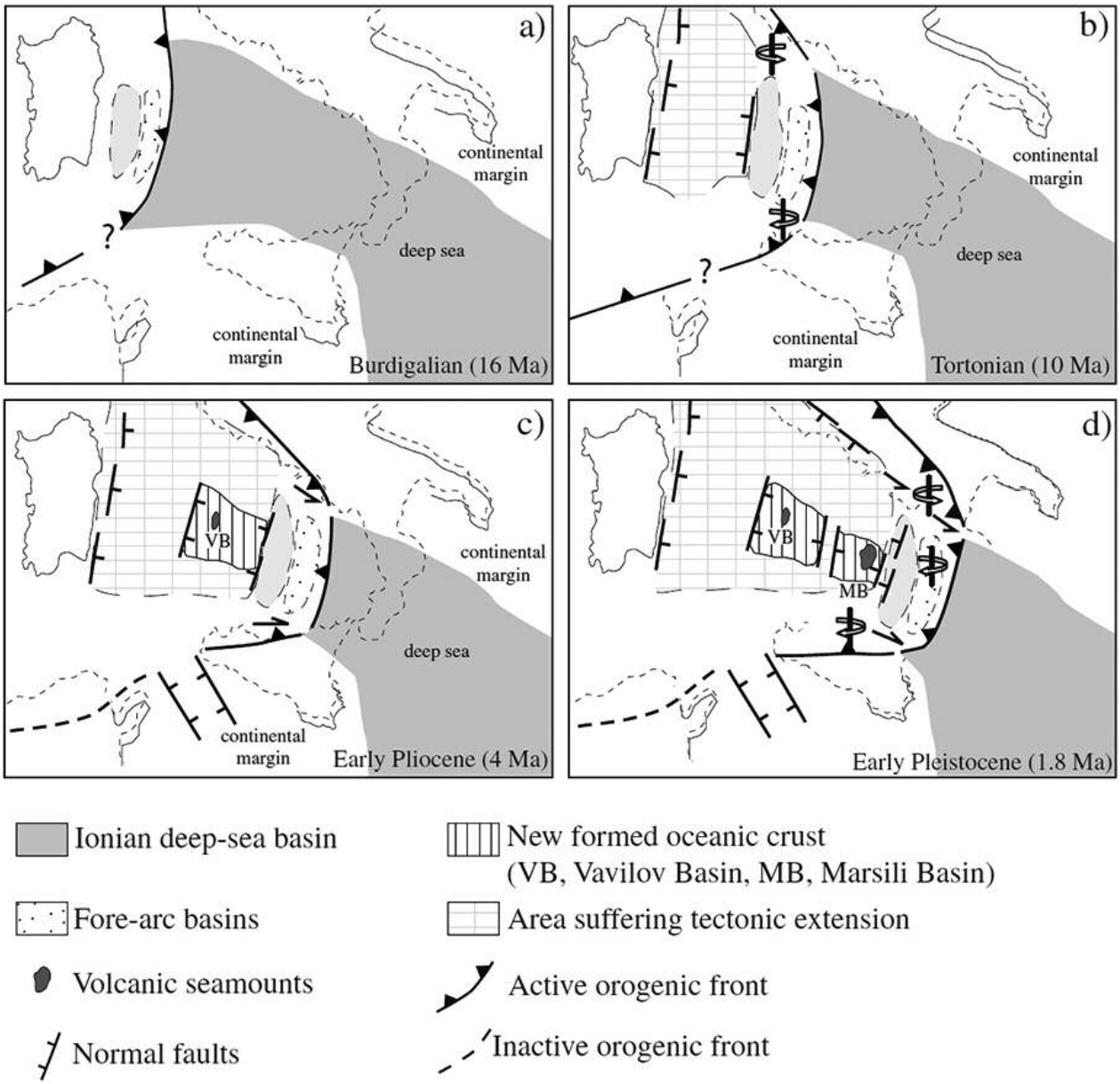

Figure 1.3: Schematic diagram showing the evolution of the Tyrrhenian Basin from the early/middle Miocene until present day (modified from Cifelli et al., 2007).

At the northern half of the basin, extension resulted in continental stretching and coeval intrusion of magmatic bodies, both intrusive plutons at deep and intermediate crustal levels, as well as volcanic edifices. (Mauffret & Contrucci, 1999). As a result, the North Tyrrhenian is characterized by small and elongated basins with a north-south trending strike, and a

homogeneous distribution along the entire area (Mauffret & Contrucci, 1999; Moeller et al., 2013; 2014). Other young basins (e.g. the Gulf of Corinth, the Suez-Rift or the Baikal Lake) display features resembling the northern Tyrrhenian, suggesting that half-graben formation and homogeneous distribution of crustal thinning are common features during rift initiation (Moeller et al., 2013; 2014).

Meanwhile towards the south, the rifting processes preceded the oceanic crust formation (Mauffret & Contrucci, 1999, Sartori et al., 2001). Because of this, the resulting tectonic structure became more complex. In this episode, rifting processes formed the Cornaglia and Campania Terraces, with lower faulting rate and a higher apparent extension. In addition, according to Sartori et al. (2001), extensional style changed from north to south of the area, with a continuous and modest thinning at the northwards of the Cornaglia Terrace, while towards the south there is the opposite situation.

Also during this stage, the convergence direction of African and European plates changed from north-south to nearly northwest-southeast, therefore the direction of convergence became more parallel to the inferred dip of the subducting slab. This event probably fastened the subduction processes and the associated extension in the back-arc region.

ODP data from leg 107 suggest that the Tyrrhenian during this time was a warm, productive and well-ventilated sea with none or scarce volcanic activity. In addition, at the base of ODP hole 654, corresponding to the Tortonian interval, transgressive sediment sequences were drilled (Kastens and Mascle, 1990). They can be related with normal faulting and subsidence, which became widespread around the basin margins during this time (Kastens and Mascle, 1990).

This tectonic episode continued throughout the Messinian, with rifting, extension and subsidence across the basin. But the paleo-environment situation switched completely: the water connection between Atlantic and Mediterranean was greatly restricted because of tectonic movements, isostasy and/or decrease in sea level (Manzi et al., 2013). Evaporites and lagoonal depositional facies became characteristic during this period. The continental shelf and much of the slope became exposed and turn into newly subaerial zones. Therefore, they suffered an important erosion during this period, providing important lateral changes in facies (Kastens and Mascle, 1990; Moeller et al., 2013).

ODP leg 107 data also displays an important presence of pyrite and high concentrations of organic carbon suggesting an anoxic environment in the Messinian. This fact can be directly related with the desiccation event (Kastens and Mascle, 1990). Evaporitic deposits became common across the entire basin, as well as at the entire Mediterranean. Analysis from ODP Leg 107 gave a marine origin for these evaporitic sequences (Kastens and Mascle, 1990). As for

the Tortonian time, there is little evidence of Messinian age volcanism within the Tyrrhenian basin, although volcanic activity in the circum-Tyrrhenian region was active at this time (Kastens and Mascle, 1990).

Towards the end of Messinian extensional processes slowed or even stopped at some locations. (Kastens and Mascle, 1990).

In the stratigraphic record, this extensional phase is bounded by two regional discontinuities known in the literature as the "L" and "X" discontinuities. The first one lies at the base of wedge-shaped sediment sequences, and marks the start of the rifting processes in the Tortonian. The "X" unconformity marks the end of this tectonic phase. It is correlated with the regional Pliocene transgression and has also been related to the eastward migration of Calabrian arc (Trincardi & Zitellini, 1987).

In addition, a third discontinuity has been described between these two. It is the "Y" unconformity, which corresponds to the Messinian salinity crisis, during the latermost Messinian (Moeller et al., 2013; and references therein).

During the lower Pliocene, the subduction trench shifted eastwards again, and therefore the extensional axis migrated too to the current location of the Vavilov Basin, iniciating a third rifting episode (fig.1.3). Throughout this stage the Vavilov and Magnaghi Basins were formed, splitting the Cornaglia and Campania Terraces, which stood together until this moment.

The Vavilov Basin is bounded to the southeast by a bathymetric ridge with a relatively thick crust: the Issel Bridge, which has been interpreted as a relic Pliocene calc-alkaline volcanic arc, coeval to the extension in this area (Malinverno, 2012). Volcanism also took place at the central part of these basins, with the Magnaghi and Vavilov seamounts. The results of the analysis of ODP leg 107 samples suggest that they were formed afterwards than the surrounding basin, probably during upper Pliocene times (Kastens and Mascle, 1990) or even later.

In the Mediterranean, the Miocene-Pliocene boundary is defined by the resumption of normal marine conditions. According to literature, this reestablishment should have been a rapid process, and places the reflooding at the end of a brief glacial interval, probably during a world-wide eustatic increase in sea level (Kastens and Mascle, 1990). However, in the Sardinia margin, the oldest Pliocene sediments are products of subaerial weathering on the continental shelf, suggesting that flooding in this area occurred later in time (Kastens and Mascle, 1990). Because of this reconnection with the Atlantic Ocean, throughout the Pliocene-Pleistocene the Tyrrhenian Sea responded to major global oceanographic and climatic events. And even additional events not seen in the open ocean, have been recorded as well (Kastens and Mascle, 1990).

Finally, about 2 Ma ago, during Pliocene to early Pleistocene, extension moved eastwards again to the current location of the Marsili Basin, and iniciated the last rifting episode in the Tyrrhenian. Here is where the Tyrrhenian sedimentary cover is thicker, reaching 5 km of Pliocene and Quaternary Sediments. Therefore, it is the site where the extension migrated most recently (Kastens and Mascle, 1990).

At the other hand, tephra layers recovered on the ODP survey suggest that the volcanism in the Tyrrhenian region during Pliocene is scarce in comparison with Pleistocene times (Kastens and Mascle, 1990). In fact, during Quaternary, volcanic activity has become widespread along the basin, and even eruptions continued today on Vavilov volcano (Kastens and Mascle, 1990).

1.4. Objectives of this work

As developed above, the Mediterranean Sea realm is a region in which basin formation has occurred in a plate convergence context. To understand the geodynamic processes that led to its formation, the Tyrrenian Basin has been selected as a natural laboratory based in its characteristics and the existence of available previous data sets. It is believed that it shares some similarities with the other Mediterranean basins, therefore is possible to extrapolate conclusions.

In addition, the Tyrrhenian fulfils some conditions that make it an ideal study area:

1. In a first place, the basin has had a continuous evolution and without interruptions since the upper Oligocene until present days. In fact, in some areas of the Calabrian Arc, at the southeast of the basin, there are geodynamic processes still active. This allows a continuous information sequence without posterior deformation.

2. From the previous point, it can be inferred that if the geodynamic processes that formed the basin are recent, the sedimentary thickness is lower in comparison with the other Mediterranean basins. This fact has allowed obtaining a detailed seafloor bathymetry, that resembles fairly well the underlying tectonic structure. This allows a better knowledge of the 3D tectonic structure of the area.

3. In a third place, both Tyrrhenian conjugated margins can be studied in a reduced area, in contrast with other basins with more developed rifting processes. This allows to easily surveying both margins in a single oceanographic campaign, and they can be correlated to study the symmetry/asymmetry of the structures and the processes that generated them.

4. To conclude, the Tyrrhenian basin shows different areas with different extensional rates.

The subduction front has migrated progressively towards the southeast of the basin throughout the time, and subduction has been slowed since the upper Oligocene. At the present day, the rifting processes are absent at the northern area, and by contrast, as it goes towards the south subduction processes stopped later. This make easier to analyse the different extensional episodes of the basin.

Therefore, broadly speaking the objectives of this thesis work can be described into the following points:

- Characterization of the structure and physical properties of the mantle and the crust at the SW of the area of study (*3rd chapter*): Physical properties of the mantle and the crust have been studied using wide-angle data acquired during the MEDOC survey. OBSs were placed following the path of a former MCS profile acquired during the Italian CROP-MARE survey (1994), reprocessed by me. The OBS data was used to obtain a tomographic velocity model of the southwestern Tyrrhenian, which has been compared with 1D velocity gradients to identify each crustal domain.

- Characterization of the tectonic processes (*5th chapter*): The multichannel MEDOC profiles were processed together with the Italian CROP-MARE section to image the crustal structure, with the aim to unravel the processes that have been working on the area and its evolution along the time. Once identified and characterized all the faults and other extensional structures in the basin using the multichannel data, crustal structure can be interpreted at basin level. From here it's possible to identify the main deformation phases, their associated structures and the geometric relations between them, and finally understand relations between them and its evolution.

- Identification the sedimentary units and basin stratigraphy (*4th chapter*): In this case, the data obtained from the multichannel sections were the geometry of the sediments – the wedging and angular discontinuities of the syn- and post-rift deposits - and their seismic facies. The ODP drilling data has been used to calibrate the horizons together with some ST multichannel profiles (from SIT survey, data also given up by the Italian team). And finally, the multichannel data has been interpreted to identify the seismic facies, and together with the results of the previous chapter, to identify the different crustal domains along the basin. Finally, altogether about 2000 km of seismic sections were analysed and interpreted.

2. METHODOLOGY

2.1. Introduction

Information from the subsurface can be obtained with different methods. Direct methods, like drilling or dredging, provide reliable data, but only from a limited area of the subsurface. While geophysical methods are indirect methods, they allow to obtain information of a more extensive area.

The data used in this work belongs to the seismic methods, the geophysical method which obtains the information from the response of the elastic waves that went throughout the subsurface. In this case, the elastic waves were produced by controlled sources, which in marine experiments consist of airguns of compressed air, as will be explained below.

Two kinds of seismic data have been used for this work. The difference between them are fundamentally the source to receiver distance, which are obtained with different experiment geometry and recording instrumentation. Then recorded data from the two methods are different and provide different information, and the way to process and interpret both data types are also different.

The first one is the marine multichannel seismic reflection (MCS) profiling, where the source and a line of receivers are towed behind the vessel, keeping the distance between them during all the experiment. In contrast, at wide-angle seismic experiments (WAS), receivers are deployed on the seafloor along the profile, and later the vessel goes over this line shooting the acoustic source. In this case, the distance between the source and the receivers is variable. In the first case, the goal of the multichannel seismic method is to obtain reflected energy from the subsurface. The wide-angle seismic method aims at recording the refracted and reflected energy of mainly large offsets. The use of these methods, their implications, and the treatment of the data is developed below.

As will be explained more detailed later, the data used in this thesis were acquired during the MEDOC survey, carried out between April 7th and May 8th, 2010. The cruise was carried out with the Spanish R/V Sarmiento de Gamboa and the Italian R/V Urania. In a first leg, four wide-angle seismic profiles were acquired crossing the entire basin, between Corsica or Sardinia to Italy mainland. A fifth line was collected from southern Sardinia to Sicily following the track of an old multichannel section from the CROP-MARE survey. During the second part of the survey the R/V Sarmiento de Gamboa collected multichannel seismic reflection profiles. Seismic sections were acquired coincident with the WAS profiles, and a number of additional lines concentrated in the central region of the basin. Also a single MCS profile from the CROP-MARE survey was provided by the Italian CNR and was added to the thesis dataset (fig. 2.1).

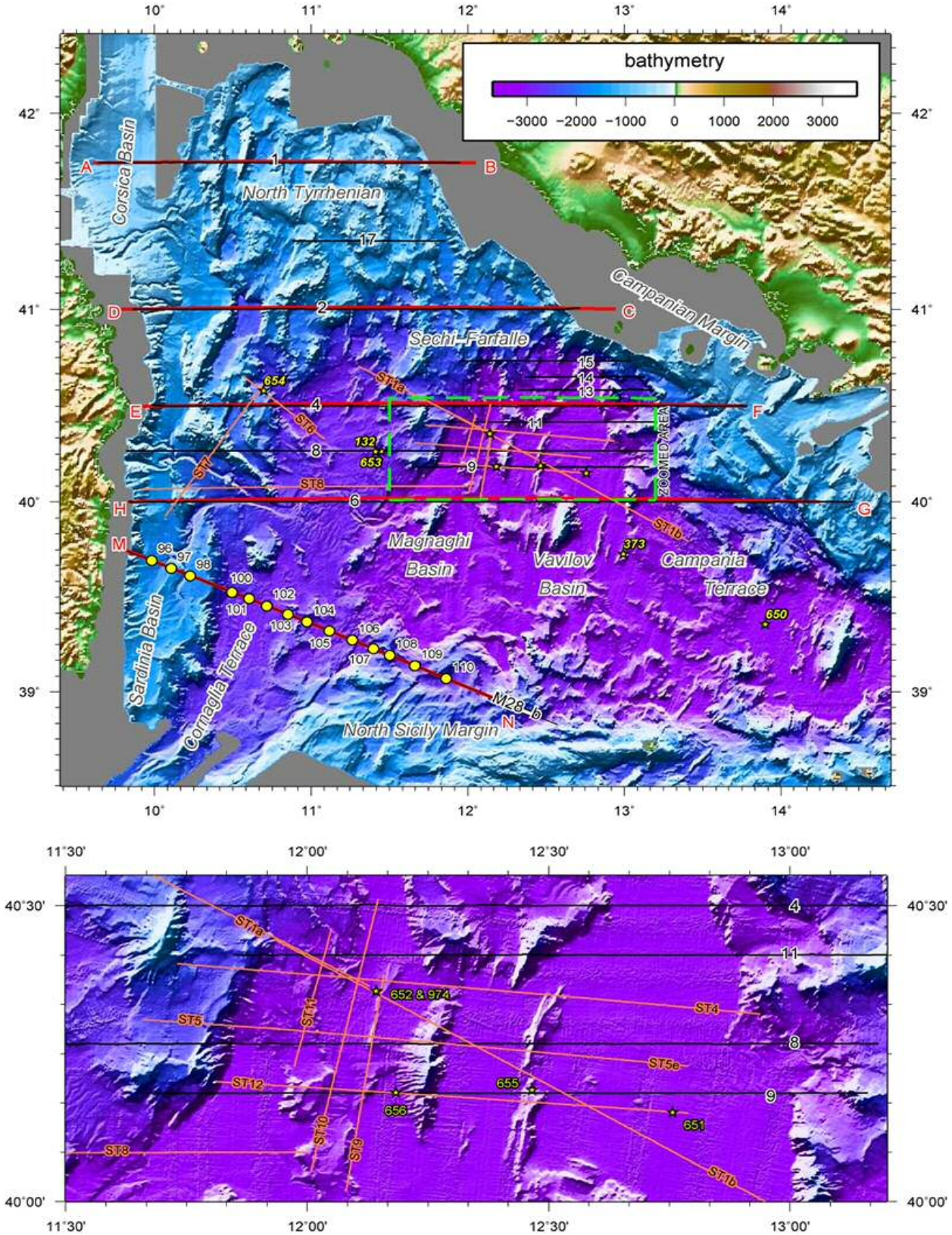

Figure 2.1: Bathymetric map showing the dataset used in this thesis. The data acquired during the MEDOC survey are the red lines (wide-angle data), and the black lines (multichannel data). Also the CROP profile (M28-b) given by the Italian CNR is plotted in black. The ST lines are the orange lines, and were acquired during the preparation of the ODP Leg 107 survey. The OBSs from the line M-N analysed in this thesis are plotted with yellow circles. Finally, the ODP and DSDP sites that were used to calibrate the horizons are the yellow stars.

2.2. Seismic waves

A seismic wave is a pulse of acoustic energy transmitted by the vibration of the solid particles. They are considered elastic waves as the medium through they propagate has elasticity and inertia, in which displaced particles transfer momentum to the adjoining particles and are themselves restored to their original position.

In seismic methods, an artificial font emits the waves at the medium, and the returning waves provide information of the subsurface through their travel time, as well as from their frequencies and amplitudes.

When a wave propagates through a solid medium, several types of seismic waves are generated. There are the body waves, which are those propagating trough the mediums, and the surface waves that travel though boundaries between two media. Within the body waves two types can be considered: the longitudinal or compressional waves, also known as P waves, and transversal or shear waves, also known as S waves. In the case of MCS data, the surface waves are considered as noise in the seismic processing. The propagation velocity of seismic waves can be defined by the following equations.

$$V_P = \sqrt{\frac{K + \frac{4}{3}\mu}{\rho}}$$ Equation 1: P wave velocity through the media.

$$V_S = \sqrt{\frac{\mu}{\rho}}$$ Equation 2: S wave velocity through the media.

where Vp is the P-wave velocity, Vs is the S-wave velocity, ρ is the density of the material, K is the bulk modulus (which measures the response of a medium to uniform compression) and μ is the shear modulus (which measures the response of a medium to shearing strains). In fluid mediums the shear modulus is null, so that for marine seismic experiments, where the energy goes through the water column, we are only interested on the P waves. Although in WAS experiments, secondary S-waves can be generated during the travel of the P-waves through the subsurface, and then can be recorded by seismometers in the seafloor.

In an ideal elastic medium the seismic waves would propagate indefinitely, but in reality as the wave spreads away from the source energy dissipates. And because of this loss, the signal amplitude decreases and the wavefront changes. The main factors causing this energy loss are the spherical divergence, the absorption and the dispersion. These two lasts mechanisms are frequency-dependent, while the first one not. This energy loss will be further explained in the processing of the MCS data, in the following sections.

2.2.1. Snell's law and Huygens principle

When a seismic spherical wave finds a change in the elastic properties of the media, it scatters by reflection, refraction and diffraction.

To explain these phenomena two ideal geological layers are considered. For simplicity, these layers are assumed to be isotropic and homogeneous, separated by a flat interface (fig. 2.2). When the wavefront reaches the interface, a portion of energy is reflected within the same medium where the energy comes, while the rest of energy is refracted and transmitted to the other medium with a change in the direction of propagation. These contacts are known in the seismic field as "reflectors". The reflection and refraction phenomena can be described by the laws derived from the Huygens principle and the Snell's law from Newton's geometrical optics.

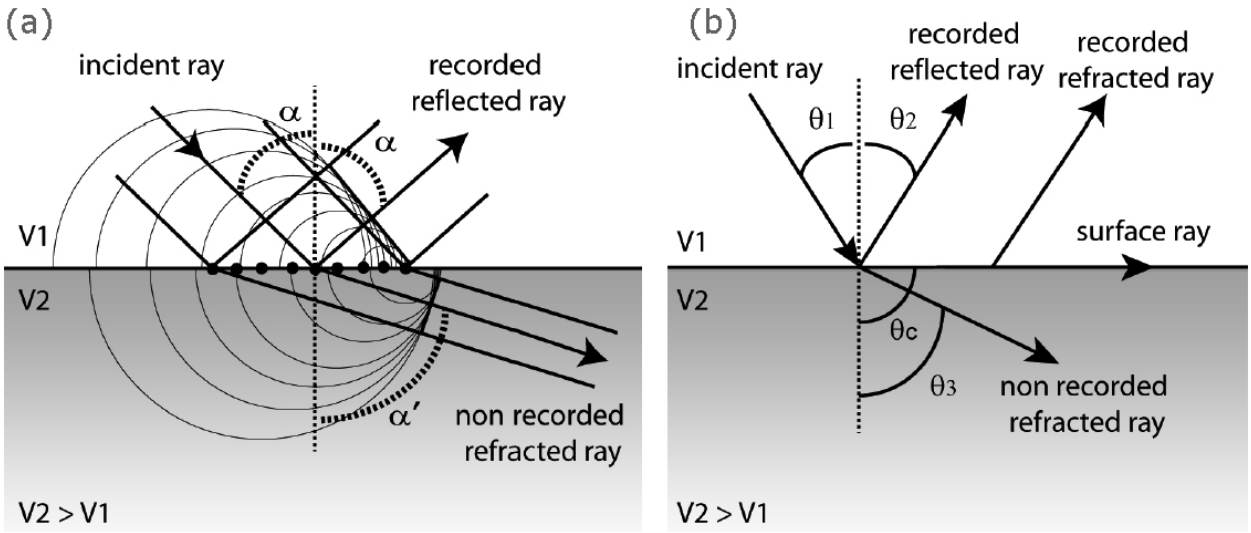

Figure 2.2: When a seismic wave reaches the interface between two strata, it scatters due to the reflection and refraction phenomena. Those phenomena can be described by Huygen's principle (a) and the Snell's law (b).

The Huygen's principle states that every single point of a wavefront can be considered as a source for a new spherical wave that propagates in all directions with an initial velocity equal to the velocity of propagation of the original wave. Then, the subsequent configuration of the wavefront can be obtained by adding up the contributions from all of the secondary sources. Therefore, when the wavefront reaches a contact between two different layers, a set of secondary sources along this reflector produce new wavefronts (fig. 2.2-b). A new wavefront returns back through the same incident medium, while other new wavefront goes through the second medium.

The reflection and refraction can also be described by the Snell's law, which relates the incidence angle of the ray, with the reflection and refraction angles. To simplify the calculations the wavefront trajectory is simplified into a raypath.

Shell's law states that in a contact between two media, the value

$$p=\frac{\sin(\theta_i)}{V_i}$$ Equation 3: Snell's law.

may have the same value for the incident, reflected and refracted rays. Where θ_i is the angle of the ray to the perpendicular of the interface and V_i is the velocity of the medium (fig. 2.2-c).

When a seismic ray reaches a planar interface, the angle of the resulting reflected ray is equal to the incidence angle, because they are travelling within the same medium, and then the velocity is the same. Meanwhile the refracted wave is propagated downwards and the refraction angle depends on the velocity of the new medium.

An important idea get from the Snell's law is that depending on the velocities and the incidence angle, sometimes the refracted wave reaches an angle of 90º with the perpendicular of the contact surface. Therefore this refracted wave travels through the interface between both layers (fig. 2.21). This incidence angle is known as "critical angle" (θ_c). In this case, as the wave travels along the interface, it perturbs also the medium around the interface, so that a refracted wave will arrive to the receivers.

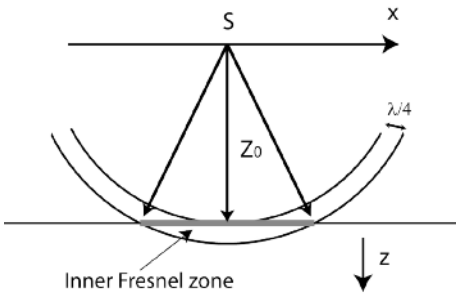

Figure 2.3: Definition of the inner Fresnel zone. Modified from Yilmaz, 2001.

The seismic prospection uses a combination of the Hyugen's principle and the Snell's law to obtain the ray tracing, the time of wave arrival, and the position of the interfaces, which produce refractions and reflections. But to know the wave amplitude, it is necessary a quantitative explanation of how secondary sources work. Fresnel theory states that the total energy arriving within a time interval equal to half the dominant period of the wave interferes constructively, and defines a circular zone on the wavefront called the inner Fresnel zone (fig. 2.3). If two reflecting points fall within this zone, become indistinguishable as observed from the surface. So, the smaller the Fresnel zone is, the easier is to differentiate between two points. Therefore, the Fresnel's zone width is a measure of the lateral resolution, which varies with the dominant frequency of the wave, the depth, and the velocity. At greater depths, the inner Fresnel zone increases and lateral resolution decreases, and vice versa for shallower depth. On the other hand, vertical resolution is determined by the dominant frequency of the

seismic source (Yilmaz, 2001).

Besides of the reflections and refractions, many geologic structures produce diffractions. For example, when a layer is cut abruptly by fault or at a discordance, in these cases the Snell's law is invalid, and the mathematical treatment becomes more complex (Trorey, 1977). In fact, mathematically speaking both diffractions and reflections are seismic waves which return to the incident medium from all directions (fig. 2.4). Thus, reflected waves represent just a singular case of diffraction.

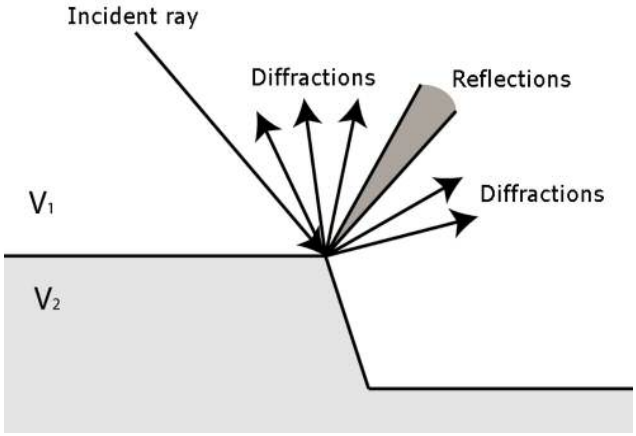

Figure 2.4: Diffractions are seismic energy scattered in all directions when the interface which separates two geologic layers with different seismic proprieties ends in a discontinuity. Reflections are a special case of diffraction where the angle of reflection equals or is close to the angle of the incident wave.

2.2.2. The convolution

During its travel through the subsurface, the wave interacts with the rocks and modifies its waveform depending on the material properties. In an ideal Earth model, the subsurface is formed by a series of layers of different physical properties. Seismically the strata are defined by their density and the propagation velocity of a wave. The product of these two magnitudes gives the acoustic impedance.

$$z = \rho \cdot v$$ Equation 4: acoustic impedance.

where *z* is the acoustic impedance, ρ the medium density, and the v is the sound velocity in this medium. Therefore the wave velocity is directly related with the density of the medium. Broadly speaking, the denser the material is, the faster the wave travels. Therefore, the arrival times of the signal to the receivers are determined by the physical properties of the strata where the wave goes through.

The impedance contrast between two layers is the reason why the incident energy is reflected and refracted in an interface. So that, the seismic signal recorded can be considered as the convolution between the initial wavelet produced by the font, and the effect that the Earth applies on it (fig. 2.11). In a simplified model can be defined:

$$x(t) = w(t) * e(t) + n(t)$$ Equation 5: seismic signal convolution.

where x(t) is the registered seismogram, the w(t) is the initial wave generated by the font, the e(t) is the Earth impulse response, and the n(t) is random noise. The "*" is the mathematical operator for the convolution, which in the frequency domain becomes a simple product. The Earth impulse response is the record that would be obtained if the initial pulse generated by the font were a spike (a Dirac delta).

Therefore the recorded wavelet is representative of the physical properties of the subsurface. As will be explained later at the MCS processing section, the aim of the deconvolution is to recover the Earth impulse response from the recorded seismogram. In fact, in MCS data processing, the deconvolution is more important than in WAS data used for travel time modelling. That is because in this last case only the time of the arrivals is important, and the wavelet shape does not affect results.

2.3. Multichannel seismic reflection

The multichannel seismic reflection method (MCS method) is the most used methods in the field of geophysics to map subsurface geological structures. It obtains subsoil information from the reflected energy of elastic waves travelling through the media. It is a non-destructive method that allows to image the subsurface obtaining information along a selected section, or even an area in the 3D MCS acquisition.

The MCS methods record amplitude changes of reflected waves, which are related to changes in the acoustic impedance of the subsurface materials. Thus, they can also be used to detect changes into the travel velocity of the waves. This characteristic allows detecting directly the physical properties that characterize the rocks conforming the crust, and so it is possible to infer the subsurface structure from these properties.

2.3.1. Data acquisition

A typical marine multichannel seismic reflection experiment consists in a seismic source that will generate an elastic pulse of energy, and a receiver array towed behind it. The pulse generated by the source travels across the water layer, goes throughout the subsurface and afterwards returns to the surface and to the receivers which record this information and send it to the recording computers. The data obtained by this method give information about the mechanical properties of the rocks and their geometry (fig. 2.5).

Data provided by the recorded signal include the time arrivals of the reflections and the waveform of the wavelet, which are conditioned by the subsurface geometry and the physical properties of the medium.

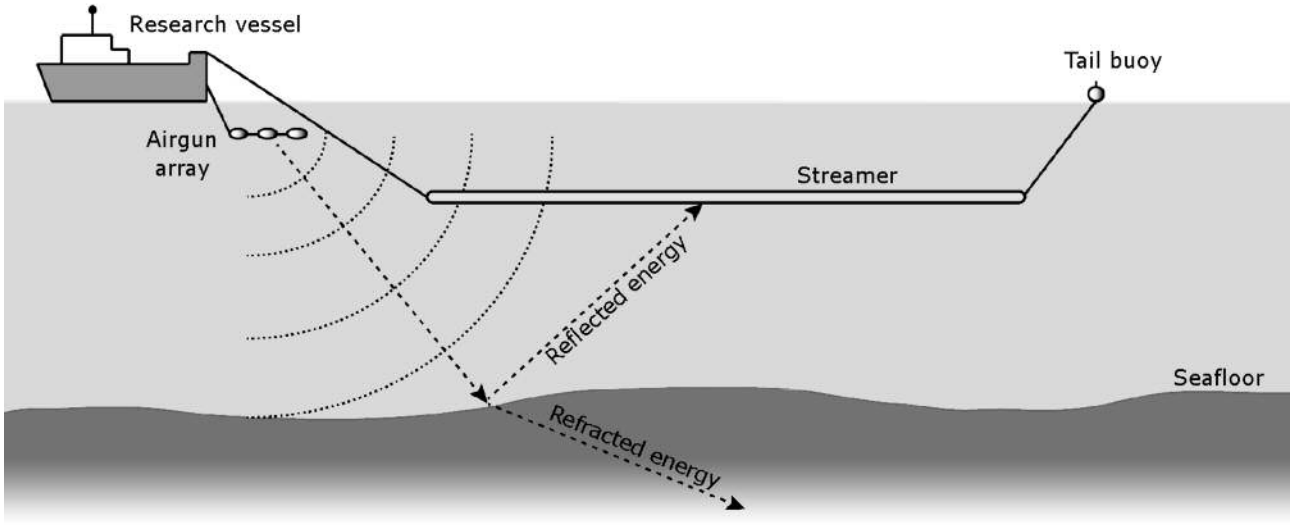

Figure 2.5:Acquisition diagram for the multichannel sections.

Different source types have been used in the marine seismic experiments through time. But since the 70's the airgun has become the most common method used by far. An airgun can be described as a chamber of compressed air that can be released rapidly into the surrounding water to create an acoustic pulse. The amplitude and frequency content of the signal generated depends on the depth of the gun into the water column and its volume. Ideally, the signal must be as close as possible to a theoretic Dirac delta (spike). But in reality, the interaction of the air bubble with the water generates secondary bursts of energy, producing a ringing in the signal. Thus, in order to minimize the bubble oscillations, an array of guns made of different chamber sizes are fired simultaneously. The aim of this procedure is to synchronize guns to obtain a constructive interference of the wavefront, increasing the amount of acoustic energy produced, and therefore, producing a greater penetration of the signal. In addition, this procedure flattens the frequency content over the range of interest for the MCS. Finally, the design of the airgun array depends on the experiment. To get higher resolutions at shallow depths the array configuration would be different from that used on an experiment where the crustal analysis is the objective, since the higher frequencies attenuates more rapidly but provide more resolution, as will be explained next (see equation 9).

Another basic element in the acquisition of the MCS is the cable with the receivers commonly known as "streamer", which is towed behind the source array. The streamer contains the receivers, which detect pressure variations of the surrounding water medium. These are the hydrophones that register the acoustic signal that comes from the subsurface. With the aim to avoid signal interferences like the swell noise or the vessel's motor, the streamer is towed about 5-20 meters below the sea surface.

These receivers are gathered in groups called "channels", and the signals registered by each hydrophone are stacked before it is sent to the recording hardware on the vessel. The

aim of this stacking is to improve the relation signal/noise, as will be explained later on the processing section. The channels configuration (spacing between them, number of hydrophones per channel, etc.) can be rearranged depending on the experiment objectives.

When the energy of an airgun shot returns to the receivers, it is detected by all of them during a certain time, known as "time recording length". This time determines the maximum depth reached by the experiment. This sequential time data is converted to sequential trace data previously to its recording on the vessel. Mathematically this operation correspond to a matrix transposition.

Finally, the signal is also pre-amplified and filtered, and converted to digital to obtain a discrete signal at regular time interval (so called sampling rate, usually between 2 and 8 milliseconds for MCS surveys). Smaller sampling interval allows for higher frequency (and resolution) to be obtained from the experiment. The maximum frequency that can be recovered is the "Nyquist frequency" (Yilmaz, 2001), defined by the following equation:

$$f_{Ny} = \frac{1}{2\Delta t}$$ Equation 6: Nyquist frequency.

where Δt is the sampling interval. The MEDOC data was sampled at 2 ms. onboard, but later it has resampled at 4 to reduce the data size without compromising frequency content. The CROP section was sampled at 4 ms. from the beginning.

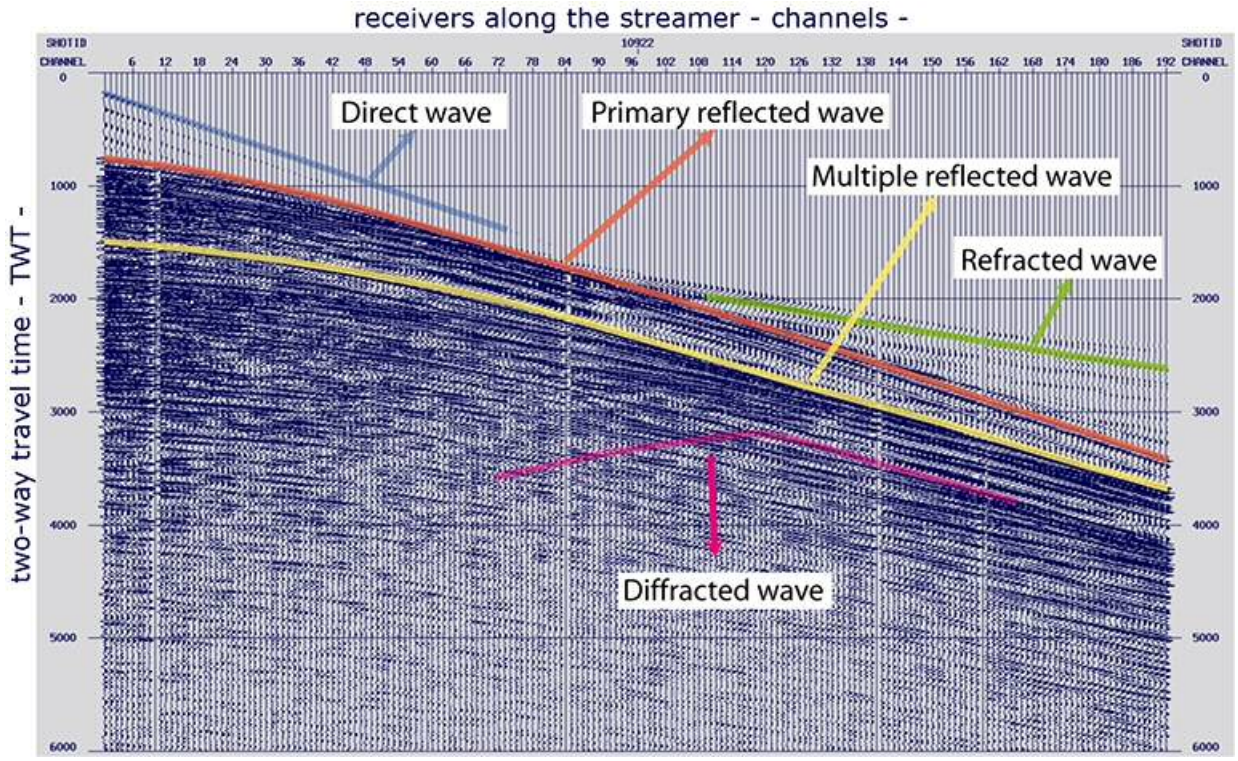

Figure 2.6: Within a shot gather can be identified the characteristic patterns of direct waves, primary and multiple reflections, refracted waves and diffracted waves.

The data recorded can be organized in different ways depending on the processing objectives. As will be developed in detail later in the processing section, the data can be grouped in shot-gathers, which implies to put all the traces generated during the same shot - single point along a seismic profile where an elastic pulse is generated - together (fig. 2.11-b). They can also be grouped into common mid-point (CMP) gathers, which gather the different traces recorded from different shots that correspond to the same mid point of source receiver pairs (fig. 2.11-c). The acquired traces can also be gathered in many other ways (e.g. by channel-gather, which gives a single-channel image of the profile acquired). For the processing of the MEDOC data, only shot-gathers and CMPs were used.

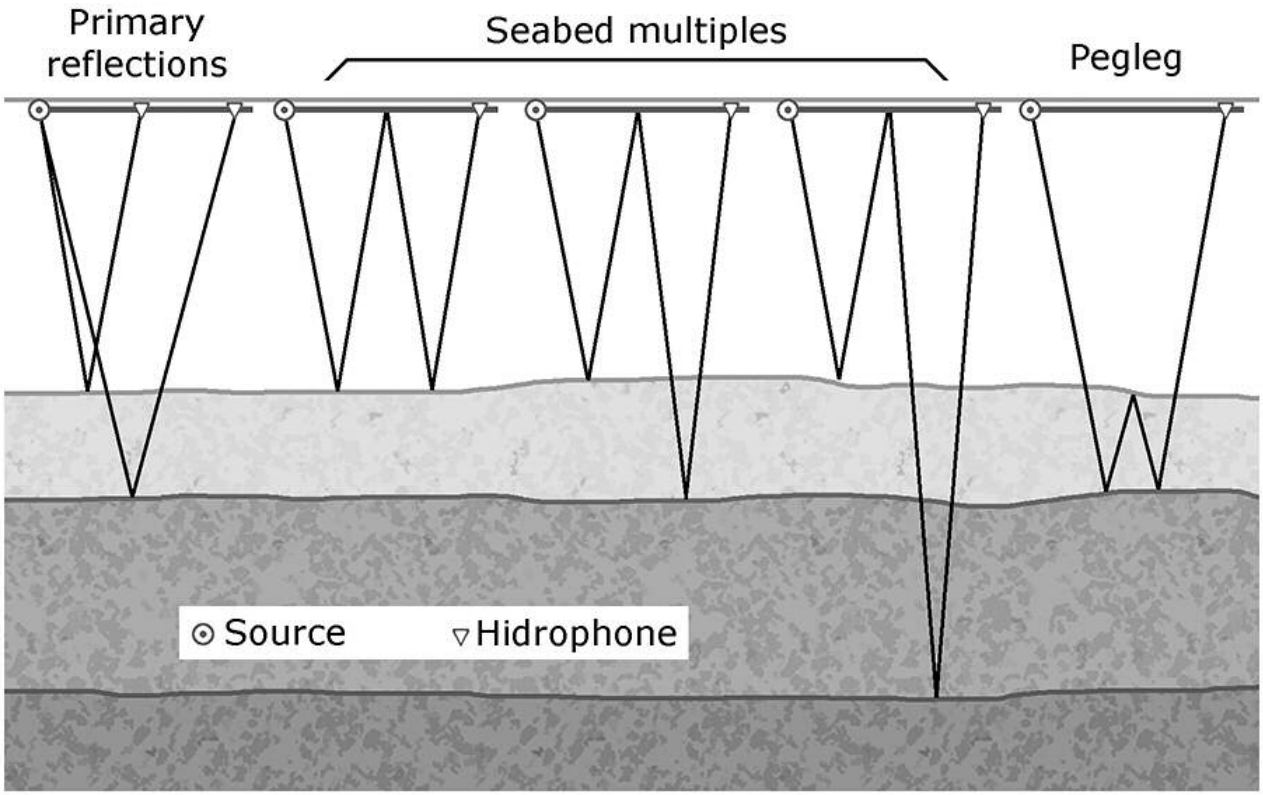

Figure 2.7: Example raypaths of some multiple noise arrivals. The minimum time for this arrivals is, at least, the double than the primay signal (left seabed multiple). A pegleg (right case) is a special type of multiple where the ray bounce more than one time within a layer.

In a shot-gather it can be distinguished different characteristic patterns corresponding to the signals of the direct wave, primary and multiple reflections, refractions and diffractions (fig. 2.6). All of them are also distinguishable in a CMP, but some of them are not as clear as the same phenomena in a shot-gather. Direct wave is energy that travels directly from the source to the receiver travelling through the water. So the time arrival directly depends on the distance between the source and the receiver (this concept is also known as "offset"). Primary reflections are first arrivals of the energy reflected in a contact between two layers, and the time of arrival varies with the offset of the receiver following a hyperbolic shape. Multiple reflections is energy that was reflected more than once before it reaches the receiver. The

figure 2.7 shows some of the possible primary and multiple reflections. The arrival time of a multiple reflection is always a multiple of the corresponding primary reflection arrival time. The refractions come from the rays that reach a reflector with a critical angle and then travels along it, as explained above. For large offsets, their time arrival is faster than the reflected rays coming of the same point. At last, the diffractions are scattered energy that returns to the incident media with an angle of reflection that differs from the incident angle. They appear also as hyperbolas in seismic records (fig. 2.6).

2.3.2. Processing flow

The final objective of the MCS processing is to obtain a final image representing a section of the earth to properly interpret seismic data and map subsurface structures. Each one of the processing steeps applied modifies the data with the purpose to enhance the reflection signal and attenuate the contributions of undesired nature as multiple reflections, coherent noise (as direct waves, refracted waves or interferences) and random noise (as instrument noise, cable noise or sea-state noise), with the aim to extract the subsurface information. That is the reason why is important to understand the operations applied to the data.

As mentioned, data from two different surveys have been used in this thesis. The first survey is the CROP-MARE survey, carried out in 1994 by the Italian CNR (Consiglio Nazionale delle Ricerche), and the MEDOC survey carried out by the Spanish CSIC (Consejo Superior de Investigaciones Científicas), which took place in spring 2010. In the first case the data consist in a single MCS section shot at the southern area of the basin: the line M28-b (fig. 2.1). The CROP survey collected high quality deeply penetrating multichannel seismic reflection data at the Tyrrhenian, Ionian and Adriatic Seas, and the Sicily Channel. Therefore, the geological context of the survey is heterogeneous and complex. But each section was planned according to structural and geodynamic processes (Bertelli et al., 2003). The acquisition parameters for this survey are specified on the table 2.1. The MEDOC survey, used two-ships for the wide-angle experiment and one ship for the multichannel reflection seismic experiment. The experiment took place on two legs. During the first one the Spanish R/V Sarmiento de Gamboa deployed the Spanish OBS pool and shot the airgun source and the Italian R/V Urania deployed the German OBS to collect five WAS sections striking E-W across the entire basin recorded on ocean bottom seismic stations and land station. The second leg with R/V Sarmiento de Gamboa collected 16 MCS profiles across the basin. Four of these MCS profiles were shot coincident with the WAS profiles, while the southernmost WAS section was acquired coincident with the CROP M28-b section. These WAS – MCS transects were located in regions with different amount of extension, while additional MCS lines were acquired covering the central region where crustal break up took place (fig. 2.1). The acquisition parameters for this survey were also specified on table 2.1.

	CROP Line M28-b	MEDOC
Year	(1995)	Spring 2010
Research vessel	OGS Explora	Sarmiento de Gamboa
Km. acquired	267 km.	1500 km.
Type of streamer	Analog	Solid state digital
Number of channels	180	276
Channel interval	25 m.	12.5 m.
Streamer length	4500 m.	3450 m.
Shot interval	50 m.	50 m.
Airgun array capacity	80.4 litres	3040.0 cu.in. (49.8 litres)
Time recording length	17 sec.	18 sec.
Sampling rate	4 ms.	2 ms.
CMP fold	45 traces	35 traces

Table 2.1: Characteristics and acquisition parameters for both oceanographic surveys, although in the CROP case (left column) it is refereed only to the single M28-b section.

Different processing flows were applied to the MEDOC and CROP M28b line depending on the quality of the RAW data, which mainly depends on the acquisition parameters, but also on the weather conditions. The general outline of the processing sequences followed in this thesis is showed in figure 2.8.

Processing on this work has been carried out basically with commercial software. For the firsts steps of the seismic processing, the GLOBE Claritas software developed by GNS Geoscience has been used. The KINGDOM Suite software from Seismic Micro-Technology was used for the geological interpretation of the seismic lines and their integration with the bathymetric data. The open source software GMT (Genering Mapping Tools) has been used to plot all seismic images and bathymetric data.

Quality control

The quality control (QC) step consists in analysing the acquired data to design the best processes to obtain a best possible signal/noise ratio. During the field work there may be acquisition problems, and thus the acquired data needs to be QC. It can present incoherent noise, like spikes, etc. The origin for these noisy records is diverse:

- It can be produced by the vessel motor, or even other marine traffic.
- A electric current noise if the streamer has some malfunction.
- The hydrophones broken, and channel fails fully or partially systematically during the experiment.
- Fish activity like bites of sharks, can also affect the receivers on the streamer punctually.

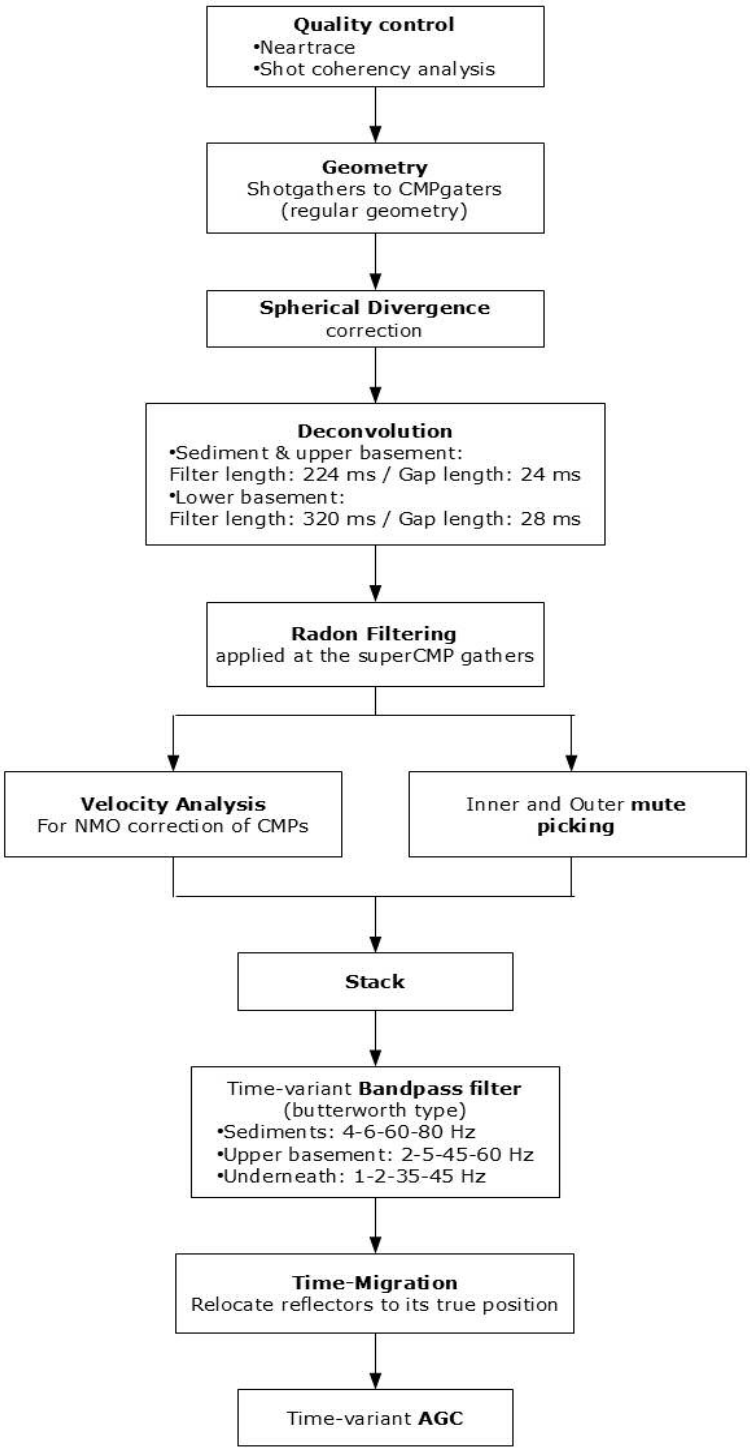

Figure 2.8: Processing flow followed for the MEDOC and M28-b MCS profiles.

To achieve the QC, data should be displayed in true amplitude to detect wrong data, for example traces with anomalous amplitude. This process can be done in several ways.

The first one is to read shot by shot to control the coherence among the traces of the same shot. This process allows to detect some anomalous amplitudes at the traces, spikes, or incoherent noise that hides the signal and that are usually related with channel malfunctions (fig. 2.9-a).

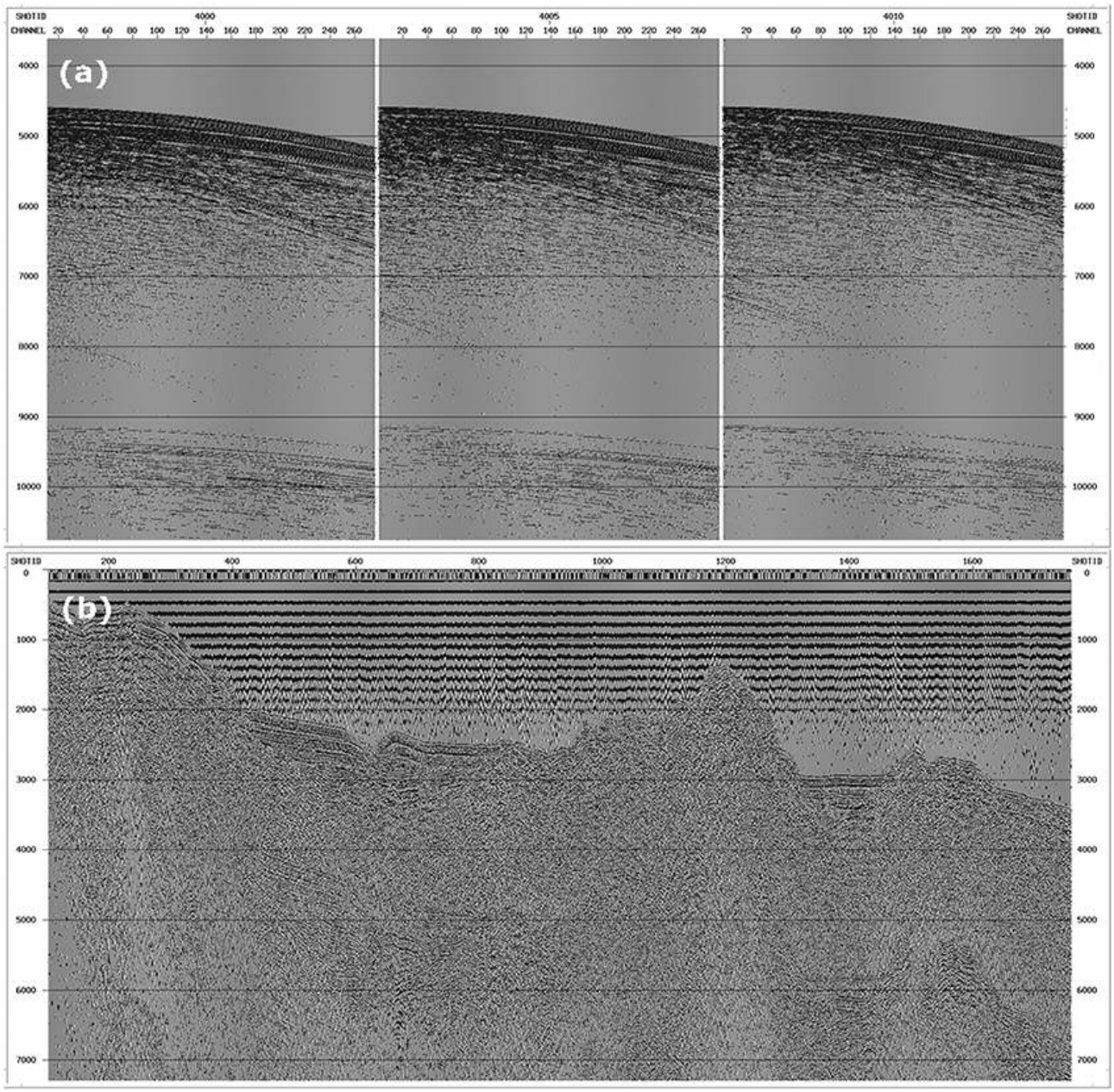

Figure 2.9: (a) Example of some shots from MEDOC 8 with no processing applied. This display allow to detect traces (or even entire shots) with incoherent noise. (b) A near-trace display consist in plot the first trace of each shot to test the lateral coherency of the data. Like in the shots case, these data have no processing applied.

A second control applied consists in imaging the complete seismic profile. It can be done plotting only the same channel for each shot, producing a single-channel profile (fig. 2.9-b). Usually the chosen channel is the nearest one because it is the one with the higher frequencies that provide more resolution. This process stands out the lateral incoherences along a profile, like abrupt changes in trace amplitude along the profile, or some sections in the profile where

no shots were recorded. However, the most common QC is to produce a brute stack with a simple velocity model either based on known velocities from previous work or by widely-spaced velocity analyses.

Spherical Divergence correction

As explained above, the seismic signal attenuates as the wavefront spreads away from the source and it acquires the approximate shape of a sphere. Then, the spherical divergence is the phenomenon that happens with the expansion of the wavefront when the signal propagates. It produces a gradual decrease in the amount of energy per unit area (intensity) of the wavefront. Since the area increases by the square of the distance travelled, intensity falls off inversely as the square of the distance, while amplitude falls off inversely as the distance. That's the reason why it is necessary to correct the amplitude during the processing of the seismic data by increasing the amplitude in inverse proportion to the distance travelled. That is by a factor of 1/VT where V is the propagation velocity and T the two-way travel time, as shown at the next equation.

$$A \propto \frac{1}{r} \propto \frac{1}{vT}$$ Equation 7: amplitude attenuation in a homogeneous medium.

But this factor is valid for a homogeneous medium. But for a geological layered model, with increasing velocity in depth, amplitude decay can be described next way:

$$A \propto \frac{1}{v_{RMS}^2 . T}$$ Equation 8: amplitude attenuation in a layered model.

where v_{RMS} is the root mean square velocity of the medium (Newman, 1973). As will be explained later on the velocity analysis section, the v_{RMS} depends on the medium. That is the reason why is necessary to do a first approximation of the velocity model to apply the correction function.

In practice, the GLOBE Claritas software uses a velocity file in order to apply a correction factor to the amplitudes. This correction factor is a gain in dB/sec.

At the other hand, the energy of a seismic wave is also attenuated by heat dissipation because of particle motion while the signal travels across the rock. The dissipation occurs because of inelastic processes like the internal friction or the fluid presence in the pore space, which is temporarily deformed by the passage of the seismic wave. This effect is frequency-dependent and leads to a loss of high frequencies that attenuate faster than the lower frequencies. Therefore, if the resolution is directly dependent of the wavelength, and this is inverse to the frequencies, at shallow depths one can get more resolution, while as the wave

advances trough the subsurface, the higher frequencies are lost and the resolution decreases. The attenuation decays according to the following law:

$$A(t) = A_{(0)} \cdot e^{(\pi f t / Q)}$$ Equation 9: attenuation for an elastic wave.

where f is the frequency and the Q is the energy lost in each period of the wave. If the high frequency components of the wavefront take the rock through more oscillation cycles per km than the low frequencies do, high frequencies lose more energy than the low ones over the same travel path, and attenuates sooner. This fact determines the bandwidth of seismic data. Thus, typically for MCS surveys shallow reflections have a wide bandwidth of up to about 120 Hz in the first second, which drops to about 60 Hz at times greater than 3 seconds.

Geometry

As introduced above, a shotpoint is the single point along a seismic profile where an elastic pulse is generated by the source. The produced wavefront can be simplified into some raypaths and as explained above, the rays travels across the subsurface and reflects at the interfaces between the layers. A single trace recorded by a hydrophone provides information from a single point of the seafloor, which falls in turn at the halfway position between the source and the receiver (fig. 2.10-a). Thus, information provided by a single shot covers a segment of the profile (fig. 2.10-b) through several traces along of this segment. Then, when the vessel advances, the segment being mapped advances too, giving an overlap with the previous position (fig. 2.10-d). This fact gives the possibility to get more than one trace mapping the same point in depth (fig. 2.10-c). This concept is known as "common mid-point" (CMP), and allows to obtain the maximum information from a single point of the subsurface. Taking this into account, the streamer length or number of channels, establishes the fold (number of traces) of a shotpoint gather. The number of traces of a CMP depends on the total number of channels, and the shot interval according to the following relation:

$$CMP\ fold = \frac{number\ of\ channels \times channel\ distance}{shot\ distance \times 2}$$

But this is the case where a theoretical ideal acquisition setting took place. This assumption implies that hydrophones are towed behind the vessel along a straight streamer that ideally goes through the shot points with the same course as the one defined by the seismic section track. This setting is obviously not real, because the streamer is a flexible wire that can be affected by superficial sea waves and cross currents. All this facts together make that the traces are allocated in a random way at the neighbourhoods of the seismic line track, and each CMP can contain a variable number of traces.

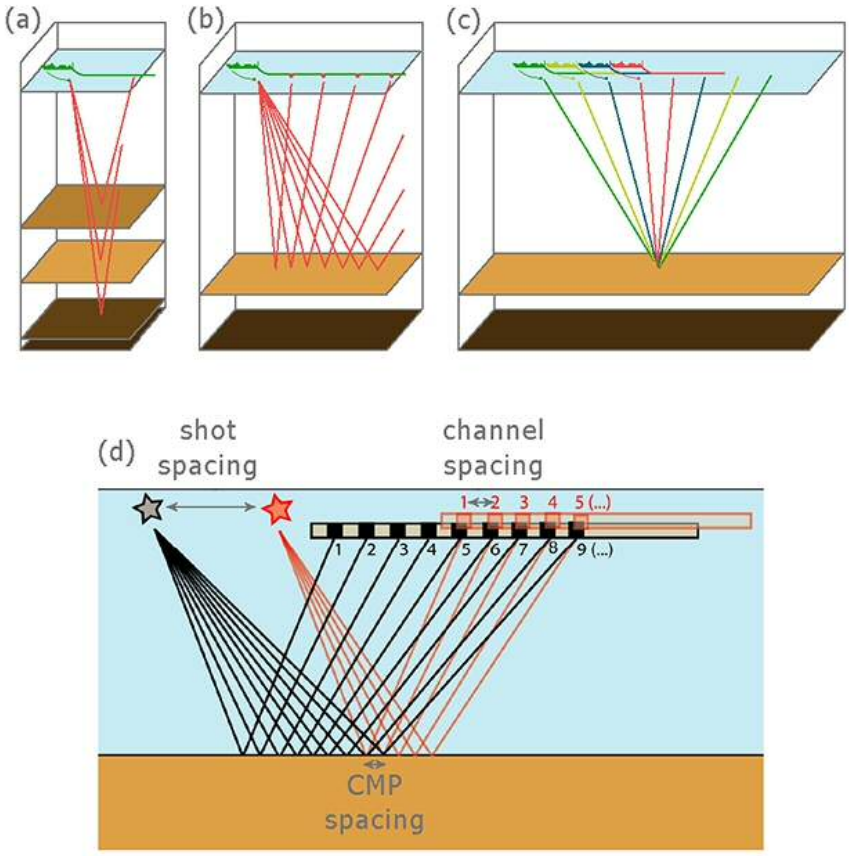

Figure 2.10: (a) The rays from a single shot travel across the subsoil and are reflected by the different layers. (b) Shot-gather concept: each shot covers a section of the profile track, which is recorded by each of the channels on the streamer. (c) CMP (common-mid point) gather concept: rays reflected in the same point in depth, coming from different shots can be gathered together in to CMPs. (d) each shot covers a section of the profile through several traces. When the vessel advances, the section covered by the new shot overlaps partially the former section. This allows a multi-coverage of several shots of a single point in depth.

Therefore, to consider a more realistic geometry requires the use of specific instrumentation to record the seismic streamer location at every shot. This special instrumentation is added to the streamer and controls the vertical curvature and the deviation angle between the streamer and the track of the towing vessel, which causes the cable to drift off-line. Instead of it, at the MEDOC and at the section of the CROP-MARE surveys a regular - theoretical – geometry has been considered because the information was not available.

Thus, according to the acquisition parameters displayed at the table 2.1, the geometry for both surveys is as follows:

	CROP MARE II	MEDOC
CMP distance	12.5 m.	6.25 m.
CMP fold	45	34.5 (*)

Table 2.2: The CMP distance can be interpreted as the CMP coverage, also known as "bin". (*) In fact, CMPs of the MEDOC survey have variable fold. This means that some of them are formed by 34 traces, and some of them by 35 traces alternatively. The number of shots and CMPs per section is shown at the annex 2.

Deconvolution

As introduced previously, a seismic trace is the result of the convolution of the initial wavelet and the Earth impulse response (equation 5), as a result of the interaction of the wave with the different layer boundaries of the subsurface because of the acoustic impedance variation (fig. 2.11). Therefore, the Earth response is representative of the subsurface physical properties. Then, to get this Earth response is necessary to remove the initial wavelet from the data, and it can be done with the deconvolution, which as the name suggest, it is the inverse process of the convolution.

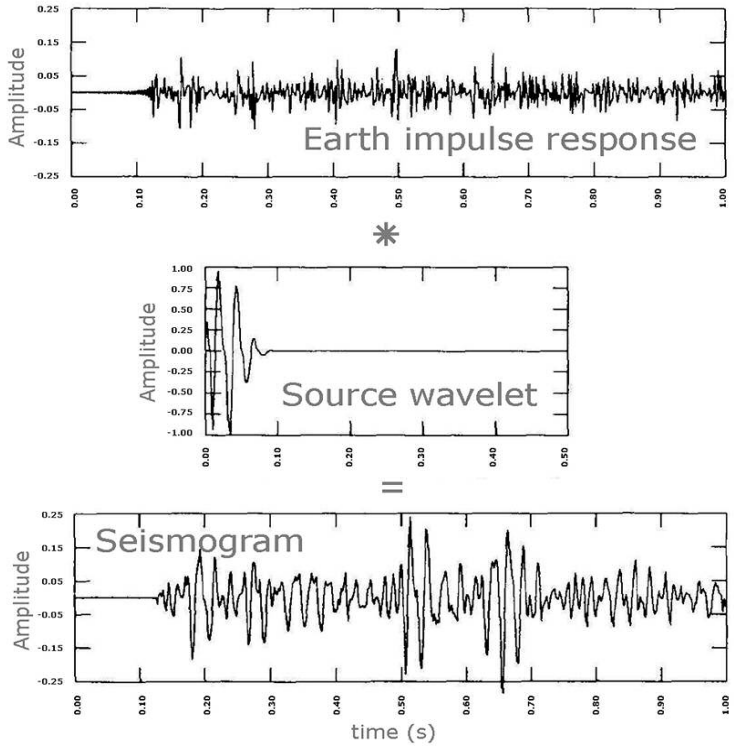

Figure 2.11: Graphical representation of a seismic trace in terms of the convolution model explained by equation 5 (without the noise term), being x(t) the recorded trace, w(t) the source wavelet and e(t) the Earth's impulse response. After Yilamz [2001].

In the time domain, the convolution consists of a quite complex mathematical operation, whereas in the frequency domain it becomes a simple multiplication. That is the reason why the recorded time signal is converted to the frequency domain using the Fourier transform to resolve the deconvolution. If the noise term of the equation 5 is neglected, then it is now written as follows:

$$A_x(\mu) = A_w(\mu) \cdot A_e(\mu)$$ Equation 10: convolution in the frequency domain.

where $A_x(\mu)$, $A_w(\mu)$, and $A_e(\mu)$ are the amplitude spectra of x(t), w(t), and e(t), respectively (Yilmaz, 2001). Therefore, if the initial wavelet w(t) is known, the solution to the deconvolution problem is merely deterministic. But in seismic experiments the initial wavelet is usually unknown, therefore e(t) should be determined with statistical methods.

The graphical representation of the equation 10 is show at the figure 2.12. In there, can be observed that the similarity in the general shape of the amplitude spectrum of the wavelet – $A_w(\mu)$ – and that of the final trace – $A_x(\mu)$ – is clear. It is generally accepted that the rapid fluctuations observed in the amplitude spectrum of a seismogram are manifestation of the Earth's impulse response, while the general shape is associated fundamentally with the input wavelet (fig. 2.12). This fact can also be observed in the autocorrelation functions of the three signals (fig. 2.12-b). That is, correlating the traces with themselves. Therefore, there is the possibility to autocorrelate the registered trace to estimate the amplitude and the phase spectra of the initial wavelet w(t). This is the base of the statistical deconvolution, which is used in the MCS processing.

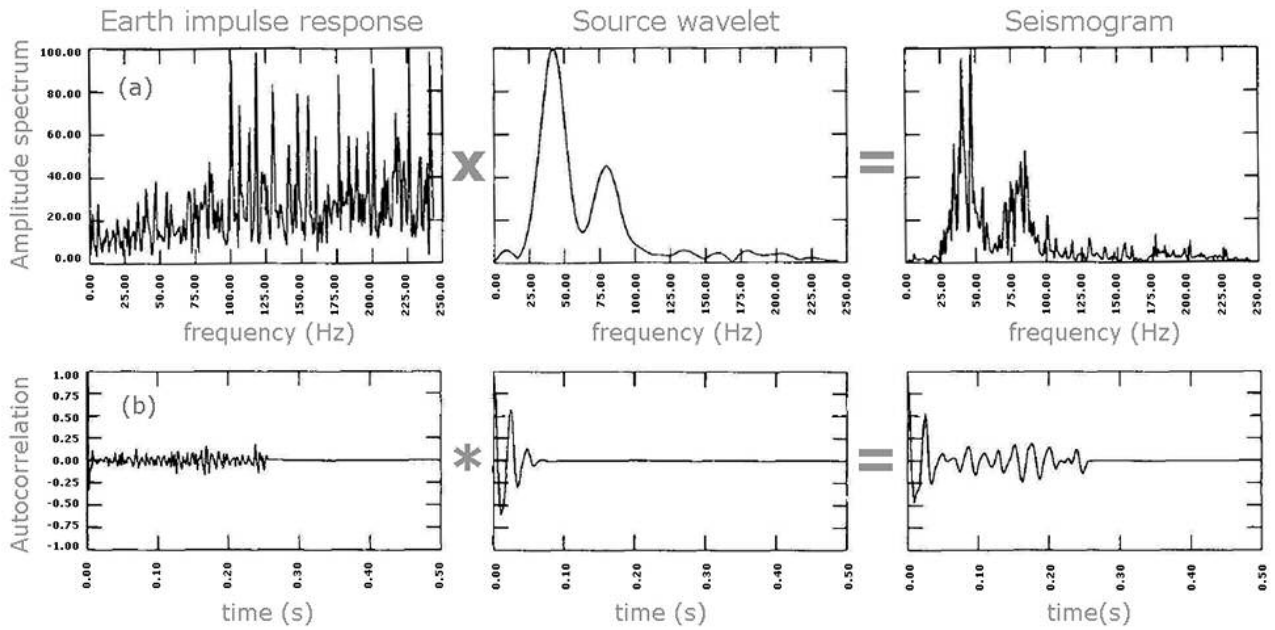

Figure 2.12: (a) Frequency spectrum of the seismogram Ax(μ) as a result of the multiplication of the seismic wavelet Aw(μ), and the Earth's impulse response Ae(μ). (b) Autocorrelation functions of the three seismograms shown in figure 2.11. The registered seismogram (left) gets the first peak from the Earth's impulse response, and the rest come from the font. After Yilamz [2001].

In practice, to apply the deconvolution is necessary to define a time interval at the CMP, called "design window" from which the autocorrelation function of the seismogram is computed to estimate the amplitude and the phase spectra of the wavelet. The deconvolution uses a Wienner filter in the frequency domain, also called "operator", which is calculated within this design window. This filter is also known as predictive filter since it can predict the coherent energy form the initial wavelet and subtract it form the waveform (Peacock and Treitel, 1969). For this filter is necessary to define an operator length too. Later, the operator is applied within a time window, or "application window", to filter the effect of the source form the recorded signal, and increase the temporal resolution.

Another important consideration is that the spherical divergence correction should be applied before the deconvolution. That is because deconvolution is formulated for plane waves

so tat the spherical divergence recovery is needed. In practice, as long as the data are well balanced, deconvolution works well.

In this thesis, after numerous tests, two design windows were used considering the different seismic facies of the sedimentary cover and the basement at one hand, and the energy loss of the seismic wavelet with depth at the other hand. It was also important not to include the multiple noise in the design windows, wherever possible. The operator length for the first window was 224 ms while for the second was 320 ms.

Velocity analysis

The final objective of the velocity analysis is to get a velocity function to correct and stack properly the traces of all the CMPs to form a seismic section to image the subsurface. Then, a stack is the lateral sum of the traces of the same CMP to obtain the maximum information of a single point in depth. But in addition, the stacking process attenuates the random noise registered. The incoherent noise is diminish by destructive interference that minimizes it because of its random character. In contrast, the signal is amplified by constructive interference. Thus, this process increases the signal/noise ratio. Strictly speaking there are two types of noise. The incoherent noise does not show any correlation between nearby traces and its amplitude is unpredictable. It does not appear in a seismic record if you shot two times in the same location, for instances the sea waves or a shark bite. At the other hand, the coherent noise appears every time you shot in the same location, for example a multiple. The stack attenuates very efficiently the incoherent noise but not so efficiently the coherent. As will be explained later, this last has to be attenuated by filtering or muting. Although in some cases stacking will attenuate it this noise does not align well with a normal move-out (NMO) correction applied, as will be discussed next.

Previously to stack the traces of a CMP it is needed to enhance the lateral coherence between them. This can be done correcting the differences in the time arrivals between the near traces and the far traces. That is, to flatten the hyperbolic behaviour of a reflection within a CMP (fig. 2.13), supposing a vertical incidence of all the rays to the reflector.

As explained previously, a CMP gather is the group of the different traces reflected to the same point in depth but at different offsets, assuming constant velocity and horizontal layers. As source-receiver distance increases so does the travel time of the ray. Then, for a theoretical horizontally layered Earth model the relation between time arrivals and the offsets, the traveltime equation, is hyperbolic. If the layers are not completely horizontal, the traveltime equation gets complicated. In practice, if the dips are gentle, the hyperbolic assumption is made for conventional velocity analysis. But in the case of reflectors with arbitrary shapes and/or with strong lateral velocity variations, this hyperbolic assumption is no longer valid.

The difference for the time arrivals of a reflection at a given offset, and at zero offset is called normal "move-out" (NMO). And the velocity required to correct this NMO to flatten the reflector is called the "NMO velocity" (fig. 2.13). It is a dynamic correction (i.e. different for each trace of the CMP) and it is one of the most important steps in the processing sequence. Applying this correction one can see the horizontal alignment of the arrivals at the different traces of a particular reflection, obtaining the maximum lateral coherence. However, the velocity that can be reliably derived from seismic analysis is the velocity that yields a best stack.

At this point, it is important to introduce the different velocities that one can work with during the processing:

- Interval velocity: Is the real velocity corresponding to each layer. That is, the geological velocity of the material which determines the wave propagation velocity. The formula is the next:

$$V_{\text{int}} = \sqrt{\frac{(V_{RMS,n})^2 t_n - (V_{RMS,n-1})^2 t_{n-1}}{t_n - t_{n-1}}}$$ Equation 11: interval velocity.

  where $V_{RMS,n}$ is the root mean square velocity for an "n" layer, and t_n is the time interval that the ray lasts to cross the layer.

- Average velocity: It is the average of all the interval velocities from the surface to the depth of a certain layer. The formula is as follows:

$$V_{ave} = \frac{\sum_{i=1}^{n} V_i \Delta t_i}{\sum_{i=1}^{n} \Delta t_i}$$ Equation 12: average velocity.

  where V_i is the interval velocity for a certain layer, and Δt the time that the ray lasts to cross the layer.

- Root mean square velocity: It is a mathematical result supposing a theoretical Earth where the layers are horizontal and homogeneous. It also allows to understand the relation between the V_{ave}, V_{int}, and the V_{NMO}. The formula is the next:

$$V_{RMS} = \frac{\sum_{i=1}^{n} V_i^2 \Delta t_i}{\sum_{i=1}^{n} \Delta t_i}$$ Equation 13: root mean square velocity.

  where, like in the former case, V_i is the interval velocity for a certain layer, and Δt the time that the ray lasts to cross the layer.

- Stack velocity: The concept is similar to the NMO velocity but it is not exactly the same. The stack velocity is referred to each reflector. That is, the correction that allows to turn a certain reflection horizontally without consider the upper corrections of other

reflectors of the same CMP.

- NMO velocity: As defined above, the normal moveout describes the shape of a seismic reflection recorded at different offsets. The necessary velocity to correct this effect is the normal moveout velocity. It allows to relocate the CMP reflections horizontally to stack them correctly.

Is important to note that each one of the first three velocity concepts cannot be calculated without to known previously the value of the other two. In fact, the only way to get these values is to measure them directly at the field during the survey, with a diagraphy on a well. But an MCS acquisition survey does not allow to measure these velocities per se. At the other hand there is a subtle difference between NMO velocity and stacking velocity that is often ignored in practice: NMO velocity is based on the small-spread hyperbolic travel time, while stacking velocity is based on the hyperbola that best fits data over the entire spread length (Yilmaz, 2001). Nevertheless, stacking velocity and NMO correction velocity generally are considered equivalent.

In practice, to get the seismic velocities for stacking there are two techniques that can be complementary. They are the semblance analysis and the constant velocity stack analysis.

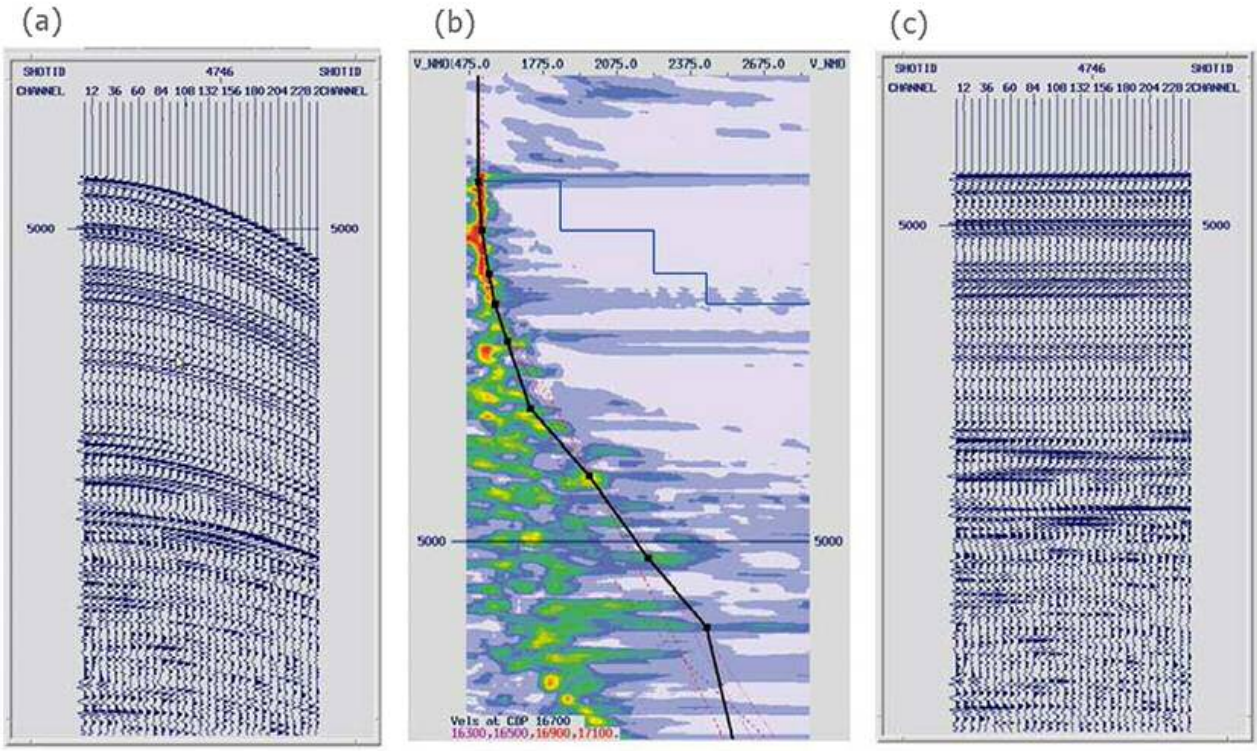

Figure 2.13: Example of a single CMP before (a) and after (c) NMO correction. The central panel (b) is the corresponding velocity function, where the black line is the velocity function and the blue steped line is the calculated (by the software) interval velocity between the picked points.

The semblance analysis consists in the measurement of the signal coherency along a hyperbolic trajectory over the entire spread length of the CMP gather. The idea is to display the

signal coherency on a graph of velocity versus two-way zero-offset time, and choosing the velocity function that produces the highest coherency at times with significant event amplitudes (fig. 2.13-b). This means that it measures the coherence between traces for several different velocities. The idea is to display the signal coherency on a graph of velocity versus two-way zero-offset time. The test of the best velocity consisting in stacking the traces of the CMP for several different velocities, producing maximums and minimums of energy depending on how well they correct the NMO. When the lateral coherency is higher, reflections becomes horizontal and the stack results in a maximum of energy, otherwise a destructive interference is obtained and it results in a minimum of energy.

Although it would be ideal to determine the velocity function for each CMP gather, it is often redundant and is not necessary as long as the region of the analysis does not present a complex geologic structure. So, this analysis is usually made at spaced CMP gathers (for example, every 2-5 km) and interpolating the results for the intermediate CMP gathers.

Accuracy in velocity picking depends on cable length, the two-way zero-offset time associated with the reflection event, and the velocity itself. The higher the velocity, the deeper the reflection and the shorter the cable length, the poorer the velocity resolution. The velocity range used in the analysis must be chosen carefully, as it should span the velocities that correspond to those of primary reflections present in the CMP gather. The velocity increment must not be too coarse, as it can degrade the resolution, especially for high-velocity events and/or far offsets. In fact, when picking the velocity function, two velocities are displayed over the semblance analysis (fig. 2.13-b). The first one is the root-mean square velocity, which by definition it always increases in depth since its formula (equation 13) includes the summation of the former interval velocities. The second is in fact the interval velocity, and in general it increases with depth since the velocity is directly related with the rock density, and because of the compaction, density always increase in depth. There is one exception to this rule: when there are salt deposits present, as is the case of the Tyrrhenian Sea. When evaporitic deposits are present, interval velocities decrease just below this layer, while the V_{RMS} keeps the increasing trend with increasing TWT.

With this in mind, it should be considered that the multiple of the seafloor at the velocity analysis is quite energetic and gives a maximum at the semblance analysis. But it is often easy to recognize and avoid since it implies unusual low velocities (around 1,500 m/sec.) at higher depths. In addition, if this maximum were picked it would imply that the V_{RMS} decreased with TWT. And as explained above, this is not possible.

At the other hand, the constant velocity stack analysis consists of the NMO correction and stack for an ensemble of CMPs with a single velocity value. As a result, some reflections become corrected and stacked in a constructive interference, while other reflections result in a

destructive interference and disappear. If the operation is repeated for different velocities, one gets several panels of different velocities with different reflections imaged in each of them. So than one can see the effect that each velocity produces over each reflection. And from here, the better stack velocity function can be determined. Nevertheless velocity resolution decreases with increasing depth, and because of that, deep events seems to stack at a wide range of velocity values, thus they should been considered with caution.

Radon analysis

As developed previously, the multiple signal is a coherent noise generated when the seismic wavefront produce more than one reflection during its travel path. In general terms, the seafloor multiple signal is the strongest noise present at the seismic section. It is easy to recognize because of its time of arrival, which doubles that of the primaries, and because of the higher frequencies in comparison with the surrounding deep lower frequencies.

For the purpose of multiple removal there is the parabolic Radon transform method (PRT) which maps the primaries and multiples into different areas without overlapping them. This transform belongs to the family of generalized Radon transforms (Yilmaz, 2001), and its application to multiple attenuation is based on the idea of velocity discrimination as a criterion to distinguish between multiples and primaries.

The PRT works on the τ-p domain, where the τ represent the zero-offset time (that is where the reflection cuts the time axis), and p represents the reflections dip at the CMP (that is, their slowness, which is the inverse of the V_{RMS}). In fact, the τ-p transform is a special case of radon transform, which works as show at the figure 2.14.

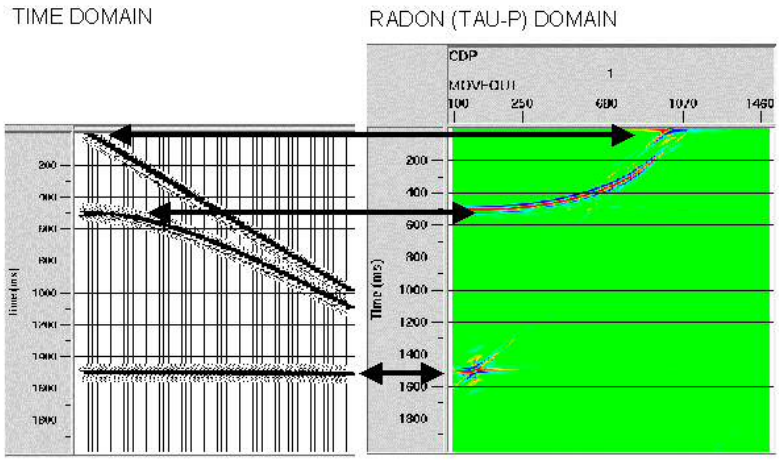

Figure 2.14: Ilustration of the PRT filtering. In the tau-p domain, straight arrivals become punctual at the tau-p domain, while hiperbolic events become parabolic. From http://www.xsgeo.com/course/basic.htm#tp

Input data should be NMO corrected CMPs, and then they show primary arrivals as flat events and multiple arrivals as NMO under-corrected events. This dip difference between the signal and the noise boost the distinction of the two signals at the τ-p space.

But prior to apply the PRT a matrix model of the noise should be constructed for the

GLOBE Claritas. This model consists of two components: a signal component, which refers to primary arrivals, and a noise component, which refers to the multiple. For each component, it should be defined the moveout ranges, which refer to the amount of parabolic moveout at the far offset. And although the model is applied at the τ-p space, it is designed at the x-t space. The parabolic moveout ranges for the two components are chosen by testing the application of the PRT in order to find the best values which remove as less as possible primary arrivals and as much as possible multiple arrivals. The moveout ranges to define the model for each section are shown at table 2.3.

The model can be applied to the data with a slight overcorrection of the NMO velocities. This way the primary signal shows positive dips while the noises dips are still negative, and therefore become easy to distinguish for the model.

	moveout ranges for the noise	moveout ranges for the signal
MEDOC 1	-	-
MEDOC 2	-	-
MEDOC 4	-	-
MEDOC 6	0 to 1650	-150 to 2000
MEDOC 8	100 to 1650	-150 to 2000
MEDOC 9	2 to 1800	1 to 1900
MEDOC 11	2 to 1800	1 to 1900
MEDOC 13	-	-
MEDOC 14	-	-
MEDOC 15	2 to 1700	1 to 1950
MEDOC 17	2 to 1650	1 to 1950
M28-b	250-1400	-150-1800

Table 2.3: moveout ranges to construct the model for PRT for each seismic section. PRT was not applied to all the MCS sections: because of the amount of time that takes to carry out this filtering, only the most representative sections were treated.

The Radon filter needs that the input data has enough internal lateral coherence. But traces within a normal CMP are usually too much spaced in meters (typically 100 m). To resolve it, is necessary to build a super-CMP gather. It consist in gathering a certain number of consecutive CMPs to get all the offsets of the geometry, and reduce the spatial aliasing caused by the long offset between traces within a normal CMP gather. This process provides more traces per super-gather and then more spatial resolution, but at the same time the definition of dipping layers becomes worse. That is the reason why when PRT filtering is finished, super-CMP gathers are reordered again into normal CMPs.

In the MEDOC data, super-CMP gathers were build with 8 CMPs, giving a fold of 276

traces per CMP and a trace distance of 12.5 m. instead of 100 m. as in the conventional CMP gather. Meanwhile in the CROP data consist in 4 CMPs, providing a trace distance of 25 m. instead of 100 m., and a fold of 180 traces.

Internal and external mutes

Because of their character, the refractions can difficult to distinguish the reflections, specially at far offsets because their amplitude are higher. One can remove these refractions simply muting them out. A mute implies a loss of some data, but sometimes is necessary to avoid signal interferences that can't be cleaned in other way. In fact, muting should only be use when noise cannot be deleted using other methods.

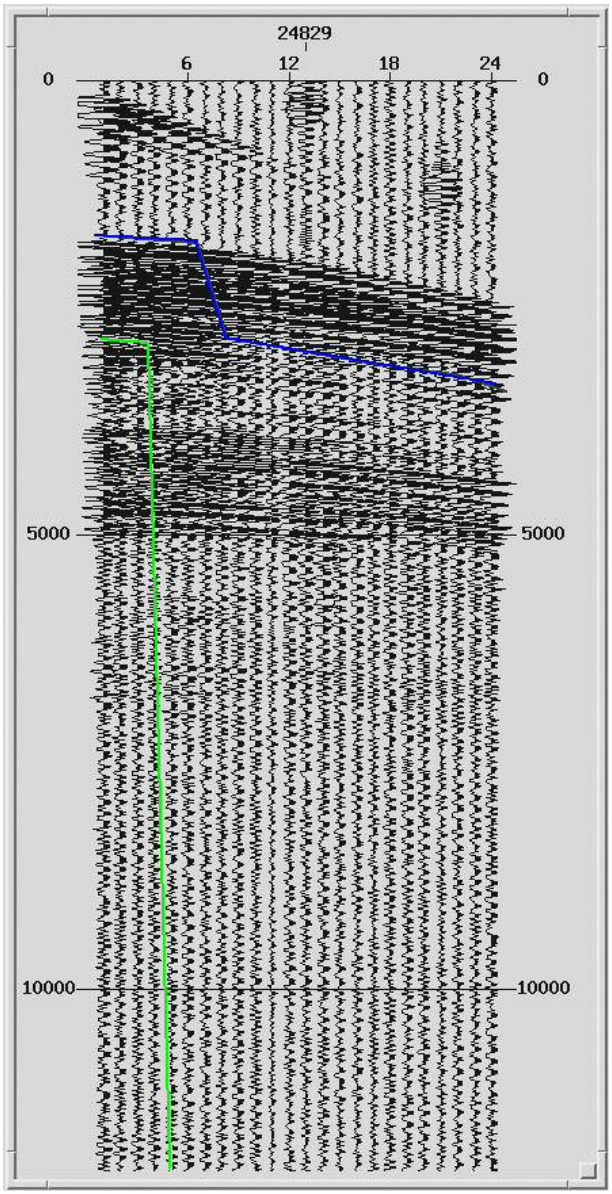

Figure 2.15: Figure caption of the mutes picked on a CMP. Blue line: external mute; green line: internal mute.

Then, two kinds of mute can be applied to the data: an external mute and an internal mute. The first one is applied in order to remove the superposition of refractions with reflections. It implies to suppress the signal of sea bottom (fig. 2.15) and to avoid to loss it,

one select only the signal on the far offstet traces, where the interferences are stronger and the signal has reduced resolution compared to near traces. As well, it allows to remove the direct wave that causes interferences where the water layer is shallow. Finally, the external mute is used where stretching of the seismic traces after NMO is severe. Stretching is a frequency distortion in which events are shifted to lower frequencies as a result of NMO correction. And if mute is not applied, stacking the NMO corrected CMP gathers will severely damage shallow events.

The internal mute has the objective to suppress the multiple noise where it has the same slope as the primary signal (fig. 2.15), and where the Radon filter can not differentiate the primary signal, typically at near traces. Further, the multiple signal has strong energy that superimposes the primary signal. Therefore, multiple energy is never completely eliminated although NMO velocities were much higher than the multiple's velocity. Thus, it is normally necessary to apply an internal mute.

Stack

It consists in the lateral sum – a stack – of all the traces of a CMP gather to obtain the seismic section. As developed above, stacking process reduces the noise and enhances the overall quality of the primary signal (fig. 2.16).

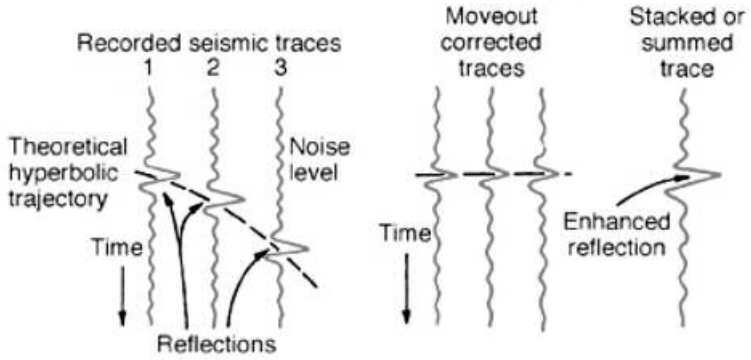

Figure 2.16: Conceptual model of a CMP stack: (left) Seismic traces of a CMP gather. (mid) Traces of a CDP gather with NMO applied. (right) Stacked trace result of the sum of all traces. From http://www.glossary.oilfield.slb.com/en/Terms/s/stack.aspx

Moreover, the stack image allows to check all previous steps of the processing flow. It is usual that the velocities should be picked more than one time once a first stack is carried out. The same occurs with the internal and external mutes, or even the PRT or filtering. That is because in a stack, the subsurface structures are more evident than in a CMP, and thus one can detect if the processing applied until this moment is good enough, or should be refined.

However, in a stack section, a zero-offset is assumed for each stack trace, that means that the source-receiver distance is zero and that the stacked trace corresponds to a normal incidence of the ray at the CMP location. Since this assumption is only valid for flat events or

geological horizontal layers, dipping reflections in a stack section are not at their true location, as well as diffractions of seismic waves that have to be properly processed before interpretation. As will be developed next, this issue is addressed with the migration, which moves dipping reflections from their apparent locations to their true location providing the proper geometry of the geological layers in the seismic section.

However, a problem with the CMP stacking is that a hyperbolic shape of the reflector is assumed, but this assumption is only correct when reflective horizons are nearly horizontal. In areas with complex structures, the wavefront is shaped by the reflective surface geometry and the travel times of each trace loose its dependence form the offset distance, so the reflection shape within the CMP looses this "regularity" (Yilmaz, 2001).

F-K filtering

Frequency-wave number (F-K) filtering is a type of double Fourier transform based on discriminating the signal and the noise energy in the F-K domain. The basic idea is that within this domain, energy of signals and noise map into different regions because of their different slope. By the double Fourier transform, time transforms to frequency (f) and the space dimension transforms to wave number (k), which is the inverse of the wavelength. Once the data has been transformed to this new domain, the area where noise energy lies is blanked and the resulting data (the estimated signal) are transformed back into the original time-distance domain. This method can be applied either in the pre-stack data, or to stacked data, as is the case of the MEDOC and CROP data.

The objectives to apply the filtering at the CMP data is to remove the multiple noise. In this case a normal moveout overcorrection of primary arrivals should be applied in order to differentiate better the multiple noise, which dips at shallow angles after overcorrection of primaries, from over-corrected primary arrivals. However, the Radon transform method removes better hyperboles and has been used for pre-stack multiple attenuation in this workflow.

In stacked sections the FK filtering has the aim to remove remainder multiple and other linear noise. It usually presents higher frequencies than the surrounding signal and can dull the posterior migration. Thus, F-K filtering was applied after stack to image deep reflections before migration.

Post-stack time migration

The migration is a process where any input signal is treated as primary reflections. That is the reason why is important to attenuate the multiple and increase the signal/noise ratio before performing migration of stacked sections. In this case a time-variable bandpass filter

has applied with the aim to further attenuate undesired frequencies from the stack. It has been built up with three windows manually picked based on geological structure. The 1st window was designed from the top of the seafloor to the base of the sediments, with filter frequencies of 4-6-60-80 Hz. The next one goes from the top of the sediment to almost the crust-mantle boundary, with frequencies of 2-5-45-60 Hz. While the last encompass from the crust-mantle boundary to the end of the bottom of the seismic section, with frequencies of 1-2-35-45 Hz.

The migration process requires an estimation of the interval velocities, which implies a geologic interpretation of the stack. Indeed, this velocity model is then used to migrate the stacked section or the pre-stack gathers - CMPs - (depending on the migration strategy used) in order to produce a geologic image. This process moves dipping reflections to their true subsurface position (e.g. opens the flanks of bowties associated to syncline structures, narrows anticlinal features, etc.), and collapses diffractions.

The migration may produce a time or depth section. The migration process that produces a migrated time section is called time migration, whereas the migration process whose output is a depth section is called depth migration. The basic principles that stay at the basis of migration are explained below.

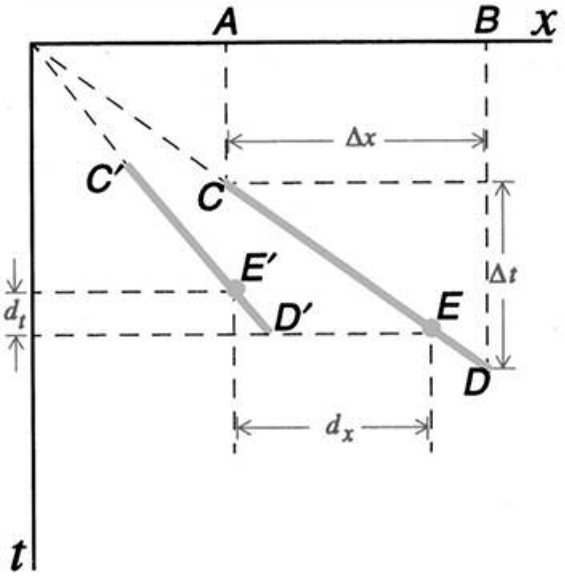

Figure 2.17: Quantitative analysis of migration process (from Yilmaz, 2001), where points C and D are moved to C' and D' after migration. The final amount of horizontal and vertical displacement (dx and dt) are calculated with equations 14 and 15.

As explain above, the reflections present in the stacked section are positioned into its true position only where they are flat; otherwise the raypath was not vertical as assumed. If the reflections dip, seismic events are erroneously treated as normal-incident events, the time arrival suggest a depth positioning that is not correct and they are located at wrong positions in the resulting stacked section. The migration moves laterally a dipping reflection to its true location (fig. 2.17). The horizontal and vertical displacements on the migrated section can be expressed in terms of the velocity of the medium v, the travel time t, and the apparent dip

Δt/Δx as measured on the stacked section (Chun and Jacewitz, 1981) by the formulas shown in equations 14 and 15.

$$d_x = \frac{v^2 t}{4} \cdot \frac{\Delta t}{\Delta x} \qquad \text{Equation 14.}$$

$$d_t = t\left(1 - \sqrt{1 - \left(\frac{v\Delta t}{2\Delta x}\right)^2}\right) \qquad \text{Equation 15.}$$

These equations show that horizontal and vertical displacements increase with time and with depth, as they are functions of velocity that usually increases with depth. Also from those equations it is clear that the steeper the dip of the reflector, the further is its true migrated position. Therefore, a reflection of the stacked section is steepened, shortened and mapped onto its true subsurface location after migration. Thus, curved geological structures as synclines and anticlines, are also true positioned after migration. When migration is applied, synclines, which appear as bowties in the stacked section, are repositioned after migration showing their true appearance. In the same way, anticlines, which appear distorted in the stacked section, are narrowed and become interpretable in the migrated section.

Migration does not only relocate the reflectors to their true positions, but also collapses diffraction curves which stand out in the stacked section when there are discontinuities along a reflector. When lateral velocity variations are mild to moderate, the diffraction curve can be approximated to a hyperbola. In this case, a common way of how migration collapses diffractions is known as diffraction summation (Yilmaz, 2001). This method is based on the summation of amplitudes along hyperbolic paths, which are modelled by the velocity field.

In practice, migration can be performed to stacked data or to pre-stacked data (CMPs). It depends basically on the nature of the subsurface geology. As long as lateral velocity variations are mild to moderate, post-stack time migration is appropriate to correctly migrate dip events and collapse diffractions, because it is the least sensitive to velocity errors, and it yields acceptable results for a reliable interpretation. Post-stack time migration is also known as zero-offset migration, since it is applied to the stack section, which simulates a zero-offset section; it is displayed in time because velocity estimation is limited in accuracy and depth conversion is not completely accurate. In addition, it is better to have both sections in the same domain, since migrated section is compared to the stacked section in order to evaluate its validity.

On the other hand, when the stack does not produce a good approximation to the zero-offset section due to the presence of complex structures with strong lateral velocity variations, depth migration is required. In fact, strong lateral velocity variations cause significant ray bending at layer boundaries, which gives rise to non-hyperbolic behaviour of reflection times

on CMP gathers. As a result, amplitudes and traveltimes associated with the reflection events with non-hyperbolic moveout are distorted during conventional CMP stacking which is based on the hyperbolic moveout assumption. Therefore, when depth migration is needed, in principle, it must be done before stack and not after in order to correctly treat the complex non-hyperbolic moveout.

But in the case of the Tyrrhenian data, post-stack migration has been considered due to the amount of sections and the time that would imply to carry out a pre-stack depth migration for each of them. In addition, in this case, a post-stack migration is enough to image properly the subsurface and carry out the first modern stratigraphy and tectonic analysis of the basin.

To build the velocity model for the time migration, interval velocities are considered. This velocity field was based on the main reflections, which follow the main geologic features that were interpreted as limits of layers with changes of seismic velocities. Secondly, post-stack time migration has been applied using a finite-difference algorithm. From the resulting migrated section, improper migrated events have been improved by a trial and error method, which consist in adjusting layer velocities and key parameters of the algorithm and repeatedly analyse the resulting migrated section. Improper migrated events due to an erroneous velocity model are distinguishable as they can produce either overmigration ("smiling"), when velocities are too high, or undermigration, when velocities are too low. Anyway, at certain depths where the reflections are not as continuous as expected, the velocity values are slightly reduced to avoid overmigrations of these reflections (fig. 2.18).

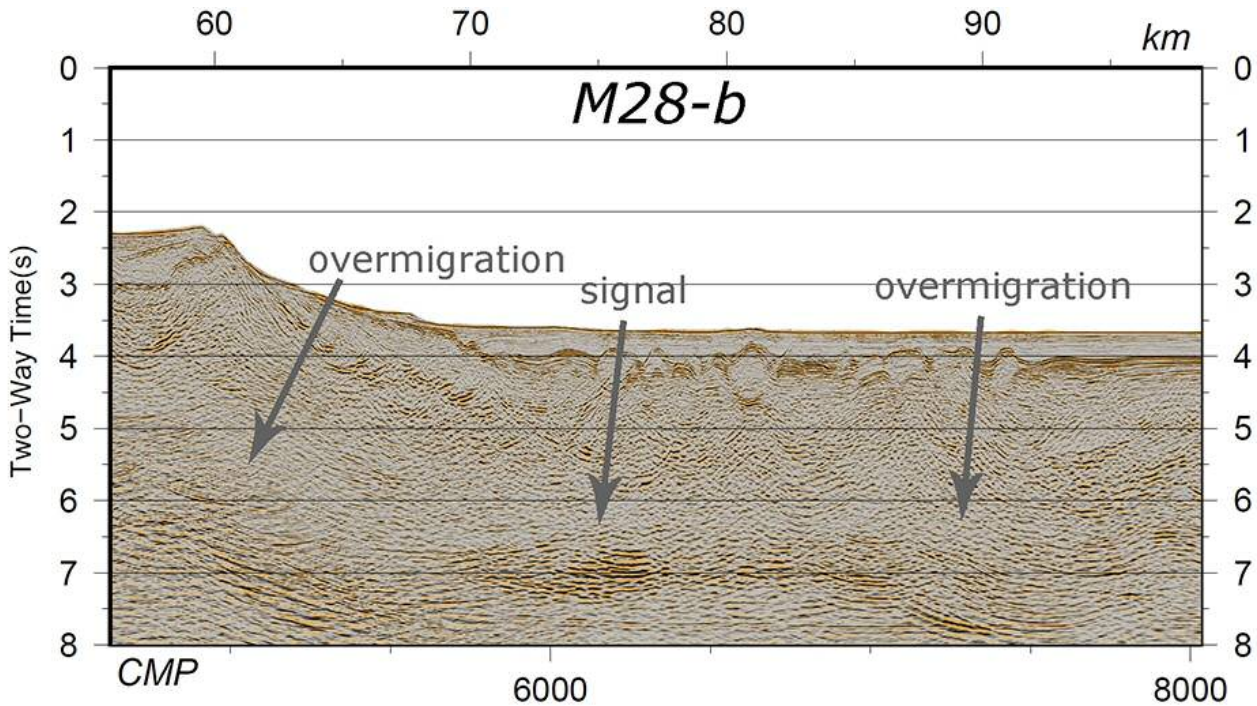

Figure 2.18: Section of the M28-b profile showing the effects of the overmigration in deep reflectors. This overmigration produces "smiles" ("u" shaped artifacts) that hide the real structure.

The software used for post-stack time migration (GLOBE Claritas) allows to vary two main migration parameters for this type of migration: the time slice to be migrated at a time, known also as the depth step or downward continuation step size and the cosine of the maximum migrated dip. The finite-difference time migration routine is based on a X-T domain implicit 45 degree migration. However, it gives reasonable results up to about a 60 degrees dip. Parameters used for post-stack time migration of the seismic data have been a depth step size of 4 ms. and a cosine of maximum dip of 0.5 (maximum dip of 60º).

2.3.3. Seismic interpretation.

Interpretation of the MCS sections acquired during the MEDOC survey would not have been possible without the consideration of other data like a high resolution bathymetry, some extra MCS lines from other surveys, and drilling data from the ODP leg 107 and DSDP (fig. 2.1).

- High resolution bathymetric data, consisting in a grid of 100x100 m., was acquired within the "Tyrrhenian Project" frame (full title: "The Tyrrhenian sea: High Resolution Morphology and Structure of a Back-arc Basin"), during a survey carried out between 1996 and 1999, by the Italian "Istituto di Geologia Marina". The acquisition was carried out by two Russian R/V, the N/O Gelendzhik during September-October of 1996, and the R/V A.N. Strakhov during February-March in 1999. Both vessels were equipped with a multibeam system EM12-120S (Konsberg-Simrad). The necessary positioning of the data was obtained through a GPS system which provided precision between 5-10 m. Also two proves XBT and CTD were used to get water velocity functions to calibrate the multibeam system (Carrara, 2002; Marani & Gamberi, 2004).

- The ST lines were acquired during the SITHERE survey, carried out in spring 1985 in the Tyrrhenian Sea by the IFP (French Petroleum Institute), onboard of the N/O Noirot from the Ifremer. The survey had the objective to acquire MCS data to prepare the forthcoming ODP leg 107. During the survey, 19 seismic profiles were shot with a total length of 1990 km. (Kastens et al., 1985).

- Finally, the data drilling data used comes from several drilling surveys that took place in the Tyrrhenian, in the context of DSDP and ODP drilling projects. First there are the DSDP site 132 acquired in September 1970 and the DSDP site 373 acquired in 1972. Finally, there are the ODP sites 650 to 656 acquired during the leg 107 carried out in 1986 (Ryan et al., 1973; Hsü et al., 1978; Kastens & Mascle, 1990). Most of these drills only bore into the sedimentary cover and does not reach the basement. But provide enough data to calibrate some important reflectors.

To work with all these data sets together with the MCS MEDOC lines, the KINGDOM Suite software was used. It allows integrating the multichannel sections with the bathymetric chart, together with the drilling information. To do this, the data needs to be georeferenced, and converted in depth the segment needed to correlate it with the drilling data.

There are two ways to georeference the seismic sections. The first one consists in applying an irregular geometry when the shot-gathers are reordered into CMP-gathers. Later, when the CMP is stacked, an average of the coordinates of each trace is calculated. Therefore each trace in the stack has their own coordinates recorded into its headers. That is not the case of the sections in this work, were a regular ideal geometry was applied. Therefore, the second way to georeference the data is to get the CMP coordinates from the shot coordinates – with a GLOBE Claritas module -, and rewrite the headers of the stacked sections. The problem with this last method is that the number of CMPs get with regular geometry and the CMPs calculated from the shot coordinates usually do not coincide, but the difference is tends to be insignificant. And if the section is not correctly positioned within the bathymetry, the KINGDOM Suite allows shifting the data.

To correlate the seismic sections with the drilling data is necessary that the MCS lines are depth converted. As explained, that is not the case of the sections in this thesis, which are time-migrated. But instead of it, the correlation with the DSDP and ODP data and calibration of horizons is still possible through the literature over these surveys (mainly Kastens & Mascle, 1990; Kastens et al., 1988; and all the corresponding shipboard reports), as will be seen on the stratigraphic chapter (number 4).

The bathymetry can be used not only to verify the correct positioning of the MCS data, In addition it can be used to correlate the tectonic structures from section to section. That is because in the Tyrrhenian, due to the thin sedimentary coverage, the bathymetry displays well a large portion of the top basement including fault blocks and volcanic constructions, and seafloor depth is even a good crustal thickness indicator. This last feature also give some hints about the boundaries of the different crustal domains, as will be explained at the structural chapter (5th chapter).

2.4. Wide-angle seismic data modelling

In contrast to the MCS velocity analysis, the wide-angle seismics (WAS) is a seismic method that consists of the acquisition and analysis of refracted and wide-angle reflected waves that result from the propagation of elastic waves through the subsurface at relatively long offsets of tens of km between source an receiver compared to a few km in typical streamer data.

Modeling of the time arrival information of these waves provides information about the velocity of propagation through the media and about the geometry of major geological discontinuities that have a contrast of impedance and produce laterally continuous reflected and refracted phases that are recorded in different receivers (e.g. the sediment-basement and the Moho boundaries). At the forthcoming sections, the acquisition system, the processing of the data, their analysis and modelling will be presented.

2.4.1. WAS acquisition system

The acquisition system of WAS data on the marine surveys consist on a seismic source, usually composed of an airgun array (fig. 2.19-a), and a set of receivers deployed at the seabed along the track of the seismic profile (fig. 2.19-b). The airgun array configuration should be different than those used for the MCS experiment, since the optimum frequencies needed for each case are different, being lower in the WAS case.

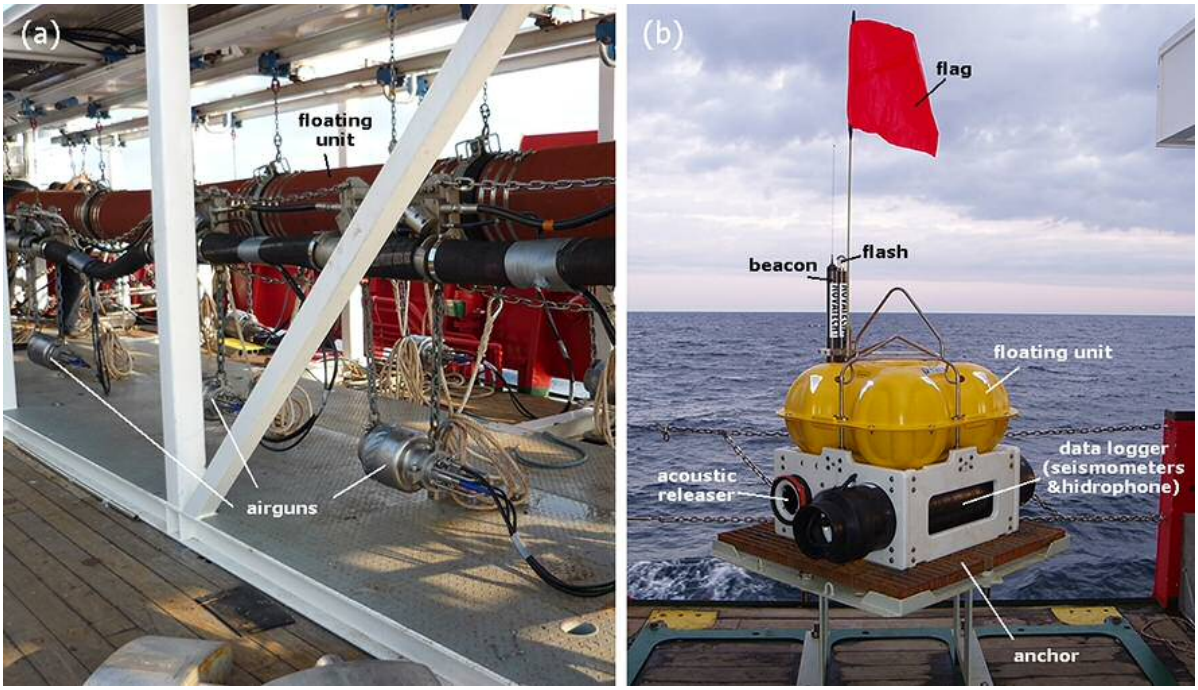

Figure 2.19: Pictures of the air-gun array (a) and the OBSs (b) used during the survey. In there, main components are tagged.

In the MEDOC case the receivers consist in Ocean Bottom Hydrophones (OBH), which can register pressure variations using hydrophones, and Ocean Bottom Seismometers (OBS) (fig. 2.19-b), that measure the three components of motion with a seismometer and also the pressure with an hydrophone. For the M-N WAS section, only OBS were used. These receivers rest on the seafloor by an expendable anchor system. When the experiment finishes, the system is recovered using an acoustic releaser that liberates the instrument from the anchor that remains on the seafloor. Then the receiver rises by buoyancy to the sea surface where it is recovered by the vessel.

The 17 OBS used in the MEDOC experiment belong to the Spanish pool and are of the L-Cheapo 4x4 type built by the Scripps oceanographic institution (La Jolla, USA), and owned and operated by the Marine Technology Unit (CSIC). Each OBS is constituted of an anchor, a 4 glass float assembly on which the lifting bail is attached, a polyethylene frame holding the sensors, an acoustic release transponder, a data logger, and a mechanical release (Figure 8.1). The float and frame components are stored separately in a custom rack system, and are assembled and tested prior to deployment on a square preparation platform which is bolted to the deck. The complete instrument weights approximately 135 kg in air. The anchor is a 45 kg iron grate held to the base of the poly frame by a single 2” oval quick-link when the release mechanism is cocked and secured. After the anchor is released for recovery, the four 12” glass balls in the float package, as well as the syntactic foam blocks provide sufficient buoyancy to lift the instrument at about 45 m/min to the sea surface. To increase visibility at the surface, an orange flag on a 48” fibreglass resin staff is attached to the floats. The recovery aids also include a Novatech low-pressure activated strobe beacon and radio. The acoustic release transponder is comprised of a main circuit board, and an ITC-3013 transducer manufactured by International Transducer Corp. These are all installed in and on a 4-5/8” aluminium pressure case. Alkaline batteries provide 18 volts power the burn, 12 volts power for the transponder, and 9 volts power for the circuit board logic. The release mechanism includes two double wire burn elements. When fresh, two battery strings are combined to provide the 18 volts to burn one of two release wires in an average of 6 minutes for water depths encountered during this experiment.

The main characteristics of the MicrOBS are the follwing:

- Dimensions: 914 mm x 660 mm x 965 cubic inches
- Weight (+ ballast): 125 kg
- Consumption: 0.270 – 0.759 W
- Authonomy: Up to 9 months
- Batteries: Alkalines (primary cells), lithium (prim cells)
- Clock: Sea Scan [0.02 - 0.05 ppm]
- ADC: Crystal CS5321 delta-sigma (24 bits)
- Dynamic range: 124-130 dB
- Sampling rate: 1 - 4000 sps
- Memory: Compact flash up to 192 Gb
- Sensors: Geophone (Sercel L-28; 4.5 Hz)
- Hydrophone (HighTech HTI 90; 0.05 – 2500 Hz)
- Release system: Two redundant electrolytic systems
- Location aids: Flash, beacon, flag

The design of the experiment includes the source design (including the number, size,

power, spatial distribution and depth of the guns), the shooting interval, and the distance between deployed receivers. These parameters are defined on the basis of the desired level of spatial and vertical resolution and the depth of the target to be sampled and modelled.

The depth of the source controls the interference of primary and ghost pulses and thus the useful frequency bandwidth of the signal emitted by the source. A ghost pulse is produced when the source is fired, and the wavelet generated spreads through the water downwards but also upwards to the sea surface. When this last is reflected down joins the original downward-traveling pulse and modifies its frequency signature. Because of this, in WAS experiments the font is set deeper than in other seismic experiments (over 10-20 meters beneath the sea surface) to get lower frequencies in the source wavelet. As explained previously, lower frequencies attenuate less than higher ones, reaching greater depth and longer offsets (e.g. source-receiver distance).

The firing frequency is longer than in MCS experiment with the aim to avoid the background noise produced by the noise from previous shots in the water layer (the so called "wrap around" noise). A typical shooting distance is about 60 to 120 sec. or 150 to 300 m.

Finally, the receiver spacing affects the accuracy of the final velocity model. The smaller the receiver spacing, the higher is the redundancy of data, and hence the information provided by the data set in the modelling process is better constrained. The interval between receivers depends on many factors, such as the bathymetry or the number of available receivers, but for modern crustal-scale experiments it is typically set between 5 to 15 km. spacing.

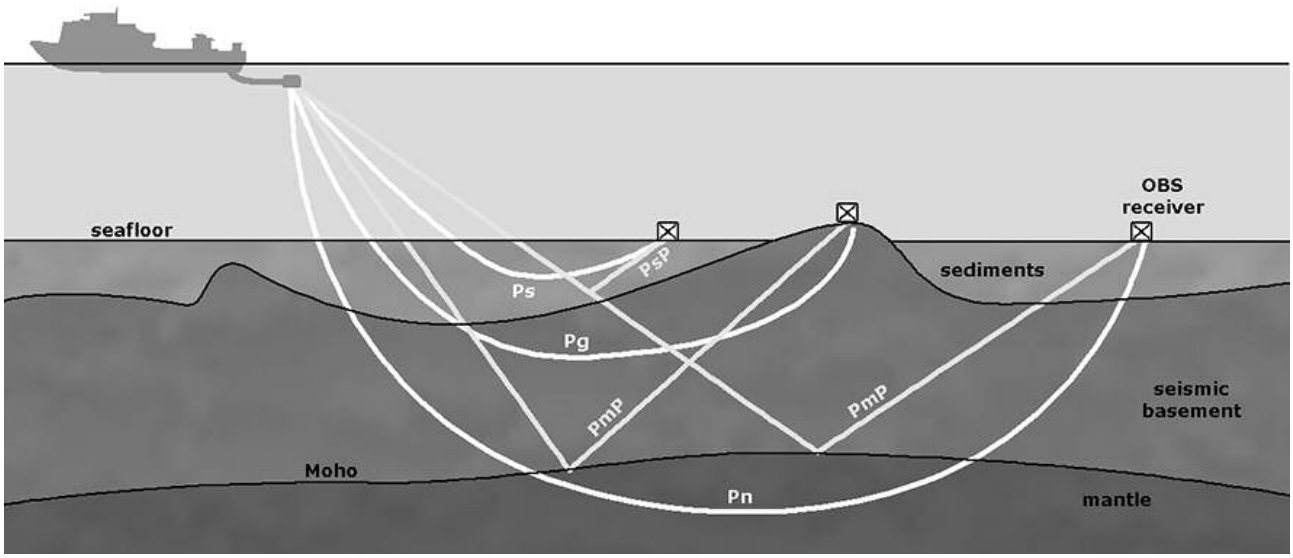

Figure 2.20: Schematic diagram of the wide-angle acquisition system, and the propagation of the different seismic phases refracted through the sediments (PsP), crust (Pg), and mantle (Pn); and reflected at the sediment-basement boundary (PsP), and at the crust-mantle boundary (PmP).

For the data acquired during the MEDOC survey, the seismic source consisted of 6 G-II airguns each, with a total capacity of 4600 cu. in. fired at a constant interval of 90 sec. (around 220 m.). receivers were deployed with an average spacing of around 10 km., although this distance increase slightly with the landstations.

As developed at the beginning of this chapter, wave phases considered in the WAS experiments are the body waves (i.e. either primary or P-waves, and secondary or S-waves) (fig. 2.20). In general P-waves are more commonly visible in seismic records and thus generally used for modelling WAS experiments. These seismic waves are reflected as a result of acoustic impedance contrasts across sharp geological interfaces, that often are steep velocity gradients in a short depth range, and transmitted or refracted through the medium following Snell's law.

As the source-receiver distance increases, the angle of incidence also increases, and then the refracted rays experience a change of direction according to Snell's law. But when the source-receiver distance reaches the critical distance the ray encounters the boundary between geological layers with a critical angle of incidence (fig. 2.21). At that point the ray is refracted with an angle of refraction of 90º and travels parallel to the boundary through the topmost region of the lower layer with the velocity of this layer. At angles greater than the critical angle refraction is no longer possible, and the energy from seismic rays that are incident more obliquely than the critical angle is entirely reflected. These reflections are known as "supercritical reflections", or simply "wide-angle reflections". They lose little energy to refractions and travel large distances providing information of boundaries like the sediment-basement boundary or the Moho (Lowrie, 2007).

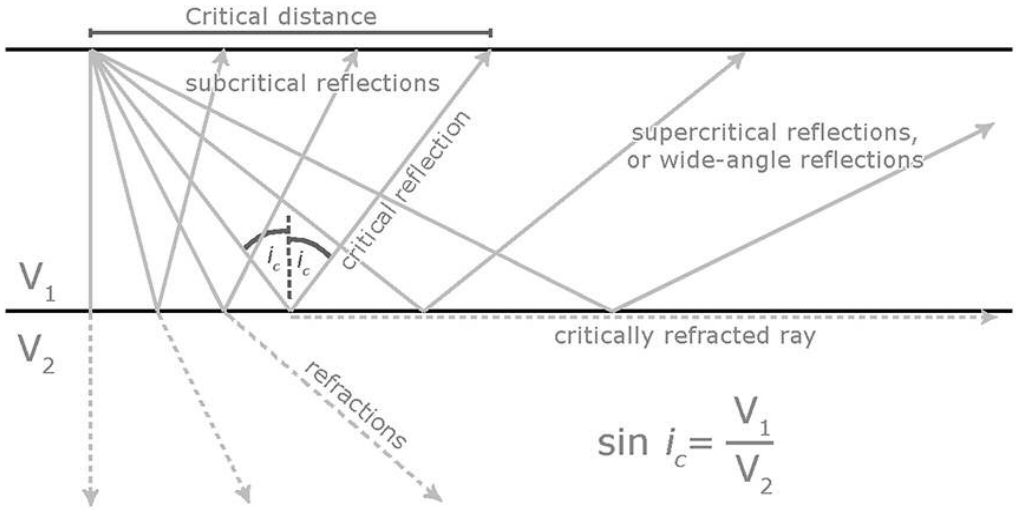

Figure 2.21: Diagram showing path of the rays through the surface and the evolution of the reflections and refractions as the source-receiver distance increases. Note that after a certain point, the ray of the seismic wave incides with the critical angle i_c and critically refracts through the top of the lower layer. Reflections that occur after the critical distance are known as wide-angle reflections.

In practice, the data recovered by the receivers consist of a continuous temporal trace that includes, at different offsets, the seismic events produced by the arrivals of the recorded waves corresponding to the different seismic phases. The sorting by offset of these seismic traces provides the so-called "common receiver gather" or "record section" that is commonly represented in an offset-time diagram, where each trace corresponds to a shot (fig. 2.22). This representation makes easier the phase identification and interpretation. As can be seen on the figure 2.22, the time axis is commonly reduced by a certain velocity with the aim to lower the slope of the first arrivals, to make them easier to distinguish. This velocity is known as "correction velocity".

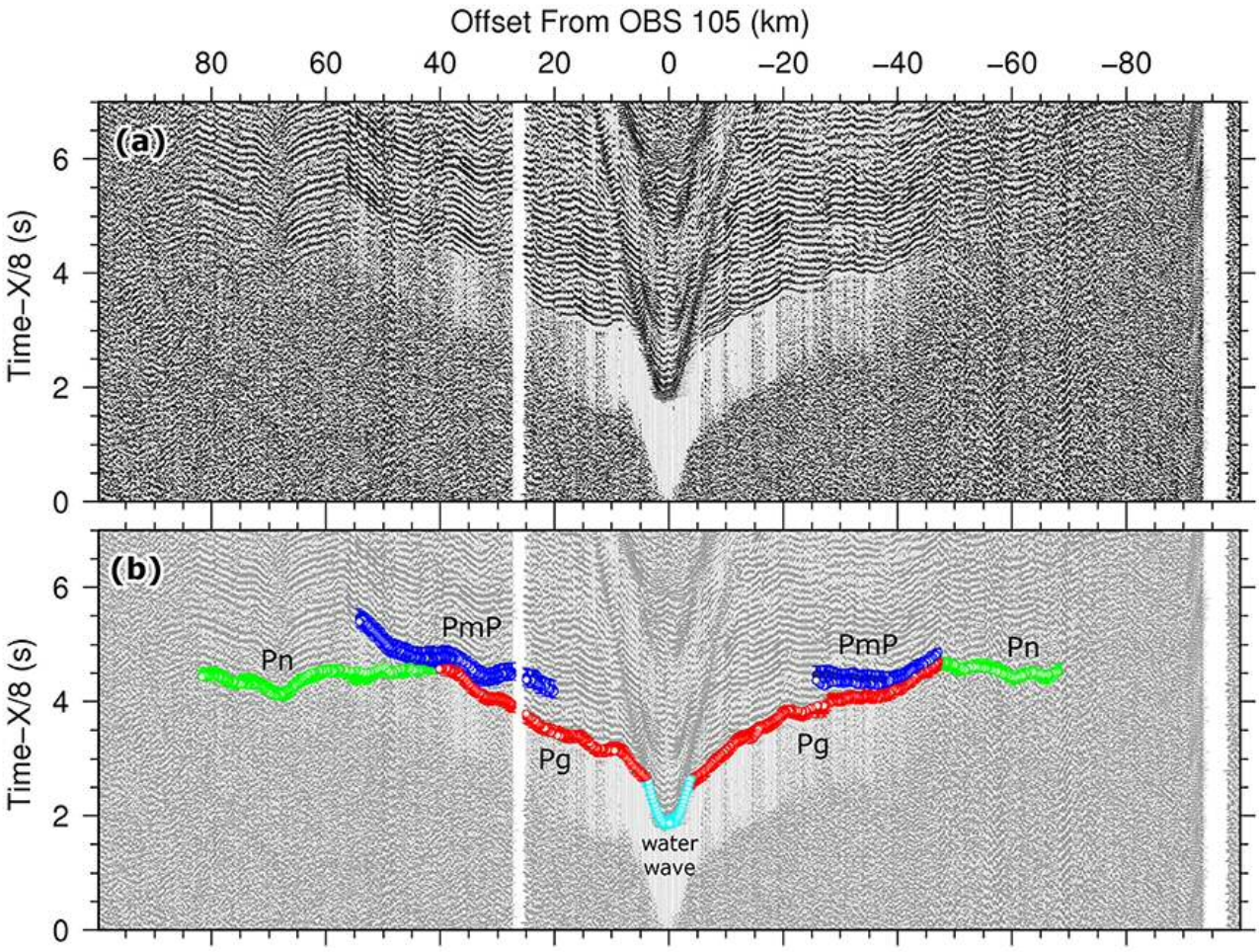

Figure 2.22: Record section blank (a), and with the identified seismic phases picked (b): the refracted through the crust (Pg: in red) and mantle (Pn: in green), and reflected at the Moho (PmP: in blue). Cyan is for the wather wave. Note that the relation between the refracted Pg and the reflected PmP is asymptotic.

Processing

Like in the MCS case, the WAS data are processed to enhance the signal/noise ratio and improve the lateral correlation of the seismic phases with the aim to identify them better. But in the WAS case, the processing workflow is considerably simpler than that applied to MCS data.

The first step consists in the relocation of the OBS/OBH in the seafloor. This must be done because the oceanic currents may drift the receiver on its way down so they reach the seafloor at a location that can differ considerably from the deployment location, normally for several tens to hundreds of meters depending on the currents and on the water depth. This correction is made by applying a "grid search," which consists on finding the seafloor location that minimizes the traveltimes of the direct water waves between source and receiver, for which the propagation velocity is known (1500 m/s).

To improve the signal/noise relation, several processes can be applied to the data. For example a predictive deconvolution (see the processing flow section of the MCS data 1.2.2.), a time and offset-variant bandpass filter (usually a Butterworth filter), and an amplitude balancing like an Automatic Gain Control (AGC), although other processing steps may be applied to the data when necessary.

In this thesis, the WAS data processing consisted of a spectral whitening to attenuate some frequency-band-limited noise (6-7 Hz.) present at most of the OBS, a predictive deconvolution, a Butterworth band-pass filter (5-15Hz), and an AGC amplitude balancing. For the land receivers only a Butterworth band-pass filtering (3-13Hz) was applied.

2.4.2. Identification of seismic phases

Once data are processed, the next step is the identification of seismic phases. To achieve this goal is important to determine the available information in the recorded section. In the case of refractions, the first arrivals are displayed as straight lines whose slope is proportional to the seismic velocity of the layer at which they turn out (fig. 2.22). Therefore, when the seismic phases display negative gradients implies that the propagation velocity of these waves is lower than the correction velocity. Meanwhile phases displaying larger gradients than the correction velocity must correspond to higher propagation velocities. When the arrival is horizontal, the propagation velocity is equal to the correction velocity.

By contrast, reflections are secondary arrivals represented by hyperbolic functions that are asymptotic to the corresponding refracted wave in the record sections. For example, PmP reflections from the mantle is asymptotic to Pg (refractions in basement) and Pn (refractions in the upper mantle) in the record section of (fig. 2.22).

Then, once the seismic phases are recognized, their time arrivals should be identified and picked. The objective of this process is to create a data set with all the travel times for each seismic phase. These selected picks will be the input data set for the next step: the modelling.

2.4.3. Modelling

There are two different ways to carry out the modelling of the picked travel times, and calculate a velocity model for the crust and the uppermost mantle: the forward modelling and the inversion.

In the forward modelling case, the velocity model and the geometry of the geological structures are manually built by an interpreter, and they are improved by more or less automatized trial-error until the coincidence between the observed data and the simulated data is acceptable. The main tool to build the velocity model is a ray-tracer algorithm (e.g. Zelt and Smith, 1992). This method was widely used until well into the 90's and is still used some experiments, particularly where the number of sources/receivers is limited. But it presents many limitations, as for example, the final solution is subjective and depends heavily on the interpreter pre-established concepts. In addition, it does not allow performing formal parameter uncertainty analysis. And finally, it becomes unfeasible or extremely time-consuming when there is a large number of sources and receivers, as is the case of most WAS marine experiments shot during the last ~15 years.

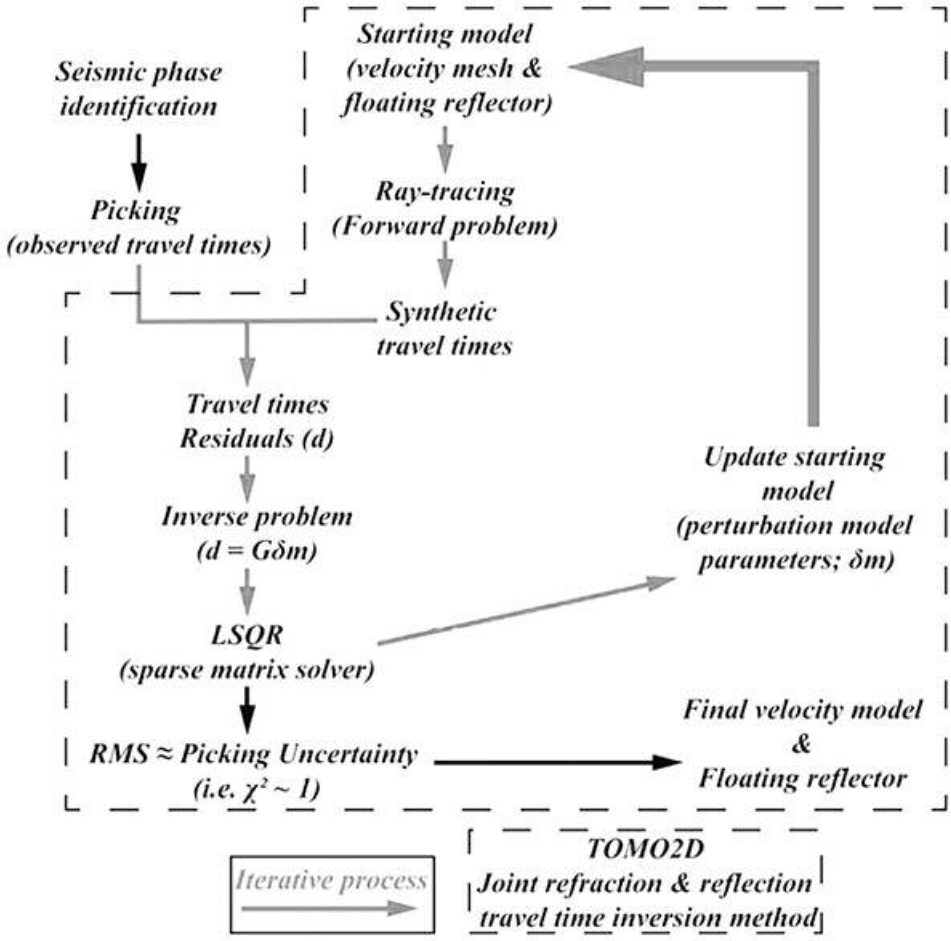

Figure 2.23: Flow diagram of the joint refraction and reflection travel-time inversion method applied with TOMO2D code [Korenaga et al., 2000].

The inverse methods also known as "tomographic" methods, consist in determining the velocity model, as well as the geometry of major reflectors, in the case that reflected phases are considered, in an automatized way (Toomey et al., 1994; Korenaga et al., 2000).

The inverse methods can be divided in two parts. The first one is the same that must be solved in the forward modelling techniques, and consist in tracing the rays and calculate the synthetic travel-times. The second part is the inverse problem, where the actual problem of travel-time calculation is approximated by a linear version, in which the travel time residuals for an initial (i.e. reference) model are related to the model changes by means of the matrix of partial derivatives (i.e. the Jacobian), which is also known as the "sensitivity", or Fréchet derivative matrix. Then the inverse problem, which is solved iteratively, consists on inverting this matrix to get the model changes out from the travel time residuals for a reference model.

The input data in this work was both refraction and reflection travel-times, therefore the WAS data have been modelled using a joint refraction and reflection travel time inversion method, implemented in the tomo2d code (Korenaga et al., 2000). The flow diagram of tomo2d program is shown at figure 2.23 and explained next.

This code allows to obtain a 2D velocity model and also the geometry of a single reflector at a time. The velocity model is represented as a sheared mesh of velocity nodes hanging from the topography (the seafloor and/or the land relief). And where the floating reflector is represented by an array of linear segments whose nodal spacing is independent of that used in the velocity mesh (Korenaga et al., 2000).

To solve the forward problem (fig. 2.23), this method uses a hybrid ray-tracing strategy that first calculates a polygonal ray trajectory using the graph method (Moser, 1991) that is refined afterwards using a ray-bending technique (Moser et al., 1992). The optimal parameters for bending the rays are calculated using the conjugate gradients method (fig. 2.24). Then, the inverse problem consists in solving equation 16, which represents the linear approximation of the forward problem around a reference model:

$$d = G\delta m \qquad \text{Equation 16.}$$

where d is the travel times residual vector, obtained from the difference between the observed and the synthetic data, G is the Jacobian matrix (Fréchet matrix) that contains the velocity and depth derivatives of the residual travel times, and finally, the δm is the unknown model perturbation vector which includes the velocity and the floating reflector depth perturbations.

The degree of perturbation of the model parameters can be also controlled with smoothing constrains that are applied to the velocity and to the reflector geometry, defining

laterally- and vertically-variable correlation lengths. These damping constraints are also used to regularize the linear system and stabilize the inversion. Thus, with these weighting parameters added to the linear system, equation 16 can then be written as:

$$\begin{pmatrix} d \\ 0 \\ 0 \\ 0 \\ 0 \end{pmatrix} = \begin{pmatrix} G_v & wG_d \\ \lambda_v L_{Hv} & 0 \\ \lambda_v L_{Vv} & 0 \\ 0 & w\lambda_d L_d \\ \alpha_v D_v & 0 \\ 0 & w\alpha_v D_d \end{pmatrix} \cdot \begin{pmatrix} \delta m_v \\ \frac{1}{4}\delta m_d \end{pmatrix} \qquad \text{Equation 17.}$$

where v and d subscripts refer to the velocity and depth components respectively, L_{Hv} and L_{Vv} are the horizontal and vertical correlation length matrices for velocity, L_d is the correlation length matrix for the depth, λ_d and λ_v are the control parameters of smoothing constrains. The depth kernel weighting is represented by w, which adjusts the depth sensitivity in the Fréchet matrix. Damping matrices for velocity and depth are represented by D_v and D_d, respectively, and finally, α_v and α_d control the strength of the damping constraints.

In the case of tomo2d, the Fréchet matrix is inverted applying the LSQR solver (Paige and Saunders, 1982). Given that the problem solved is a linear approximation of the real one, equation 17 must be applied iteratively using as input the model parameters obtained in the previous iteration. This scheme is repeated until convergence is achieved (fig. 2.23). For that reason, the reference model is modified successively by δm until the root mean square (RMS) value of travel time equals approximately the uncertainty of the observed data (i.e. ~70-60 ms), or, what is the same, when the chi-squared (χ^2) value becomes ~1. The linear sensitivity of the inversion, which is also a measure of the ray coverage throughout the model, is provided by the Derivative Weight Sum (DWS) (Toomey and Foulger, 1989) (fig. 2.24).

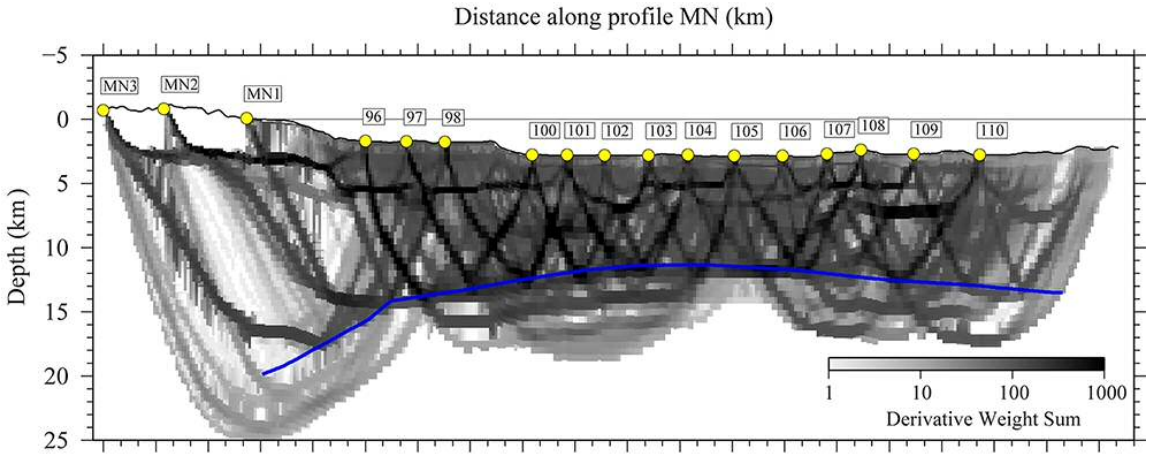

Figure 2.24: Derivative weight sum for the velocity model obtained. The higher is the DWS, the higher is the ray coverage.

The mesh built for this work is 315 km. wide and 35 km. deep, with node spacing varying in the vertical component from 0.125 km. at the seafloor to 1.5 km. at the bottom, and a constant spacing of 0.5 km in the horizontal. Finally, the node spacing for the floating reflector is also 0.5 km. and constant. In order to select the most appropriate set of regularization constraints, several combinations of correlation lengths, damping and smoothing parameters were tested.

Layer stripping method

As mentioned above, the tomo2d program just allows inverting a single reflected phase at a time, that is, a single reflector. Therefore becomes necessary to define a strategy in the case that different boundaries, or layers have to be inverted. In this case it consisted in a top-to-bottom layer-stripping strategy (Sallarès et al., 2011; 2013a, b).

This is a multi-step inversion strategy consisting in working with the data sequentially, starting with short offsets (e.g. sediment phases), and finishing with the longest (e.g. mantle phases). This strategy permits to account for sharp geological contacts such as those occurring across the sediment/basement interface or the Moho (Sallarès et al., 2011).

But in practice, the data of this work do not show clear sediment/basement boundary phases probably because of the thin sedimentary layer. Therefore, the Moho is the only reflector to invert, and the layer-stripping strategy consisted in inverting first the crustal phases and then the upper mantle ones. In the first step the refracted phases through the crust (Pg) and basement (Pb) and reflected at the crust-mantle boundary (PmP) were jointly inverted to account for the entire crustal velocity field and the Moho reflector geometry. And in the second stage the crustal velocity model and Moho reflector obtained were used as initial model, whereas Pn phases were incorporated to the data set.

To avoid the changes in the crustal part of the model, the velocity nodes above the Moho reflector were over-damped. As a result, the obtained velocity model displays a sharp velocity contact that coincides with the Moho location.

Uncertainty analysis

Actually, there are several deterministic methods to estimate the parameter uncertainty based on the covariance matrix, but most of them only consider the mathematical indetermination intrinsic to the approach and do not take into account other indetermination sources such as for example the dependence of the solution on the initial model used. In practice, the only methods to estimate the model uncertainty for a large scale and non-linear inversions are the stochastic, Monte Carlo-type ones (Tarantola and Valette, 1982; Tarantola, 1987).

This approach consist in randomly perturbing the velocity values of the initial model and the depth of the Moho reflector using a Gaussian distribution with a reasonable variance taking into account a priori information (σ_v=1 km/s and σ_z=4 km). This way, we created a set of 500 2D reference models and their modified reference Moho reflectors. Is important to apply a Gaussian filter to the reference velocity mesh to avoid abrupt changes of velocity within the model caused by this perturbation process. Additionally, 500 noisy travel time data sets were constructed by adding a Gaussian distribution for timing errors (σ_t=65ms), which includes the potential influence of common phase errors (±25ms), common receiver errors (±25ms) and individual picking errors (±15ms). Then, randomly selected pairs of perturbed reference models and reflectors, and noisy data sets are inverted. The average mean deviation of all inversion solutions is taken as a measure of the uncertain of the model parameters (velocity and reflector's geometry) uncertainty (Tarantola, 1987).

3.CORTICAL DOMAINS

3.1. Introduction

Recent results from the geophysical data acquired during the MEDOC survey integrated with available basement sampling information have shown that the tectonic structure in the transition from the North to the Central Tyrrhenian basin is far more complex than previously assumed (Moeller et al., 2013; 2014; Prada et al., 2014; 2015). Seismic velocity models of the basement of Cornaglia and Campania Terraces, display a two-layer velocity with lower crustal velocities relatively high compared to normal continental crust, and that are typically associated to magmatic rocks beneath. In contrast, the structure beneath the Magnaghi and Vavilov basins (fig. 3.1) is characterized by a strong vertical velocity gradient and the lack of both wide-angle and near vertical Moho reflections, which together with the recovery of serpentinized peridotite in the Ocean Drilling Program (ODP) Leg 107 site 651 (Bonatti et al., 1990; Kastens and Mascle, 1990) (fig. 3.1) supports that the basement is fundamentally made of exhumed mantle rocks with no overlaying crystalline crustal material (Prada et al., 2014; 2015). This recently discovered basement configuration implies abrupt variations of strain and rapid changes of magmatism.

The analysed data consist in a 300 km long geophysical cross-section with a NW to SE orientation that goes from the continental margin of Sardinia to the North Sicily margin across the Cornaglia Terrace. The geophysical data of this transect include WAS and gravity data acquired along the MEDOC transect M-N with ocean bottom seismometers (OBS), and the coincident MCS M28-b section (fig. 3.1). Travel times from refracted and reflected phases identified in the WAS data were inverted to get a 2D P-wave velocity (Vp) model of the crust and uppermost mantle together with the geometry of the Moho boundary. Then, from the vertical Vp structure of our model can be infered the petrological nature of the basement and the velocities of our model can be converted into densities (ρ) using different Vp-ρ laws of different rock-types. Gravity data were used to verify the consistency of petrological interpretations, and the MCS images were used to interpret the tectonic structure along the same profile and complement the information of the Vp model. The tomographic results of this transect have been compared with those obtained along MEDOC transects E-F (40.5ºN) and G-H (40ºN) (fig. 3.1) to identify the variations of the crustal structure of the Cornalgia Terrace from north to south. The results of this study allow to analyse the effect of magmatism beneath the Cornaglia Terrace and to explore the relation between magmatism and back-arc extension during the different phases of formation of the Tyrrhenian basin.

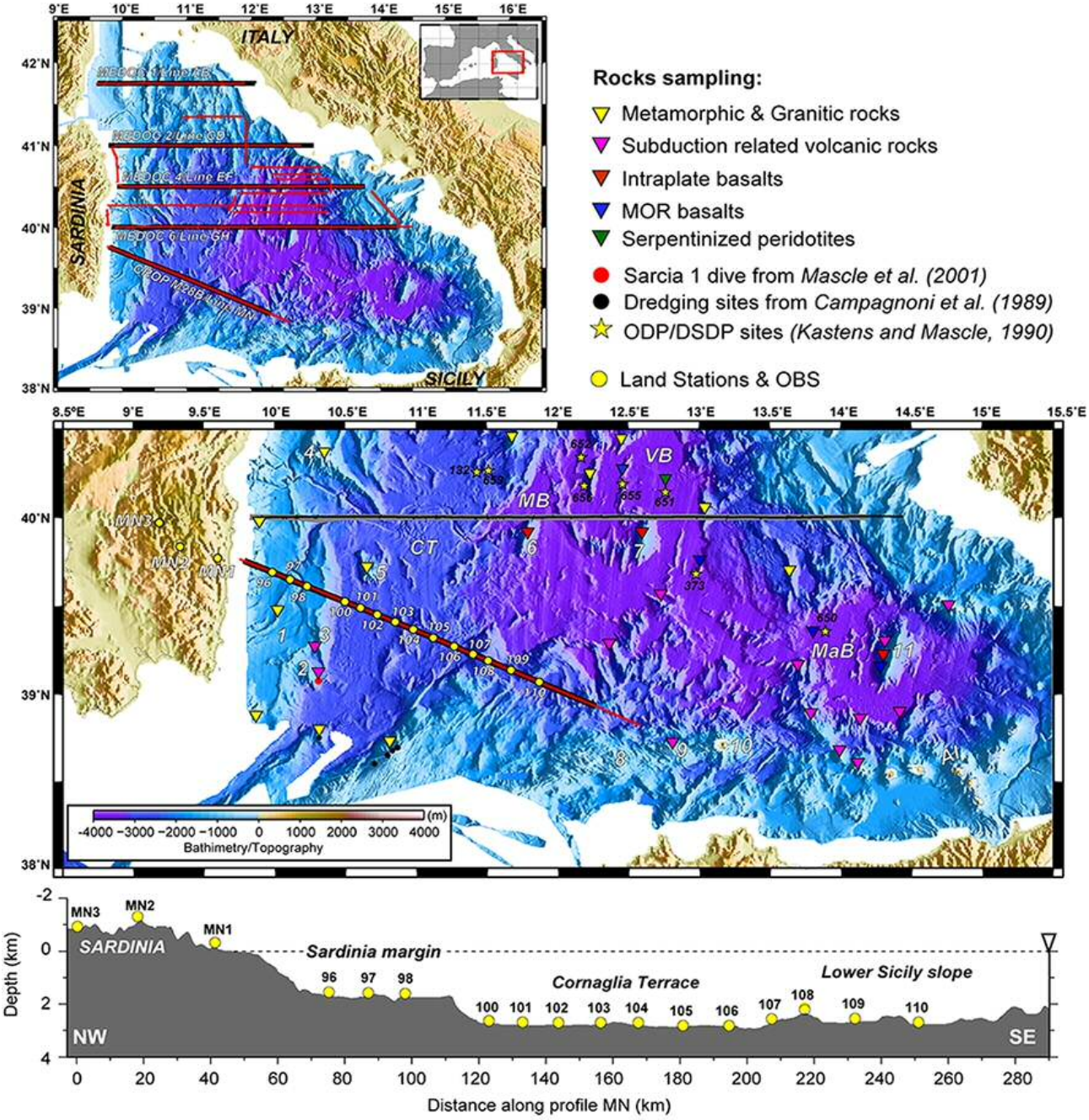

Figure 3.1: Upper image shows the bathymetric and topographic map of the Tyrrhenian basin. The MEDOC Wide-Angle seismic (WAS) and Multichannel seismic (MCS) lines are represented with black and red lines, respectively. The data from line M28-b and the coincident WAS MEDOC transect M-N are used in this thesis to infer the crustal structure of the southwestern region of the Tyrrhenian basin. Middle image displays a close up of the study area with the location of MCS line M28-b (red line) and WAS Line M-N (thick black line), as well as the location of the Ocean Bottom Seismometers (OBS) and Land stations (LS) deployed along Line M-N (yellow circles). WAS transect G-H (thick grey line) and MCS line MEDOC 6 (thin black line) are also shown in the figure. Ground truthing in the area is depicted by colored triangles, yellow stars, and red and black dots (Dietrich et al., 1977; Colantoni et al., 1981; Campagnoni et al., 1989; Kastens and Mascle, 1990; Mascle et al., 2001). Numbers are 1: Sardinia basin, 2:Quirra volcano, 3: Cornacya volcano, 4: Baronie seamount, 5: Cornaglia seamount, 6: Magnaghi seamount, 7: Vavilov seamount, 8: Drepano seamount, 9: Anchise seamount, 10: Ustica Island, 11: Marsili seamount. CT: Cornaglia Terrace, MB: Magnaghi basin, VB: Vavilov basin, MaB: Marsili basin, AI: Aeolian Islands. Lower panel depicts the topographic and bathymetric profile together with the LS and OBS locations along WAS transect M-N.

3.2. Methodology

3.2.1. Seismic phase identification

Three types of seismic phases were identified in the record sections of transect MN (fig. 3.2 and annexes). Two phases refracted within the crust (Pg) and mantle (Pn), and one reflected at the crust-mantle boundary (PmP). Most of the OBS recordings do not show clearly identifiable sedimentary phases, so they were not used separately in the inversion process.

Land record sections display a ~50 km-long Pg phase with apparent velocity of 6.0-6.5 km/s and few Pn phases with higher apparent velocity around ~8 km/s. PmP reflections are also observed. The OBSs deployed in the Sardinia margin recorded clear Pg phases up to 40-50 km offset with a similar apparent velocity to Pg in LS. Pn phase is observed up to 80 km offset displaying apparent velocity of ~ 8 km/s (fig. 3.2-a). PmP reflections are rather clear in all these receivers, particularly in OBSs 96 and 97 (fig. 3.2a).

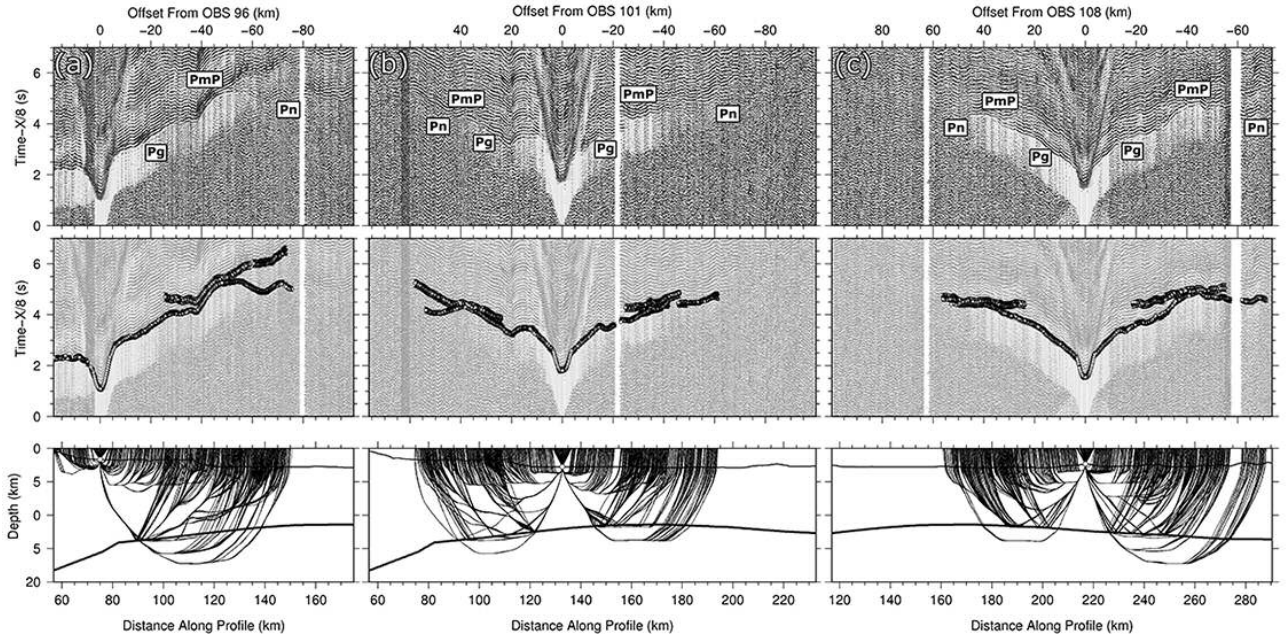

Figure 3.2: From top to bottom: record section, travel time fits and ray-tracing representation of OBSs 96 (a), 101 (b), and 108 (c). Seismic phases of interest are shown in the upper record sections, while white and black dots in the middle sections depict the calculated and observed travel times, respectively. Black thick line in the lower image represents the PmP-inverted Moho.

Southeastwards, the OBSs deployed in the Cornaglia Terrace also recorded Pg, Pn, and PmP phases. Pg phase offsets decrease towards the centre of the Terrace evidencing crustal thinning (fig. 3.2-b). PmP phase is also identified indicating the presence of a continuous crust-mantle boundary beneath this region. For OBSs deployed in the lower Sicily slope (fig. 3.1), offsets of Pg phases slightly increase southeastwards denoting a gentle thickening of the crust towards Sicily. Pn phases as well as clear PmP reflections are also observed in all the record

sections (fig. 3.2-c). As a result, a total of 6451 first arrivals including Pg and Pn refracted phases and 2671 travel times of PmP reflections were manually picked in the 17 record sections. Data picking uncertainty is 60 ms for Pg and Pn, and 70 ms for PmP. It is greather by PmP because reflexion time arrivals are masked by the reververations of the first arrivals of the refracted waves and by noise

3.2.2. Travel-time tomography

As explained at the methodology chapter, the initial Vp model was 290.5 km long and 50 km deep. The starting depth for the Moho reflector was set 15 km deep beneath sea surface, and 25 km deep beneath Sardinia based on previous tomographic results from MEDOC WAS data (Moeller et al., 2014; Prada et al., 2014). The velocity model is parameterized as a sheared mesh of nodes hanging from the topography, in which vertical nodal spacing varies from 0.1 to 0.5 km from top to bottom of the model, whereas horizontal spacing is 0.5 km for both the velocity grid and the floating reflector.

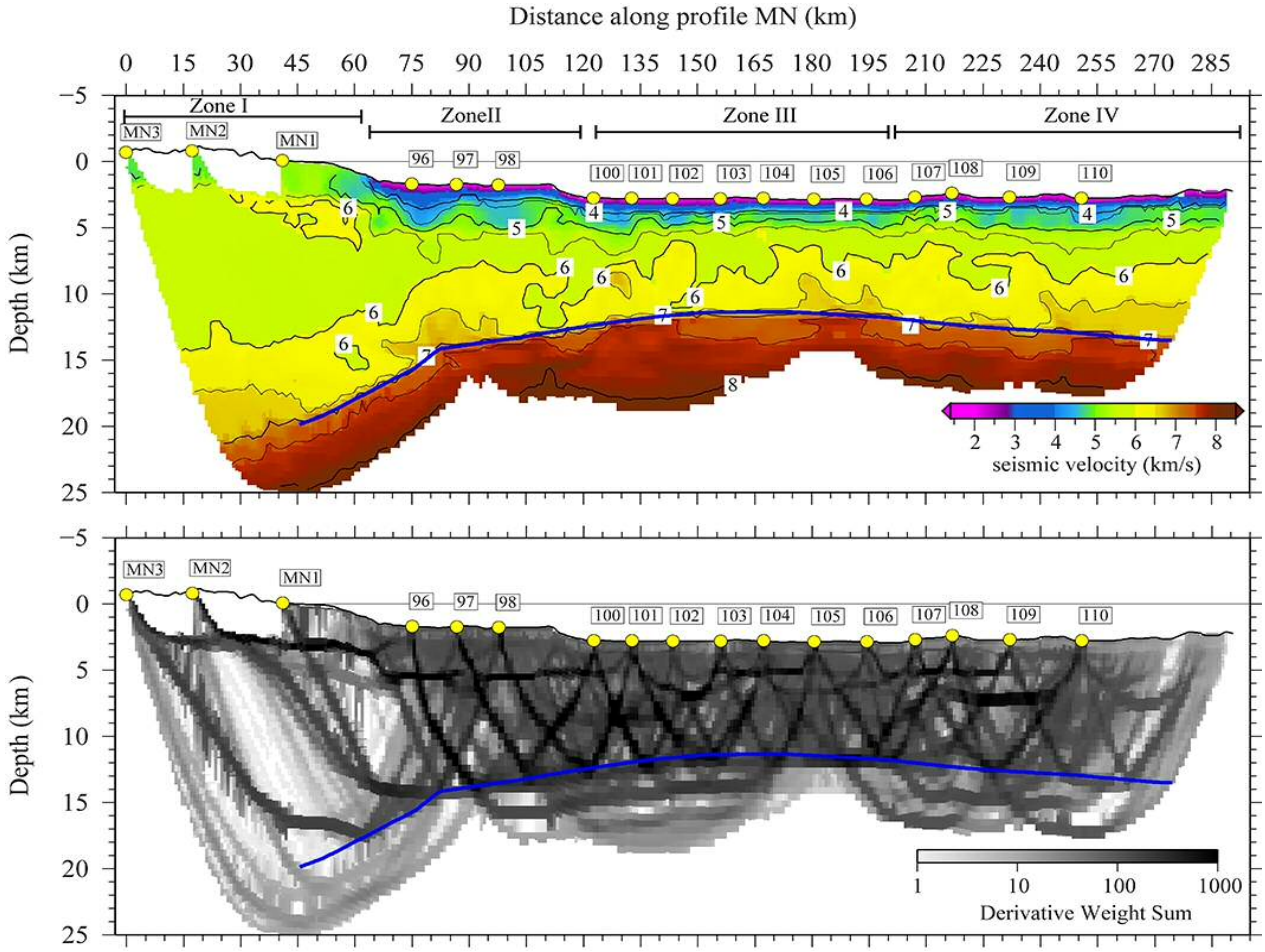

Figure 3.3: Upper profile is the 2D P-wave velocity model of the crust and uppermost mantle, and geometry of the PmP-derived Moho boundary (blue line) along transect M-N. LS and OBS are depicted by yellow circles. Lower profile represents the derivative weight sum (DWS) which is used as a proxy of ray density along the profile.

As developed previously, to invert the data a multi-scale layer-stripping strategy has been applied. Given that no sedimentary cover phases were systematically identified, all crustal phases were inverted at once (Pg and PmP) resolving thereby the crustal structure and the geometry of the Moho discontinuity. Then, in a second and last step all the phases were inverted together (i.e. Pg, Pn, and PmP) using as starting model the crustal model obtained in the previous step and adding a 1D velocity gradient – from 7 to 8.2 km/s - below the reflector This way we obtain a sharp velocity contrast at the reflector location, which in our case corresponds to the Moho (fig. 3.3-a).

At each step of the layer stripping the data was inverted following a multi-scale approach with three-step successive inversions, varying the smoothing constraints from high to low values. This way, the values for the vertical (VCL) and horizontal (HCL) correlation lengths at each step (inversion) progressively decrease, solving the velocity structure of the model from gross to fine-scale sequentially. This approach demonstrates that the inversion results are more robust and independent of the initial model following this strategy than running a one-step inversion with a single set of smoothing parameters. The VCL and HCL values used in every step are presented in table 3.1.

	1st step	2nd step	3th step
HCL top (km)	1.0	0.5	0.1
HCL bottom (km)	2.0	1.6	1.0
VCL top (km)	10	6	2
VCL bottom (km)	18	14	10

Table 3.1: correlation lengths used in each inversion step.

The final Vp model was obtained after 5 iterations with a root mean square (RMS) misfit of 65 ms, which corresponds to a chi-squared value (χ^2) of 1.18. The RMS for first arrivals (Pg and Pn phases) is 67 ms and 60 ms for PmP reflections. A measure of the ray density is calculated as the average of the derivative weight sum (DWS) of each iteration (fig. 3.3-b).

Uncertainty analysis

To assess the uncertainties of the final crustal velocities, and depth of reflector caused by the influence of the initial model and the picking error we have performed a Monte Carlo-type analysis similar to that proposed by Korenaga et al. (2000). Hence, 500 velocity models were created by randomly modifying the Vp values of our initial model as well as the depth (z) of the Moho reflector. The range of variation of each parameter is 1 km/s for Vp and 4 km for z. Similarly, we added random timing errors that include common phase errors (±25ms), common receiver errors (±25ms), and individual picking errors (±15ms) to the original data set and obtained 500 noisy data sets. Then, were inverted randomly selected velocity model-data set pairs.

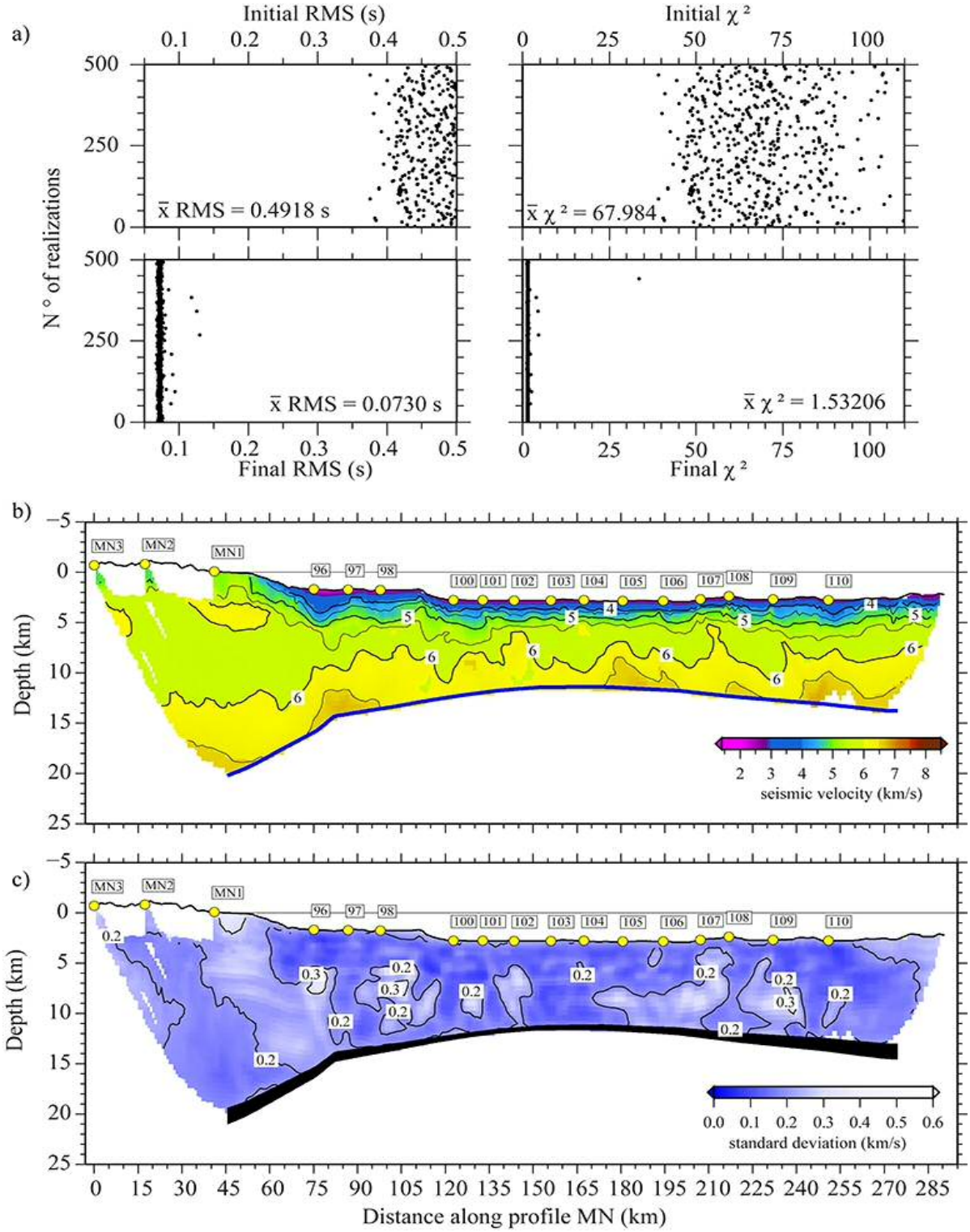

Figure 3.4: a) RMS (left) and χ^2 (right) values of each Monte Carlo realization before (upper) and after (lower) the uncertainty assessment. The figure shows the initial random distributions of models and the good convergence after inversion. b) Average crustal tomographic model of the 500 Monte Carlo realizations. Moho geometry is represented by the blue line. The velocity structure and Moho geometry reported by the average tomographic model shows important similarities with the model presented in figure 3.3a, indicating that most features observed in the model of figure 3.3a are not artifacts from inversion but real crustal features explained by Pg and PmP travel times. c) Uncertainty values for the crustal velocity field and the depth of the Moho reflector (black band).

This way, were created a stochastic distribution of initial models, reflectors and data sets to analyse the distribution of model parameters (Vp, z). This is graphically shown in the upper panels of figure 3.4-a, which display the distribution of RMS of travel-time residuals for the different models and their corresponding chi-squared values before and after the inversions. Based on Tarantola (1987), the averaged model of all realizations (fig. 3.4-b) is the most probable solution and the standard deviation of the model parameters can be taken as a measure of the model parameters uncertainty (fig. 3.4-c).

Analysis results (fig. 3.4) give a Vp uncertainty of ±0.1-0.2 km/s in most of the model, although there are several parts of the model where the uncertainty reaches ±0.2-0.3 km/s. The parts with high uncertainty coincide with regions with poor or no coverage of crustal refractions (Pg), which implies that both velocity and Moho depth are only controlled by PmPs (fig. 3.4c). The depth uncertainty for the Moho reflector ranges between ±0.25 km in regions well covered by both Pg and PmPs, such as the centre of the model, and ±0.8-1.0 km in poorly covered areas like both ends of the model.

3.2.3. Gravity modelling

Gravity modelling was used to further constrain the interpretations of the basement petrology based on seismic velocity (fig. 3.3-a). This analysis consists of transforming the Vp of the model into densities (ρ) using empirical Vp-ρ relationships for specific rock-types according to our interpretations for the different domains - those used in this study are presented in the results section -. Since Vp-ρ conversion laws are defined at specific pressure (P) and temperature (T) conditions, it is necessary to correct the velocity values to in-situ conditions. Therefore linear corrections were applied using the partial derivatives of Vp with respect to P and T when applying the Vp-ρ conversion with *rho2d* code from Korenaga et al. (2001). The goal of this analysis is to explore whether our petrological interpretation of the crustal affinity in the different domains is compatible with the gravity data. Hence, the gravity anomaly was generated by the density models using *grav2d* code (Korenaga et al., 2001), which is based on Parker's (1972) spectral method.

3.3. Seismic structure of the crust and the uppermost mantle

The tomographic model obtained from inversion of Pg, PmP, and Pn phases displays the velocity structure of the crust and uppermost mantle together with the Moho reflector geometry (fig. 3.3-a). Overall, the Vp model is characterized by sedimentary basins up to ~4 km-deep (i.e. below OBS 96 in fig. 3.3-a) and by a strong velocity gradients of 0.7 to 1.0 s^{-1} in the uppermost 3-4 km. The basement below shows velocities between 5.5 and 6.8 km/s, and reflects an abrupt crustal thinning from Sardinia towards Cornaglia Terrace (fig. 3.1). The velocity structure of the basement along line MN shows small lateral variations compared to

the velocity models of MEDOC transects GH and EF (fig. 3.1), where lower crustal velocity is more heterogeneous (Prada et al., 2014; 2015) and is anomalously high compared to neighbouring continental lower crust (Moeller et al., 2013; 2014; Prada et al., 2014; 2015). The small lateral changes of velocity of the basement along transect M-N, support that its nature remains similar. For the interpretation of the crustal structure, we integrated the tectonic structure inferred from seafloor relief and seismic images with the crustal thickness variations defined to change in 4 zones along the profile (fig. 3.5 and 3.7).

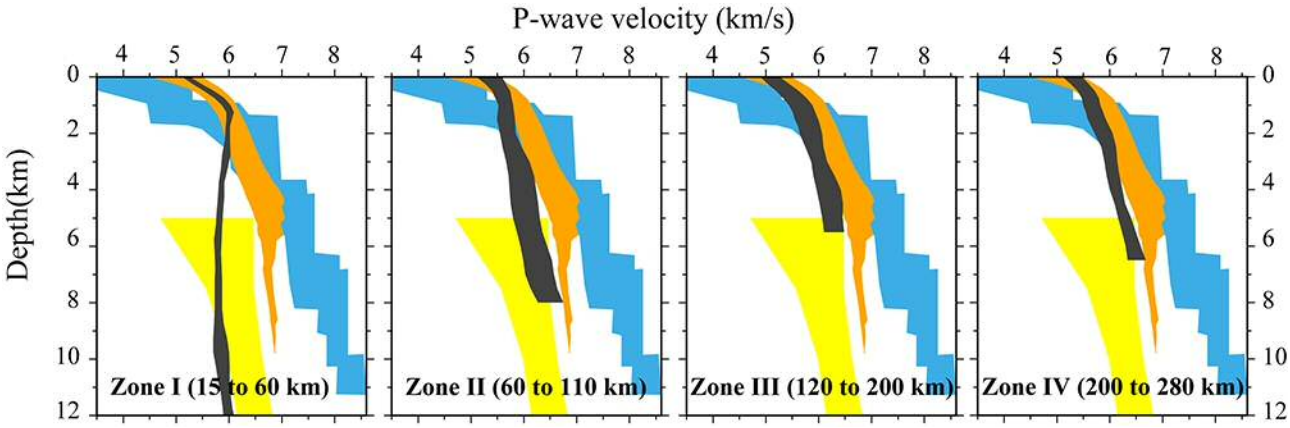

Figure 3.5: 1D Vp-z profiles of each zone along the profile (black band) compared to the Vp-z reference of continental crust (yellow band) (Christensen and Mooney, 1995), transitional continental crust (orange band) (Prada et al., in prep), and 0-7 Ma Atlantic oceanic crust (blue band) (White et al., 1992). The gray bands represent the lateral variability of Vp along each zone, while the colored bands depict the standard deviation of each Vp-z measurement.

Zone I includes the first ~60 km of profile across Sardinia. In there, the crust thins from ~22 km under the landmass centre to 12 km under the upper continental slope in ~45 km horizontal distance and upper crustal Vp is ~5.5 km/s and the lower crust ranges from ~6.06.5 km/s. However, as noted before, this is the worst constrained segment of the model due to poorer ray coverage and lack of reverse shooting.

Zone II starts at ~60 km along profile and extends across the Sardinia margin and basically is coincident with the Sardinia basin, which is formed by two up to ~4-km thick sub-basins (fig. 3.3-a), where sediment velocities range between ~2.0-4.5 km/s. Below, basement thickness ranges from 9-10 km, and velocities do not exceed 6.5 km/s, except for the lowermost crust, where they locally reach 6.7-6.8 km/s (fig. 3.3-a). The highest velocities are localized in the area where crustal thinning is more pronounced. Further east, the crust slightly thins by ~1.5 km towards Zone III (fig. 3.3-a).

Zone III is ~80 km long and runs across the Cornaglia Terrace, extending from 120-200 km along the transect (fig. 3a). Basement relief forms several deeper segments that appear to have a thicker sediment cover in the northern part of the Terrace (e.g. beneath OBSs 100 to 102 in fig. 3.3-a). Zone III has two distinct sectors: a western sector from km 120-165, and eastern sector from km ~165-200. The basement in the western sector is the thinnest along

the transect, ranging from ~5-6 km and increasing to about ~7-8 km easterly. Basement velocities are similar to those in the other zones, ranging from 5.5-6.5 km/s and locally 6.7-6.8 km/s in the lowermost crust (beneath OBS 105-106 in fig. 3.3-a).

Finally, Zone IV extends from km ~200 across the north Sicily margin (fig. 3.3-a). In this segment the crust thickens from ~9 to ~10 km towards Sicily. Basement highs and intervening lows correspond to large tilted fault-blocks and corresponding grabens in the seismic image (Figure 5). Middle and lower crustal velocities remain similar ranging from 5.5 km/s to 6.8 km/s near the Moho.

The mantle velocity structure is resolved with crossing rays up to ~5 km below the Moho reflector in some regions of the model where ray penetration is deeper (fig.3a). In the uppermost 3-4 km of the mantle, velocity ranges from ~7.4 to 7.7 km/s that is lower than normal mantle velocity of 8.1-8.2 km/s.

3.3.1. Petrological interpretation

The velocity structure along transect MN (fig. 3.3-a) has been interpreted in terms of its petrological affinity by comparing the vertical velocity structure of each zone with 1D Vp-z references of a thinned continental crust (Christensen and Mooney, 1995), a 0-7 Ma-old Atlantic oceanic crust (White et al., 1992), and ultra-thin continental crust gathered from rifted magma-poor continental margins (Prada et al., 2015) (fig. 3.5). The comparison supports that the basement along the whole transect has continental affinity. Zones I and II have velocity-depth relationships similar to the reference for average extended continental crust (Christensen and Mooney, 1995). Zones III and IV, have the thinnest crust, and hence, are slightly closer to the depth-velocity relationship of ultra-thin continental crust (fig. 3.5). The thin crust of Zones III and IV is possibly due to important tectonic extension – as normal faulting in seismic images supports - of crust similar to the crust under Sardinia Island. Thus none of the zones show evidence for the presence of the magmatic crust or exhumed mantle, which is in contrast with models from the northern Cornaglia Terrace and Magnaghi-Vavilov Basins (Prada et al., 2014; 2015).

For gravity modelling, Hamilton's law (1978) for marine sediments has been used to transform the sediment layer velocity to density, which was taken up to 5.0 km/s in regions where salt deposits were imaged in MCS data (see section 4.2.3). For the basement, we applied Christensen and Mooney's (1995) law for a 10 km-thick continental crust because the depth-velocity relationship strongly indicates a continental crust nature (fig. 3.5). The lower-than-normal uppermost mantle Vp suggests serpentinization and we used Carlson and Miller (2003) Vp-ρ relationship for low-T partially serpentinized peridotites. In the latter conversion we used partial P ($3.9x10^{-4}$) and T ($-8.21x10^{-4}$) derivatives for serpentinized peridotites from

Kern and Tubia (1993) to correct Vp from in situ to laboratory conditions. For normal mantle Vp > 8.1 km/s we set a uniform ρ of 3.3 g/cm^3. The resulting gravity response from the density model shows a good correlation respect the observed gravity anomaly with a RMS misfit of 9.6 mGal (fig. 3.7). The largest misfits occur in two areas with the deepest basins: one area is near the coast and the other in the Cornaglia Terrace where there is the thickest accumulation of salt and the basement top structure is constrained worse (fig. 3.5 and 3.6).

3.3.2. Tectonic structure

The processed section M28-b has been interpreted to get the tectonic structure and integrate it with the information from the tomographic velocity model (fig. 3.3-a). The interpretation of the MCS image has been endorsed with the PmP-inverted Moho boundary after transformation from depth to two-way time (TWT) assuming near-vertical propagation (fig. 3.5). To show the correspondence between tectonic structure and Vp distribution, the velocity model converted to TWT is overlaid on the MCS image (fig. 3.6).

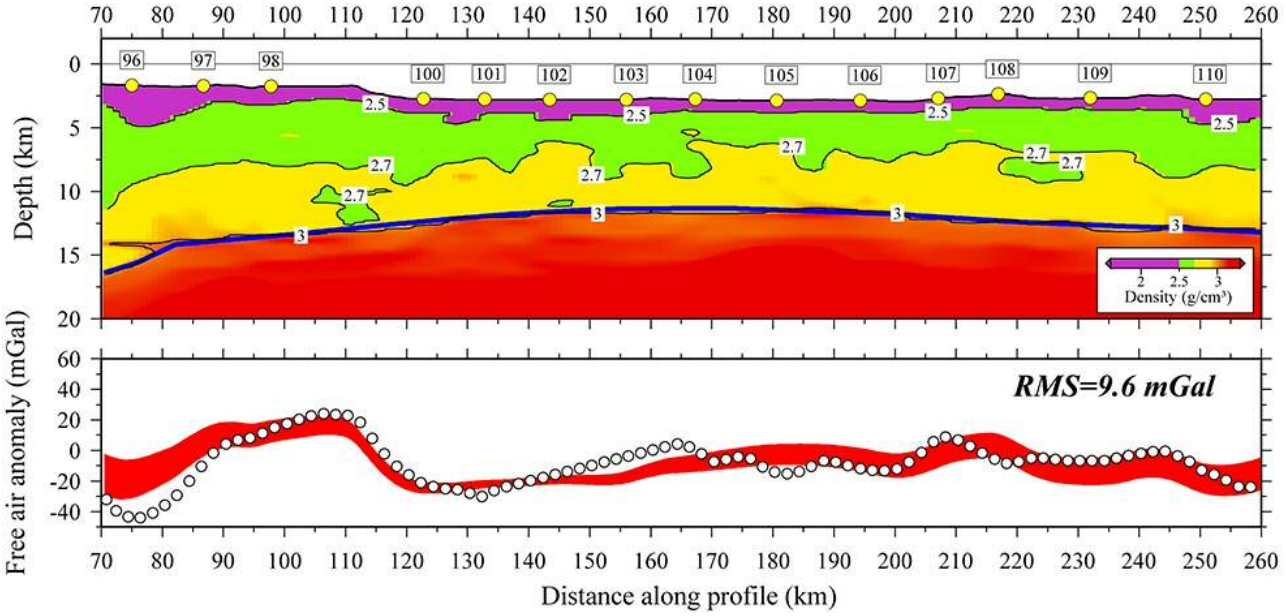

Figure 3.6: Upper panel shows the Vp-derived density model along transect M-N. Blue line and yellow circles depict the Moho geometry and the OBS location along the profile. The gravity response of this model is shown in the lower panel (red band) compared to the observed gravity response (white circles). The misfit is rather good with a RMS of 9.6 mGal.

Along the MCS profile, groups of layered reflections corresponding to crust-mantle transition are observed beneath Zone II and III at 6.5-7 s TWT (although locally obscured by not fully attenuated water-layer multiple noise), coinciding with the location of the PmP-inverted Moho (fig. 3.7 and 3.8). In Zone IV, however, Moho reflections are discontinuous because they are often masked by the remaining energy of the multiple, so that they are less clear, but still, they are locally visible at ~7.0-7.5 s TWT and agree well with the WAS-inverted Moho within a few hundreds of milliseconds (fig. 3.7). The mismatch may indicate complex structure or actual differences in velocity due to anisotropy. The MCS image displays different

tectonic structures for offshore Zones II, III, and IV, supporting the classification based on crustal thickness variations established with the Vp model.

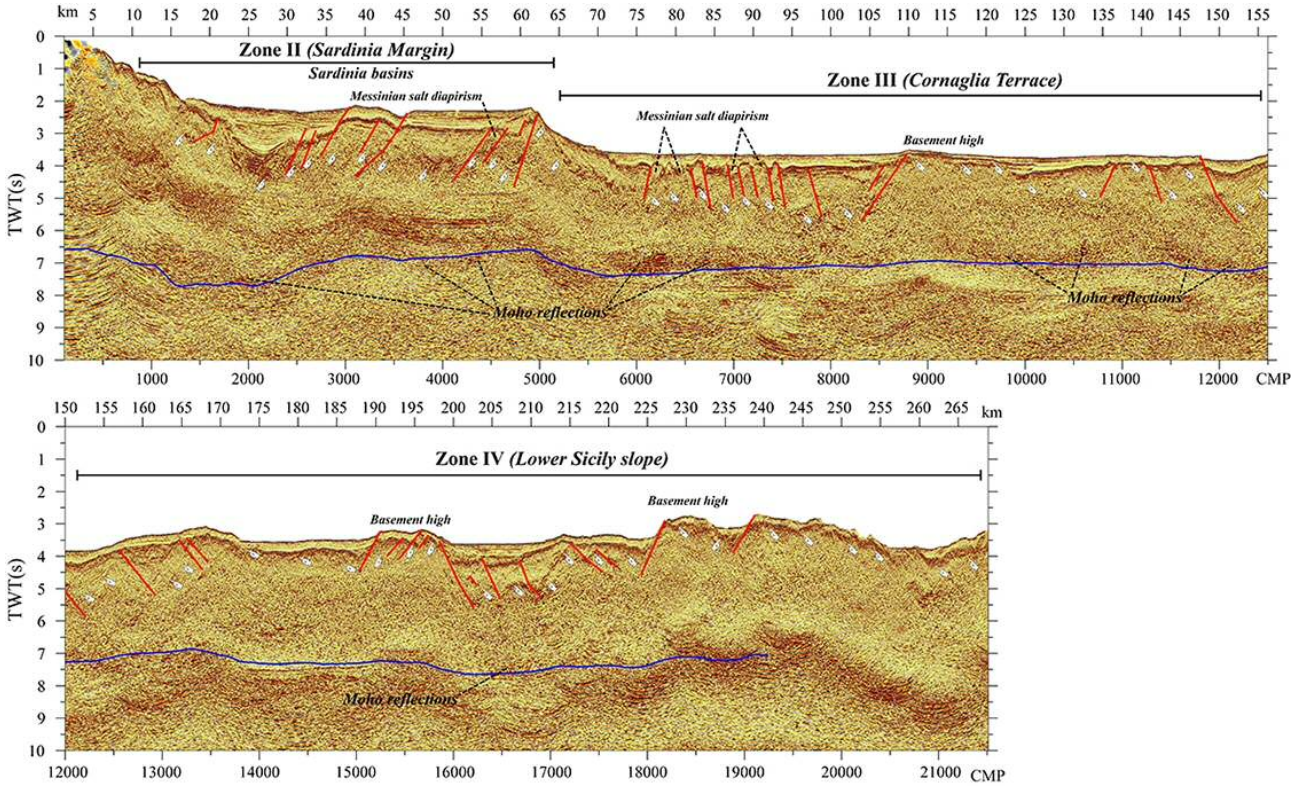

Figure 3.7: Post-stack time migration image of CROP profile M28B overlaid with the tectonic interpretation (red lines). The location of the top of basement is depicted by pointing hands, while Moho reflections are indicated by dashed black lines. The TWT-converted PmP-derived Moho boundary is represented by the blue line along the profile.

The tectonic structure of Sardinia Basin (Zone II) is characterized by two 15-20-km-wide half-grabens formed by westward dipping large main faults and other faults associated to them that cut the fault-blocks pervasively (fig. 3.7). The two half grabens have about 2 s TWT of sediment in their corresponding depocenters (about 2 km thick using wide-angle seismic velocity). At least ten large west-dipping normal faults bound and rotate syn-tectonic sediment packages to steep angles, making imaging and identification difficult. The syn-tectonic infill reaches ~1.0 s TWT and is overlaid by a ~0.5-1.0 s TWT of post-extensional package (fig. 3.7 and 3.8). The basement structure is obscured by the insufficient attenuation and shallow arrival of water-layer-multiple energy under most of the basin.

The transition between Zone II and III occurs with an abrupt crustal thinning and associated deepening of the sea bottom (fig. 3.5) across the western Cornaglia slope (fig. 3.7 and 3.8). The two sectors of Zone III occur under the rather smooth sea bottom of Cornaglia Terrace, but the seismic image displays clear differences in tectonic structure for them, unanticipated from the seafloor morphology.

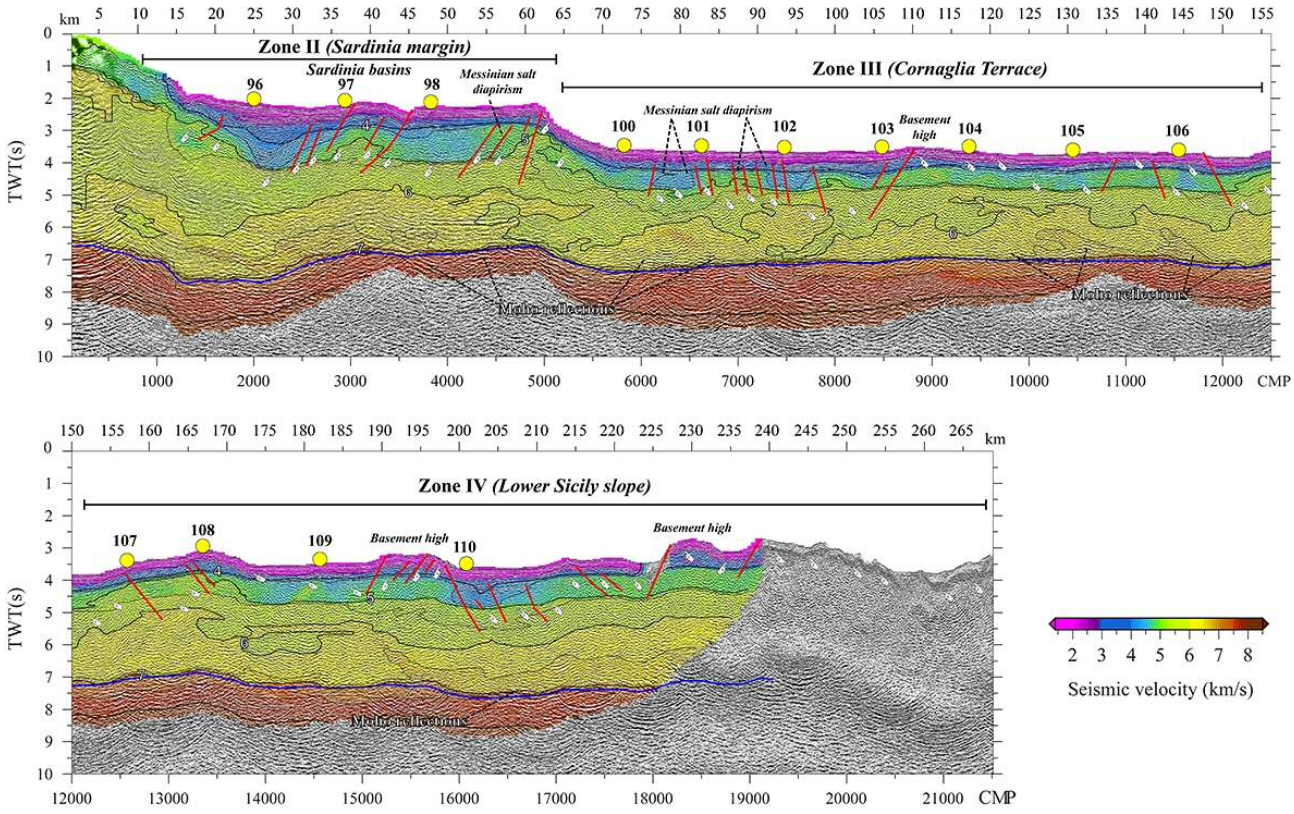

Figure 3.8: MCS profile M28B overlaid by the velocities of the tomographic model and the Moho geometry (blue line) converted from depth to TWT assuming near-vertical propagation. Yellow circles represent the OBS/H location.

The tectonic structure in western sector of Zone III (km ~70-110) is insufficiently imaged because the thickest Messinian salt deposit obscures the underlying structure. However, the Moho and lower crust reflections are clearly visible so that the imaging problems are possibly due to structural complexity rather than signal penetration. The basement here is the deepest in the transect, and the sediment under the Messinian evaporites is possibly as much as ~1.0-1.5 s TWT thick (~1.5-2 km) and provably extends back into Tortonian time. The western sector structure appears controlled by a major west-dipping normal fault (CMP ~8,500 in fig. 3.5 and 3.6) bounding the segment with the deepest basement. Here Messinian salt forms diapiric structures and underlying strata is imperfectly imaged as discontinuous packages that seem rotated.

In the eastern sector of Zone III (km 110-145) the basement is shallower and in most of the sector covered by a few hundreds of meter of sediment only with comparatively less important faulting, although a small half-graben with ~1 km of sediment occurs between km 125-135. However, no Messinian salt deposits are visible, indicating that the eastern sector was shallower than the western sector during the Messinian crisis. Again, imaging seems to be hindered by complex structure rather than signal penetration because lower crustal and Moho reflections are visible as few hundreds of millisecond thick – although indistinct - packages that

match well the Moho location obtained with WAS data. The crust slightly thickens from ~6-8 km in Zone III to ~9-10 km in IV (fig. 3.3). In the seismic image, the transition between these zones occurs at CMP ~12,000 (fig. 3.7 and 3.8), to the SE the basement is cut every 10-15 km by east-dipping normal faults of ~1-2 s TWT offset (~1.5-2.5 km) forming a series of half grabens. The half grabens are filled with syn-tectonic sediment that is truncated at the top by the Messinian unconformity, which only in a few examples appears cut and with rotated –only a few hundreds of meter - by faults. All large half-graben-bounding normal faults stopped rotating before the Messinian desiccation erosional surface at ~5.33 Ma. The post-rift sedimentary blanket is along most of the Zone IV < 0.5 s TWT (< ~0.4 km thick).

3.4. Discussion

3.4.1. Formation of the the Sardinia - NW Sicily conjugated margins

The results of the velocity and gravity analyses clearly evidence the continental nature of the basement along the whole transect. However, rock sampling information suggests that the geology of the basement beneath this region is somewhat more complex in detail (fig. 3.1) (Colantoni et al., 1981; Campagnoni et al., 1989; Mascle et al., 2001). In this section the nature of the basement along each of the four zones is assessed in this section by combining the geophysical data and models with previous geological observations.

In Zones I and II, available geological observations are consistent with the continental nature inferred from the geophysical models. The basement of Sardinia in Zone I is composed by Palaeozoic Variscan granites with their Mesozoic and Lower Cenozoic cover deformed during the Alpine orogeny (Cherchi and Montardert, 1982; Malusa et al., 2015). In Zone II, rock sampling of basement highs found Variscan granitic and metamorphic rocks (Colantoni et al., 1981; Sartori et al., 2004) (fig. 3.1). However, both zones contain igneous material associated to subduction processes (Savelli, 1988; Mascle et al., 2001). South of Zone II, in the Sardinia margin, this magmatic activity is evidenced by the presence volcanic rocks sampled at Quirra and Cornacya seamounts (seamounts 2 and 3 in fig. 3.1, respectively). Quirra samples are Late Miocene-Pliocene alkali-olivinic basalts (Colantoni et al., 1981; Mascle et al., 2001), while Serravallian andesites were found in the Cornacya (12.6 ± 0.3 Ma; Mascle et al., 2001) (Sarcia 1 dive in fig. 3.1). Along Zone II, a small region of the lower crust shows Vp that range between 6.7-6.8 km/s, slightly higher than most of the observed lower crustal Vp along the model (6.0-6.5 km/s) (fig. 3.3-a and 3.4-b). Although these velocities are not anomalous for crystalline continental rocks (Christensen and Mooney, 1995), they could be also attributed to syn-rift magmatic intrusions in the lower crust related to the subduction system as in the Central American arc (e.g. Sallares et al., 2000). These comparatively high Vp concentrate in the zone where lateral thinning is pronounced (from 20 to ~12 km in 45 km) suggests that

extension might have triggered some limited amounts of magmatism.

Zone III has a ~6 km thick basement that is the thinnest (stretching factor; β~4 compared to Sardinia) (fig. 3.3-a) and with a velocity structure somewhat lower than the transitional continental crust reference (fig. 3.3-a and 3.5). Near this region, dredged samples from the Cornaglia seamount found Variscan metamorphic rocks supporting the continental nature of the basement (4 in fig. 3.1) (Colantoni et al., 1981). Although the overall lower crustal velocity of Zone III is 6.0 - 6.5 km/s (fig. 3.3-a and 3.4-b), as in Zone II, locally Vp ranges 6.7-6.8 km/s (between 180-195 km along profile in fig. 3.3-a and 3.4-b). In this case, these Vp overlap sub-horizontal high-amplitude reflections in the MCS profile image (fig. 3.7 and 3.8), somewhat similar to observations attributed to sill-like intrusions in other extended systems (White et al., 2008; Thybo and Artemieva, 2013).

The upper mantle displays significantly lower-than-normal mantle Vp (7.0-7.5 km/s) (fig. 3.3-a). In convergent and rifted margins low mantle Vp is usually attributed to serpentinization of mantle peridotites triggered by fluid percolation throughout crustal-scale faulting (Pérez-Gussinyé and Reston, 2001; Ranero et al., 2003; Ranero et al, 2004). In non-volcanic rifted margins crustal-scale faulting may occur when the entire crust becomes brittle, which is thought to happen when stretching factors (β) are above ~3 for magma-poor rifting (Pérez-Gussinyé and Reston, 2001). Although this region is not a magma-poor extensional system (Prada et al., 2014; 2015), the relatively low amount of magmatism inferred from our data along this transect, and the β ~4, may imply that the low upper mantle velocity is caused by serpentinization.

The crust of Zone IV has a velocity-depth structure somewhat lower but similar to the transitional continental crust reference (fig. 3.5). Here, also locally, lower crust velocity is slightly higher than its average (fig. 3.3a). Basement samples dredged in the western scarp bounding Zone IV (fig. 3.1) found Variscan plutonic and metamorphic rocks (Colantoni et al., 1981; Compagnoni et al., 1989). To the East of Zone IV, the Catena degli Elimi is formed by the Aceste (5 Ma), Drepano, and Anchise seamounts (5.3-3.5 Ma), and Ustica Island (0.8-<0.2 Ma) (Savelli, 1988, 2002), all from subduction-related volcanism origin (fig. 3.1).

Overall, geological and seismic evidences indicate that the basement across the transect is mainly composed by inherited metamorphic and plutonic rocks of a former orogenic crust locally intruded by a limited amount of magma. The nature of this magmatic activity is mainly related to subduction processes, although a minor amount might be potentially linked to extension.

3.4.2. Along-axis variations of magmatic crustal accretion on the Cornaglia Terrace

The interpretation of the observations of MN transect across the southern Cornaglia Terrace is in contrast to the interpretation of the results of transects E-F and G-H across the northern Cornaglia Terrace (Prada et al., 2014; 2015). The crust beneath the southern Cornaglia appears to be ultra-thin continental crust of 5-6 km thick in Zone II, and 7-8 km thick in Zone III. In spite of the inferred high amount of thinning of both zones (compared to crustal thickness of Sardinia), there is little evidence in the observations of significant rift-related magmatic additions. In stark contrasts, the Cornaglia Terrace basement to the north is interpreted to be magmatic crust formed by back arc spreading with little, if any, evidence of continental crust rock forming the basement. To further analyse this along-axis variability of magmatic crustal accretion in the Cornaglia, the crustal structure along the terrace has been evaluated by comparing lower crust Vp and basement thickness along each segment of transect that maps the basement under Cornaglia Terrace (fig. 3.9). Only lower crust velocities were compared because they are possibly more representative of the nature of the basement since they should be less affected by fracturing and secondary mineral precipitation than the upper crust. Fracturing and mineral precipitation may dominate the Vp structure of the upper crust, and may not be always closely related to petrology, but to the tectonic regime and age of the basement as it occurs for young oceanic crust (Mutter and Mutter, 1993).

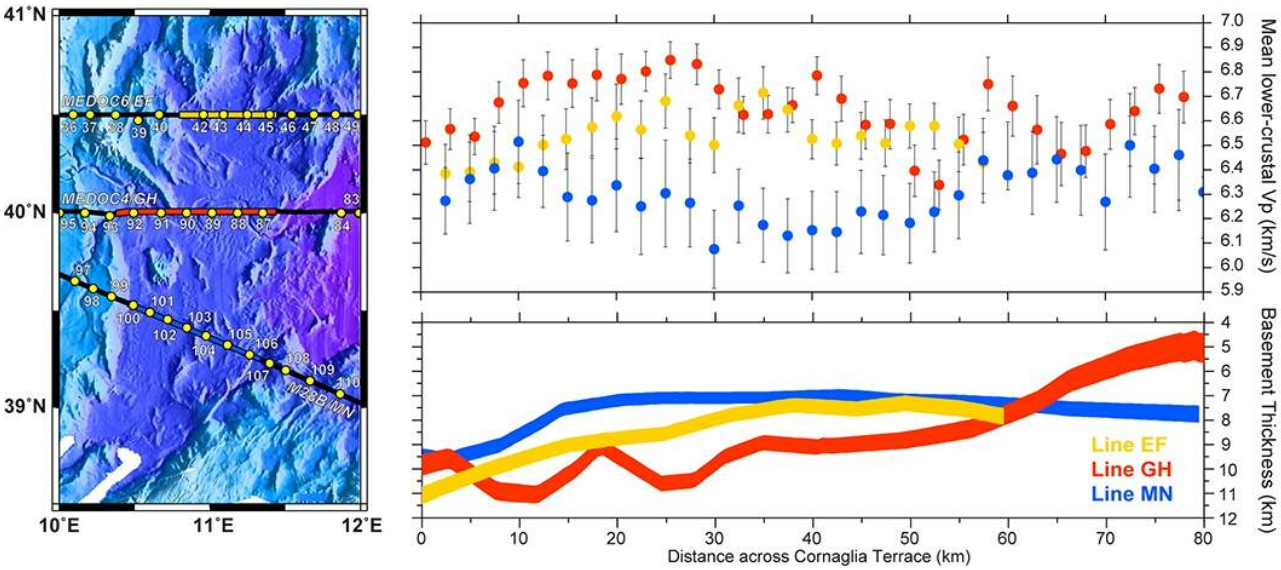

Figure 3.9: Left panel shows the bathymetric map of the Cornaglia Terrace and the location of the WAS MEDOC transects E-F (Prada et al., 215), G-H (Prada et al., 2014), and M-N (this study), as well as the corresponding OBS/H location (yellow circles). Colored sections along each line depict the selected portions of each tomographic model along which mean lower crustal Vp (right upper panel) and basement thickness variation (right lower panel) have been extracted. The Vp of 6.0 km/s has been taken from each model as the top of the lower-crust to extract velocity values in the right upper panel, whereas Vp of 5 km/s has been taken as the top of the basement to calculate basement thickness.

The lower crust Vp along the northern E-F and central G-H transects is higher than in the southern M-N transect. The highest values are observed along the central G-H transect being ~0.4-0.6 km/s higher than in the South, and locally ~0.2 km/s higher than in the North,

although along much of the area are similar (fig. 3.9), so that the variation is larger than the velocity uncertainty estimated for each transect. The higher lower crust velocities of E-F and G-H transects compared to the velocities in other clearly continental areas of the Tyrrhenian basin and Sardinia Island support that magmatic crustal accretion produced a type of crust different than the pre-existing crust to the extensional back arc phase in the central and northern region of the Cornaglia Terrace. However, it appears from the comparison to other clearly continental domain that along transect MN a certain amount of magmatic accretion may have locally occurred.

Along-axis variations of back arc magmatism imply differential back-arc extension along the Terrace axis. Even though we are not able to quantify the amount of extension along the profile due to the influence of magmatism, in figure 3.9 can be observed that the basement along G-H transect is progressively thinner easterly and that break up and later mantle exhumation occurs further east (Prada et al., 2014). In contrast, in the northern and southern profiles, the basement gradually thins and remains constant at 7-8 km thick with no imminent crustal break up.

Differential back-arc extension along the terrace axis is the result of a complex history of slab roll back in the Tyrrhenian. Back arc rifting along the terrace axis started E-W according to geodynamic reconstructions (Rosenbaum and Lister 2002; Faccena et al., 2004) and evidenced by the NS pattern of normal faults along the western flank of the Cornaglia, as can be seen at the bathymetry (fig. 3.1). However, the along-trench interaction from the northeast and south of more buoyant continental plates and plateaus with the subduction system triggered the rotation of the fore arc blocks modifying the orientation of back-arc extension during Messinian times (e.g. Faccena et al., 2004), and hence, during the formation of the Cornaglia Terrace. Numerical models show that the lateral collision of buoyant indentors with the sybduction system reduces the width of the subducting oceanic plate by means of slab tearing and that accelerates slab rollback, which results in rapid opening of localized back arc basins (Maghi et al., 2014). Based on this, can be suggested that along trench variations caused back arc extension to slow down across the northern and southern regions of the Cornaglia, whereas it continued across the central region towards the E-SE (Faccena et al., 2004), triggering the production of partial decompression melting. We interpret that this magmatism might have propagated towards the north favouring the northward opening of the Cornaglia, whereas little amount of it occurred in the southern region where the interaction of the continental African lithosphere with the subduction system stopped the southward retreat of the subduction system (Faccena et al., 2004).

3.5. Crustal variability across the section

The crust along the M-N transect is characterized in 4 regions on the basis of

geomorphological, Vp structure, gravity data and tectonic structure. The basement Vp - depth distribution shows minor lateral changes along the transect. However, there are important crustal thickness and tectonic fabric variations. From west to east, the crust thins from 22 km thick below the Sardinia margin to 7 km thick below the Cornaglia Terrace, where the basement is thinnest and a thick package of Messinian salts dominates the thickest syn-rift sequence along the profile. Easterly, the crust thickens towards the NW Sicily margin, where the crust reaches 11-12 km thick.

The nature of the basement is evaluated with velocity and gravity data together with available rock samples. The results indicate that the basement is mainly constituted by continental crust that has been locally intruded by magmatic rocks. Surface rock sampling indicates the presence of rocks related to melts triggered by slab-derived fluids. However, the geophysical data supports that a minor amount of magmatic intrusion may have locally occurred in the lower crust linked to back-arc extension.

The geophysical observations support that the crust under the southern Cornaglia Terrace is made of continental crust, which is in contrast with results obtained along MEDOC transects E-F and G-H to the north where back arc magmatic crust has been previously interpreted (Prada et al., 2014, 2015).

Based on the geodynamic evolution of the Tyrrhenian subduction system, the lateral interaction of continental bodies with the trench reduced the width of subducting oceanic plate, which in turn resulted in variations on the style of back arc extension and consequently in spatial variations of back-arc magmatism. This way, we suggest that subduction of continental blocks slowed down slab roll back and hence back arc extension in the northern and southern Cornaglia, while in the central area extension continued due to the uninterrupted retreat of the slab towards the E-SE, which potentially triggered the production of partial decompression melting in the area.

4. BASIN-SCALE STRATIGRAPHY

4.1. Introduction

As discussed in the introductory chapter, the Tyrrhenian is a relatively young basin, and thus its sedimentary cover is comparatively thin and largely restricted to local depocenters with numerous highs presenting basement outcrops. Although this fact provides a good opportunity to identify the main structures using the bathymetric data, it implies that sedimentary deposits are discontinuous, and therefore the correlation of the horizons along the entire seismic data set becomes complicated.

In the methodology chapter we described several ODP and DSDP drilling surveys that have been carried out in the area. These drills provide enough data to calibrate the reflectors, at least, at local level. Seismic facies described in the literature (e.g. Kastens & Mascle, 1990; Kastens et al., 1988; and others), together with older seismic lines like ST lines and CROP-MARE lines (see map at fig. 4.1), and the bathymetric data, have been used to identify horizon markers to constrain seismic units throughout the seismic sections.

In a general view, observations give a Neogene-Quaternary sedimentary filling at almost the entire basin. The oldest deposits have been identified at the western margins of the basin, specifically at the sub-basins of Corsica and Sardinia. On the other hand, the most recent sediments are Pleistocene deposits that can be found widespread in the Tyrrhenian, although they acquire its maximum thickness at the deepest regions of Vavilov and Magnaghi Basins.

Depending on the region, the sedimentary units present different seismic behaviour. This is the reason why they have been presented separately for each region. These regions correspond to the tectonic domains that will be described in the next chapter.

4.2. Basin stratigraphy

4.2.1. Seismic basement

Broadly speaking, materials below the sedimentary cover have been considered as basement. The criteria to distinguish them are merely based on their seismic attributes. Therefore, the basement considered in this chapter is a seismic basement and strictly speaking has no real petrological significance. However, where the seismic images are coincident with the five wide-angle seismic profiles collected in the MEDOC experiment (Moeller et al., 2013; 2014; Prada 2014; 2015; and 3rd chapter of this thesis), the basement interpreted in seismic images has a correspondence with the basement type defined based on their velocity, velocity gradient and velocity-derived density.

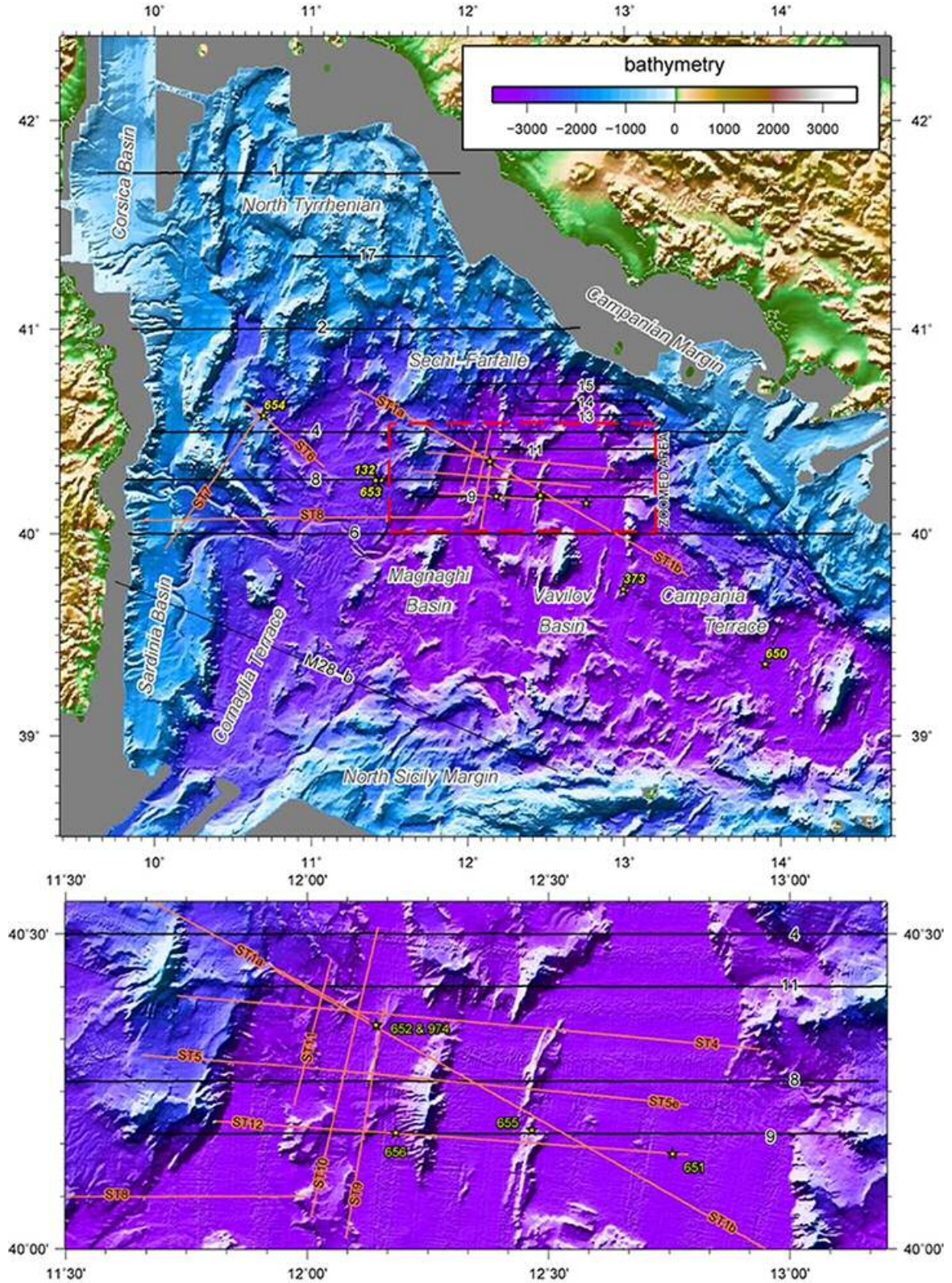

Figure 4.1: General map of the working area, showing the profile tracks used to get the interpretation: the MEDOC lines (from MEDOC survey, 2010), the ST (from ODP leg 107 survey), and the M28-b line (form CROP survey, 1994). Also ODP leg 107, used to calibrate the horizons, were plotted. Black lines are the lines processed (or reprocessed in the M28-b case) by me, while the orange ones were got already processed, and only were used to calibrate the horizons.

Even though their nature could be highly variable along the basin, some characteristics are common: everywhere there have been observed intra-basement reflections, with high

amplitudes and low frequencies. Lateral continuity of these reflections is also highly variable, but in general are shorter in continental domains, where most of them have a continuity of a few km (for example, at MEDOC-8, CMPs 27,000 to 27,500, at 5,5 to 6 s TWT, fig. 4.4-b). In contrast, s they are more continuous in the Campania and Cornaglia Terrace, reaching about 10 km in MEDOC-6 (CMPs 14,700 to 16,400, around 6,5 s TWT, fig. 4.7-b).

In general, the presence of these reflectors is usually scarce and the basement does not show any clear internal structure in most parts of the basin. These two facts together give a poor -or even absent- internal coherence to the basement structure in comparison with the overlying sediments. Thus, materials with no or scarce internal coherent reflections and with any inner structure have been considered as belonging to this unit. On the other hand, the overlying deposits display a clear stratification that is generally well developed, and a better lateral continuity of the reflectors.

The top and base of the basement seismic unit are attributed to reflectors that are not evident in some areas of the basin. The contact between the overlying sedimentary deposits and the seismic basement is unclear in most parts of the study area, because of the poor internal coherency of the lowermost sediments of the stratigraphic column in most areas of the Tyrrhenian. In addition any available drill - ODP or DSDP surveys - provide information about this contact. This is the reason why the lowermost recognizable reflector of the sedimentary cover has been taken as top of the basement. And where it is not clear, it has been taken the internal coherence contrast between the basement and sediments.

In addition, where the seafloor is shallower, as in the continental areas, this boundary becomes usually hidden by the fast seismic signal attenuation and a usually strong water-layer multiple. Furthermore, in some regions like Cornaglia and Campania Terraces, the presence of the Messinian evaporitic deposits mask the seismic signal of the materials below them, and therefore the basement contact (and also the underlying internal basement reflections) are weak and in many places, absent.

On the other hand, the crust-mantle contact corresponds to the base of the basement. This corresponds to the Moho reflector, which can be recognized by its strong reflectivity, high amplitudes, and low frequencies that contrast with the non-reflective background.

In the Cornaglia and Campania Terraces, the Moho reflection is clearly visible, as is explained at the next chapter. Due to the high lateral continuity of these reflectors in these areas, the base of the unit is easy to track. However, in continental domains (Corsica-Sardinia Margin, North Tyrrhenian, Italian Margin and Sechi-Farfalla region) the Moho tends to be obscured by the multiple of the water wave, and where visible, its reflectivity is comparatively lower, probably due to a higher signal attenuation. Therefore, it becomes more discontinuous

(for example at MEDOC-4, CMPs 28,000 to 31,000, around 7 s TWT, fig. 4.4-b), and in some segments it is not visible at all.

As will be developed at the forthcoming chapter, the Moho presents also discontinuous character at the North Sicily margin (M28-b, CMPs 10,000 to 15,000, fig. 4.10-b), although is still possible to outline it. Finally, at the Magnani-Vavilov Basin no Moho reflection has been described. As is also explained in the next chapter, this fits well with the exhumed mantle interpretation (Prada et al., 2014). So, in this case, the peridotite - the mantle - makes the seismic basement.

4.2.2. Tortonian

Although there are relatively few ground-truthing evidences (Colantoni et al., 1981) throughout the Tyrrhenian, Tortonian has been dredged in a small number of places, for example on the Sardinia basin, or in a ridge southwards of Baronie seamount (Colantoni et al, 1981; Sartori et al., 2001) (MEDOC-6, fig. 4.2-b). But dredging data doesn't provide criteria to stratigraphically locate properly these deposits.

Only the ODP drilling site 654 of leg 107, located in the Sardinia margin, provides a stratigraphic position for the top of this unit (Kastens et al., 1988). But this site is located at a small basin, surrounded by rotated fault blocks making an isolated half-graben, and therefore this information has just a local significance and the correlation of the horizon in the rest of the basin should be done with caution. Another qualitative criteria to locate this limit is the "L" discontinuity, an isochron described by several authors (Trincardi & Zitellini, 1987, and references therein). It is a regional discontinuity thought to be related with the start of the opening of the Tyrrhenian. It is interpreted to mark upper Tortonian time across the entire Tyrrhenian. From this we infer that the contact between the pre-rift and syn-rift sediments approximately coincides with the end of the Tortonian. This proxy has been taken as an indicator to interpret the top of the Tortonian, where it is difficult to find this boundary.

To extrapolate the extension of this unit, some common seismic features can be associated to the Tortonian, although the character of stratification changes considerably across the basin. Usually the top is marked by a strong reflection, with fairly good continuity, over which upper Messinian sediments lay unconformable. Typically, the internal coherence of the reflections and their continuity are poor, although there are some internal layers with a higher reflectivity that tend to be associated to local unconformities and have a fragmentary character, as can be seen on Sechi-Farfalle region (MEDOC-11 between CMPs 3,900 and 5,200, fig. 4.4-b).

In general, thickness of these deposits greatly varies across the basin, and it is difficult to

determine because of the difficulty to constrain its base in some areas. But probably the thickest Tortonian deposits can be found in the North Tyrrhenian, near the Italian coast, reaching 0,7 sec. TWT at MEDOC-1, at the easternmost part of the line (fig. 4.3-b).

As discussed next, the Tortonian sedimentary unit has been identified only in continental basement-type domains (see explanation at the next chapter), although its presence is uncertain in the Campania Margin area as is explained below.

Corsica-Sardinia margin

This unit is present all along the entire Sardinia-Corsica continental margin. In this region, Tortonian units lie over older Miocene sediments. Due to signal attenuation, this contact is not well constrained, but where visible, the layers show a parallel disposition with respect to older sediments.

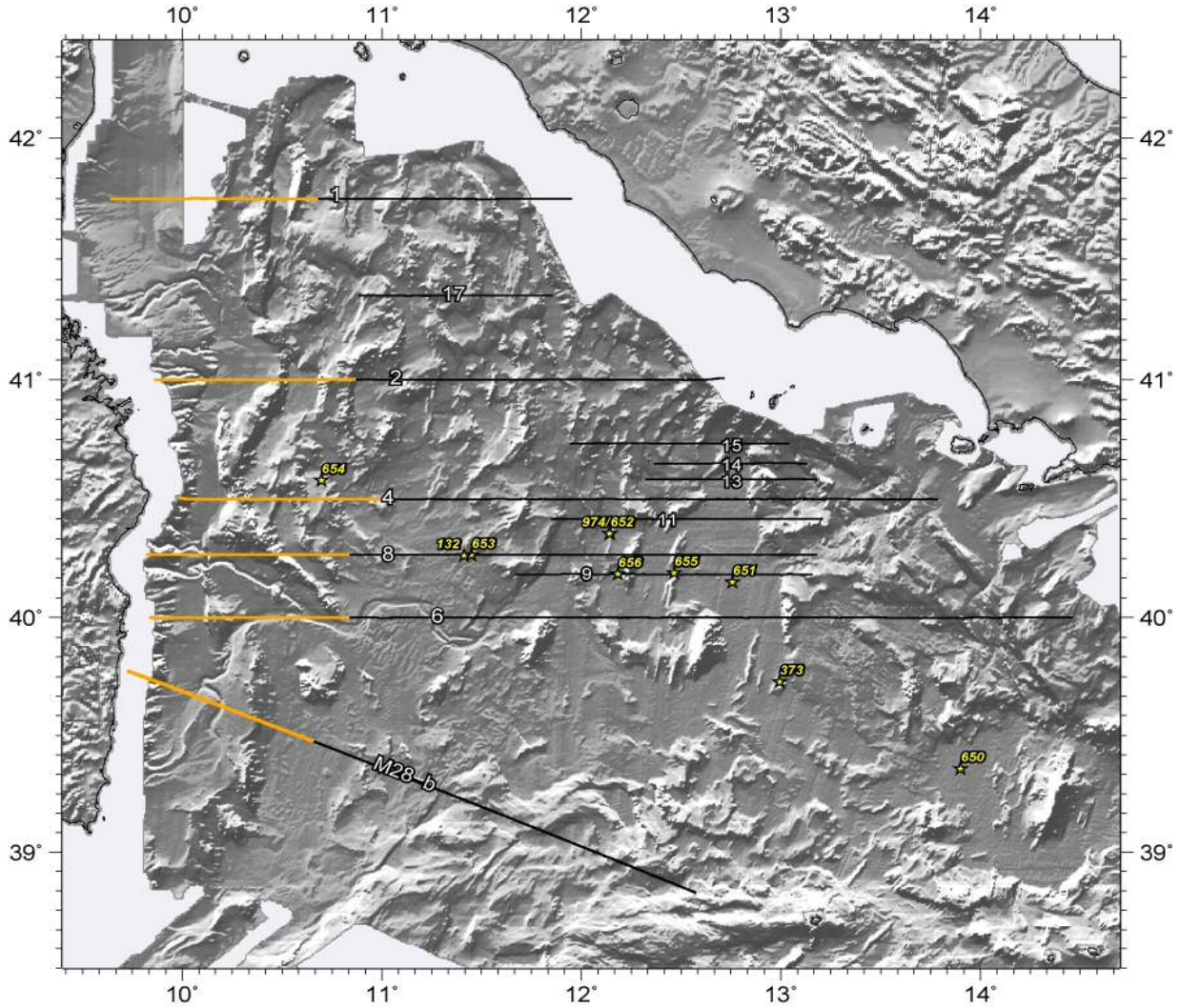

Figure 4.2-a: Topographic map of the Tyrrhenian with analysed MCS sections. Location of the segments used to work the Corsica-Sardinia continental margin (see figure 4.2-b) are highlighted in orange.

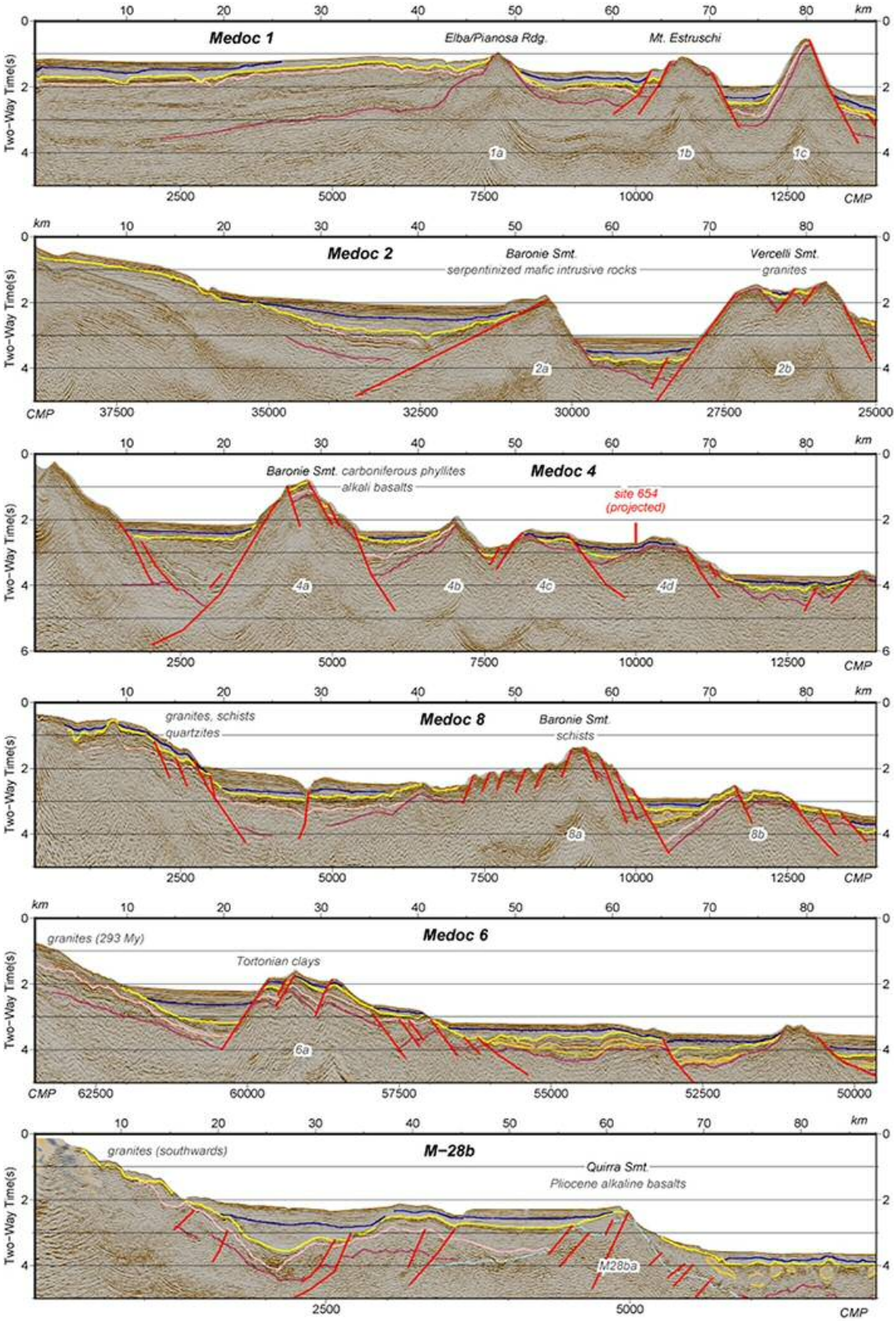

Figure 4.2-b: MCS sections crossing the Corsica-Sardinia continental margin. At the places were dredging data were available, it has been pointed out (Colantoni et al., 1981). Also the ODP site 654 location has been plotted (see figure 4.2-c).

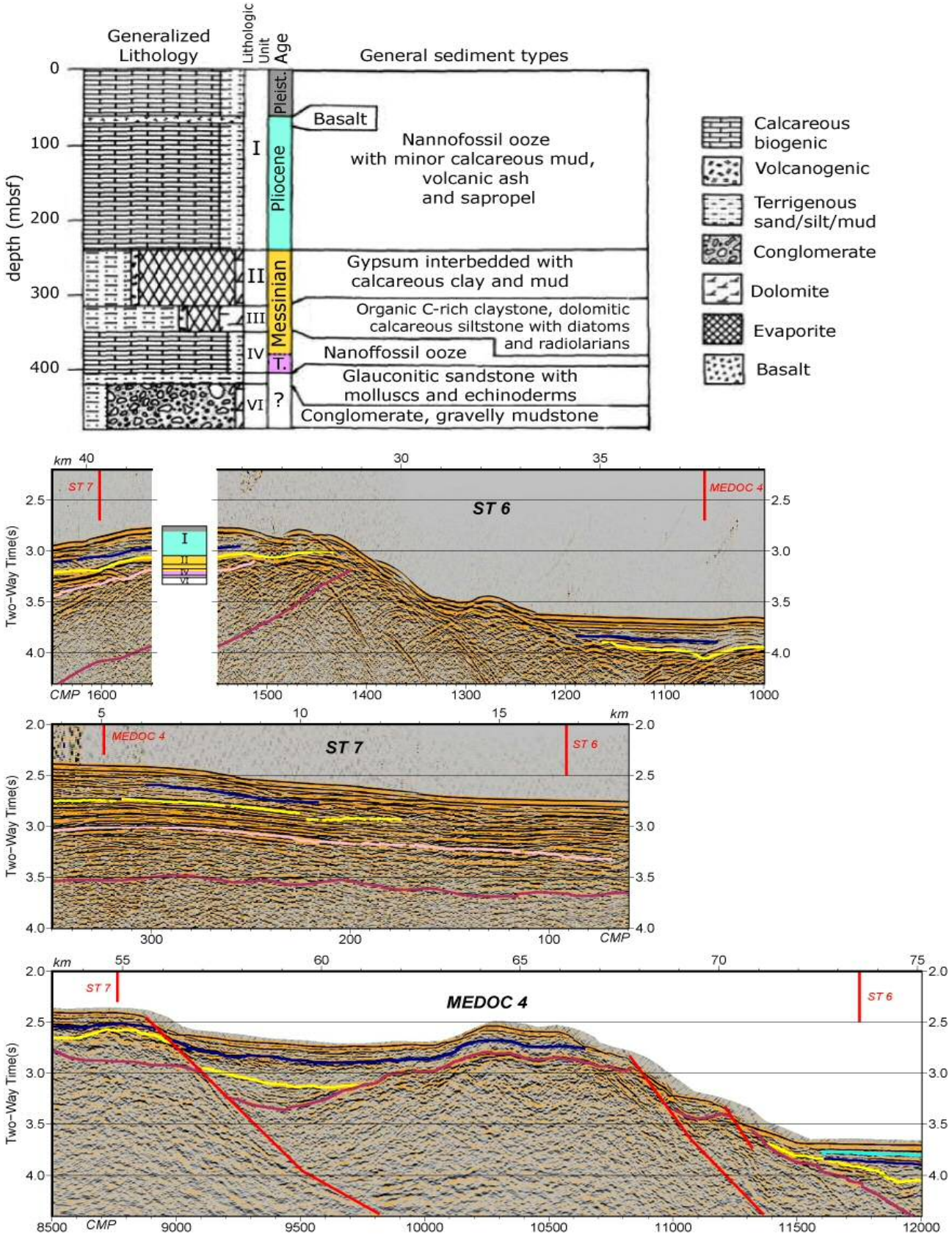

Figure 4.2-c: Stratigraphic column of ODP site 654 (modified from Kastens & Mascle, 1988), and its position at the ST 6 section. ST sections were used to bring the horizon location from ODP 654 to the MEDOC survey (and M28-b) profiles. Red vertical lines show the places were these sections cross with each others.

The contact with the upper unit is discordant: layers toplap against the Messinian, and even in some points, erosional surfaces are observed, giving a strong reflection with a fairly good continuity. For example, the erosional surface is visible at M28-b, between the CMPs 1,500 to 2,500, or at the MEDOC-6 between CMPs 61,000 to 62,500 (fig. 4.2-b).

In this region, ODP site 654 drilled the top of the unit. In this case, seismic profiles belonging to the ST survey have be used to extrapolate the Tortonian top towards the surrounding basins (Kastens et al., 1988) (fig. 5.2-c).

Tortonian thickness is not clear in this region because the base is not well constrained. However, important lateral thickness variations are observed, mostly related with syn-rift character of strata: the unit reaches a maximum thickness of 0.7-0.8 s TWT at the depocenters, while the thinnest deposits are around 0.3 s TWT near or on top of the ridges.

Broadly speaking, stratification is weak making it difficult to characterize strata geometry. However, there is some indication of fan geometry, hinting at syn-rift deposition. This characteristic can be seen almost everywhere, for example, at MEDOC-2 between CMPs 33,000 and 35,000 (fig. 4.2-b). Only in some places, the base of the Tortonian shows parallel layering or sub-horizontal attitude of the reflectors, suggesting a locally post-rift sedimentation (fig. 4.2-b, MEDOC-6, CMPs 57,000 to 59,000).

The lateral continuity of reflections from the stratification is generally poor, or locally absent as can be seen on MEDOC-8 between CMPS 3,000 and 6,000 (fig. 4.2-b). These short reflections and poor reflectivity probably imply small-scale faulting or fracturing (e.g. water escape features), for example at M28-b between CMPs 2,500 and 4,000 (fig. 4.2-b). However, two areas show good strata continuity: at MEDOC-4, (CMPs 2,000 to 3,500) and MEDOC-6 CMPs 56,500 to 57,700, at the eastern flank of the Baronie seamount, where the unit is fairly well stratified in comparison with the rest of the unit in this area.

In the southernmost region, imaged by line M28-b, stratification style changes laterally alternating between segments with good continuity and segments where stratification disappears laterally.

North Tyrrhenian region

Here again, the base of the Tortonian unit is not well defined. This is because the corresponding reflections show weak stratification - fairly discontinuous layering with low reflectivity - giving a seismic image similar to the basement. Although frequencies in the sediments are higher than in the basement, this difference is not enough to clearly locate the boundary in some areas. This pattern, together with a transpressional deformation in the eastern part of the region, makes it difficult to define the base and the top of this unit with

confidence.

In contrast, the contact with the overlying Messinian strata is clear because of the contrast between the low reflectivity of Tortonian sediments and the high reflectivity of the basal unit of the Messinian. In most parts of this region, stratification of both units is concordant, but locally Messinian strata onlaps this unit, as can be seen on MEDOC-1 between CMPs 22,700 and 23,500 (fig. 4.3-b).

In this region, the unit seems to have a pre- and/or early syn-rift character. In general, the oldest sediments present a pre-rift disposition whereas the most recent ones are syn-rift, as can be observed on MEDOC-1 between seamounts 1a and 1b (fig. 4.3-b). In this point, lower Tortonian has a constant thickness with parallel reflections, which span from depocenter to top of seamount 1c. It appears rotated with respect to pre-tectonic deposition. Conversely, syn-rift Tortonian has been observed only at the center of the half-graben, between CMPs 11,800 to 12,500 (fig. 4.3-b). But in some of these depocenters pre-rift sediment are not visible, and only syn-rift sediments are imaged.

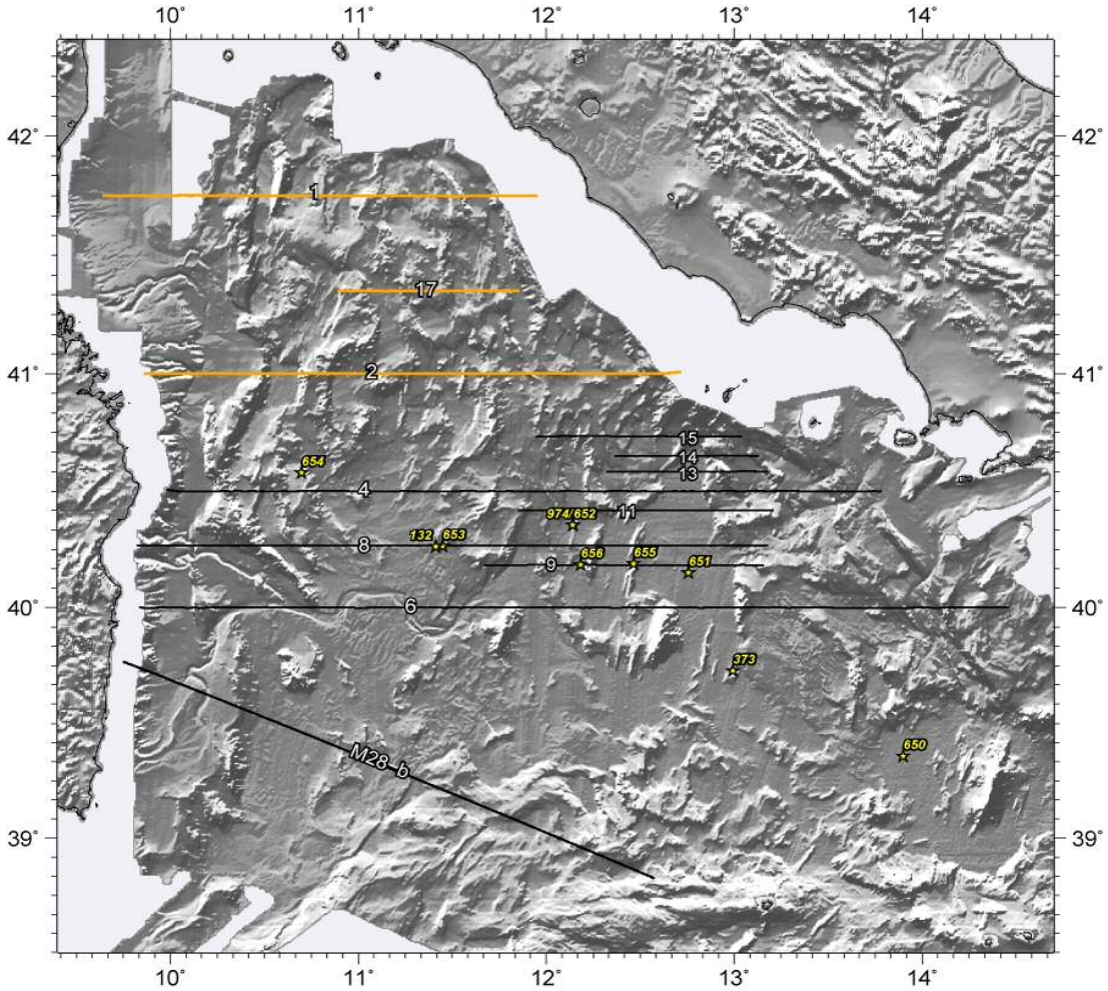

Figure 4.3-a: Topographic map of the Tyrrhenian with analysed MCS sections. Location of the segments used to work the North Tyrrhenian (see figure 4.3-b) are highlighted in orange.

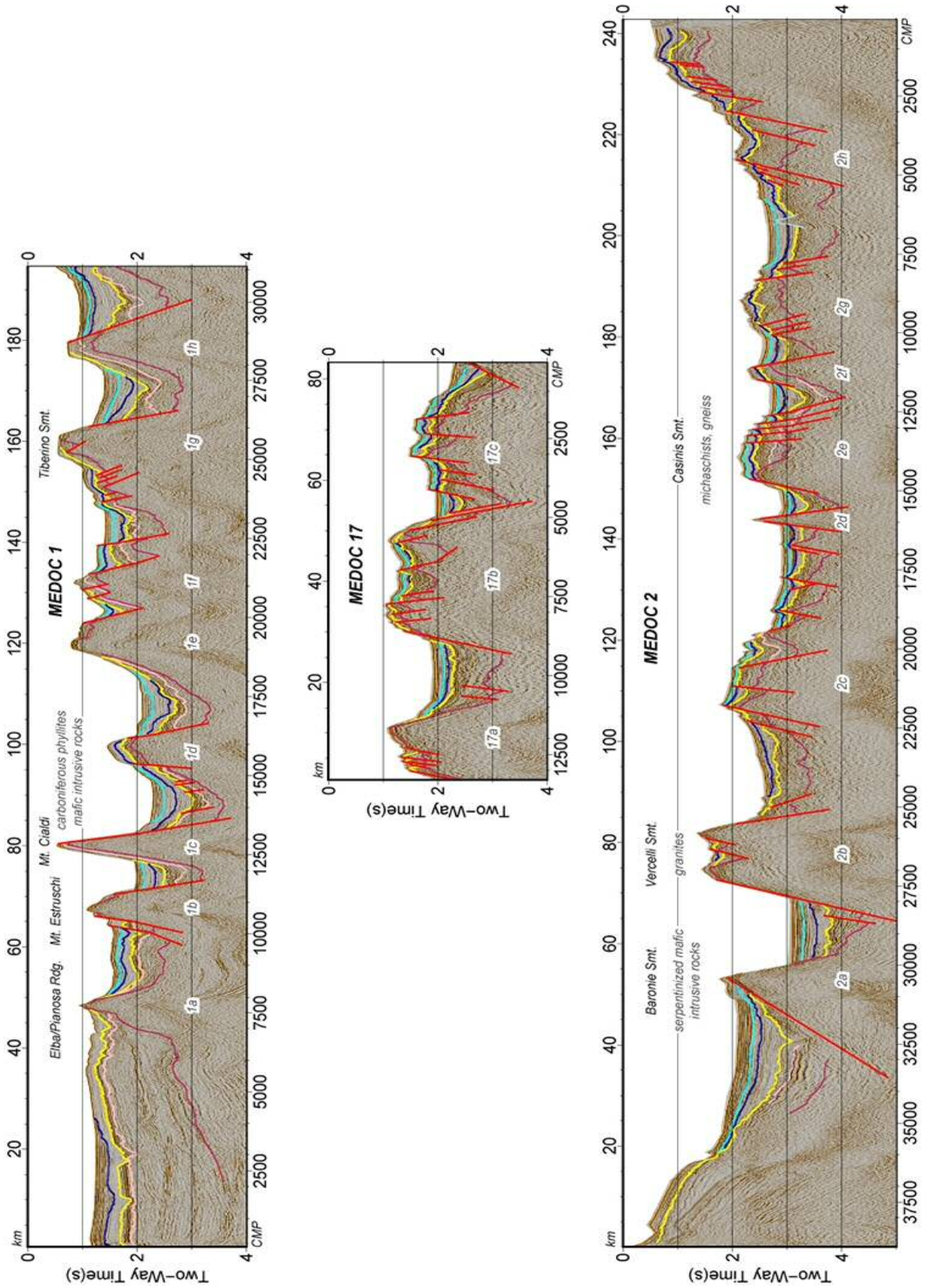

Figure 4.3-b: MCS sections crossing the North Tyrrhenian. At the places were dredging data were available, it has been pointed out (Colantoni et al., 1981).

The presence of this unit is not uniform across the region. In general, the unit fills the depocenters, and in most cases it is not present at the basement highs. But its presence is heterogeneous: at MEDOC-1 it has been imaged all along the section, whereas its presence is limited along the MEDOC-2 and MEDOC-17.

It reaches its maximum thickness at the center of half-grabens, and it can disappear laterally due to the wedging of sediments. The maximum Tortonian thickness is near the Italian margin: at MEDOC-1, CMPs 29,500 to 31,500 (fig. 4.3-b).

Sechi-Farfalle region

The Tortonian has been described at all the seismic sections that cross this region, and occurs confined to the deepest zones (fig. 4.4-b).

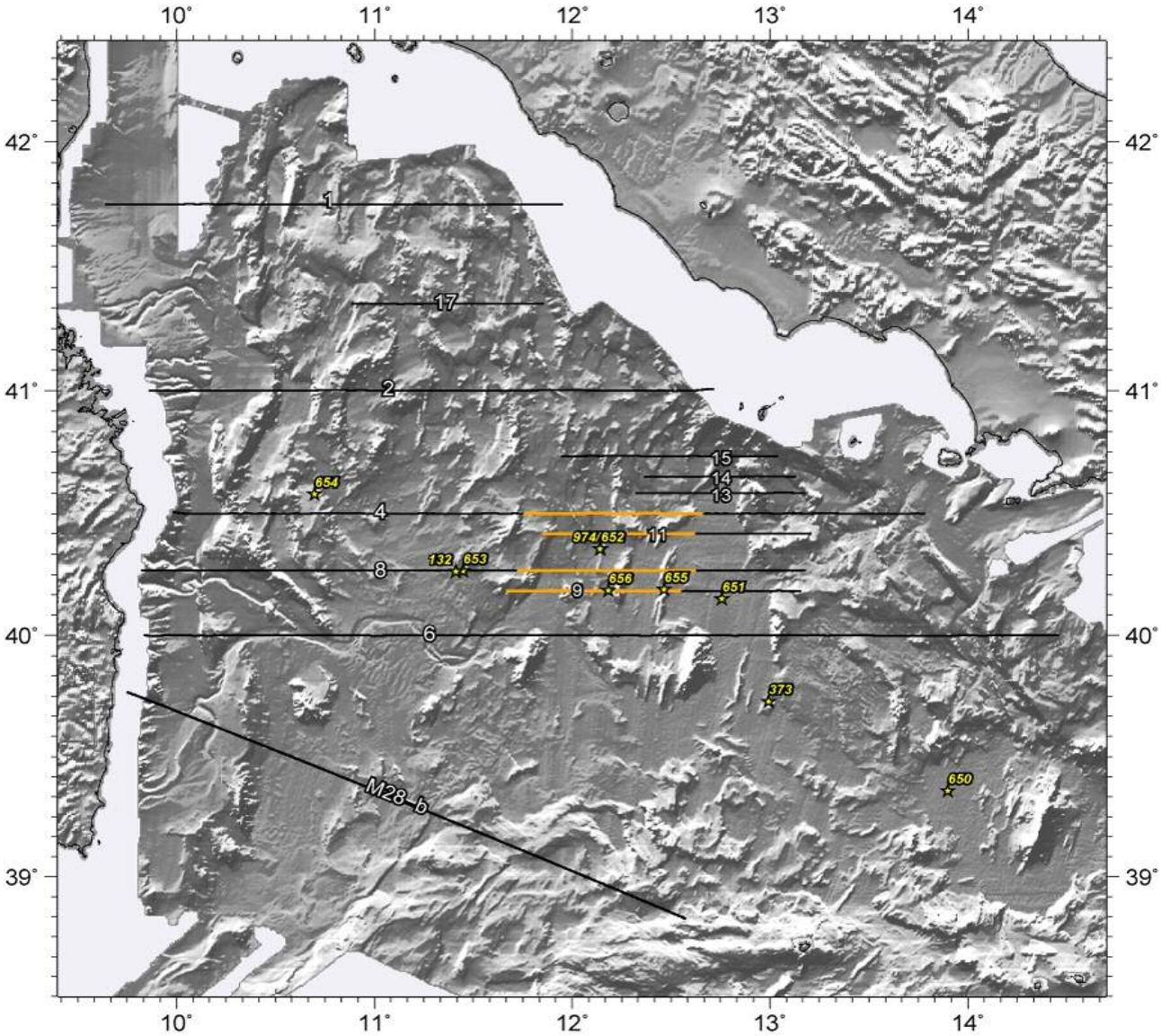

Figure 4.4-a: Topographic map of the Tyrrhenian with analysed MCS sections. Location of the segments used to work the Sechi-Farfalle region (see figure 4.4-b) are highlighted in orange.

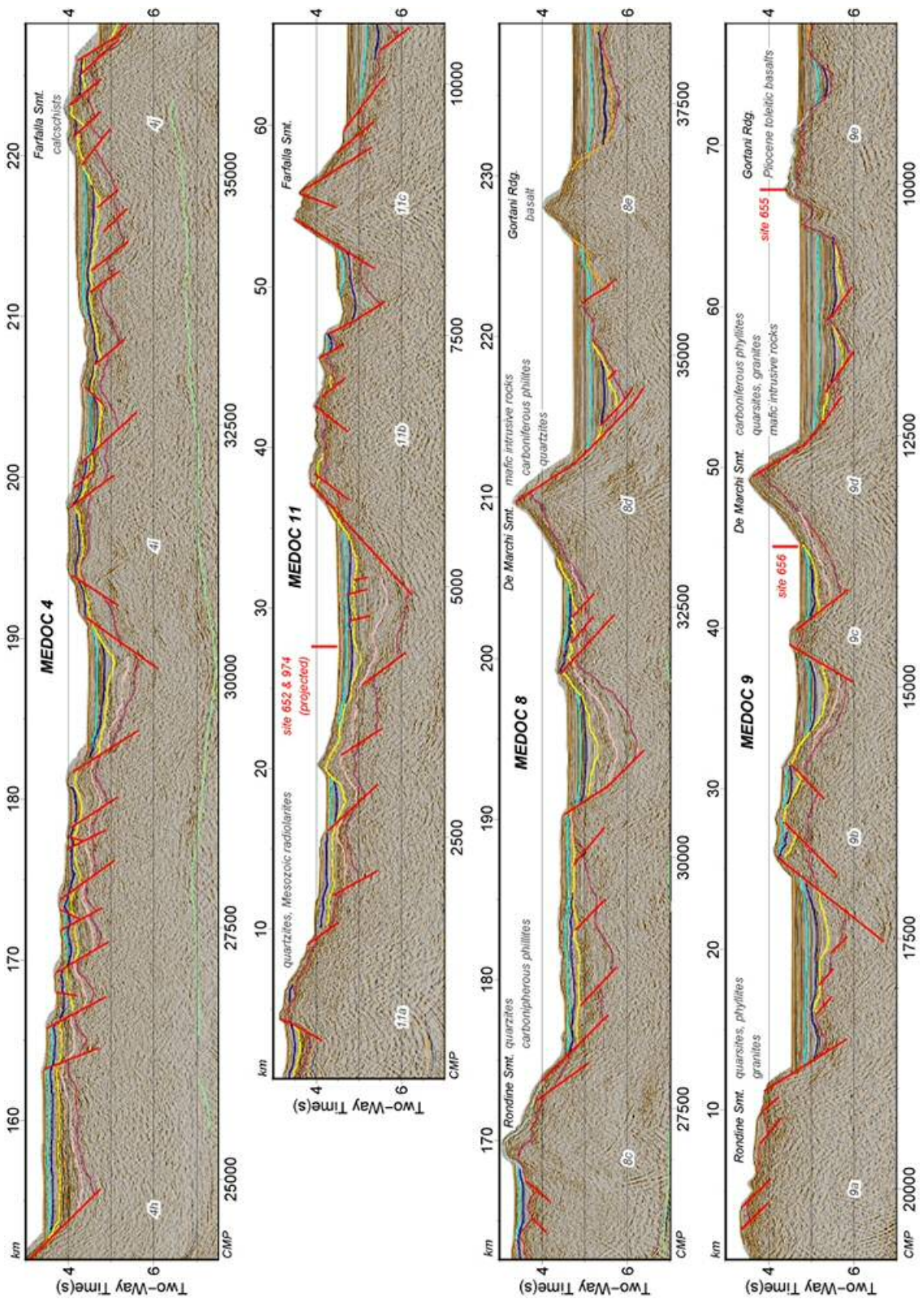

Figure 4.4-b: MCS sections crossing the Sechi-Farfalle region. At the places were dredging data were available, it has been pointed out (Colantoni et al., 1981). Also the ODP sites 652 and 656 location have been plotted (see figure 4.4-c and 4.4-d).

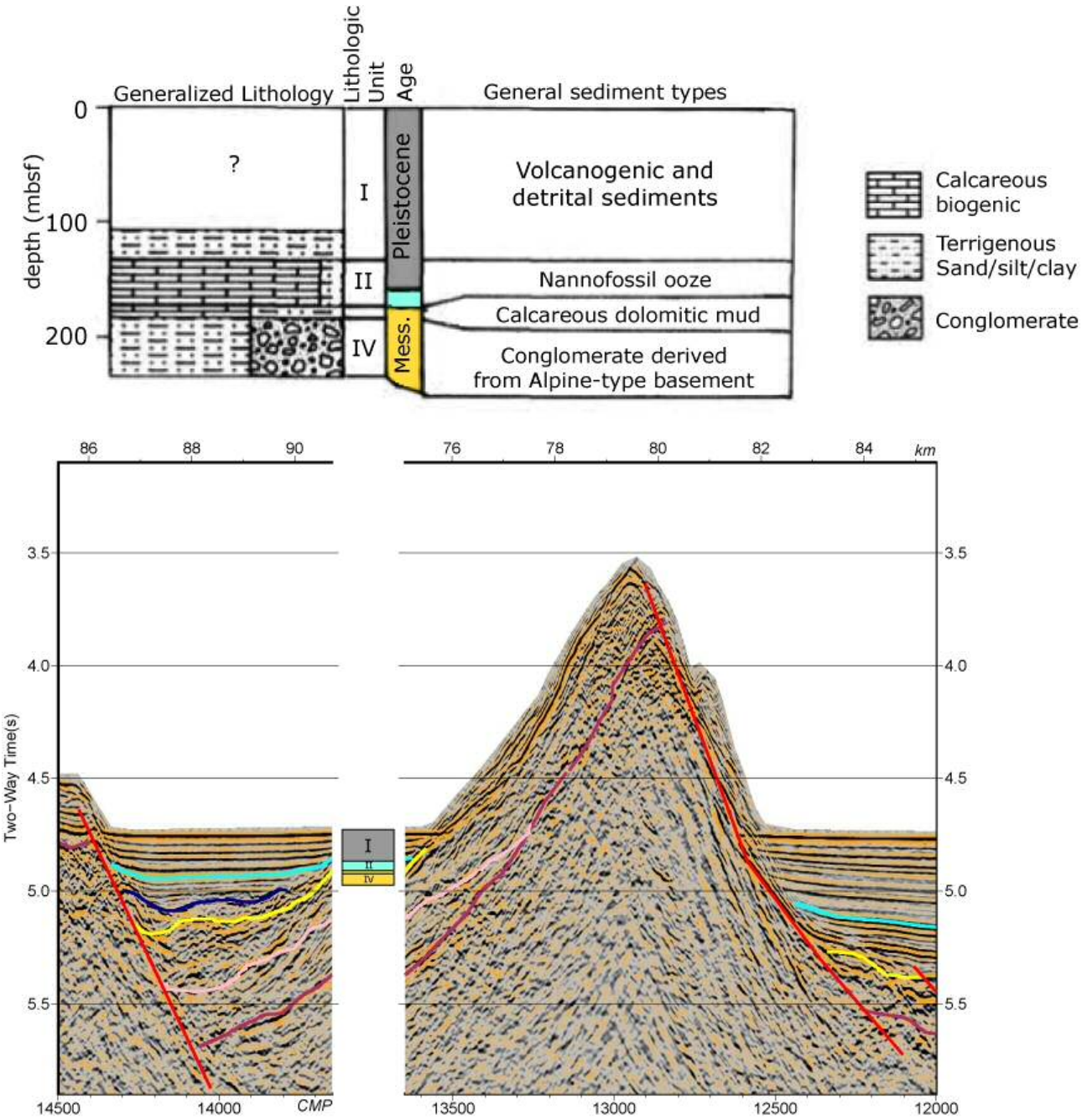

Figure 4.4-c: Stratigraphic column of ODP site 656 (modified from Kastens & Mascle, 1988), and its position at the MEDOC 9 section.

Base and top of this unit in this area are marked by the contrast of seismic facies between the basement and the Messinian units, respectively. The basement shows lower frequencies than the sediment and no internal reflectivity has been observed, in contrast with the Tortonian unit. The overlying Messinian appears to be more stratified than this unit, with also higher reflectivity. In this region, ODP site 652 reached pre-rift sediments, which considering seismic facies, ODP report description (Kastens et al., 1988), and its stratigraphic position, have been taken as Tortonian in age or perhaps lowermost Messinian.

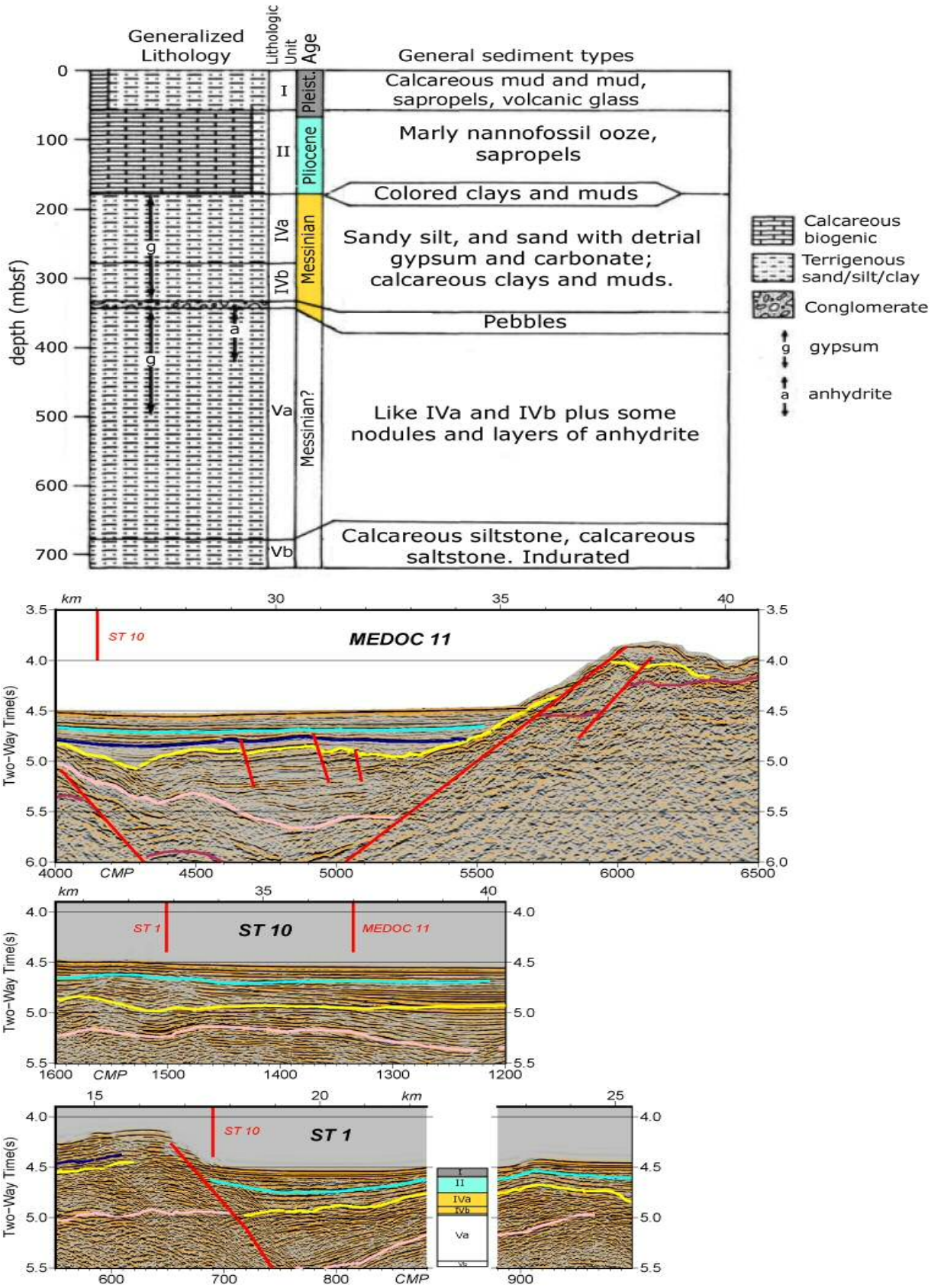

Figure 4.4-d: Stratigraphic column of ODP site 652 (modified from Kastens & Mascle, 1988), and its position at the ST 1 section. ST sections were used to bring the horizon location from ODP 652 to the MEDOC survey (and M28-b) profiles. Red vertical lines show the places were these sections cross with each others.

The shape of these deposits in 2D is lenticular. Their maximum lateral extension is about 35 km imaged at MEDOC-4 (fig. 4.4-b). Although its thickness varies considerably, it reaches a maximum of 0.5 s TWT at depocenters (MEDOC-11, at CMPs 4,400 to 5,000, fig. 4.4-b), while its minimum thickness is about 0.2-0.1 s TWT. In most cases the unit disappears laterally, because it is confined to grabens. Also, at MEDOC-13, in the western side of seamount 13a (fig. 4.5-b), deposits belonging to this unit reach 0.3 s TWT thickness, but rapidly disappear laterally.

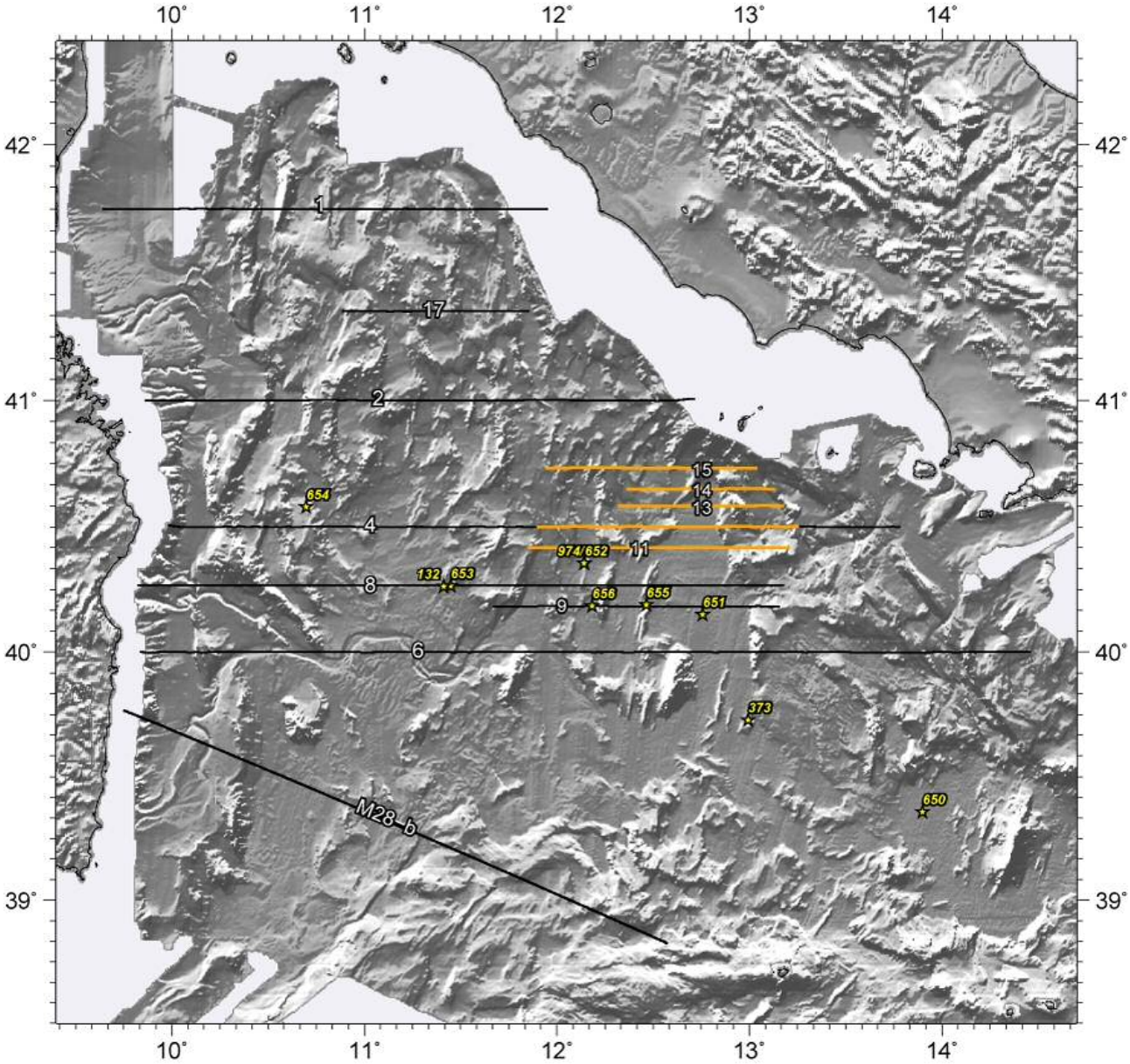

Figure 4.5-a: Topographic map of the Tyrrhenian with analysed MCS sections. Location of the segments used to work the Vavilov and Magnaghi basins (see figure 4.5-b) northern area are highlighted in orange.

In some places a fan-like disposition of strata is observed, although with no clear syn-rift wedged strata geometry. In these cases it can be inferred that strata where deposited during fault activity (for example, at MEDOC-8, between CMPs 30,600 to 32,000, fig. 4.4-b). In general, reflections show more continuity – up to tens of km – than in previous regions, but

tend to have a fragmentary/chaotic aspect with cross bedding stratification (i.e. MEDOC-11, between CMPs 4,200 to 5,000, fig. 4.4). Its reflectivity changes laterally as well as in the vertical column.

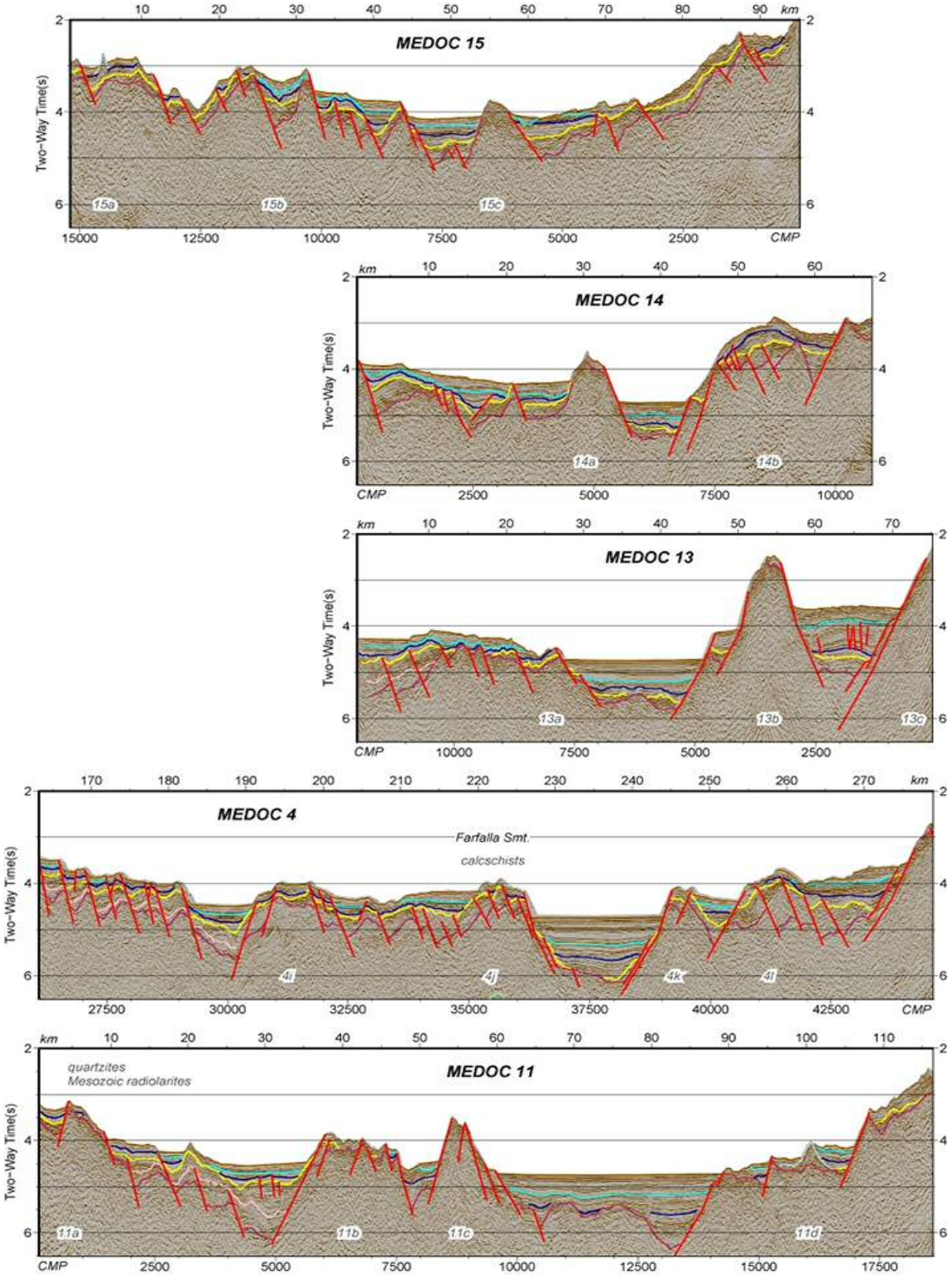

Figure 4.5-b: MCS sections crossing the Vavilov and Magnaghi basins northern area. At the places were dredging data were available, it has been pointed out (Colantoni et al., 1981).

North Sicily Margin

In the North Sicily margin, like in the North Tyrrhenian, there is not sampling information, but the contrast between well-stratified Messinian and a weaker stratification of the Tortonian give some certainty about the contact location. Moreover, the syn-rift base have been considered as belonging to the upper Tortonian, making a parallelism with the North Tyrrhenian and the Sechi-Farfalle region.

In this region, the Tortonian shows a homogeneous transparent aspect with few internal reflections. These reflections have low reflectivity and poor lateral continuity, reaching at most 2 km (fig. 4.6-b, line M28-b between CMPs 12.900 and 12.000). Deposits show a constant thickness and fill the half-grabens.

Because of its often transparent and homogeneous aspect, this unit is hard to separate clearly from the underlying basement. Thus, a contrast in frequency content of the strata has been often used as a criteria to mark the boundary: Tortonian frequencies are higher than the basement-type frequencies as has been inferred also in the other regions. In some areas, high-frequency continuous reflections have been considered as the last sediment stratification evidence, and therefore they are interpreted as the base of this unit.

4.2.3. Messinian

This unit has been described all across the Tyrrhenian with the exception of Vavilov and Magnaghi Basins (fig. 4.1). Drilling and dredging data provide clear Messinian evidences across the basin. Thus, we can assume that it is present almost over the entire continental and oceanic crust regions (see explanation about the regions at the next chapter). The thickest deposits have been observed at the southern Cornaglia Terrace, reaching the 1.5 s TWT (fig. 4.6-b, M-28b, between CMPs 7,500 and 8,500).

Although its character changes widely across the basin, common features are observed everywhere. In general, the entire sequence presents higher reflectivity than the previous Tortonian sediments and the overlying Pliocene. The top of this unit also has often an erosive and/or high reflectivity character, which can be easily identified. Usually Pliocene strata overlies unconformably with onlap geometry. It provides a reasonably good isochron across the entire basin, even if no nearby drilling exists. Therefore, the top is easy to calibrate everywhere. This isochron corresponds to the Messinian Salinity Crisis, and lies at the uppermost Messinian column instead of the Messinian-Pliocene boundary (Manzi et al., 2013). Nevertheless in the Tyrrhenian, the ODP data from leg 107 locate this isochrone very close to the contact (Kastens & Mascle, 1990), and at basin-scale they can be considered basically coincident for our study.

The base of this unit is not always as clear as its top. But in general a loss of clear

reflections and internal coherence occurs near the Tortonian-Messinian boundary. In some places, a clear stratigraphic discontinuity has also been observed. ODP data also provide detailed information to calibrate this limit on the seismic lines.

Within the Messinian, several sub-units have also been identified. They can be found across all the regions where Messinian is present. Although their seismic character changes depending on the region, they show some common features that are recognizable everywhere.

Broadly speaking, the lower sub-unit, which has been called M1, tends to present high variability in its features, although in general presents low reflectivity. Its internal coherency and stratification are highly variable. The common feature is the reflectivity, which tend to be low. Because of this, in some places it is difficult to distinguish it from the underlying Tortonian. The second sub-unit, labelled as M2, has been observed more locally. It consists of short, lenticular deposits with varying diapiric geometry. It generally presents poor stratification, low reflectivity and low internal coherency. Finally, the youngest sub-unit, the M3, presents high reflectivity, and well-stratified aspect with quite good internal coherence and continuity of the reflections. This unit is fairly constant within the Messinian column, being observed basically everywhere.

The boundaries between these sub-units are often not sharp, and sometimes occur as gradual transitions. Where stratification is visible, the units tend to be concordant. Although in some places, progressive unconformities have been observed apparently related to diapirism or tectonic processes, as discussed below.

Corsica-Sardinia margin

This region is where Messinian sediments are worst constrained, because of the weaker contrast between the bounding upper and lower units. However, the ODP site 654 of leg 107 near this area (fig. 4.2-b) gives information about its stratigraphic position. The contact with previous Tortonian units is concordant, so there is no geometrical discontinuity to distinguish them. Similar to the rest of the basin, the reflectivity and lateral continuity of Messinian reflections are higher, allowing mapping the base throughout this region.

The top consist of a discontinuity with the upper deposits of Pliocene age. Although this discontinuity is not present everywhere, the ODP site 654 data can be used to locate the boundary, but the extrapolation of this contact across this region should be considered with caution because of the local character of this information.

In the Corsica-Sardinia margin region, the Messinian sub-units present a gradual transition between them, so that their boundaries are not as clear as in other regions. In addition, the intermediate - M2 - sub-unit has not been observed in this region. The lower sub-

unit - M1 - has not been well described here, but at CROP line M28-b and at the MEDOC-4 (fig. 4.2-b) a weaker reflective band below the upper Messinian sub-unit is interpreted as the lower sub-unit. The characteristics of these strata are low reflectivity, but fairly good stratification, and good internal coherency. The base of the M1 is unclear here because of the uncertainty of the Tortonian-Messinian contact, and their similar seismic character.

The frequency content for the upper and lower sub-units is similar, and their contact consist in a transitional change, with no clear abrupt limit. This upper sub-unit (M3) can be observed everywhere. It presents highly reflective strata with good stratification and good internal coherence.

The layering displays parallel stratification, suggesting a post-rift deposition (for example, at M28-b, between CMPs 3,500 to 4,500, fig. 4.2-b), but locally, there are places where its wedged shape suggests syn-rift sedimentation (for example, at M28-b, between CMPs 1,700 to 2.300, fig. 4.2-b).

Therefore, upper Messinian has a post-rift character in most cases. The contact between the syn-rift and post-rift sediments is unclear because of the gradual transition between them.

Lower Messinian syn-rift deposits are commonly observed, while post-rift is more restricted, although visible for example at MEDOC-6, CMPs 60,000 to 61,000 (fig. 4.2-b), near the Baronie seamount. Further, there are a few places where the syn to post rift contact occurs near the Messinian-Pliocene limit, as imaged in MEDOC-4 (CMPs 1,900 to 3,500, fig. 4.2-b).

North Tyrrhenian region

Messinian sediments fill all depocenters in this region, and even cover some ridges (for example 17b, 2c or 2e, fig. 4.3-b). Because of this geometry, it presents a distribution in discrete deeps separated by tilted blocks. But the correlation of the unit across the several half-grabens is simple due to the characteristic high reflectivity of the Messinian top. In some areas, like at the Tiberino seamount, the erosional event at the end of the Messinian eroded the highs that must have been exposed during this event leading to characteristic reflective flat top (1g seamount, at fig. 4.3-b). In the sectors where no erosion is present, the high reflectivity of the upper sub-unit allows the correlation of the Messinian top.

The Messinian base is given by a gradual loss in reflectivity and coherency contrast with the underlying sediments, although here this change is not as evident as in other areas. Therefore the boundary has also been interpreted based on information provided by bibliography (Möller et al., 2013; Trincardi & Zitellini, 1987), which locate the limit nearby to the pre-rift/syn-rift contact. This contact is the only available criteria to locate the base of the unit in some places.

The thickness of these deposits increases towards the east, although in general, they are thinner than in other regions of the basin. The maximum values are found in MEDOC-1, near CMP 26,500, or in MEDOC-2 near CMP 13,000 (fig. 4.3-b).

Almost all Messinian deposits in the North Tyrrhenian show a wedge-shaped geometry. So it can be assumed that they represent a syn-rift sedimentation. Here, the base of syn-tectonic sediments lies within the upper Tortonian, while the top occurs in the lower Pliocene. However, in some places faults apparently worked just until upper Messinian, and the syn-rift top roughly coincides with the Messinian-Pliocene contact (for example at MEDOC-1, CMPs 11,500 to 12,500, fig. 4.3-b).

In this region, as in the other continental areas, there are only two sub-units. In this case they can be clearly distinguished, although they are not present together in all places. The upper sub-unit (M3) has been described everywhere. It shows high reflectivity with fairly good internal coherency. However, in some areas it displays rather abrupt lateral changes in stratification particularly towards faults, becoming more chaotic approaching the fault (for example, at MEDOC-17, CMPs 9,000 to 11,000, fig. 4.3-b). This pattern has been taken as an indicator of sedimentation while fault was active, so and indicator of syn-rift sedimentation.

On the other hand, M1 is not present everywhere. It has been observed locally in places like at MEDOC-17, at CMPs 9,000 to 11,000, and 3,500 to 4,800; or at MEDOC-1 between CMPs 21,500 to 22,500, and 26,500 to 29,500 (fig. 4.3-b), but no clear criteria to match its discrete distribution has been found. These sediments present low reflectivity and poor internal stratification. However, there are a few places where a lower high-reflectivity package with a good internal coherency has been locally observed (like at MEDOC-1, CMPs 21,500 to 22,500, or 27,300 to 28,200, fig. 4.3-b).

Cornaglia Terrace and Campania Terraces

Messinian deposits share enough common features at these two regions to be treated together. And in addition, they both present completely different character from the surrounding areas.

The thickest Messinian deposits, reaching 1.5 s TWT, have been identified at the southern Cornaglia Terrace, (M-28b, CMPs 7,500 to 8,500, fig. 4.6-b). But this unit changes its thickness widely along the region: towards the northern Cornaglia Terrace, Messinian thickness decreases until 0.2-0.3 s TWT at MEDOC-4 (fig. 4.6-b). In contrast, at the conjugated Campania terrace, thickness remain quite uniform along the only available profile, and it keeps around 0.3 s. TWT (fig. 4.7-b).

Unlike other regions, at the Cornaglia and Campania Terraces these deposits do not

remain as isolated filling of depocenters, but they show good continuity across the region, although some basement highs like the Baronie seamount break locally this continuity (imaged on MEDOC-4 and 6, fig. 4.6-b).

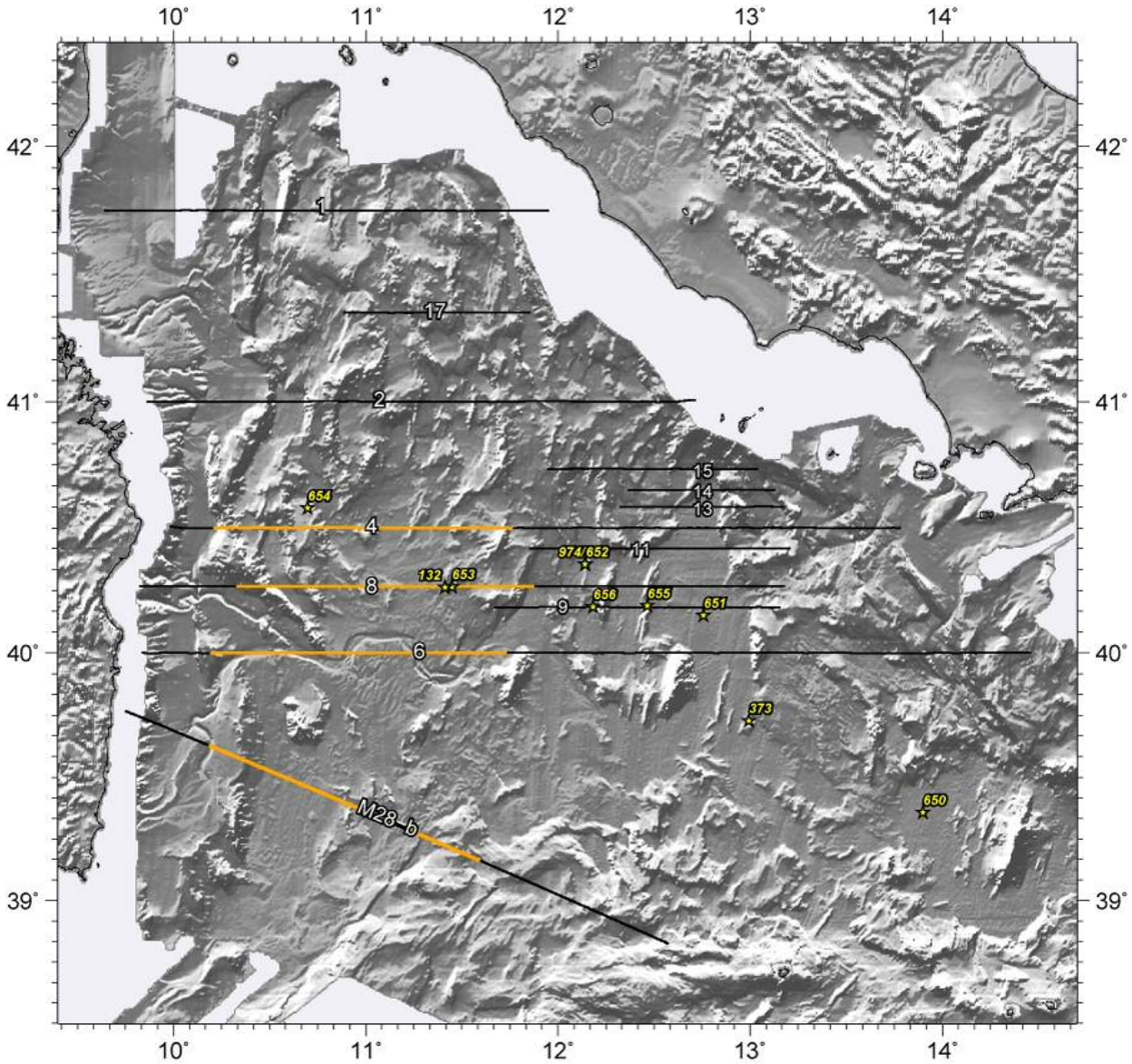

Figure 4.6-a: Topographic map of the Tyrrhenian with analysed MCS sections. Location of the segments used to work the Cornaglia Terrace (see figure 4.6-b) are highlighted in orange.

Apparently, the Messinian sediments lay directly over the seismic basement top across the whole area with an unconformity contact. While the upper strata, the Pliocene deposits are parallel with a concordant contact over the Messinian top across most part of the regions.

In both Cornaglia and Campania Terraces regions all the three Messinian sub-units have been identified. Stratification for the lower M1 sub-unit change widely laterally in few tens of kilometers, and it changes too, from poor to intermediate stratification in the vertical direction. Also the internal reflectivity is highly variable, with a poor reflective character generally TWT (fig. 4.6-b).

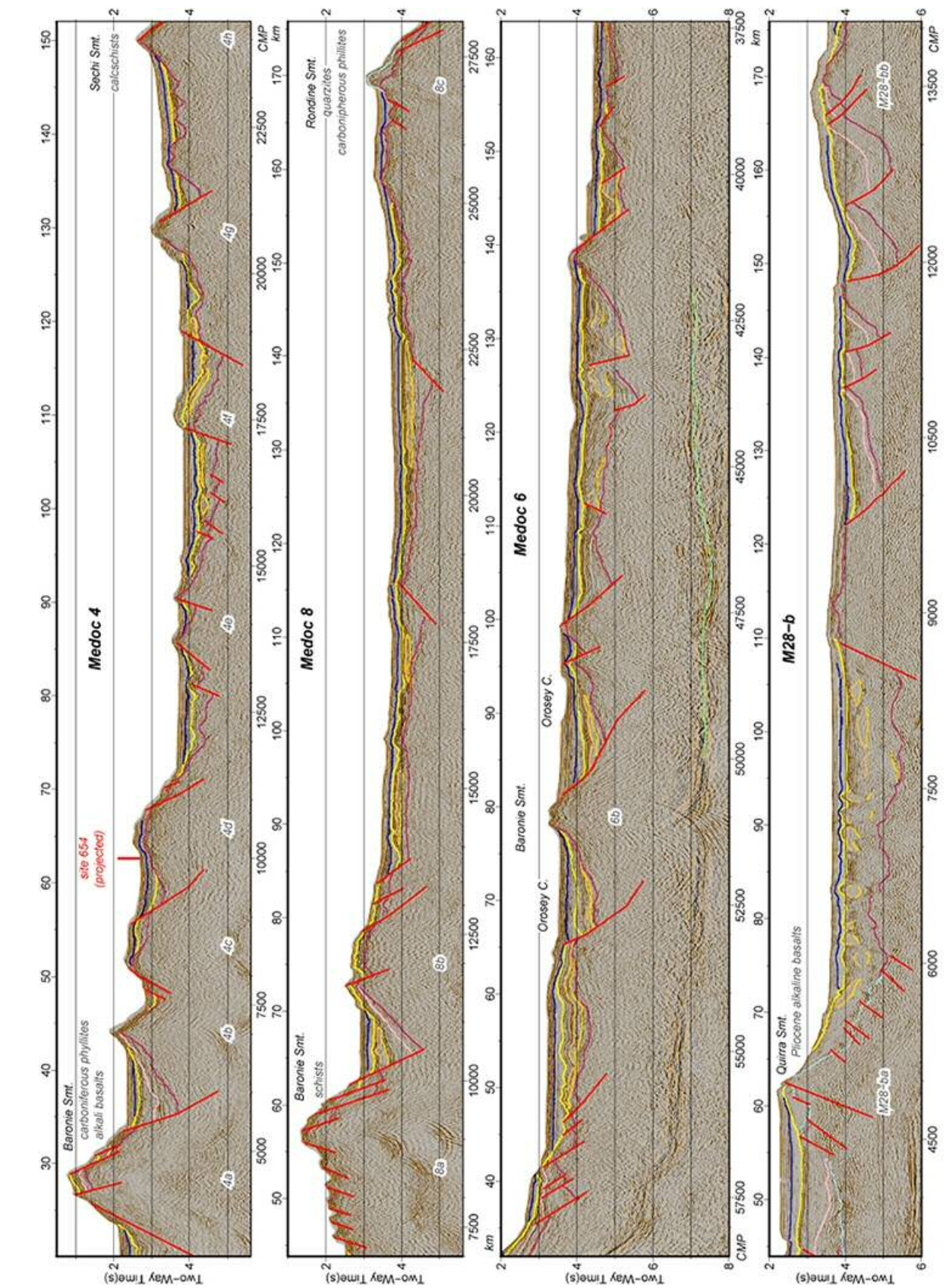

Figure 4.6-b: MCS sections crossing the Cornaglia Terrace. At the places were dredging data were available, it has been pointed out (Colantoni et al., 1981). Also the ODP site 653 location has been plotted (see figure 4.6-c).

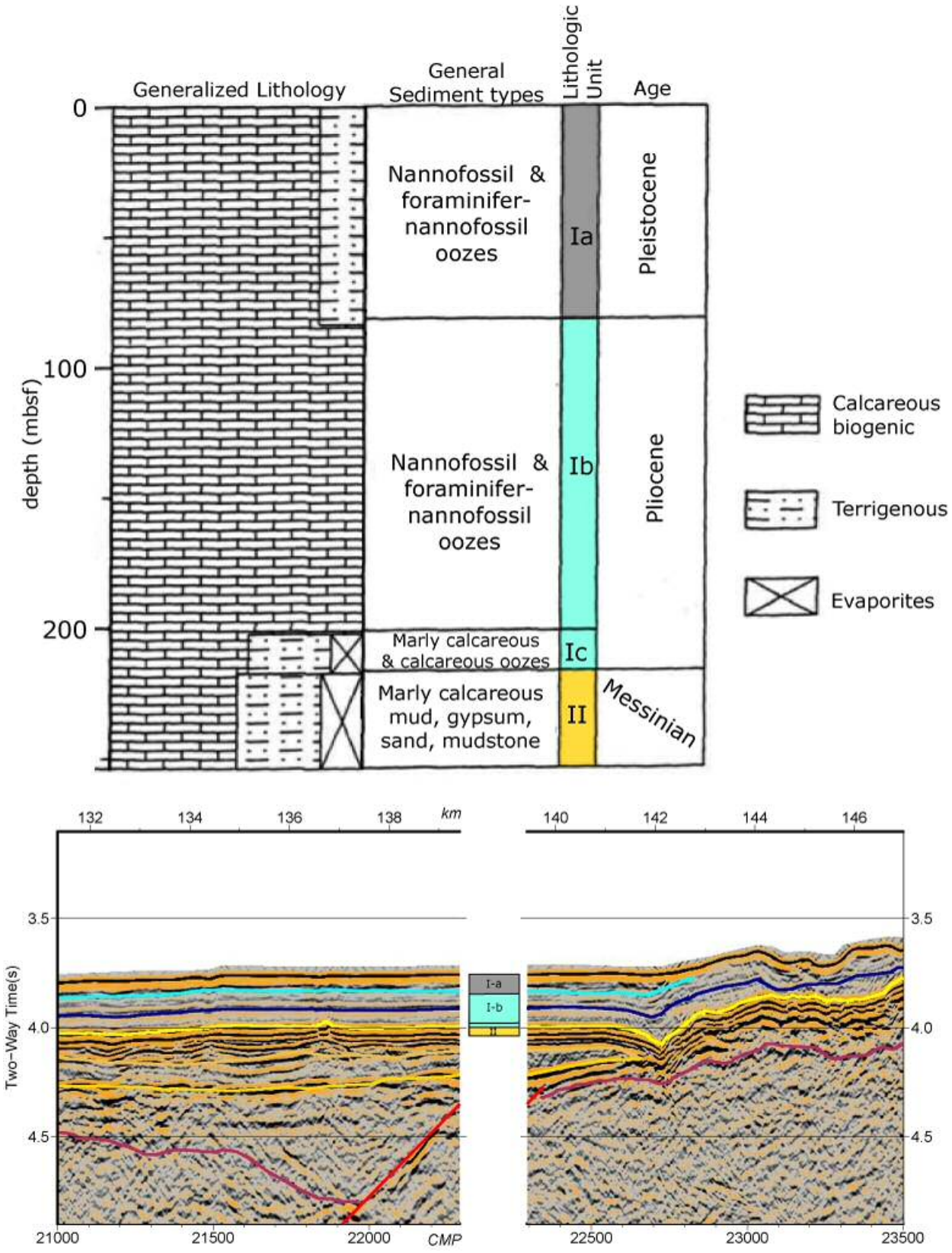

Figure 4.6-c: Stratigraphic column of ODP site 653 (modified from Kastens & Mascle, 1988), and its position at the MEDOC 8 section.

Next, the M2 sub-unit has only been clearly observed at Cornaglia and Campania Terraces in the basin. It consists of lenticular deposits with little internal reflectivity. Their base,

where clearly visible, is a negative polarity reflector, so it can be easily identified.

These deposits change widely their character within the same region. At the northern Cornaglia Terrace they present approximately 0.2 s. TWT thickness, long deposits with weak stratification within them, while going towards the south, they reach 0.4 s. TWT, and appear as shorter deposits without internal stratification. While at the Campania Terrace, the only profile crossing it does not allow to observe any variation along the area.

Finally, the upper sub-unit M3 does not change in character in comparison with other regions of the basin. M3 shows higher reflectivity than the underlying sub-units, good internal coherency and good continuity of reflections. These show parallel configuration, although they appear locally folded due to the diapiric behaviour of the underlying M2 sub-unit (for example, M-28b, CMPs 6,000 to 7,500, fig.5.6-b; or MEDOC-6, CMPs 13,000 to 16,000, fig. 4.7-b).

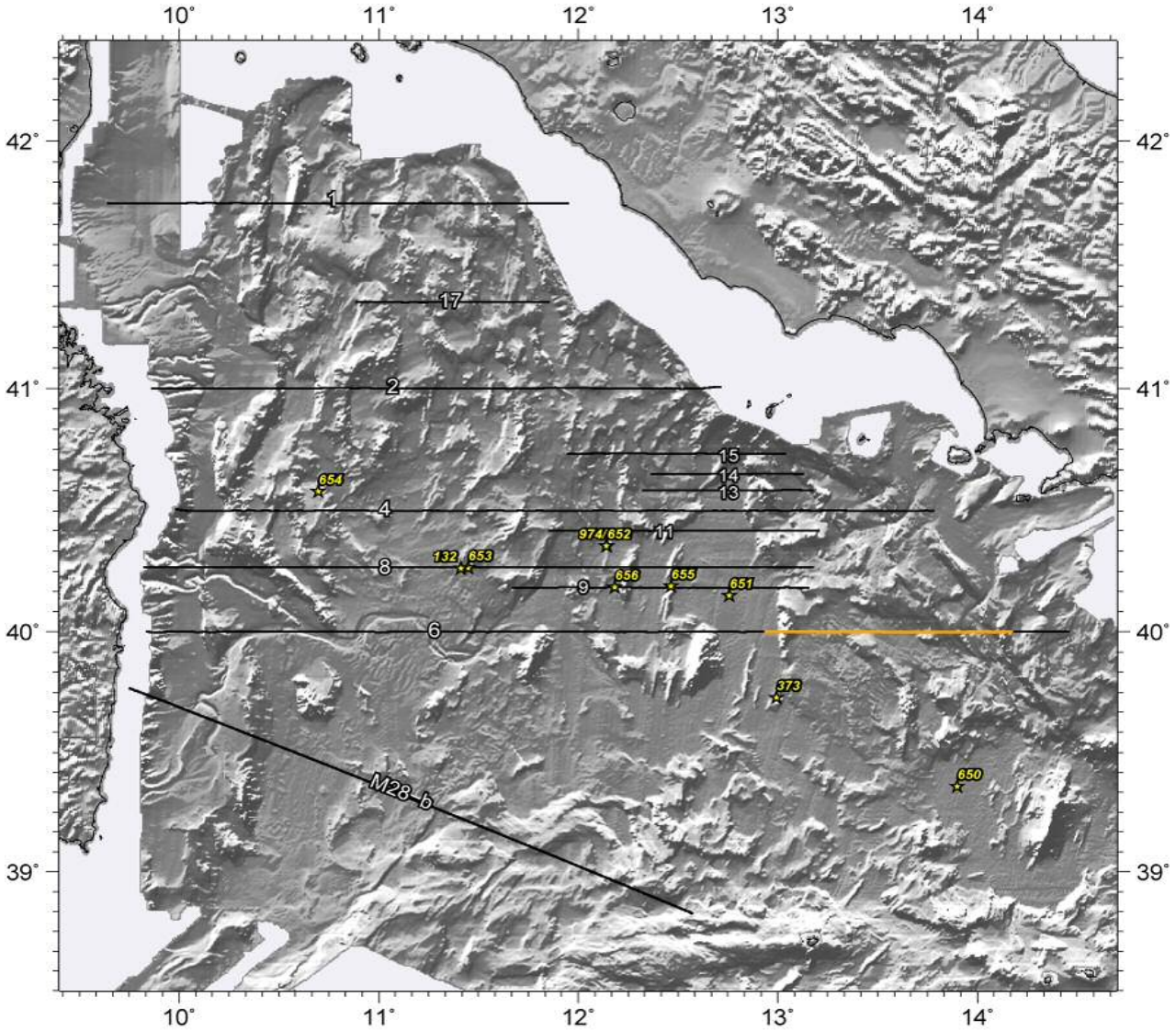

Figure 4.7-a: Topographic map of the Tyrrhenian with analysed MCS sections. Location of the segments used to work the Campania Terrace (see figure 4.7-b) are highlighted in orange.

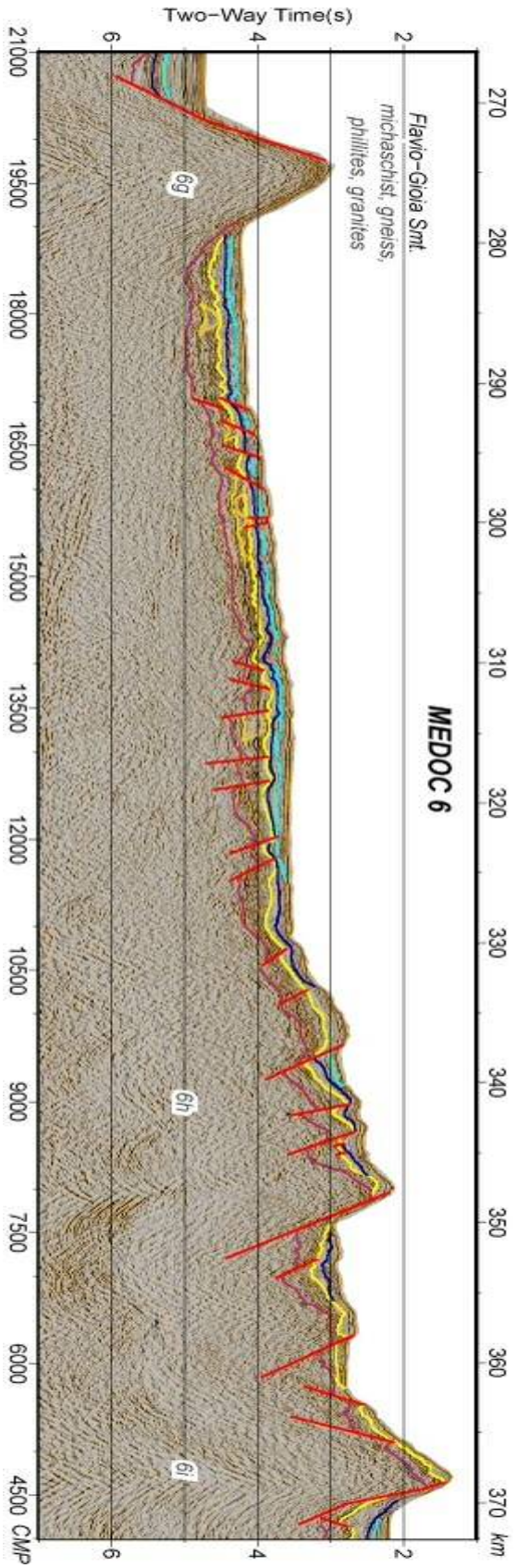

Figure 4.7-b: MCS section crossing the Campania Terrace. At the places were dredging data were available, it has been pointed out (Colantoni et al., 1981).

Almost all the Messinian deposits in the Cornaglia and Campania Terraces show parallel stratification, although locally the lowest sub-unit M1 shows a wedge-shaped geometry (fig. 4.6-b, MEDOC-6, CMPs 46,200 to 47,500; MEDOC-4, CMPs 15,500 to 17,500). This fact suggests that some faults worked until early Messinian, while at most part of these regions tectonics remain inactive during this period. However, deformation due to diapiric movements of sub-unit M2 masks the original reflectors geometry, especially towards the south, where these deposits are thicker. This makes difficult to analyse their relation to tectonics. Towards the north, where diapiric behaviour is weaker, it can be observed that the syn-rift character affects only the deepest sediments.

In contrast to this general behaviour, two locations show an entire Messinian column with apparent syn-rift geometries: at MEDOC-6, between CMPs 48,700 to 50,200, and MEDOC-4 between CMPs 11,500 to 13,000 (fig. 6.5-b).

Sechi-Farfalle region

Messinian deposits are imaged in all the seismic sections crossing this region. The strata show a fairly constant thickness, although their current geometry is controlled by faulting-controlled basement relief, giving them a blocky appearance. Like the underlying Tortonian deposits, Messinian deposits reach maximum thickness at fault-controlled depocenters, while the basement relative highs remain mostly uncovered.

The contact with the underlying Tortonian strata is marked at most places by an angular discontinuity, as observed in MEDOC-11, CMPs 3,300 to 5,000, for example (fig. 4.4-b) but not by a reflectivity contrast as that observed at the Sardinia margin. Like in the nearby North Tyrrhenian region, this discontinuity is related with the pre-/syn-rift boundary, which roughly coincides with the Tortonian-Messinian contact.

Seismically, both units show a similar appearance, and only ODP site 656 reached undated pre-rift sediments (Kastens & Mascle, 19990), which are probably Tortonian. Thus it drilled the Tortonian-Messinian boundary. Where Tortonian is not present (or has not been identified), contact with the basement is an unconformity. However, the top of the Messinian is clearer in seismic images because of the comparatively low reflectivity of the lower Pliocene in contrast with the usually bright Messinian top (for example, MEDOC-8, CMPs 30,500 to 32,000, fig. 4.4-b).

Seismic facies in this region are variable. Reflectivity of the entire sedimentary deposits changes considerably, both laterally and in the vertical direction, with no clear pattern. Stratification is generally poor and reflections show complex bedding at depocenters with stratification dipping in opposite directions in the cross section. In other places, strata tend to be parallel, although deep reflections lose their parallel disposition and acquire a wedge-

shaped geometry in some places (as in MEDOC-8, between CMPs 29,500 to 30,200, fig. 4.4-b). However, the transition between wedge-shaped and parallel reflectors is gradual, so that the contact between syn- and post-rift is not an angular well- delineated unconformity. Although thickness variations are minor, in places deposits slightly thicken towards a fault. Locally, the entire column seems to have been affected by tectonics (MEDOC-4, CMPs 24,700 to 26,200; MEDOC-8, CMPs 30,500 to 32,000, fig. 4.4-b).

In this region Messinian sub-units are unclear. In some locations a fairly reflective sub-unit, which could correspond to M3, overlies a more transparent one, possibly the M1, with a gradual transition between them (MEDOC-8, CMPs 28,800 to 29,500, fig. 4.4-b). However, in most places, no clear variation in seismic facies occurs within the sedimentary column to distinguish the sub-units.

Italian Margin

The unit is imaged in all seismic section crossing the region, extending from depocenters to cover most part of the basement ridges.

Messinian deposits overlay the seismic basement with an unconformity contact. The boundary is clearly visible because of a strong contrast in seismic character between the sedimentary (more or less stratified, high frequencies) and the basement units (no stratification, lower frequencies). As discussed above, no Tortonian sediments have been previously described for this region, although Tortonian deposits have been described in the other continental domains. Thus, it is possible that the deepest strata of sedimentary package identified as the Messinian top could be Tortonian in age. Therefore, Messinian thickness is not well constrained, although the deposits are thicker at the depocenters.

The top of the Messinian seems to be concordant with the overlying Pliocene unit at some places (for example at MEDOC-2, CMPs 700 to 2,500, fig. 4.8-b), while in other locations Pliocene layers onlap the Messinian ones (for example at MEDOC-1, CMPs 26,400 to 27,500, fig. 4.8-b).

The deposits present a wedged shape in most areas of the region, although they may locally have a parallel geometry (for example at MEDOC-6, CMPS 1,200 to 2,800, 5.8-b). However, its syn-rift geometry appear to be deformed by further compression/transpression deformation (as will be discussed in the next chapter), although the wedging of the layers is well preserved and easy to discern. Because of this recent deformation, lateral continuity of the reflections is worse than in other regions. Further, the highly-faulted terrain gives them a blocky character like at the Sechi-Farfalle region.

These observations together with the fact that Pliocene in some places lies concordant,

while in other places an angular unconformity appears between both units, suggests that some faults ended its activity during Messinian, and uppermost Messinian there belongs to post-rift, remaining concordant with Pliocene. Conversely, the activity of other faults lasted until the end of the Messinian, and therefore the Miocene-Pliocene contact coincides well with the syn-/post-rift boundary across this region.

In this region, the Messinan unit presents seismic facies similar to those observed at the Sechi-Farfalle region, although deposits are thinner. In general, strata show roughly parallel attitude at top, acquiring a wedge geometry towards the base where reflections are discontinuous, giving a more chaotic facies. Layering loses internal coherence with depth, and the stratification becomes indistinct. As in all the previous region, the most recent sediments show comparatively high reflectivity, that decreases towards the base, suggesting the presence of sub-units M1 and M3, although no clear abrupt boundary exists between them.

The lowest part of this sediment package shows low reflectivity and low internal coherency, which may indicate sub-unit M1, or perhaps even Tortonian. This uncertainty also occurs in the conjugated Sardinia Margin; with the difference that there is no available drill data to calibrate the boundary in that place.

North Sicily Margin

Messinian deposits in the North Sicily Margin region have been imaged all along line M-28b, with the exception of easternmost 40 km (fig. 4.10-b). In this region sediments accumulate mainly in depocenters (fig. 4.10-b).

Because of the signal attenuation, the contact with the underlying unit is weak, although in some areas a clear discontinuity can be identified, similar to that observed at the northern Tyrrhenian continental domains. In general, Messinian strata seem to onlap the previous tilted unit, as imaged near CMP 11,500 (fig. 4.10-b). In the places where Messinian sediments overlay the basement, the contact is a clear unconformity (M28-b, CMPs 13,800 to 16,000, fig. 4.10-b)

Overlying the Messinian the Pliocene units onlap the Miocene deposits in most areas of the region. Although locally the strata from both units are parallel (like at M28-b, CMPs 15,000 to 16,000, fig. 4.10-b). In general the Messinian-Pliocene contact is clear because the strong reflectivity of uppermost Messinian layers contrasts with the lower Pliocene. Locally, the Messinian top is covered by deposits that have been interpreted as volcanic or volcanoclastic packages (M28-b, CMPs 16,000 to 17,200, fig. 4.10-b).

In this region, the seismic facies of the Messinian deposits are fairly homogeneous in contrast to the other regions. Although there is a gradual transition from less reflective base to

a highly reflective top, variations in internal reflectivity are small in comparison to other places, and sub-units M1 and M3 cannot be well defined. There is also a gradual decrease in internal reflectivity towards the east where stratification is undefined. In the western area stratigraphy is fairly continuous and shows a good internal coherency.

Broadly speaking, all deposits display a wedged shape, although there are locations where upper Messinian strata are flat, suggesting that almost all these sediments were deposited during the syn-tectonic phase, with the exception of some locations where they were deposited during the uppermost Messinian.

4.2.4. Pliocene

Pliocene age deposits comprise the units with more lateral extension in the basin, although they are not present everywhere in the continental areas. In contrast to sediments deposited before the Messinian salinity crisis, Pliocence deposits thicken towards the central areas of the Tyrrhenian. That is the Vavilov and Mangnaghi basins, corresponding to the deepest basement areas. Towards the continental margins, Pliocence deposits progressively thin and eventually disappear in some areas. And where present, this unit fills depocenters, although locally it covers some basement highs.

These sediments are bounded by two regional discontinuities; therefore the Pliocene can be considered an unconformity-bounded unit across almost all the basin. At its base, there is the Messinian Salinity crisis erosional boundary. This limit lies actually within the uppermost Messinian, and may have some minor overlying Messinian strata, but it generally has been taken as an approximation of the Messinian-Pliocene boundary at basin scale.

The top Pliocene also corresponds to a regional discontinuity. This unconformity is not as clear as the Messinian crisis, but it is also observed in most parts of the Tyrrhenian. Its interpretation is presented in the discussion section, at the end of this chapter.

In addition to these two discontinuities, another one has been observed within the Pliocene sedimentary column, dividing it into two sub-units. This intra-Pliocene discontinuity can be identified basically in all the Tyrrhenian. The discontinuity becomes more evident towards the continental margins, specially at the North Tyrrhenian and in the Italian margin. It is not as clear in the central Tyrrhenian in the deep Magnaghi and Vavilov basins, where it has been calibrated using ODP drills from leg 107, in particular sites 651 and 655.

Although the character of both Pliocene sub-units changes depending on the region, they display several features that are recognizable everywhere. In general, the lower unit has more transparent facies in comparison with the upper unit, and the internal coherence of this upper unit tends to be higher, as will be explained next. Furthermore, locally a strong reflectivity

layer has been identified just above the discontinuity, making it easier to map the contact. The ODP drilling results were used to calibrate this discontinuity where seismic images do not provide clear evidence to map it, like in the deep Magnaghi and Vavilov basins.

Corsica-Sardinia margin

Pliocene is present all across this region, and crops out at the seafloor in several places along several tens of km, as imaged along the MEDOC-1 section at Corsica sub-basin, and in line M28-b at the eastern half of Sardinia basin (fig. 4.2-b). A maximum thickness of ~1.2 s. TWT for these deposits is observed at M28-b (CMPs 2,000 to 2,500 in fig. 4.2-b).

The contact with the underlying Messinian sediments is an unconformity, where Pliocene layers lap on Messinian layers, although locally the two units show a parallel relationship. For example, at MEDOC-2, in the Sardinia basin (fig. 4.2-b) no unconformity has been observed in this contact, while eastwards, Pliocene layering laps on the previous unit across a basal discontinuity. This geometric pattern, together with the ODP site 654 drilling results, located near Baronie seamount along line MEDOC-4 (fig. 4.2-c), has been used to calibrate and map the base of the unit in this area.

In this region, the Pliocene have good internal coherence, and reflections have strong lateral continuity. Reflectivity for the upper sub-unit is higher than for the lower one, showing a gradual transition between them, with a weaker seismic facies contrast than in other regions. Locally a high-reflectivity layer has been observed just above this contact, which can be used as a horizon marker (MEDOC-8, between CMPs 10,000 to 11,000; M28-B, between CMPs 1,800 to 2,500; fig. 4.2-b). Anyway, the entire strata column shows a parallel trend, where both sub-units are concordant. Thus, the middle-Pliocene discontinuity described in other regions, is not observed in the Corsica-Sardinia margin region.

Across much of this region, the parallel disposition of reflections suggests a post-rift sedimentation. But at the CROP line of M28-b (CMPs 1,700 to 2,400) a slightly fan disposition for the strata has been observed at the lowermost part of the lower sub-unit, suggesting syn-tectonic deposition in the southernmost area.

North Tyrrhenian region

Pliocene unit is imaged all along the seismic sections acquired in this region, with deposition focused at depocenters, and leaving uncovered most of the basement highs. In general, Pliocene is thin with deposits that at most reach 0.7 s TWT imaged on MEDOC-1, near CMP 30,000, or at MEDOC-2, near CMP 32,500 (fig. 4.3-b). The contact with the Messinian sediments is mostly marked by the contrast between the high reflectivity of the erosive Messinian top horizon, and the low reflectivity of the lower Pliocene sub-unit, with strata that

laps on the Messinian top (for example, at MEDOC-1, CMPs 2,500 to 7,500; or at MEDOC-2, CMPs 22,500 to 25,000, fig. 4.3-b).

In this area, strata of the lower sub-unit shows a fan-like internal geometry (MEDOC-1, CMPs 14,000 to 15,500, and MEDOC-2, CMPs 32,000 to 35,000, fig. 4.3-b), while reflections of the upper sub-unit are parallel and onlap them. This discontinuity can be observed clearly on MEDOC-1, between CMPs 26,000 to 28,000 (fig. 4.3-b), near the Tiberino seamount. Thus, the discontinuity in this area appears to be related to the end of tectonics during the rifting process. Some faults did not work until the lower Pliocene, so that the boundary is not clear in some areas, but it can be mapped by correlation from adjacent depocenters.

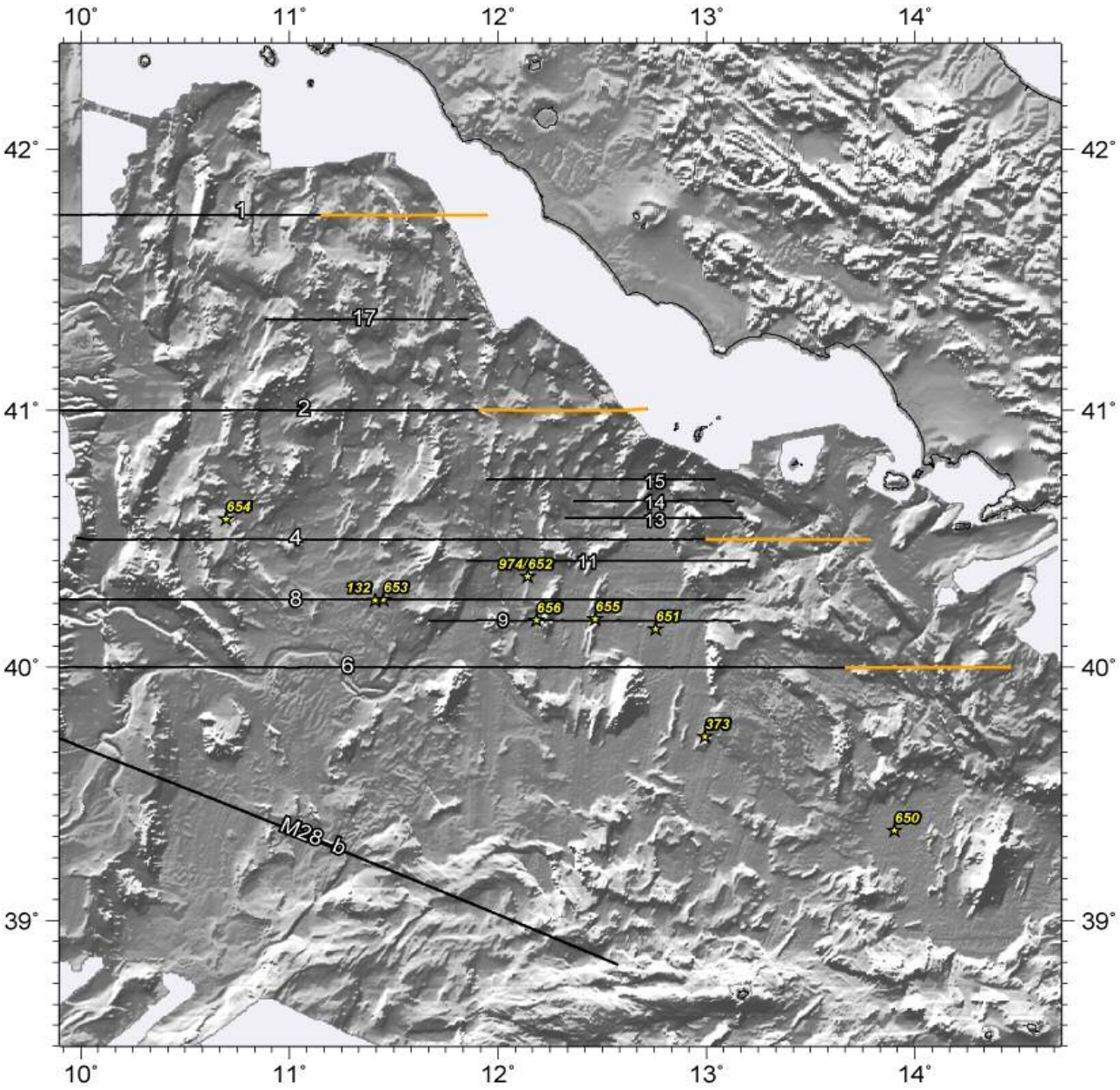

Figure 4.8-a: Topographic map of the Tyrrhenian with analysed MCS sections. Location of the segments used to work the Italian continental margin (see figure 4.8-b) are highlighted in orange.

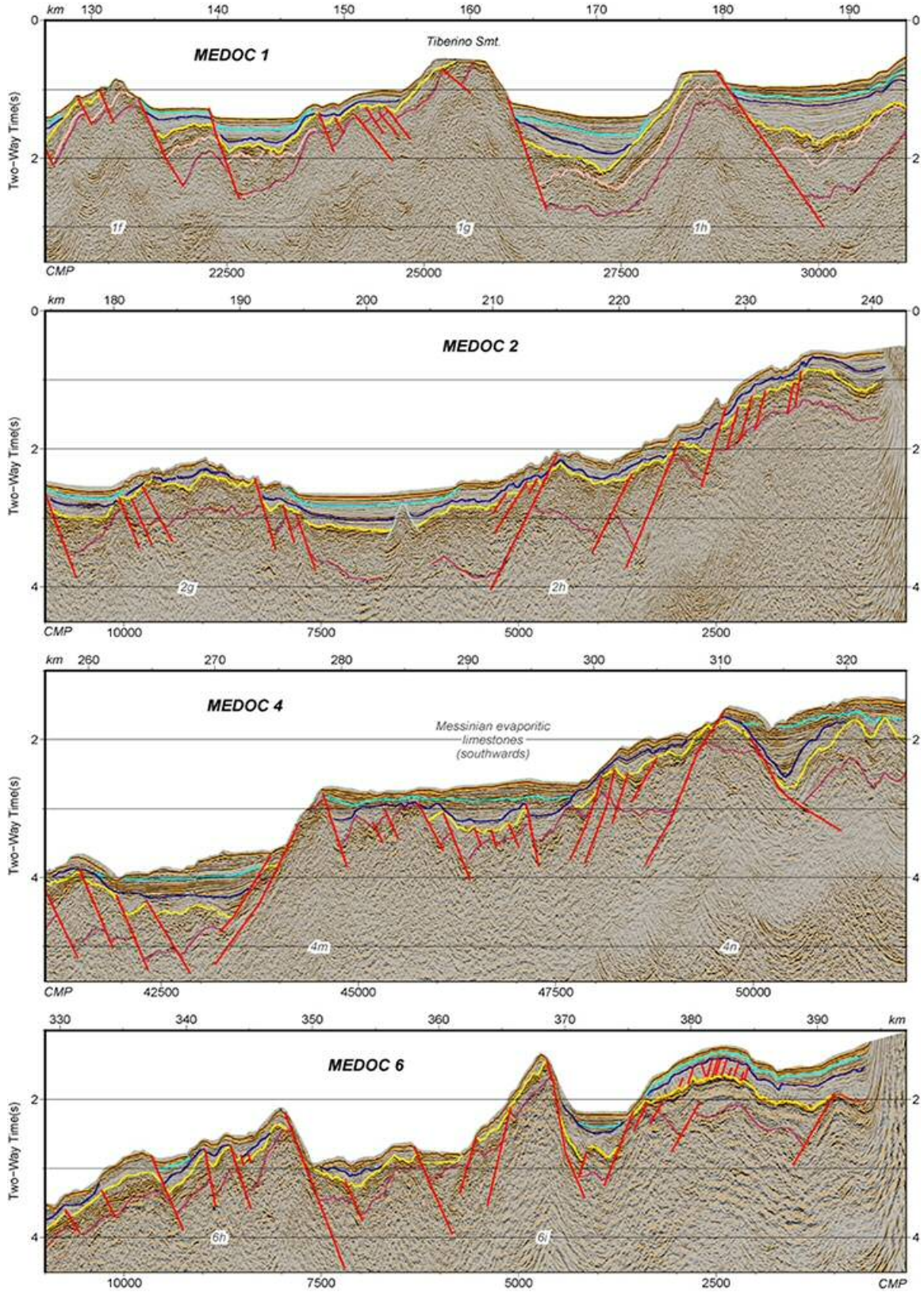

Figure 4.8-b: MCS sections crossing the Italian continental margin. At the places were dredging data were available, it has been pointed out (Colantoni et al., 1981).

The two sub-units show different seismic facies, which makes their distinction easier. Lower Pliocene is comparatively more transparent and this difference is even clearer towards the Italian margin side. The difference has also being described in the margin of Sardinia (e.g. Sartori et al., 2001). Further, along most of the North Tyrrhenian a high amplitude reflection occurs just above this discontinuity. Usually, this horizon has not exceptional extension, though it is clearly observed all along this region (e.g. MEDOC-1, CMPs 13,200 to 14,000, fig. 4.3-b), while at the rest of continental regions its presence is occasional.

Pliocene in this area seems to be tectonically affected by several types of deformation. As discussed in the tectonics chapter this area underwent transpressional deformation after extension forming a complex pattern, especially towards the east of the region, where deposits appear highly tilted (e.g. MEDOC-1, CMPS 26,000 to 28,000, fig. 4.3-b). Here the lower sub-unit is highly tilted too, while the overlying upper sub-unit doesn't seem to be as affected by the transpresional deformation.

Cornaglia Terrace and Campania Terrace

Pliocene deposits have are widespread throughout these regions, covering almost all the Messinian units. These sediments display long lenticular shapes with fairly good lateral continuity and gentle thickness variations.

In the Cornaglia Terrace, strata show parallel, sub-horizontal trend in most areas of the region, with good lateral continuity across the entire Pliocene column. Because of this conformity, the intra-Pliocene regional discontinuity cannot be well identified in this area, although locally an upper sub-unit laps on a lower one (MEDOC-6, between CMPs 47,200 to 48,500, and 41,700 to 45,200; or at M28-b, between CMPs 6,600 to 7,500, fig. 4.6-b).

Drilling at ODP site 653 did not find evidence for a discontinuity between the two sub-units, and the reports describe a continuous carbonate sedimentation (Kastens et al., 1988). But regardless of the presence or not of the intra-Pliocene discontinuity, a reflectivity contrast can be identified between lower and upper strata. In addition, a strong reflectivity layer similar to that observed in the North Tyrrhenian region can be observed locally allowing the mapping of the intra-Pliocene boundary (MEDOC-8, between CMPs 15,500 to 15,900; MEDOC-4, between CMPs 11,700 to 13,000 and 18,200 to 18,800; M28-B between CMPs 8,100 to 10,200, fig. 4.6-b).

In the Campania Terrace, the intra-Pliocene discontinuity is visible along almost all the MEDOC-6 line (CMPs 11,000 to 15,000, fig. 4.7-b), with an upper Pliocene lapping on the lower one. Locally, a high amplitude reflection appears to be related with this discontinuity, similarly to other regions of the basin.

In general, stratification of the lower unit is weak, although where it is visible, it shows Pliocene strata concordant with the underlying Messinian strata across most of the region. But locally, nearby the continental margins, where Pliocene is not affected by salt tectonics, it laps on the Messinian sediments (for example at MEDOC-6 between CMPs 54,500 to 56,500; or at MEDOC-4, between CMPs 18,000 to 20,000, fig. 4.6-b).

In some areas, diapirism from underlying Messinian salt produces deformation that masks the depositional relationships of the strata (e.g. at MEDOC-4 near CMP 16,000, fig. 4.6-b). Where the Messinian diapiric deposits are thicker (towards the southern Cornaglia Terrace) this deformation becomes stronger and affects both Pliocene sub-units (MEDOC-6 between CMPs 42,000 to 44,000, fig. 4.6-b).

Sechi-Farfalle region

Pliocene deposits in this region closely resemble those described in the North Tyrrhenian region. The deposits fill almost all the depocenters in this region, and cover some ridges like the 9b at MEDOC-9 (fig. 4.4-b). The unit thickness in this area is fairly constant with little lateral variations, and it reaches its maximum at MEDOC-8 with 0.5 s TWT (fig. 4.4-b, MEDOC-8, CMPs 31,000 to 31,400), while the minimum is attained in the same section, over the 8d ridge (fig. 4.4-b, MEDOC-8, near CMP 32,500). Both Pliocene sub-units present well-stratified layers with parallel disposition and good internal coherence. But in general, reflectivity of the sediments is significantly higher at the upper unit, especially at depocenters (MEDOC-8, between CMPs 30,500 to 31,800, fig. 4.4-b), whereas this contrast becomes weaker at the sediments that cover the ridges.

Reflections have a parallel geometry across almost all the region, with local exceptions where the lower unit strata show a weakly-developed fan geometry, like at MEDOC-9, between CMPs 16,500 to 16,900, or at MEDOC-4 between CMPs 26,600 to 28,500 (fig. 4.4-b). These observations support a post-rift deposition of Pliocene sediments for most of the region, although locally a few faults still worked during lower Pliocene.

Vavilov and Magnaghi Basins

As mentioned previously, this region is the place where these sediments acquire the maximum thickness, reaching 1 s TWT near the Vavilov eastern boundary, at MEDOC-8, CMP 41,000 (fig. 4.9-b). The entire sequence presents a parallel disposition of the strata, with a fairly horizontal attitude. In a few places, the deepest layers appear tilted, like in MEDOC-6 between CMPs 29,300 to 30,000 (fig. 4.9-b) or even with a clear wedge geometry, like in MEDOC-6 (CMPs 20,400 to 21,000 and, fig. 4.9-b). These thin packages of dipping layers belong to the lowermost part of Pliocene, and its syn-tectonic character suggests that the region opened in a really short time lapse.

The discontinuity that separates the two Pliocene sub-units is not as clear as in other regions, because both upper and lower Pliocene show a similar seismic aspect, although ODP drilling has confirmed the presence of both units (Kastens and Mascle, 1988). The upper Pliocene is fairly similar to other regions, with a highly reflective character, continuous and parallel reflections, and high frequencies, while the lower sub-unit displays similar features that makes its distinction difficult. Only in few places, the lower Pliocene has a weak reflectivity in comparison with the upper Pliocene, as in MEDOC-9, between CMPs 10,500 to 12,200, or in MEDOC-6 between CMPs 39,000 to 41,000 (fig. 4.9-b).

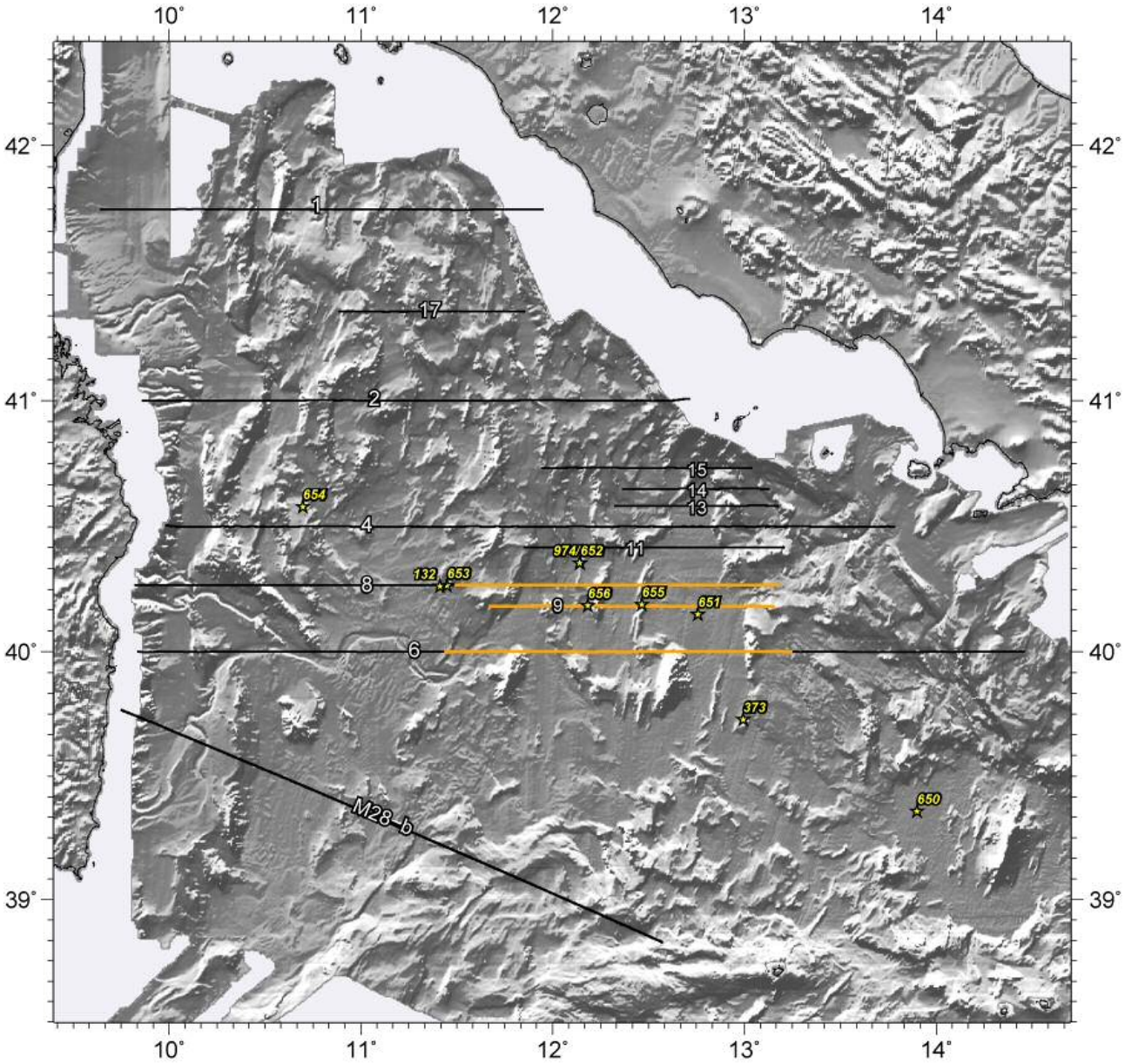

Figure 4.9-a: Topographic map of the Tyrrhenian with analysed MCS sections. Location of the segments used to work the Vavilov and Magnaghi basins southern area (see figure 4.9-b) are highlighted in orange.

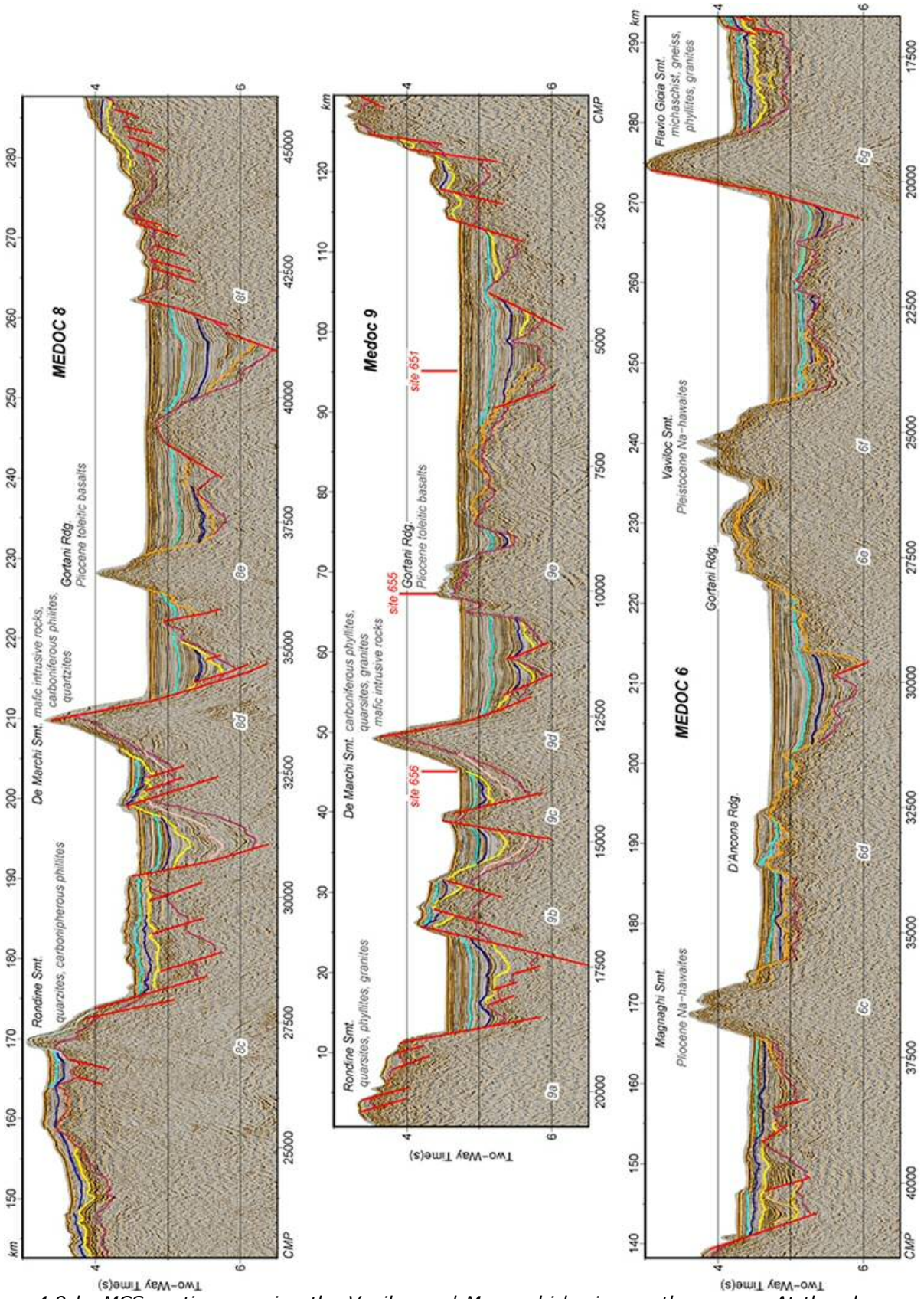

Figure 4.9-b: MCS section crossing the Vavilov and Magnaghi basins southern area. At the places were dredging data were available, it has been pointed out (Colantoni et al., 1981). Also the ODP sites 651 and 655 location have been plotted (see figure 4.9-c and 4.9-d).

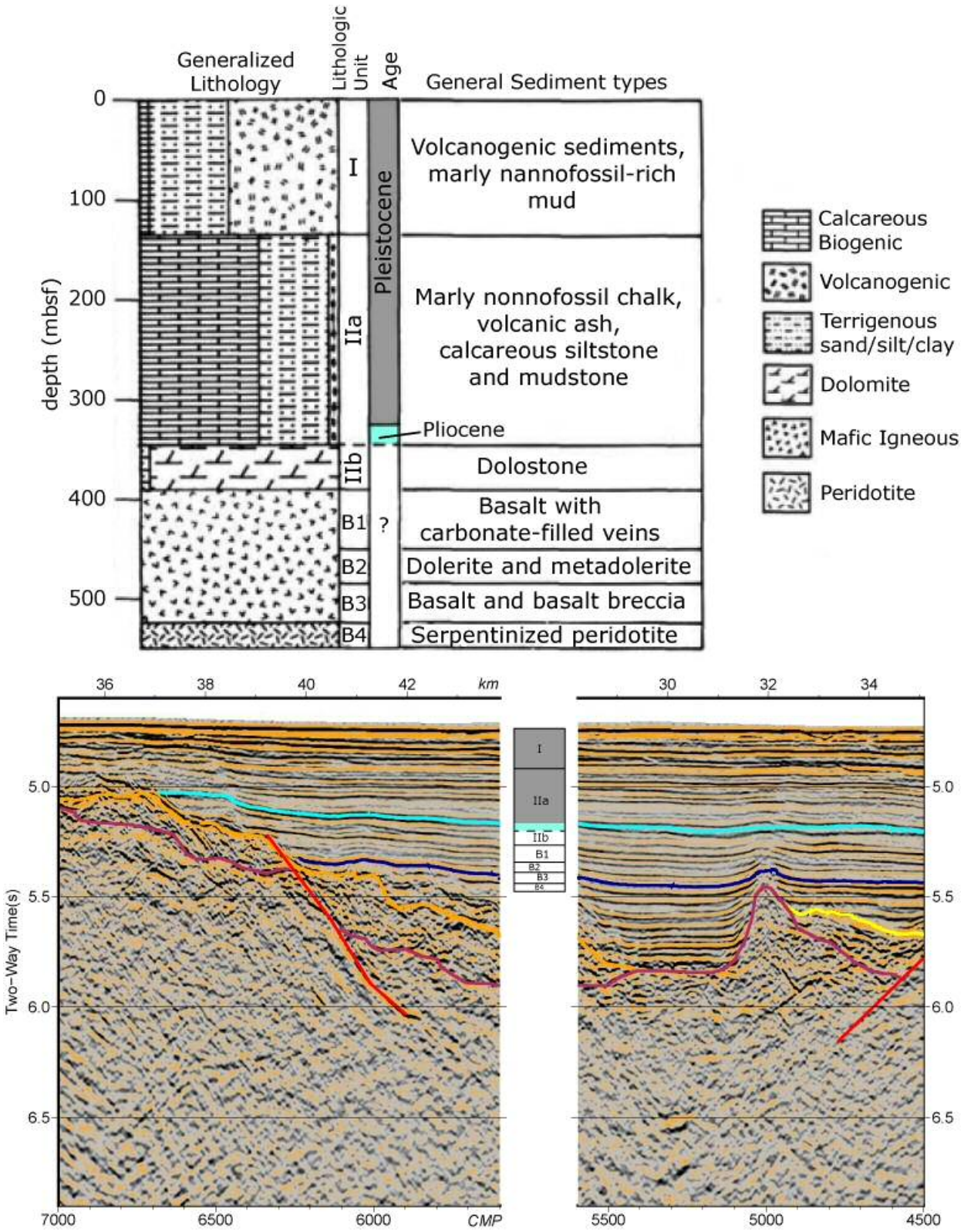

Figure 4.9-c: Stratigraphic column of ODP site 651 (modified from Kastens & Mascle, 1988), and its position at the MEDOC 9 section.

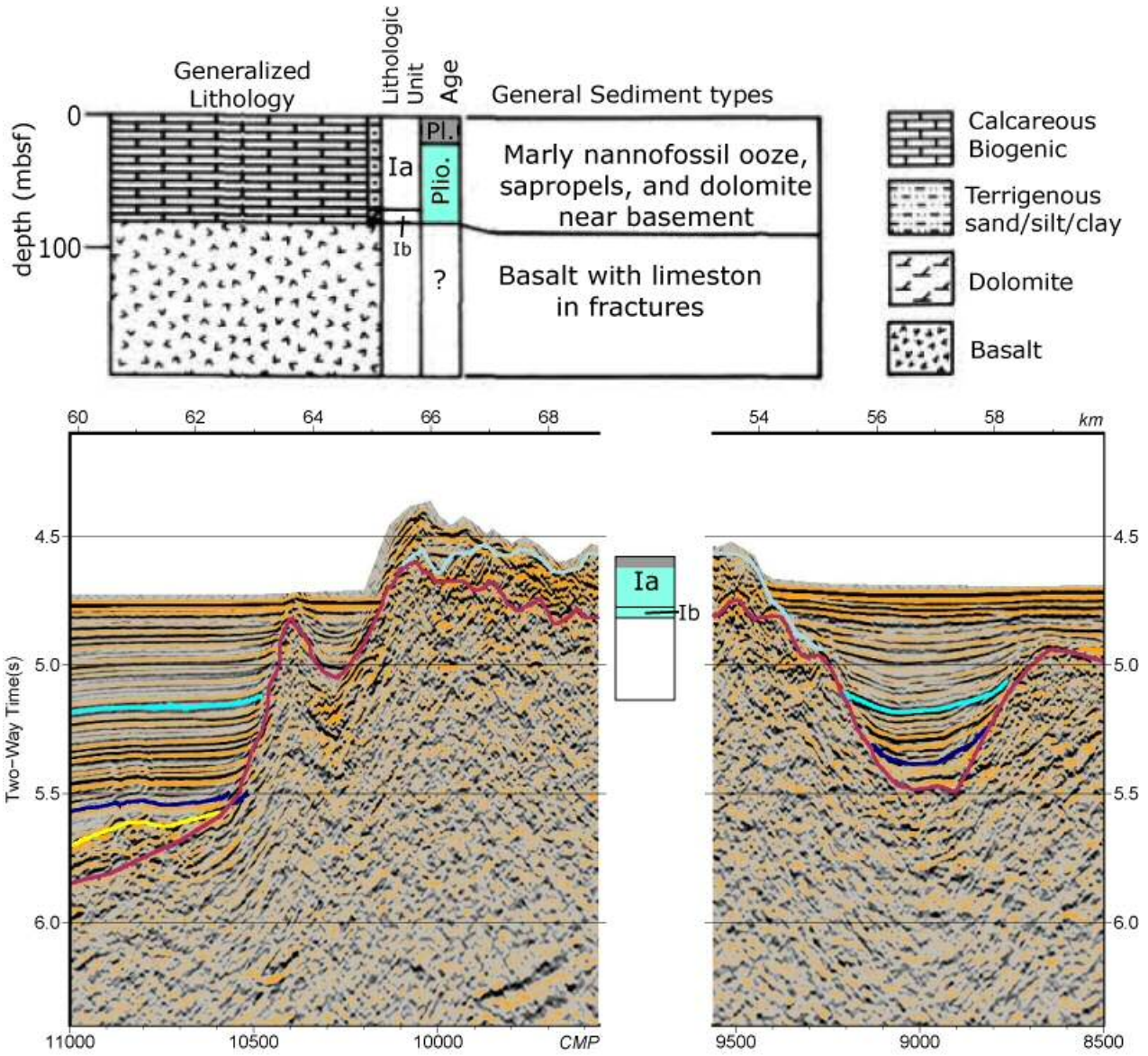

Figure 4.9-d: Stratigraphic column of ODP site 655 (modified from Kastens & Mascle, 1988), and its position at the MEDOC 9 section.

In addition, upper Pliocene sediments lay parallel over the lower unit, and only at basin edges several gentle unconformities are observed, probably related to differential compaction. Thus the lack of clear distinct facies makes difficult to separate them. So, the horizon has been calibrated based on the ODP drilling results.

Italian Margin

In this region, Pliocene deposits are quite different to those observed at the conjugated margin. Thickness is variable, thinning from depocenters towards ridges were they display more constant thickness. The maximum thickness is about 0.7 s TWT at MEDOC-1, at the easternmost part of the profile, and at MEDOC4, near CMP 50,500 (fig. 4.8-b).

The intra-Pliocene discontinuity is easy to follow across the whole region based on its

seismic character, despite lack of drilling data in this region. As in other regions, the lower Pliocene tends to be less reflective than the upper sub-unit. Although the change in reflectivity is in often gradual, the limit is clear because it is marked by a geometrical discordance. Also, in some depocenters it is observed a highly reflectivity layer just above the boundary, for example in MEDOC-1 between CMPs 22,500 to 23,500 (fig. 4.8-b). Though this area has been affected by post-rift transpressional deformation (as is explained in the next chapter), rifting sedimentary geometries are still recognisable. The lower Pliocene sub-unit mostly shows parallel strata, although they can appear highly tilted (MEDOC-4, between CMPs 48,000 to 49,500; and MEDOC-2, CMPs 4,000 to 1,200), and towards the easternmost sector even folded (MEDOC-6, CMPs 2,000 to 3,700; and MEDOC-2, CMPs 1,000 to 2,500). These parallel layers suggest a post-rift deposit, although locally a wedge-shaped sedimentation is also observed (MEDOC-4 near CMP 45,000; or at MEDOC-6 between CMPs 3,500 to 4,500, and 8,900 9,400; fig. 4.8-b). Therefore, depending on the timing of fault activity, the lower Pliocene sediments show syn to post-rift geometries. Where sediments show parallel arrangement, they lay unconformably over the Miocene units, onlaping them, while the syn-rift sediment doesn't show any clear discontinuity with the underlying unit.

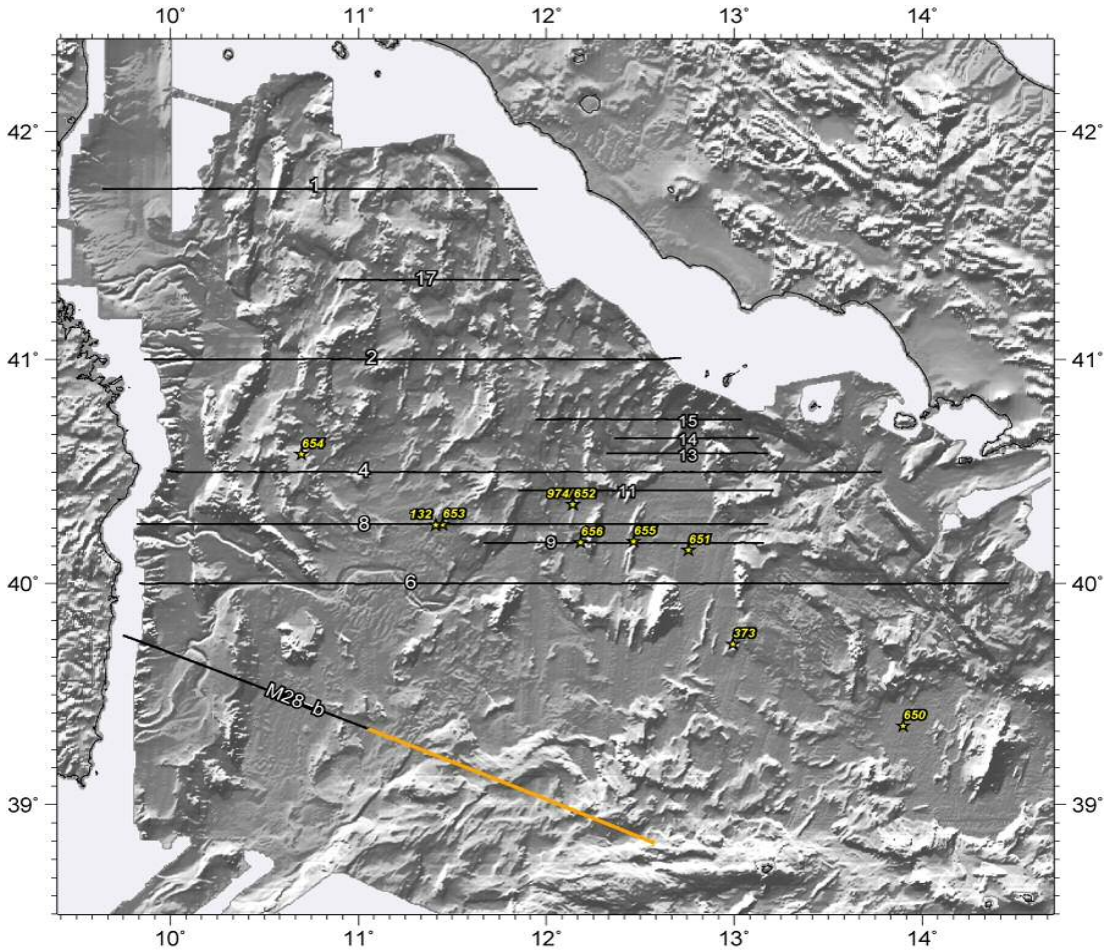

Figure 4.10-a: Topographic map of the Tyrrhenian with analysed MCS sections. Location of the segments used to work the North Sicily margin (see figure 4.10-b) are highlighted in orange.

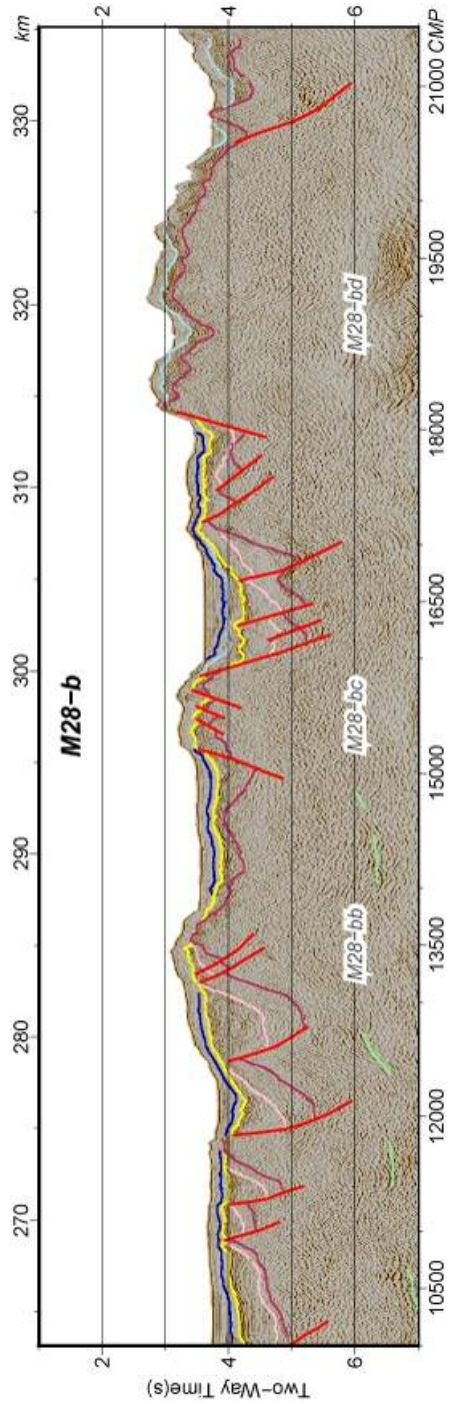

Figure 4.10-b: MCS section crossing the North Sicily margin. At the places were dredging data were available, it has been pointed out (Colantoni et al., 1981).

The entire upper Pliocene column shows parallel strata, suggesting a post-rift deposition across the whole region. Although locally they are tilted and/or folded (for example, at MEDOC-6, between CMPs 1,500 to 3,500; or at easternmost sector of MEDOC-2; fig. 4.8-b), their deformation doesn't seem to be as strong as in the lower sub-unit.

North Sicily Margin

Along this region, the Pliocene shows a monotonous character with fairly constant thickness, ranging from 0.2 to 0.3 s TWT, and parallel stratification. Layering tend to conform the former Messinian-top topography (M28-b, CMPs 12,500 to 13,000 and 15,000 to 17,200, fig. 4.10-b). Seismic facies resemble those described at other regions, with good lateral continuity of the reflections and good internal coherence.

Contact with the underlying units is discordant, with the Pliocene strata lapping on them with low angle across most of the area. The reflections display low amplitude, with little differences between upper and lower sub-units, in comparison with the previously described regions. In addition, across most of the area, the contact between both sub-units is concordant, and only locally upper sub-unit strata lap on the lower ones. Therefore, the intra-Pliocene discontinuity is poorly developed in this region and the boundary is difficult to map. It has been interpreted based on the presence of a high amplitude reflection as that observed in previous regions, although its presence is local and fainter than in other areas (for example at M28-b, CMPs 12,700 to 13,200, fig. 4.10-b).

4.2.5. Pleistocene

Pleistocene sediments constitute the most recent unit identified in the Tyrrhenian, and like the Pliocene, its presence is widespread through the basin. Its thickness is fairly constant across the deepest areas of the Vavilov and Maghnaghi basins, with values that range from 0.4 to 0.6 s TWT, reaching its maximum value at the western half of the Vavilov basin (fig. 4.9-b). In the rest of the Tyrrhenian, its thickness is quite variable, and its presence tend to be confined to local depocenters. In the Cornaglia and Campanian Terrace regions it is where this unit presents the thinnest deposits, ranging between 0.1 to 0.2 s TWT. In those regions, the thickness is fairly constant, as it occurs in the central basin, but in the two terraces it is not present in most of the basement highs, that remain uncovered. Finally, in the continental margin regions the thickness of the Pleistocene sediments show is more variable. They tend to be confined at some depocenters and cover few of the ridges (MEDOC-2, 2e seamount; MEDOC-17, 17b seamount; fig. 4.3-b).

The seismic facies of this unit are quite monotonous across the entire basin. Reflections have lateral continuity, with good internal coherence, high frequencies, and display high amplitudes almost everywhere. The layers have a fairly horizontal trend, in most cases parallel to the Pliocene and sub-parallel to the seafloor.

These seismic facies are similar to those described for the upper Pliocene sub-unit, and across most of the basin (with the exception of north-east margin), strata of both units are

parallel making difficult to map their boundary. The boundary has been mapped from the initial location proposed based on the drilling information from ODP leg 107.

In contrast to the previous description, in the western half of the North Tyrrhenian region and in the Italian continental margin, this contact is observed as a clear discontinuity (fig.5.8-b), providing a fairly continuous boundary all along the region. In there Pleistocene layers are mostly horizontal and lap on the underlying deformed sediments (for example, at MEDOC-1 between CMPs 26,000 to 28,000; or MEDOC-6 between CMPs 3,500 to 4,500; fig.5.8-b). But not all Pleistocene sediments appear undeformed. There are a few places where deformation also involves Pleistocene strata (MEDOC-6, CMPs 1,700 to 3,500, fig.5.8-b). This discontinuity has been identified in several places through the Tyrrhenian, and specially close to the Italian continental margin, were it gradually becomes more pronounced.

4.2.6. Volcanics

Along the MEDOC profiles, several structures have been interpreted as magmatic bodies. In general, they show more reflective character than the surrounding sediments of the host rock and poor or no clear internal structure. The volcanic nature of a few of them has been confirmed by available sampling (e.g. drill cores or dredges) usually near some profiles. The character of those ground-truthed events is used to interpret other structures that have not been sampled.

In the North Tyrrhenian region, there is the Elba/Pianosa ridge (MEDOC-1, CMPs 7,200 to 8,500, fig. 4.3-b), which is a documented volcanic edifice (Mauffrett et al., 1999). Around it, sedimentary layers are dome-shaped, in relation to the magmatic intrusion. Also MEDOC-2 images a buried body that is not visible in the bathymetry and has not been sampled, between the CMPs 6,200 to 6,800 (fig. 4.3-b), which is associated with some high amplitude reflections that might be related to volcanic flows. This structure has been interpreted as a volcanic building. Finally, MEDOC-15 images a reflective structural high, perhaps of volcanic origin near CMP 14,500 (fig. 4.5-b). It is also visible at the bathymetry, but no sampling is available to confirm the nature.

In the Corsica and Sardinia margin region the Quirra seamount is imaged at its northernmost segment by line M28-b (CMPs 4,500 to 5,500, fig. 4.2-b). Although it is visible in the seafloor relief, the structure appears largely sediment covered at the seismic images. According to Sartori et al. (2001) it consists of Pliocene Alkali-basaltic lavas.

The Vavilov and Magnaghi Basins are characterized by the homonymous volcanoes, which are both imaged on MEDOC-6 profile (Vavilov seamount at CMPs 24,000 to 29,000, and Magnaghi seamount at CMPs 35,500 to 37,000, fig. 4.9-b). Dredge samples (Colantoni et al,.

1981) confirm that both volcanoes have a basaltic composition. Lustrino et al. (2011) suggest a Na-Hawaiite composition for both of them. Sartori et al. (2004) give an age of 2.4 to 0.7 Ma for Vavilov seamount, while Lustrino et al. (2011) give an age of 0.7 to 0.1 Ma for Vavilov seamount and an age of 3.0 to 2.7 Ma for Magnaghi seamount.

MEDOC-6 also crosses the d'Ancona Ridge (CMPs 31,500 to 33,800, fig. 4.9-b), although no information about its nature is available. Finally, the Gortani Ridge is imaged at MEDOC-8 (CMPs 35,500 to 37,000) and MEDOC-9 (CMPs 9,000 to 10,200). Dredge samples indicate a basaltic composition (Colantoni et al,. 1981), and the ODP site 655 recovered enriched tholeiites (Kastens & Mascle, 1990).

In addition to large volcanic edifices, a number of high amplitude reflections are imaged on top of the seismic basement in different locations across almost the entire Vavilov Basin (e.g. MEDOC-6, CMPs 23,000 to 37,500), laying over the volcanic edifices of Vavilov and Maghaghi seamounts, and d'Ancona Ridge; (MEDOC-8 CMPs 35,700 to 41,000; MEDOC-9, CMPs 5,400 to 8,700, fig. 4.9-b). They present a chaotic stratification, and follow approximately the geometry of the basement top. These deposits have been interpreted as volcanoclastic and/or far-flow volcanic deposits, as suggested for ODP site 651 (Kastens & Mascle, 1990).

In the Sechi-Farfalle region, MEDOC-8 crosses the Rondine seamount (CMPs 26,700 to 27,700, fig. 4.4-b), which has also a volcanic origin (Cella et al., 1998).

In the Italian margin, line MEDOC-11 goes across a reflective basement high (CMPs 15,500 to 16,500, fig. 4.5-b), for which a volcanic composition is inferred from available sampling of vulcanoclastic breccias at nearby dredges (Colantoni et al., 1981).

In the North Sicily margin, the M28-b profile images reflective deposits with low internal coherency and poor stratification, lapping on the Messinian sediments and below the Pliocene layers (CMPs 16,000 to 17,000 and 18,200 until end of profile, fig. 4.10-b). Although no volcanic edifice has been identified, this area has a well-documented volcanism, therefore we infer a volcanoclastic and/or far-flow volcanic deposits origin.

And finally, the Cornaglia and Campania Terraces are the only regions where no magmatic effusive body has been interpreted in our seismic sections. In addition, there is no basement sampling in these regions (Colantoni et al,. 1981).

4.3. Discussion

The Tyrrhenian basin has enough drilling and dredging data to constrain its general basement configuration. However, it is also a young basin with restricted sedimentary supply

that has filled isolated depocenters for most of its history, which makes the correlation of the sedimentary horizons across the regions often difficult, particularly for the oldest units.

It should be kept in mind that the ODP drilling data used to calibrate the reflections define stratigraphic units, and therefore, their boundaries have a stratigraphic significance.

Nevertheless, the units defined in this work are seismic units, which are based on their seismic facies and geometrical relationships, and they not necessarily coincide with the stratigraphic limits. Further, some amount of interpretation is necessary to make jump correlations in areas where horizons are not continuous.

Seismic Basement

The basement concept used in this work is not a petrological notion. It is rather based on the seismic properties of materials below the sedimentary cover. And although their origin differs greatly, their aspect at the seismic profiles share similar features. Therefore, they must not be interpreted as a simple seismic unit with a common origin. Thus, recent work suggest that the Tyrrhenian basement rocks comprise a range of compositions with different origins, although they have mostly been sampled at the continental margins, and few direct evidence exist for the basement nature in the rest of the regions (Collantoni et al., 1981; Lustrino et al., 2011; and others).

Although there are common seismic facies across the basin, the seismic character changes slightly between the different tectonic regions (understanding tectonic regions as defined in the 5th chapter). In the continental margins, basement sampling has found a broad range of rock types with different ages (Collantoni et al., 1981), from Paleozoic to Neogene volcanics. Also their composition is highly variable, and includes igneous (both effusive and intrusive rocks), metamorphic and pre-rift sedimentary rocks. These last ones should have been deposited before the rifting processes and deformed by previous tectonic phases (Alpine and/or Apeninic orogenies), losing partially or even completely their sedimentary features.

In these continental margin regions, corresponding to the North Tyrrhenian, the Sardinia-Corsica and Campania margins, and the Sechi-Farfalle region, the basement has been imaged as a faulted and stretched continental crust, with important lateral thickness variation. Internal reflectivity is generally low, and no clear internal structure or stratification can be observed, though weak laterally discontinuous layering locally exists (MEDOC-8, CMPs 27,000 to 27,500, at 5.5 to 6 s TWT, fig. 4.4-b). These structures are probably pre-rift sedimentary (perhaps volcanoclastic) materials with poor definition and continuity in the seismic images, that cannot be calibrated with available data. If these structures belong to old pre-rift sediments, no clear boundary with the underlying crystalline basement has been identified. Thus, they have been considered together with the seismic basement. No relation with the rifting-related structure

has been observed, and they have been probably affected by a former orogeny either Alpine or even Apeninic.

In the regions interpreted as ocean-like, back-arc magmatic crust areas (see next chapter), which correspond to the Cornaglia and Campania Terraces, the basement displays stronger reflectivity in terms of structures, and it is more homogeneous. The Moho reflection is often strong, and in addition there are also some strong internal reflections that do not appear to be related with any clear tectonic or sedimentary structure (MEDOC-6, CMPs 14,700 to 16,400, around 6.5 s TWT, fig. 4.7-b). In general these reflections have slightly lower frequencies than those observed in the continental basement. Probably these reflexions represent internal structure of the magmatic crust.

With the exception of few dredges and/or cores located at the Issel and Cornaglia seamounts, where continental type rocks have been dredged, no basement samples have been recovered in these regions (Colantoni et al., 1981). The scarce information suggests a continental composition for the basement in both regions. But as discussed in the next chapter, the Vp velocity information (Prada et al., 2014; 2015) indicates a back-arc oceanic domain in these regions, thus magmatic or magmatically intruded crust should also be expected there, and these two seamounts could represent drifted continental blocks.

A few seafloor samples have been taken in the Magnaghi and Vavilov basins. Basaltic rocks have been dredged at the seamounts, and ODP leg 107 site 651 reached basement in the middle of Vavilov Basin, where serpentinized peridotites were found (Kastens, et al., 1988; Kastens & Mascle, 1990). The seismic velocity models of the WAS MEDOC data (Prada et al, 2014; 2015), strongly suggest the presence of exhumed mantle through the Magnaghi and Vavilov basins, whereas the dredging samples of the seamounts reflect a basaltic composition (Vavilov seamount, Magnaghi seamount and Gortani ridge), supporting a volcanic origin.

In this region there are some basement-internal reflections imaged in the seismic data that look similar to those observed at the back-arc areas but with shorter length and lower reflectivity (for example at MEDOC-9, CMPs 7,500 to 10,000, 6-6.5 s TWT, fig.5.9-b). They are mostly located nearby volcanic seamounts or ridges, which may indicate that they are related with volcanism posterior to mantle emplacement.

Finally, in the north Sicily margin, both continental and volcanic bedrock has been dredged (Collantoni et al., 1981). Here, seismic images show structures reminiscent of tilted fault blocks made of rifted continental basement.

Tortonian

Tortonian units have only been described in the continental margins, with the exception

of the Italian side, where they have not been identified. It is reasonable to expect that they are also present in the Italian margin, because they are observed in the rest of continental domains, and because of the geological context. But neither the seismic data, nor available dredging data provide evidence of Tortonian deposits in this area.

Few Tortonian samples have been acquired along the basin. ODP site 654 from ODP leg 107 gives a transgressive sequence of a subaerial depositional environment such an alluvial fan, and over it, oyster-bearing glauconitic sands, in a probable nearshore environment (Kastens et al., 1988). There are also some dredges along the basin, like one acquired at the basin Sardinia sub-basins (Colantoni et al., 1981; Sartori et al., 2004), which sampled Tortonian clays.

The Tortonian upper and lower limits are uncertain across almost all the Tyrrhenian, because there's only one drill – site 654, ODP leg 107 - that reaches its top within the area of study and there are no data for the stratigraphical position of the base. But as explained previously, several assumptions have been made to infer it.

Northwards of our study area there are two industry wells in the Cosica Basin (Mauffert et al., 1999; Mauffert & Contrucci, 1999; Möeller et al, 2013). These wells go through the Tortonian and reach syn-rift sediments below it. But the geological history of this sub-basin, like the Sardinia one, started much earlier than the rest of the Tyrrhenian (Mauffert & Contrucci, 1999, Sartori et al., 2001), therefore the presence of pre-Tortonian syn-rift sediments at these two sub-basins doesn't mean that they would be present at the rest of the Tyrrhenian.

Indeed, some authors interpret the “L discontinuity” as the beginning of the rift in the rest of the basin (Trincardi & Zitellini, 1987), which lays within the upper Tortonian. Therefore, the pre-rift/syn-rift contact marks the beginning of the rift (at least, at the continental areas) and coincides well with the Tortonian top, with the exception of Corsica and Sardinia sub-basins. This contact also coincides well with a loss in reflectivity intensity of the strata. Thus, this characteristic change has been taken as guiding criteria to locate top of the Tortonian unit across the basin, where the contact is not clearly imaged.

However, the base of the unit is difficult to locate. Across almost all the Tyrrhenian basin it has been placed at the top of the seismic basement, considering that all sediments belonging to this unit consist of pre-rift sediments. Again, this interpretation is not valid at the Corsica and Sardinia sub-basins, where rifting processes started earlier (Mauffert & Contrucci, 1999, Sartori et al., 2001), and therefore the limit there should be taken with caution.

In a broad view, all the Tortonian deposits have a discontinuous aspect and a variable thickness with the exception of the Corsica and Sardinia basins, where they show rather

parallel disposition of the strata. Therefore its variable thickness in wedge-shaped deposits located at the half-grabens supports that they were deposited during the beginning of the rifting, with the exception of the two sub-basins mentioned above. It is worth noting that its presence is however local and it is not present everywhere, suggesting that some half-grabens formed later, during Messinian time.

In addition, the lack of these deposits in magmatic crust regions and exhumed mantle regions suggest that these tectonic domains formed later.

Messinian

This unit has been observed across almost all the working area with the exception of the Vavilov and Magnaghi basins.

Its top is typically well-defined across the Tyrrhenian because it coincides with the Messinian salinity crisis event, which gives an horizon that is fairly close to the Messinian top and becomes a good isochron for our purpose and that is observable all along the Mediterranean. The Messinian salinity crisis is currently dated from 5.97 to 5.32 Ma (Manzi et al., 2013). During this period, emerged areas suffered important erosional processes, leading to erosive discontinuities that are clear on the seismic profiles due to their strong impedance contrast and geometry. In some places, flat-top highs of large tilted blocks indicate that they could have been exposed and eroded during the Mediterranean desiccation event (for example the 1g seamount, at fig. 4.3-b). The areas that remained submerged during this period have a top of the unit characterized by a well-stratified series of reflections with high amplitude and continuity. This is the case of the upper sub-unit observed all along the Messinian domains, which in this work has been named M3.

Therefore, this top-unit horizon that approximately marks an isochron is not a tectonic, but rather a regional stratigraphic event caused by the Mediterranean desiccation at the end of the Messinian. In general, this top boundary is very close in time with the Messinian-Pliocene boundary. This allows calibrating the top of this unit everywhere within the Tyrrhenian, and even at the rest of the Mediterranean. However, it must be recalled for any high-resolution study that this horizon does not usually correspond to the top of the Messinian time or sediments, because of the erosion and limited subsequent sedimentation; it generally lies just below the real top.

In general, Messinian deposits display a wedge-shaped geometry in the continental domains. Thus, we interpret them as syn-rift almost everywhere with the exception of the Corsica and Sardina Basins and the Sechi-Farfalle regions, where they are mostly post-rift.

In the magmatic crustal regions – the Campania and Cornaglia Terraces -, Messinian

show a more complex character. In general their strata are mostly parallel suggesting a post-rift sedimentation, with the exception of some layers at the bottom of the Messinian column. This fact suggests that the crust in these areas was already formed when Messinian was deposited, but no Tortonian sediments have been described in these two regions, so the rift here didn't open during much of the Tortonian times, but probably during the end. This can be explained with a short period of activity of the faults in the area, during the uppermost Tortonian and/or lowermost Messinian. But as will be developed at the next chapter, faults in this region are scarce and their fault offsets are too small to explain the whole extension at both regions. Therefore, part of extension should be explained with seafloor spreading (Prada et al., 2014; 2015). This magmatic crust formation could justify the lack of syn-rift deposits and the total amount of extension, although the exact timing for this magmatism remain unsolved with the available data.

Finally, in the Vavilov and Magnaghi Basins, Messinian sediments have been observed only near the edges of the two basins, where the geometry of the reflections gives a pre-rift character for them. These deposits are scarce and with little extension, and most of them are related with fallen blocks previous to the opening of these areas. But, in general, no Messinian sediments have been observed in the whole region. Therefore these regions opened later, at least during the lower Pliocene.

In addition, at the Sechi-Farfalle region, a unit with pebbles has been drilled in the ODP site 652. It includes lithologies found in the apenninic nappes of Italy and Sicily, but not in Sardinia or Calabria (Kastens et al., 1988). This fact could be an indication that during Messinian this region was united at the Italian margin, and that the Vavilov basin didn't exist.

In general, the seismic stratigraphy for the Messinian consists of a lower sub-unit - M1 - with discontinuous reflections. This fact could reflect an unstable syn-rift sedimentation and/or with seismic signal attenuation. Overlaying it, there is the M2 sub-unit, which has only been observed at the Cornaglia and Campania Terraces. It consists of evaporitic deposits usually showing diapiric deformation, and with a transparent aspect probably due to their high seismic velocities. At last, the uppermost sub-unit - M3 - show a comparatively higher reflectivity and continuity, allowing its correlation everywhere across the regions.

M2 and M3 sub-units have an evaporitic origin. Considering the diapiric behaviour of M2, its higher velocities in comparison with the underlying sediments (given by the negative polarity of their base at the seismic images), and knowing the desiccation environment where these sediments were deposited, they are arguably saline diapirs. While the M3 sub-unit got a composition of laminated gypsum according to drilling results of ODP site 653 (Kastens et al., 1988), at least at the Campania and Cornaglia Terraces.

In the continental regions, ODP site 656 provides evidences from transgression from subaerial to subaqueous environment. ODP site 652 drilled a monotonous barren, gypsiferous, calcareous, sandy and silty mud and mudstone section, which has been related with a closed lake, and sometimes a fluviatile or beach environment (Kastens et al., 1988). And the ODP site 654 reached an organic carbon rich, claystone and dolomitic/calcareous siltstone, which seems to mark the onset of restricted conditions. Overlaying it, there is gypsum interbedded with calcareous clay, sandstone and dolostone (Kastens et al., 1988), which probably corresponds to the M3 sub-unit of the Sardinia margin. All these sites provide evidence of a sub-aerial environment at continental regions during Messinian time.

There are some revealing differences between the continental regions and the back-arc ones. In general the deposits of the continental regions are thinner, although their thickness is more variable in these areas, while at the Cornaglia and Campania Terraces they have a rather uniform thickness. There exist also the M2 sub-unit, which has only been observed in these two regions, whereas the presence of the M1 sub-unit has a scarce or even uncertain presence there. Nevertheless, it must be taken into account that the apparent absence of the M1 unit is possibly not real but due to seismic imaging issues caused by the overlying salt deposits. The presence of M2 and M3 sub-units at back-arc regions implies a submerged environment during the Messinian Salinity Crisis. And the greater thickness of M3 in comparison with the continental regions, suggest that these regions were the deepest areas during this time.

However, sedimentation is not homogeneous within these regions. In the Cornaglia Terrace, the deposits are thicker south of the Orosey Canyon than to the north. The overlying unit - M3 - is deformed by salt diapirism of the M2 sub-unit southwards of the Orosey Canyon. While to the north, M2 is thinner and discontinuous and deforms with scarce diapirism. Some authors have defined two sub-regions, taking the Orosey Canyon Line as a natural boundary between them (Sartori et al., 2001). They suggest that the Orosey Canyon is a transfer zone that could explain the differences listed above, as well as the arched shape of the faulted continental block of the Baronie seamount (fig. 4.1) . But although these differences have been observed in our seismic sections, the Medoc 6 profile, which images the Orosey Canyon Line, doesn't show any structure that might be easily related with transfer activity.

In the opposite side of the basin, under the Campania Terrace, there is only one seismic profile crossing the region. Here, scarce faulting affecting the basement resembles the area south of Cornaglia Terrace, however the thickness of the unit in Campania is moderate, resembling the north area of the Cornaglia Terrace.

Pliocene

The Pliocene is the first unit found to be spread everywhere across the basin, suggesting

that the studied area finished to open during the lower Pliocene. This fact agrees with the age of the two fissural volcanoes in the middle of the area of study: the Vavilov and Magnaghi seamounts (Kastens and Mascle, 1990; Savelli, 2002; Rosenbaum and Lister, 2004; Lustrino et al., 2011). It can also be observed that the maximum unit thickness occurs in these central areas, and thus it can be interpreted that they were the deepest areas during Pliocene times.

Across most of the Tyrrhenian it has been observed that this unit is bounded by two regional discontinuities. As discussed above, the contact with the underlying Messinian sediments is marked by the Messinian Crisis horizon. The upper limit is marked by a regional discontinuity near coincident with the Pliocene-Pleistocene contact, although it is not visible everywhere.

This upper discontinuity seems to be related with a tectonic event, and it becomes more evident at the continental areas, towards the east, especially towards the Italian Margin. The origin of the unconformity is unclear, but several authors described a change in the stress field during the lower Pleistocene, related with the southeastward migration of the extension locus from the Vavilov Basin to the Marsili Basin (Faccenna et al., 2004; Ciffeli et al., 2007; Chiarabba et al., 2008). This change in the kinematic frame could be related with the origin of this unconformity.

A third discontinuity has been described within the Pliocene, dividing it into two sub-units, named in this work as upper and lower sub-units. Mid-Pliocene discontinuity is not as clear as the Messinian crisis boundary. However, there are several features associated with its presence allowing its identification almost everywhere. The lower sub-unit tends to be more transparent than the upper one, which usually is more reflective and shows more continuous reflections. This change can be gradual or abrupt, depending on the area. In addition, a highly-reflective layer has been observed locally, just above the contact, helping to locate the boundary.

In general, in the continental regions, the lower sub-unit shows a syn-tectonic character, while the upper sub-unit has a post-tectonic character. Thus, in these regions, the discontinuity consists of an angular unconformity, making it easy to identify. Although at the Sechi-Farfalle region, the whole Pliocene column is post-tectonic, with the exception of a few half-grabens. For example, at ODP site 652, the end of syn-rift lays within the Pliocene (Kastens et al., 1988; Kastens & Mascle, 1990). Also, in the Corsica and the Sardinia Basins, both sub-units are post-rift, with the exception of some places along line M28-b, where the lowermost lower subunit seems to be also syn-rift. Thus, in general the Messinian top coincides pretty well with the end of rifting at the Sardinia-Corsica margin. Also, at ODP site 654, the syn-rift top lays within the uppermost Messinian, and all the Pliocene unit belongs to post-rift (Kastens et al., 1988).

In the rest of the domains, the whole Pliocene column seems to be post-rift. At the Campania and Cornaglia Terraces, the strata have a sub-horizontal disposition supporting a post-rift deposit. ODP site 653 show a continuous carbonate sedimentation representing the transition to open marine conditions, and no apparent distinction between the upper and lower Pliocene sub-units is observed (Kastens et al., 1988). However, in the MEDOC sections, the two sub-units can usually be easily distinguished because of the presence of the highly reflective layer and high reflectivity contrast between the units. In any case, the lack of syn-rift sedimentation doesn't mean that opening processes ended up. Seafloor spreading has been documented in the back-arc areas as is explained in the next chapter, and probably worked until the beginning of the formation of the Vavilov and Magnagui Basins.

In the regions where mantle was exhumed, the contact between the two sub-units is faint, and therefore it is difficult to detect the presence of the middle Pliocene discontinuity. Although several unconformities have been observed in the seismic images, they are very local and seem to be related with differential compaction, rather than with a tectonic event. Based on the stratigraphy, there are just a few places with a little pre-/syn-rift sediment, belonging to the lowermost lower sub-unit, suggesting that the region opened in a short time lapse during the beginning of Pliocene.

In summary, the middle Pliocene limit seems to be linked to the end of the rifting processes across much of the study area, that coincides with the interpretation of several authors of the “X” unconformity (Trincardi & Zitellini, 1973; Möller et al., 2013).

In addition to the events discussed above, transpressional tectonics occurred towards the Italian margin. Here, the Pliocene lower sub-unit appears to be highly tilted, suggesting a pre-transpressional deposition, while in comparison the overlying upper sub-unit does not seem as affected by the transpressional deformation. It is possible that the upper unit was partially deposited as syn-tectonic. However, there is no evidence that the beginning of transpression caused the middle-Pliocene discontinuity in the region or the basin.

Finally, at the North Sicily Margin, Pliocene layers are parallel and conformable to the previous Messinian top suggesting a later deformation. This fact can be related with a later folding related to a posterior compressive deformation, or with a regional updoming related with magmatic activity in the area, that is near the volcanic arc.

Pleistocene

Pleistocene is the most recent sedimentary unit differentiated in the basin, and can be found everywhere. It presents however sporadic character in the continental areas, where has only been found at some depocenters. In contrast, in the central regions of Magnaghi and Vavilov basins, and at the back-arc crust regions it is widespread. It reaches its maximum

thickness at the Magnaghi and Vavilov basins, like the previous underlying unit.

Across almost all the study area, strata are horizontal, with the exception of the Italian margin and nearby areas, where layers are tilted and sometimes folded. This fact suggests that, with the exception of the region described above, the unit has not suffered any deformation process at the whole area.

Deformation of these deposits near and at the Italian margin could be related with the transpression underwent in the area beginning in the Pliocene. But there are places where Pleistocene remains undeformed, and therefore we can assume that stresses working at the area have not been homogeneous in space and/or in time.

As will be discussed in the next chapter, the contact with the underlying unit is an angular unconformity in most cases, that becomes clearer towards the Italian margin and the eastern North Tyrrhenian. The unconformity is probably related to the sudden displacement of the axis of extension at the beginning of the Pleistocene.

Volcanics

Evidence of volcanic activity is widespread across the Tyrrhenian basin. Indeed, in some areas magmatism is still active: southeast of Italy and at the actual volcanic arc, although both areas are outside the working area.

The oldest volcanism observed in the Corsica basin is in the Elba-Pianosa ridge (fig. 4.11), described as an intrusive/eruptive complex by Mauffret et al. (1999), which has an age from lower Messinian to lower Pliocene (Rosenbaum & Lister, 2004). But it is a complex structure, and uplift of the sedimentary layers imaged at MEDOC-1 can also be related with Miocene compressional tectonics (Mauffret et al., 1999), although this fact cannot be confirmed nor rejected with our seismic data.

In the Sardinia margin, there is also the Vercelli seamount (fig. 4.11), imaged in the MEDOC-2 line, which consists in granitoid intrusions at the basement (mostly monzogranite) and K to ultra-K volcanics with an age of upper Tortonian to middle Messinian (Savelli, 2002; Rosenbaum & Lister, 2004; Lustrino et al., 2011). Southwards of the area of study, there is also the Cornacya seamount (fig. 4.11). It is a volcanic edifice of ultra-K volcanics dated as Serravalian (Savelli, 2002; Lustrino et al., 2011). Although it occurs south from the area covered by our seismic sections, its presence gives an important hint about the formation age of the Sardinia basin.

The presence of the volcanic deposits at the eastern end of M28-b profile can be explained with the volcanism occurred in the area since the lower Messinian. In the vicinity of

this sector there are the Acheste and Anchise Seamounts (fig. 4.11). The first one was active 5 Ma, and erupted trachytic and rhyolitic lavas (Savelli, 1988; Rosenbaum & Lister, 2004), while the Anchise seamount was active from 5.3 to 3.5 Ma and erupted basaltic shoshonitic lavas and dacites (Savelli, 2002; Rosenbaum & Lister, 2004). This activity can explain the volcanic deposits described, which lay over Messinian sediments.

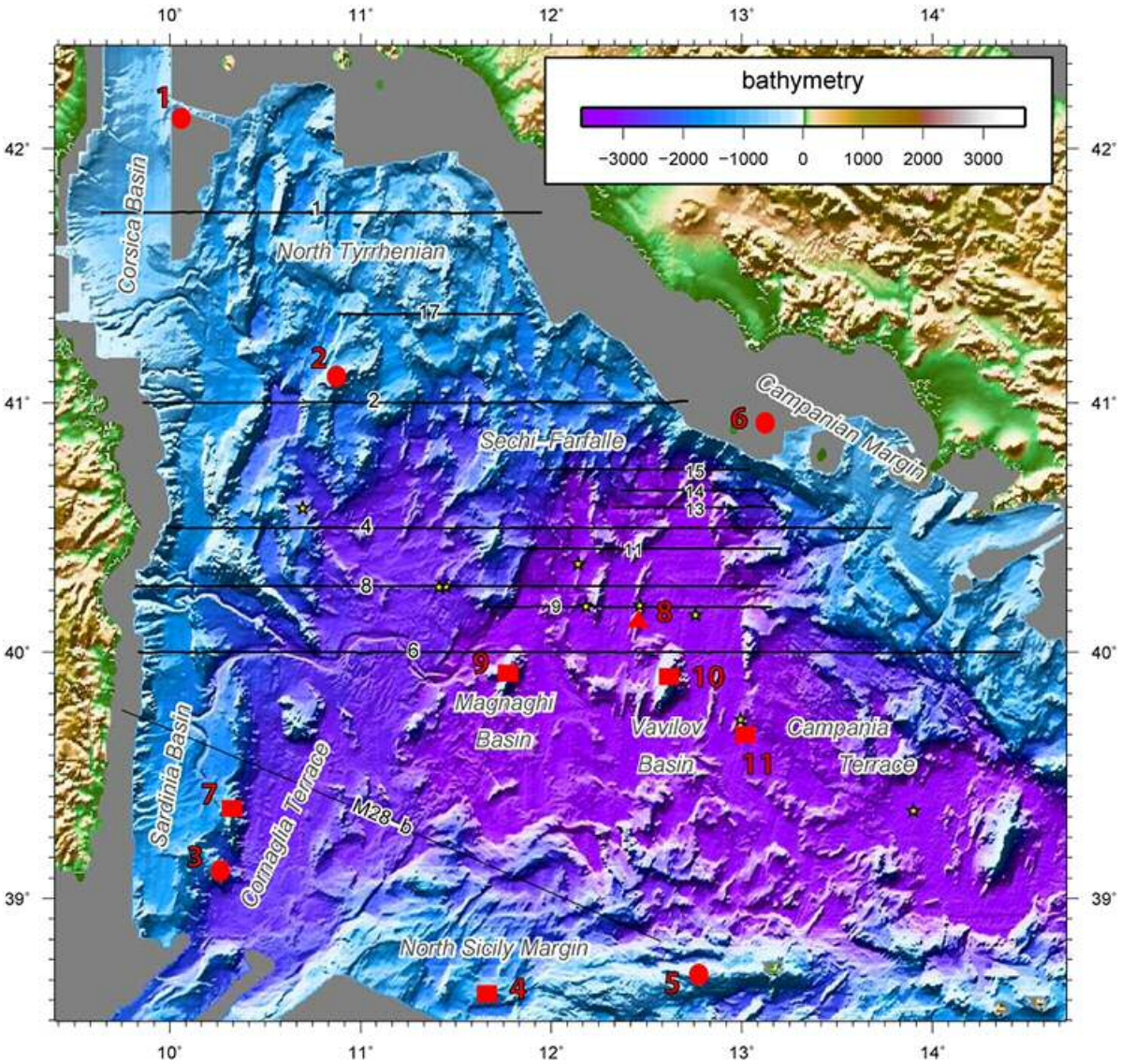

Figure 4.11: Magmatic events (effusive and intrusive) described at the text are marked with red dots. Circles for subduction-related magmatism, squares correspond to intraplate volcanism and triangles are MOR-type basalts). Places: 1: Elba-Pianosa Ridge, 2: Vercelli Seamount, 3: Cornacya Seamount, 4: Ancheste Seamount, 5: Anchise Seamount, 6:Pontine Islands, 7: Quirra Seamount, 8: Gortani Ridge, 9: Magnaghi Seamount, 10: Vavilov Seamount, 11: DSDP drilling site 373.

Concurrently, acid volcanism (trachytes and rhyolites) occurred northwards, at Pontine Islands at the Italian margin (fig. 4.11), with an age of 4.4 Ma (Savelli, 2002; Rosenbaum & Lister, 2004) or 4.2-1 Ma (Lustrino et al., 2011). Although MEDOC profiles do not reach this area, the structures are located nearby the eastern end of line MEDOC-2. This activity could explain the possible volcano observed in this seismic section between CMPs 6,200 to 6,800 (fig. 4.3-b). However, there is no available information concerning the age of this structure.

The surrounding sediment reflections appear uplifted, at least until the top of Miocene. Thus, it remains uncertain whether it was active during lower Pliocene.

Also, in the Sardinia margin Pliocene volcanism has been documented. As described above, the M28-b section images the northernmost apex of the Quirra seamount (fig. 4.11, and M28-b section, CMPs 4,500 to 5,500; fig. 4.2-b), with an alkali-basaltic composition (Sartori et al., 2001).

Finally, magmatism began in the central Magnagui and Vavilov Basins during lower Pliocene. At the Gortani ridge (fig. 4.12), ODP site 655 made of enriched toleiitic composition (Kastens et al., 1988; Kastens & Mascle, 1990), has an age of 4.6-4 Ma (Rosenbaum & Lister, 2004) or 3.4-3.5 Ma (Harland et al., 1982).

Subsequent volcanism occurred during upper Pliocene in the Magnaghi basin. Magnaghi seamount and Vavilov seamount (fig. 4.11) are the two known large fissural volcanoes of this central area. Lustrino et al. (2011) suggest a Na-Hawaiite moderately enriched in Nb for both volcanoes. This composition is anomalous with respect to typical MOR basalts, and suggests the existence of sources affected by slab-derived melts (Lustrino et al., 2011). The age of Vavilov seamount has been estimated in 2.4 to 0.7 Ma by Sartori et al. (2004), while other authors give an age of 0.7 to 0.1 Ma for Vavilov seamount and 3 to 2.7 Ma for Magnaghi seamount (Lustrino et al. 2011). These ages coincide well with observations in seismic images: some sedimentary layers around Vavilov seamount appear to be affected by the intrusions until the most recent strata, while this effect has not been observed near the Magnaghi seamount.

Volcanic activity in the area can also explain the highly-reflective volcanic layers imaged at MEDOC-6, MEDOC-8 and MEDOC-9. These deposits have been interpreted as volcanoclastic and/or far-flow volcanic deposits, as suggested by the ODP site 651 data (Kastens & Mascle, 1990). And their chemical analysis give an age of 3-2.6 Ma (Ferraud et al., 1990). Finally, according to Bertrand et al. (1990) all the Vavilov basalts drilled during ODP leg 107 and the DSDP site 373 reflect a chemical evolution that could be associated to slab migration.

There are two regions where no magmatic eruptive evidence has been found. These are the Cornaglia and Campania Terraces. But as will be explained in the forthcoming tectonic chapter, these areas have been identified as magmatic type trust (Manel et al., 2014; 2015), but lack basement outcrops or drilling information.

In conclusion volcanism evolved together with the opening of the basin. Oldest magmatism occurs at the continental margins and begun during middle Miocene times, while most recent activity fundamentally focused in the Pliocene Magnaghi and Vavilov basins.

4.4. Stratigraphic evolution interpretation

From observations of the localization and the distribution of each sedimentary unit, their seismic facies and their pre/syn/post-rift character, is possible to define a general outline regarding the evolution of the basin since the late Miocene. The key to understand this evolution is that the distribution of these sediments reflect the areas that were extending or had already formed during their sedimentation (fig. 4.12).

The oldest sediments have been described at the Corsica and Sardinia Basins, while no evidence of them exist throughout the rest of the Tyrrhenian basin. These deposits belong to pre-Tortonian Miocene, and therefore the other regions were formed in younger times.

The onset of rifting across the rest of the basin falls in the upper Tortonian (the L discontinuity). Evidence for this is that the Tortonian sediments can be found at all the continental areas in local depocenters, typically half grabens (fig. 4.12), with the exception of the Italian margin. However, considering the younger transpressional deformation that took place in this region, and the potentially important signal attenuation and imaging issues (e.g. multiple attenuation) in shallower areas, the lack of reported Tortonian should be taken with caution.

The Messinian is more widespread than the Tortonian, and can be found everywhere with the exception of the Vavilov and Magnaghi Basins, pointing out that they are more recent. It should be noted that it has also been described at the areas with magmatic crust, like the Campania and Cornaglia Terraces, where it is the thickest. The lower limit for this unit is poorly defined, because the presence of the basal sub-unit - M1 - is ambiguous, and in some areas has a weak reflectivity, even if it has been described at both continental and back-arc domains. It appears clear that it less abundant than the upper sub-units, and therefore not all depocenters and faults observed currently existed during the early Messinian.

Another point to be made is that the M2 sub-unit has been described exclusively at the back-arc regions of Campania and Cornaglia Terraces. Their evaporitic nature suggests that these regions were the deepest areas of the basin during salt deposition in the Messinian Crisis (fig. 4.12).

Finally, both Pliocene sub-units and the Pleistocene have been imaged everywhere (fig. 4.12), including the Vavilov and Magnaghi Basins. Opening of these two sub-basins occurred in a short time lapse mainly during the lower Pliocene. However, the Magnaghi basin started its opening during the uppermost Messinian, since at the occidental part of this region there are some Messinian deposits including M2 and M3. So they indicate that this area started its formation during the latemost Messinian.

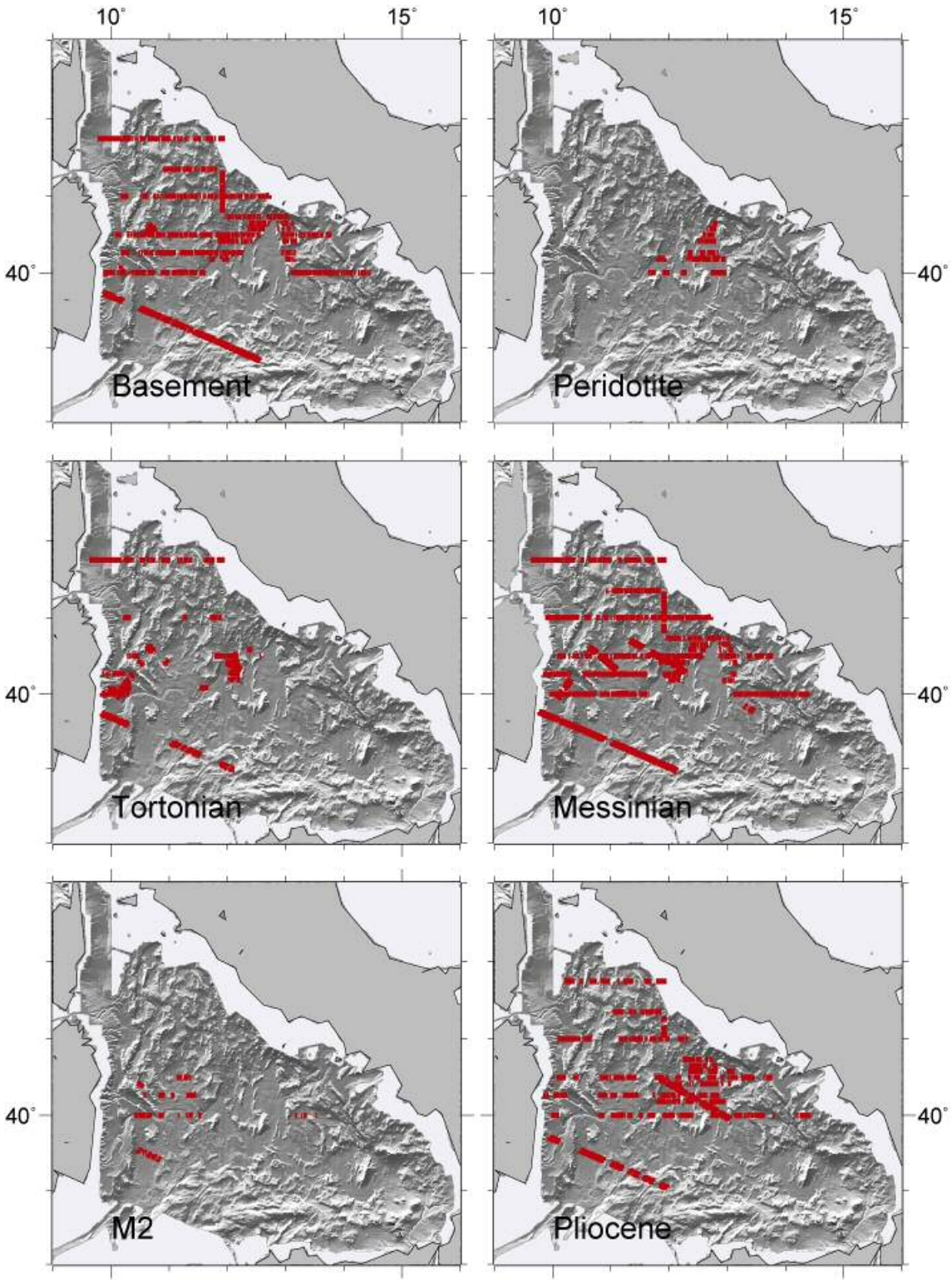

Figure 4.12: Sedimentary distribution for most important units worked at the text. "Basement" refers to the seismic basement identified as crustal basement, regardless of its continental or oceanic nature. While "peridotite" location is mostly based on tomographic work from MEDOC survey (Prada et al., 2014). Also the M2 Messinian sub-unit is important because of its relation with submerged areas during the Messinian Salinity crisis. Finally, Pleistocene has been ignored in this figure because is the youngest unit and its presence is widespread, giving any relevant information (and in addition, its distribution coincides pretty well with the Pliocene one).

The seismic basement nature is an indicator of the opening processes that worked in the basin. In the areas where Moho has been described, some type of crust should be present. In the continental areas, this reflection is faint, probably due to signal attenuation, whereas in the magmatic crust it consists of clear reflections. On the other hand, at the Vavilov and Magnaghi basins, there is no crust, and exhumed peridotite is present. As will be discussed in the next chapter, their widespread occurrence is supported by the seismic tomography models obtained with the MEDOC WAS data (Prada et al., 2014; 2015).

In summary, the Tyrrhenian opened stepwise with the extension locus moving towards the SE. Opening starts when extension jumps from the Corsica and Sardinia pre-Tortonian Basins towards the east, and the continental crust starts stretching.

At a given moment during lower Messinian, continental crust break up ocurred, and extension started in the Cornaglia and Campania Terraces, with the formation of new oceanic crust concurrently to the continental rifting in the north Tyrrhenian region.

Later on, in the uppermost Messinian or lower Pliocene, magmatism ceased, and crustal break up led to mantle exhumation in the Magnaghi basin, opening apart the back-arc areas. Simultaneously, stretching of the continental crust to the north slowed down or stopped in some areas in the north. Next, during the lower Pliocene, the rifting of the continental crust finished completely, and the Vavilov basin opened. So during the upper Messinian to lower Pliocene the extensional axis moved again towards the east.

Finally, in the lower Pleistocene, extension jumped again towards the southeast into the Marsili Basin area.

All these jumps of the extensional locus are reflected in the regional discontinuities described in this chapter. The oldest one, the L discontinuity, responds to the onset of rifting due to the displacement of the stress field. The end of the rifting corresponds to the middle-Pliocene discontinuity, which also coincides with another jump of the extension locus towards the east. At last, the tectonic discontinuity of the Pliocene-Pleistocene limit responds to the jump of the extension during the lower Pleistocene from the Vavilov Basin to the Marsili Basin, in the southeast of the Tyrrhenian.

In contrast, the discontinuity at the end of the Messinian responds to a regional event giving a prominent boundary, although it has a stratigraphic origin, and there is no tectonic event associated with it in the basin. That is the reason why there is no important change in sedimentary configuration with the exception of the erosive gap.

Is important to note that both middle-Pliocene and Plio-Pleistocene discontinuities are clearer at continental domains, especially towards the east of the basin, because the evolution

and displacement of the stress field becomes more evident in these areas. In contrast, in the back-arc areas these changes went unnoticed in the sedimentation, because when they occurred, all the sedimentation was post-rift in a relatively deep water sub-basin.

5. TECTONIC SETTING

5.1. Introduction

As explained at the methodology chapter, the tectonic processes of the working area have been studied based on information provided by the multichannel seismic data acquired during the MEDOC survey, the reprocessed image of CROP line M28-b, and the additional constraints of the ST seismic images provided by CNR-Bologna.

Most of the MEDOC profiles were shot across the basin in a west-east direction with the aim to image the structures perpendicularly. Sections obtained this way show the real dip of each structure, allowing for an accurate analysis. For this analysis the multichannel profiles, although tomographic velocity models obtained from MEDOC wide-angle seismic data (Moeller et al., 2013; 2014; Prada et al., 2014; 2015, and the velocity model presented in chapter 3) have been also integrated to help constraining the nature of the basement rock.

In addition, a basin-wide full-coverage multibeam bathymetric data map provided by CNR-Bologna is an important additional tool to study the tectonic structures because much of the basement structure is not fully covered by sediment. As explained in the previous chapter, the sedimentary cover in the Tyrrhenian basin is thinner in comparison with the other basins of the Western Mediterranean Sea, because of its more recent geological evolution. That's the reason why the seafloor relief displays well the trends of the basement top, and therefore it is possible to have a good overview of the tectonic framework of the area. In addition, assuming that the crust is locally isostatically compensated, the relative seafloor depth can be used as an indicator of crustal thickness. As mentioned in the methodology chapter 2, the data used in this work consists of a mesh with a resolution of 100 x 100 m that covers almost the entire basin (fig. 5.1).

The seafloor relief shows a general north-south trend for most of the structures along much of the Tyrrhenian, although they have a NW-SE orientation approaching the Italian coast as will be discussed next. To describe the tectonics of the area, several features have been considered. These are the fault density, the fault offset, their size and orientation, their distribution along the seismic section (homogeneous vs. heterogeneous), the deformation type, and the vergence of the fault planes, where needed. Depending on the combination of those features we have defined seven different tectonic domains (fig. 5.1).

5.2. Corsica-Sardinia Margin domain

This domain comprises the two western sub-basins of the Tyrrhenian: the Corsica Basin and the Sardinia Basin. The region is bounded by the Corsica and Sardinia islands to the west, and the Cornaglia Terrace, the Baronie Seamount and the Mt. Etruschi to the east. The northern and southern limits fall outside our study area, but they correspond to the Italian

shoreline in the north/northeast and the Ichnusa sub-basin in the south (fig. 5.1).

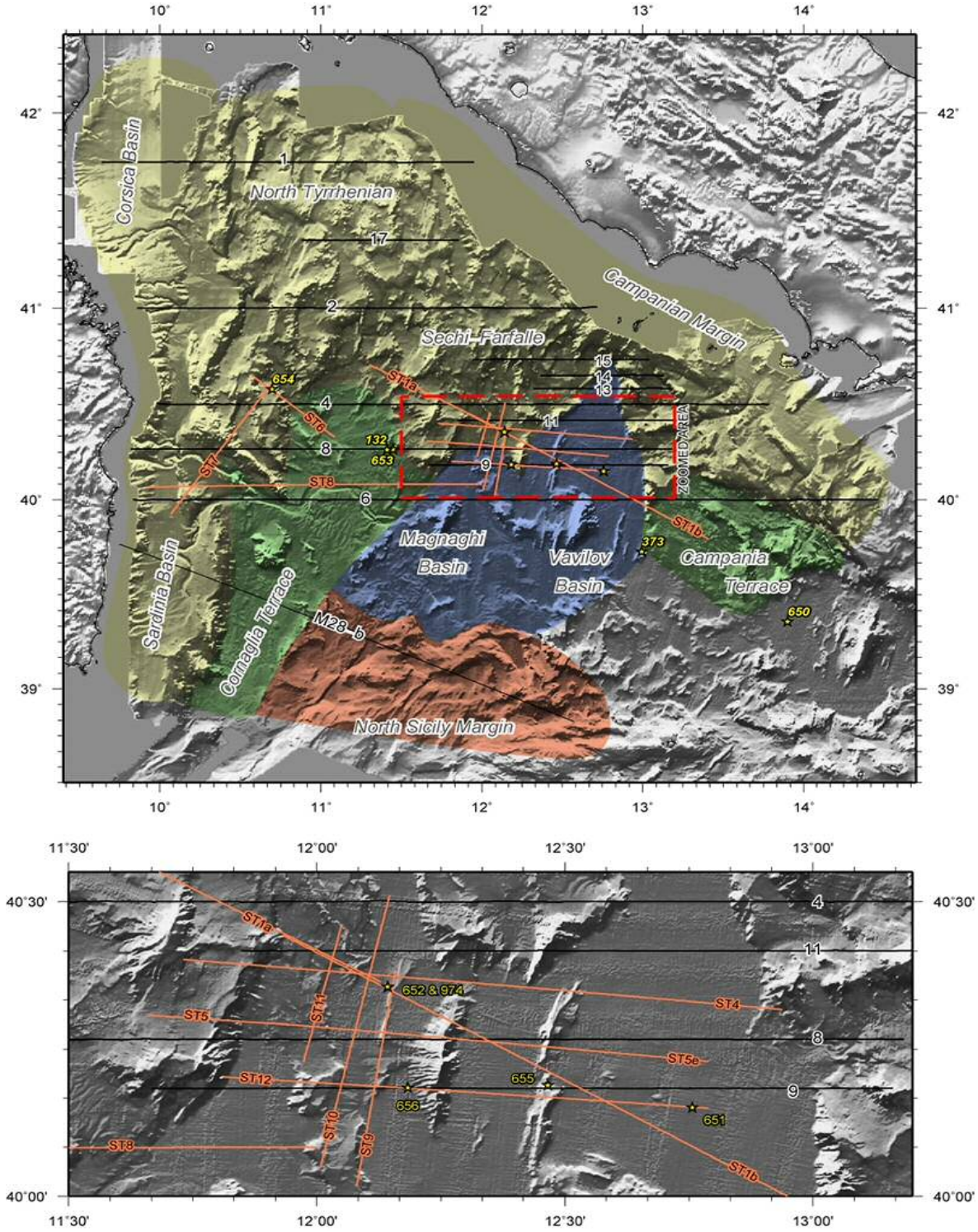

Figure 5.1: General map of the working area, showing the profile tracks used to get the interpretation: the MEDOC lines (from MEDOC survey, 2010), the ST (from ODP leg 107 survey), and the M28-b line (form CROP survey, 1994). Also ODP leg 107, used to calibrate the horizons, were plotted (see stratigraphy chapter for more information). Black lines are the lines processed (or reprocessed in the M28-b case) by me, while the orange ones were got already processed, and only were used to calibrate the horizons. Also domain names were plotted, and the colour code correspond to the that were working during their formation. At the yellow shaded areas only rifting processes worked. At the green shaded areas the magmatism was the main extensional mechanism. The red area correspond to a mix of rifting and volcanism. And finally, at the blue area exhumed mantle have been found.

The shape of these two basins is similar, consisting in elongated depocenters, with a N-S disposition running parallel to the Corsica and Sardinia coast (fig. 5.2-a). But in comparison with other Tyrrhenian rifted depocenters, they are larger, with breadths that get ~60 km.

The bathymetric map shows a rough seafloor topography with similar features to the North Tyrrhenian domain, as will be explained next. The depth is also similar, suggesting an alike crustal thickness, although the Moho signal is hidden by the multiple noise so crustal thickness cannot be verified. Furthermore, dredging data provides Variscan and Alpine basement samples (Collantoni et al., 1981), indicating the presence of a stretched continental crust. In addition, the velocity gradients obtained in the tomographic velocity models (Prada et al., 2014; Moeller et al., 2013) support this interpretation.

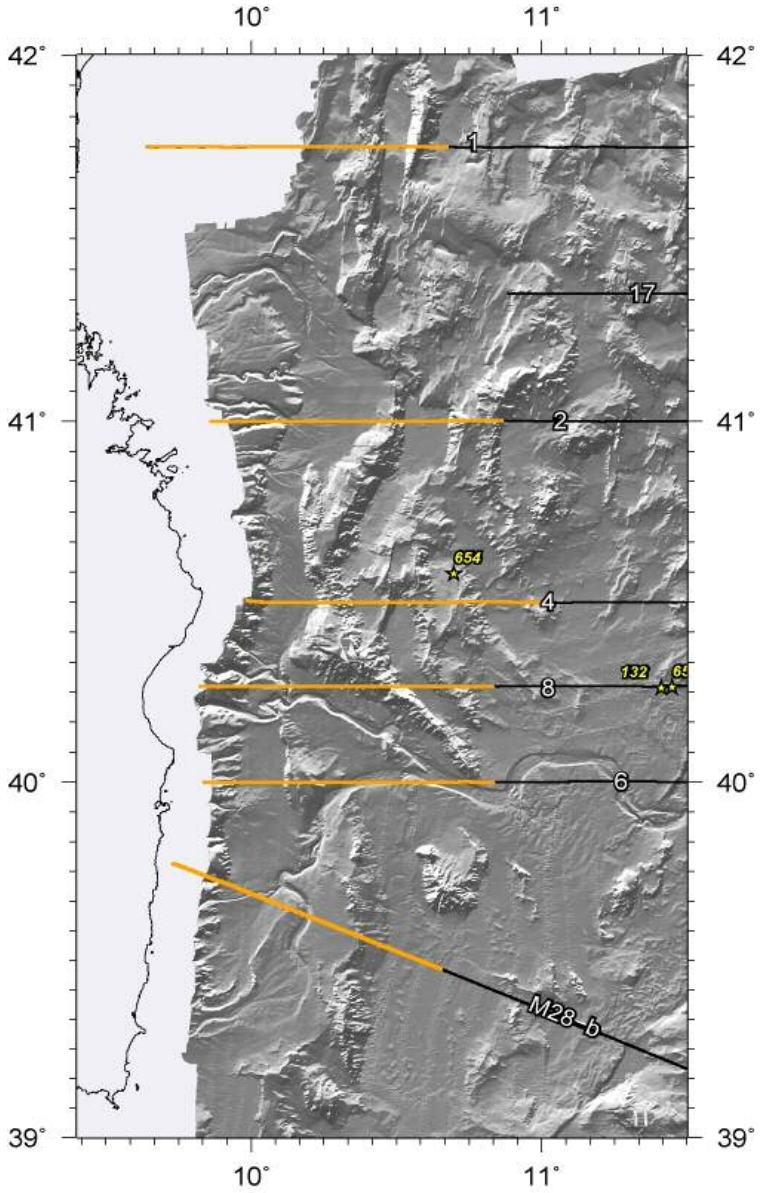

Figure 5.2-a: Local map of the Corsica-Sardinia margin domain. Location of the segments used to work this domain (see figure 4.2-b) are highlighted in orange.

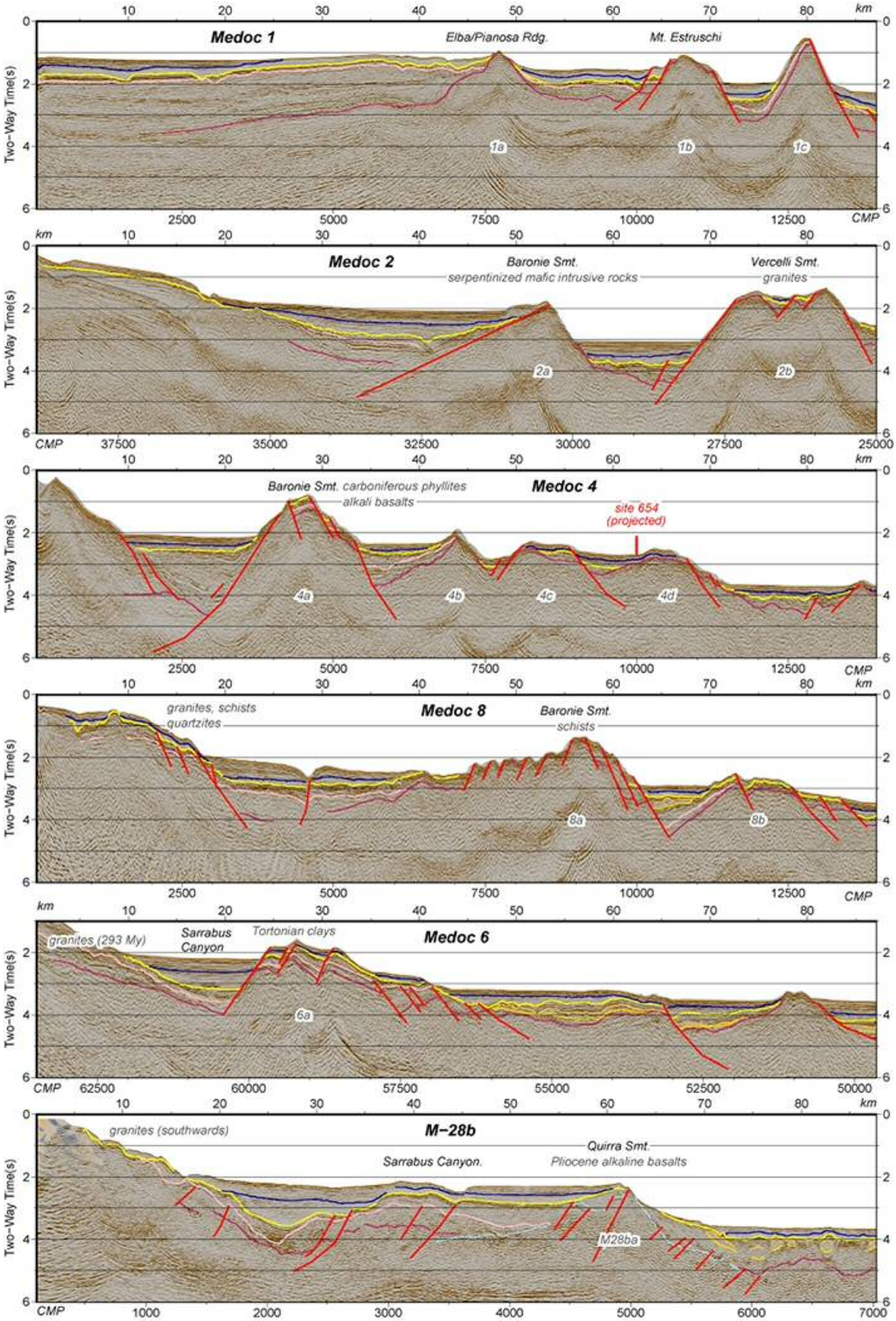

Figure 5.2-b: MCS sections crossing the Corsica-Sardinia continental margin. At the places were dredging data were available, it has been pointed out (Colantoni et al., 1981). Also the ODP site 654 location has been plotted (see explanation on stratigraphy chapter).

Six seismic profiles cross this region at different latitudes (fig. 5.2-a), but only one of them crosses the Corsica Basin: the MEDOC-1. This section shows a lower fault density in this area in comparison with the eastern nearby basins as can be seen along the rest of the section. Faults observed here are west-dipping structures mainly located near the Mt. Etruschi (fig. 5.2-b). Several authors describe these faults as antithetic structures related to a main fault related with the opening of the Corsica basin, which lays outside the profile, beyond its western edge (Mauffret & Contrucci, 1999), but no evidence of such a fault has been observed in our data.

No pre-rift deposit has been identified in this area, probably due to imaging problems caused by the water-layer multiple noise, but several authors locate the beginning of the opening during the Burdigalian or even in the upper Oligocene (Mauffret & Contrucci, 1999; Mauffret et al., 1999; Moeller et al., 2013). Finally, the top of syn-rift wedges indicates a lower Pliocene age for the end of rifting in this region, although the geometry of the reflections suggests an attenuation of rifting previous to the end of the Messinian.

The Sardinia Basin shares similar features with the Corsica basin, like its low fault density in comparison with the rest of the domains. Here again, the noise of the water-layer multiple energy does not allow to image well the top of the crystalline basement, and even the top of pre-rift sediments in most of profiles. Previous studies locate the start of rifting in this area during the Serravalian times (Sartori et al., 2001; Sartori et al, 2004).

At the Sardinia Basin the structure is imaged on four MEDOC and one CROP sections (the M28-b). The northernmost profile is MEDOC-2, and it shows only one large fault related with the opening of the Sardinia basin. It is a west-dipping structure with the Baronie Seamount as the footwall. The syn-rift wedge presents a significant thickness, although its base is unclear due to poor imaging and thus it is not well constrained in depth. The top of syn-rift has been interpreted to occur within the lower Pliocene, although the Sardinia-Basin-forming main activity period ended much earlier.

Towards the south, MEDOC-4 presents a similar fault structure, but with some antithetic east-dipping faults associated to the main fault. Here, the top of the syn-rift coincides with the Messinian-Pliocene contact, but the base is poorly imaged.

Line MEDOC-8 displays a completely different structural arrangement compared to lines 2 and 4. Here the sedimentary cover is thinner than northwards, supporting that the fault offset diminishes in this area, so that it indicates that the large fault observed to the north dies near here. Therefore, it is not possible to know if faults are linked in depth, especially at the Baronie Seamount flanks. Thus, large offset faults appear to constrain the internal geometry of the Sardinia basin, while towards the center fault activity decreases. At the Sardinia continental

slope, faults verge towards the east, while at the western flank of the Baronie Seamount, they dip to the opposite side. In general, fault offsets are much smaller than in the northern sections, but extension is distributed over a larger number of faults. At last, at the center of the basin there is a nearly vertical fault with short offset in comparison with the rest of the faults (around CMP 4,500, fig. 5.2-b), making interpretation more difficult.

Southwards, line MEDOC-6 has a structure resembling that of MEDOC-2 and 4 profiles. It presents an east-verging main fault with significant slip, accompanied by other minor faults also related with the Sardinia Basin opening. In the nearby Sarrabus Canyon, faults have shorter fault slips and verge towards the east. This is the only section where early syn-rift deposits have been observed, giving a syn-rift age of intra-Tortonian to lower Pliocene at the Sarrabus Canyon area (CMPs 56,000 to 58,000, fig. 5.2-b). In the rest of the section, the beginning of rifting is not well defined.

The southernmost line M28-b crosses the Sardinia basin where it reaches its maximum breadth. In this area there are evidences of effusive magmatism at the Quirra seamount following the deformation, which hides partially the previous structure at the eastern side of the domain (Sartori et al., 2001). The section presents west-dipping faults, with small offset in comparison to the faults described in the northern sections.

5.3. North Tyrrhenian region

This region is located in the northernmost part of the study area, between the Corsica Basin at the west and the Italian continental margin to the northeast (fig. 5.3-a). The southern boundary has been taken considering an abrupt change in the tectonic style. This change, which can be easily observed in the bathymetric chart (fig. 5.1), occurs near the parallel 40º30'. North from this limit, seafloor topography shows large fault blocks with an approximate north-south trend, while towards the south the seafloor presents smoother topography and fault blocks become smaller and scarce.

Two different domains with different features have been defined within the North Tyrrhenian. They share some features like the above-mentioned large faulted blocks, which are the main characteristic of this domain. These blocks display lateral continuity and an approximated north-south orientation, leading to restricted large and narrow half-grabens that can be well observed in the bathymetry (fig. 5.3-a). This orientation suggests a fairly east-west component in the extension direction, in contrast with the rest of the Tyrrhenian where basin structures present more variable orientation. However, towards the east the orientation of fault blocks becomes more oblique, as will be discussed later.

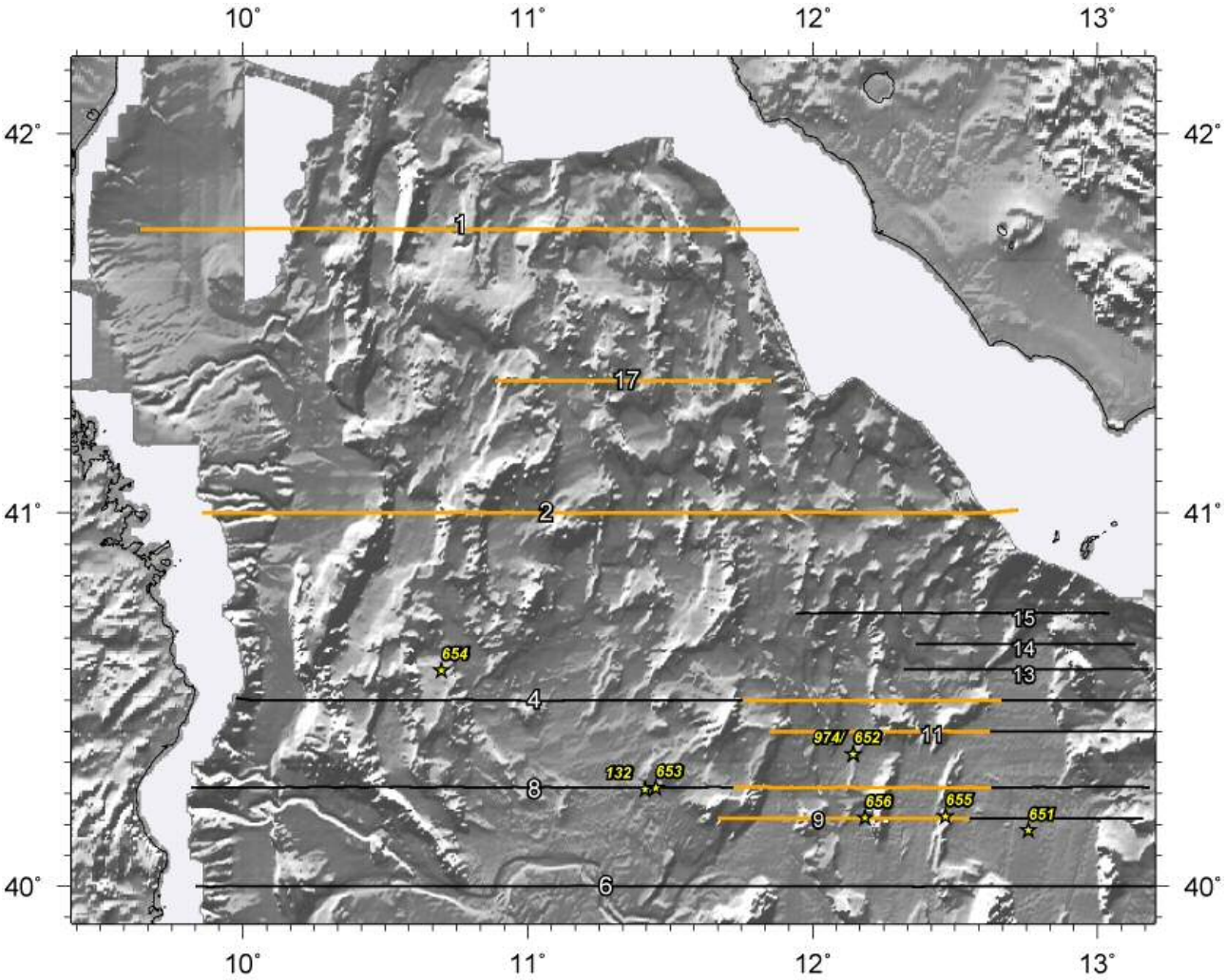

Figure 5.3-a: Local map of the North Tyrrhenian domain. Location of the segments used to work this domain (see figure 4.3-b and 4.3-c) are highlighted in orange.

Several multichannel sections cover the area. All sections show blocks with large fault offsets, although in comparison with the nearby Corsica and Sardinia basins, fault slip is smaller and faulting is distributed more homogeneously across the region (along the profiles). The images show a wide range of displacement lengths, fault dips and vergences. Although like in the former domain, the multiple noise obscures the image of the deep crustal structure, hindering to observe well the structures in the lower part of the crust.

The first tectonic domain of the region corresponds to the central part of the North Tyrrhenian. It is covered by several MEDOC sections (fig. 5.3-a), which show that broadly the size of the rotated blocks decrease towards the Italian coast. This characteristic can also be observed in the bathymetric map (fig. 5.1). Sections that show well this characteristic are MEDOC-1 and 2 (fig. 5.3-b), which span the basin from east to west allowing to see this gradual change. Also, towards the south, at the Tavolara and Vercelli basins, faulted blocks present a fairly NNW-SSE orientation, in contrast with the north-striking ones (MEDOC-2, CMPs 22,000 to 30,000; fig. 5.3-b), and the structures at the bathymetry seem to be shorter.

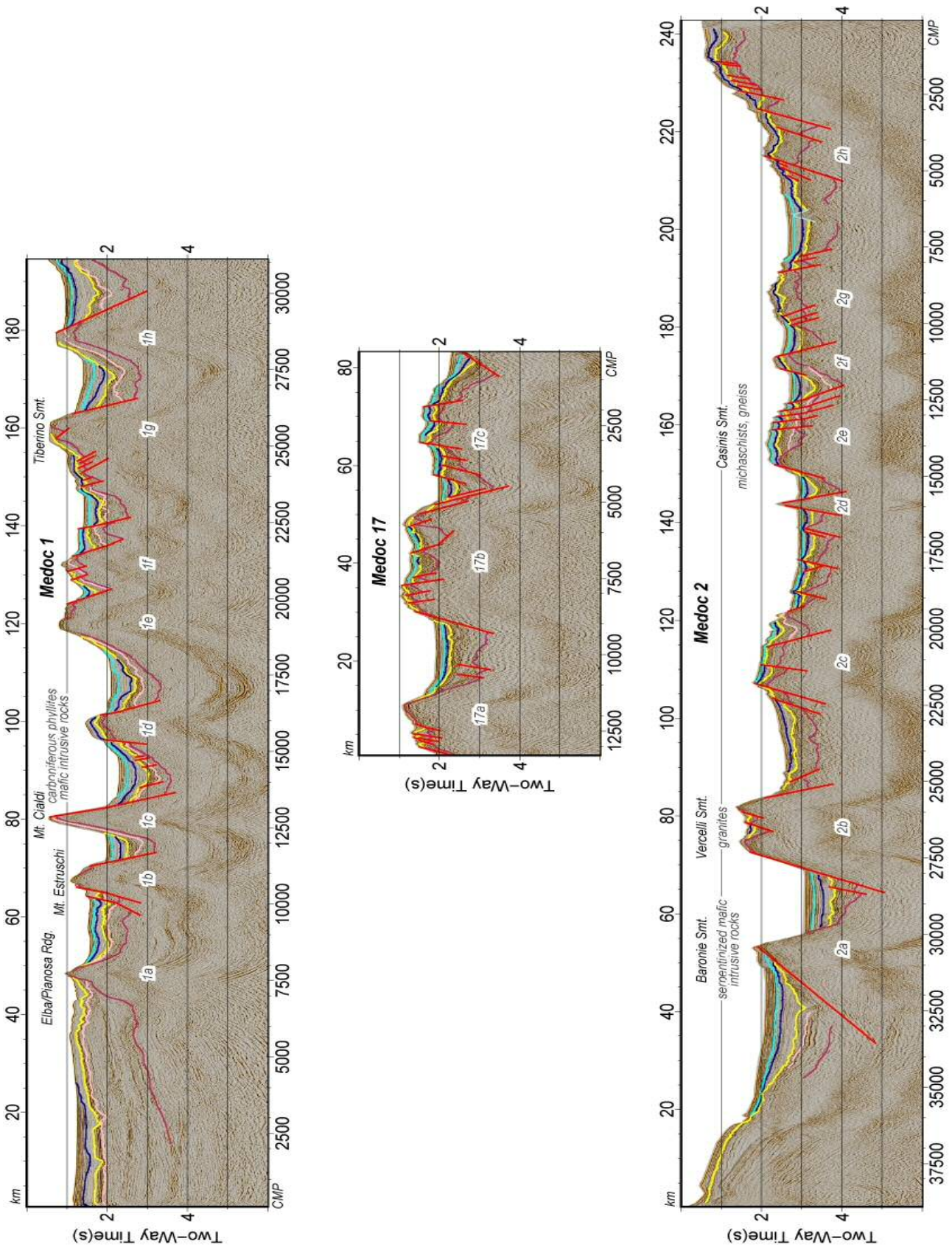

Figure 5.3-b: MCS sections crossing the North Tyrrhenian. At the places were dredging data were available, it has been pointed out (Colantoni et al., 1981).

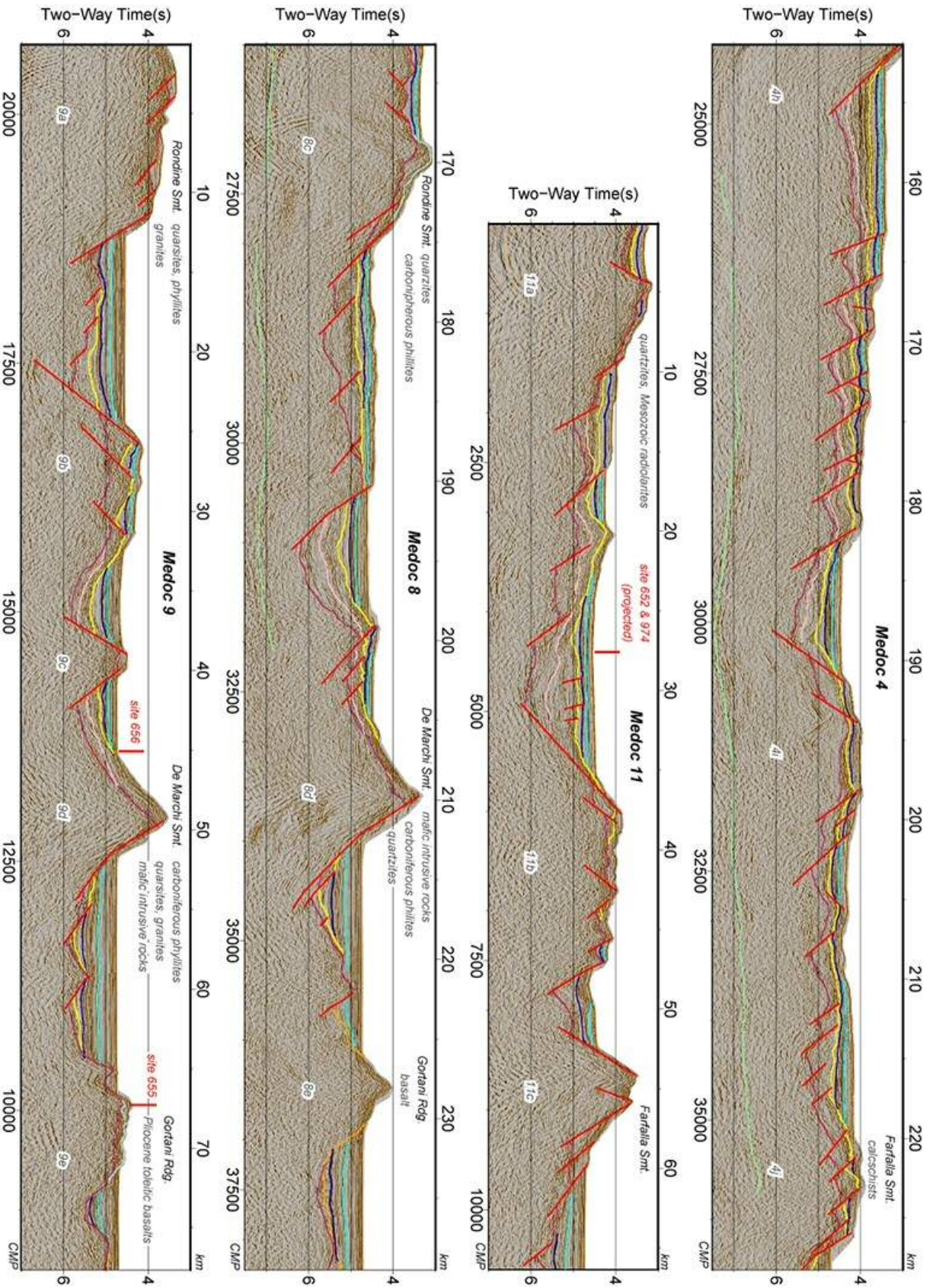

Figure 5.3-c: MCS sections crossing the Sechi-Farfalla region. At the places were dredging data were available, it has been pointed out (Colantoni et al., 1981).

In this area, almost all the faults cut the seismic basement and reach the sediments until lower Pliocene or even the entire sedimentary column. The presence of the ODP drill 654 near this area provides information to calibrate the base and top of syn-rift wedge (see stratigraphy chapter). Based on drilling results, an intra-Tortonian age has been assigned to the base of the syn-rift wedge, while the top corresponds to the lower Pliocene. However, there is also a set of faults where the top of syn-rift deposits are Messinian (e.g. MEDOC-1, CMPs 16,500 to 18,500, fig. 5.3-b), suggesting that their activity ended earlier.

In general, fault vergence is variable trough the region, but most faults are east-dipping structures, especially in MEDOC-1, 4 and 8. Conversely, in MEDOC-2 faults tend to be west-dipping with the exception of a sector between CMPs 7,000 to 16,000 (fig.4.3-b), and in MEDOC-17 vergence of faults is highly variable (fig.4.3-b). Furthermore, the distance between sections is greater than the fault length and prevents any correlation from section to section. Also, fault offset is highly variable, with the main faults that can reach 1 s TWT - about 1 km offset – (fig. 5.3-b), and some related synthetic faults with comparatively small fault offset (fig. 5.3-b). Antithetic faults are scarce.

The second tectonic domain is the Secchi-Farfalla region (fig. 5.3-a). In general, in this domain faults are distributed more homogenously. They show also similar fault offset and fault vergence across the sections, especially at the MEDOC-4 (fig. 5.3-c), although towards the south deformation is more heterogeneous.

A comparison between some of the northern sections and one of the profiles crossing this area show a clear variation in block size. In the Sechi-Farfalla region these rotated fault blocks are smaller in size, and faults present smaller offsets than in the northern domain. Additionally, fault density along the MCS sections crossing the Secchi-Farfalla region is higher. Here, it also differs in the time of rifting, because extension only lasted until the Messinian.

5.4. Cornaglia Terrace domain

The boundaries of the Cornaglia Terrace are well defined in the bathymetry, due to its homogeneous seafloor relief which contrasts with the surrounding areas. It presents a smooth seafloor without relevant topographic features, with the exception of the Cornaglia Seamount in the central part (fig. 5.1). The area also displays a characteristic constant smooth slope towards the center of the Tyrrhenian (fig. 5.4-a). The domain is bounded by the continental rifted margin of Sardinia to the west, and the Magnaghi Basin with the North Sicily margin to the east. Here, the Selli Line (also called Central fault) acts as a natural boundary line between the Magnaghi basin and Cornaglia Terrace. Finally, to the north there is the stretched continental crust of the North Tyrrhenian.

But instead of its homogeneous appearance at the bathymetric map (fig. 5.4-a), multichannel data shows a widely changing deformation style along the region. Three MEDOC and the M28-b lines cross the domain, and each of them present a different crustal structure (fig. 5.4-b).

The northernmost line crossing the area is the MEDOC-4. It presents a high fault density in comparison with the rest of the sections in the area. Considering the trace of these faults in the bathymetry, most of them seem to be the continuation of the faults observed in the adjacent domains of Sardinia continental margin or the North Tyrrhenian (fig. 5.4-a), although the seismic data coverage is not enough to map it. The faults described in this profile cut the basement and rotate much of the sediment cover. Syn-rift wedges suggest a main fault activity within the Messinian, even though a few of these structures may extend their activity until the lower Pliocene, for example, some of the faults of MEDOC-4 and 6 (fig. 5.4-b).

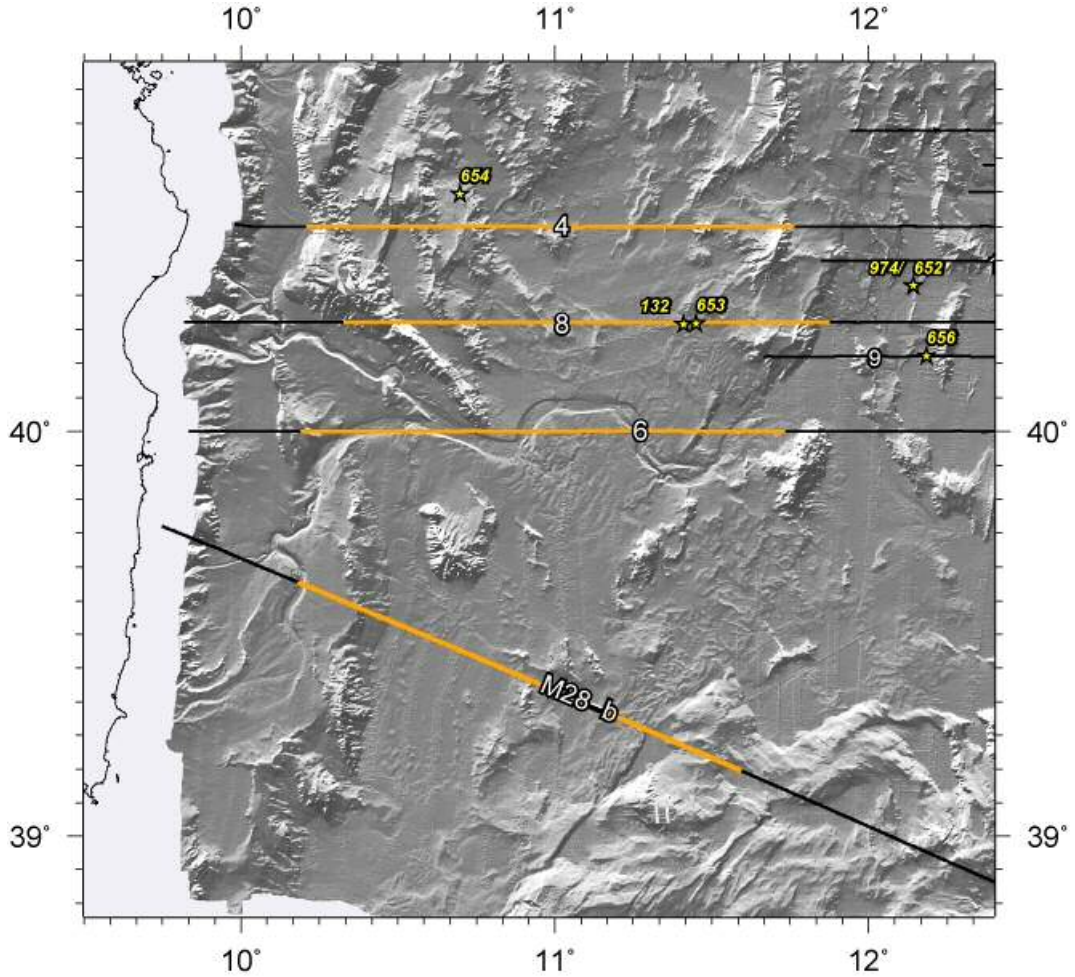

Figure 5.4-a: Local map of the Cornaglia Terrace domain. Location of the segments used to work this domain (see figure 5.4-b) are highlighted in orange.

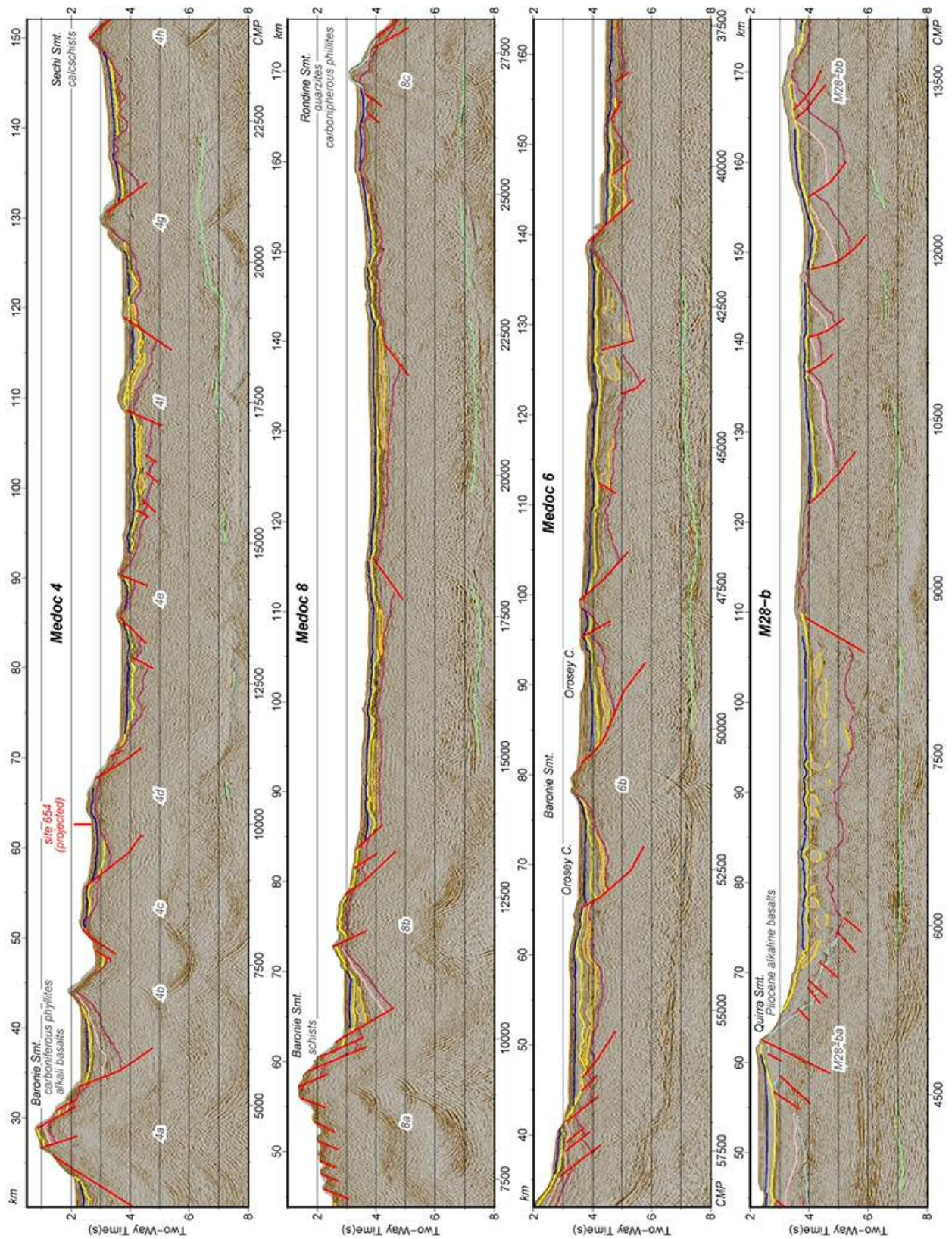

Figure 5.4-b: MCS sections crossing the Cornaglia Terrace domain. At the places were dredging data were available, it has been pointed out (Colantoni et al., 1981). Also the ODP sites 652 and 656 location have been plotted (see explanation on stratigraphy chapter).

MEDOC-8 profile presents a different structure compared to the other sections. In this area faults are scarce, and their offset is small in comparison with the northern ones. These structures appear to affect only the basement. However, in spite of the observed offset, no syn-rift sedimentary wedges have been identified. This can be due to several factors. First, it could be that faulting velocity was fast and short-lived. However, comparison between this profile and the nearby ones show a similar amount of extension all across the region (fig. 5.4-a and b). Besides, seafloor depth is fairly constant along the whole Cornaglia Terrace, suggesting a similar crustal depth, and so a similar stretching factor for the entire region. Therefore, it is unlikely that this area suffered different extension velocities, giving a similar basin width. There's also the possibility that during the rifting, low sedimentation rates occurred. But again, nearby sections present normal syn-rift wedges, suggesting sedimentation during the rifting processes. Then, it will be hardly difficult that just at the neighbouring of the MEDOC 8 section trace, scarce sedimentation occurred. Finally, there's also the possibility that these faults are not related with rifting, but with magmatic events instead. Some evidences support this theory: modelling of wide-angle data obtained during the MEDOC survey suggest the presence of a magmatic type crust (Prada et al., 2013; 2015), so that the presence of volcanic structures in the region is reasonable. In addition, some elongated highs are observed in the bathymetry, which appear to spatially coincide with these structures. These bodies are smaller than the surrounding faulted blocks, and could well correspond to volcanic edifices. This last option, although plausible, cannot be tested due to the lack of basement rock samples in the area.

Southwards, the deformation style changes again. In this area, line MEDOC-6 shows larger faults in comparison with the previous sections, and fault density is higher (fig. 5.4-b). In this case, faults cut the crystalline basement and tilt the sedimentary column from Messinian until the lower Pliocene. In contrast with MEDOC-8 imaged structure, these faults present well developed syn-rift wedges, allowing a good delimitation of their activity. However, some salt deposits are observed in the area that partially mask the underlying deposits, and fault geometry (fig. 5.4-b).

Finally, the southernmost section of this domain (CROP line M28-b) shows evidence of important salt tectonics, which masks extensional faulting in the underlying basement. Like in the MEDOC-6 profile, the presence of evaporitic deposits mask the real geometry of the sedimentary deposits.

5.5. Vavilov and Magnaghi Basins region

This domain comprises the Magnaghi, Vavilov and North Sicily sub-basins, although this last one was not considered in this work because no seismic MEDOC section is available for the study. Like the previous region, the boundaries are fairly well delineated in the bathymetric

data due to the clear structures marking the edges and its fairly homogeneous internal structure (fig. 5.1). Wide-angle data acquired during the survey confirms these limits, and indicates an exhumed mantle nature for most of the basement in this area (Prada et al., 2014; 2015).

The Magnaghi-Vavilov region is the deepest area of the Tyrrhenian basin, and presents a flat topography and fairly constant depth in contrast with the surrounding areas, although several seamounts break the smooth seafloor relief (fig. 5.5-a). The region lies between the Cornaglia Terrace to the west and the Italian continental margin together with the Campania Terrace to the east. To the south it is limited by the north Sicily margin, and to the north by the stretched continental crust of the North Tyrrhenian area (fig. 5.1; Moeller et al., 2014; 2015; Prada et al., 2014; 2015).

A remarkable feature of this domain is that no Moho reflection has been found at any of the multichannel profiles shot across it (fig. 5.5-b and 5.5-c). In contrast, at surrounding regions, like the Cornaglia and Campania Terraces, Moho is clearly visible. Moreover, serpentinized peridotites were drilled at the ODP site 651, near the Vavilov Seamount (Bonatti, et al., 1990; Kastens et al., 1988; Kastens & Mascle, 1990). Although these rocks were originally interpreted as a local feature, results from wide-angle seismic profiling support the widespread exhumation of mantle rocks across the region (Prada et al., 2014; 2015). Serpentinized peridotites lay directly below younger volcanic layers, and are covered by Pliocene sediments.

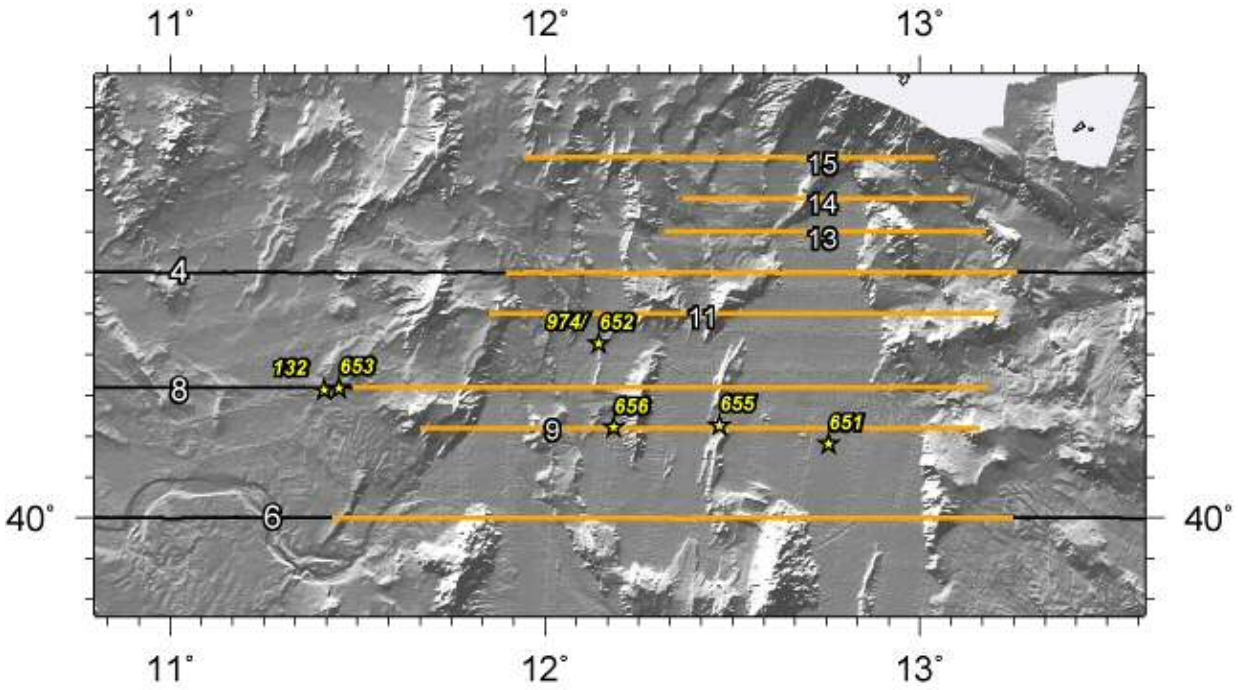

Figure 5.5-a: Local map of the Vavilov and Magnaghi basins domain. Location of the segments used to work this domain (see figure 5.5-b) are highlighted in orange.

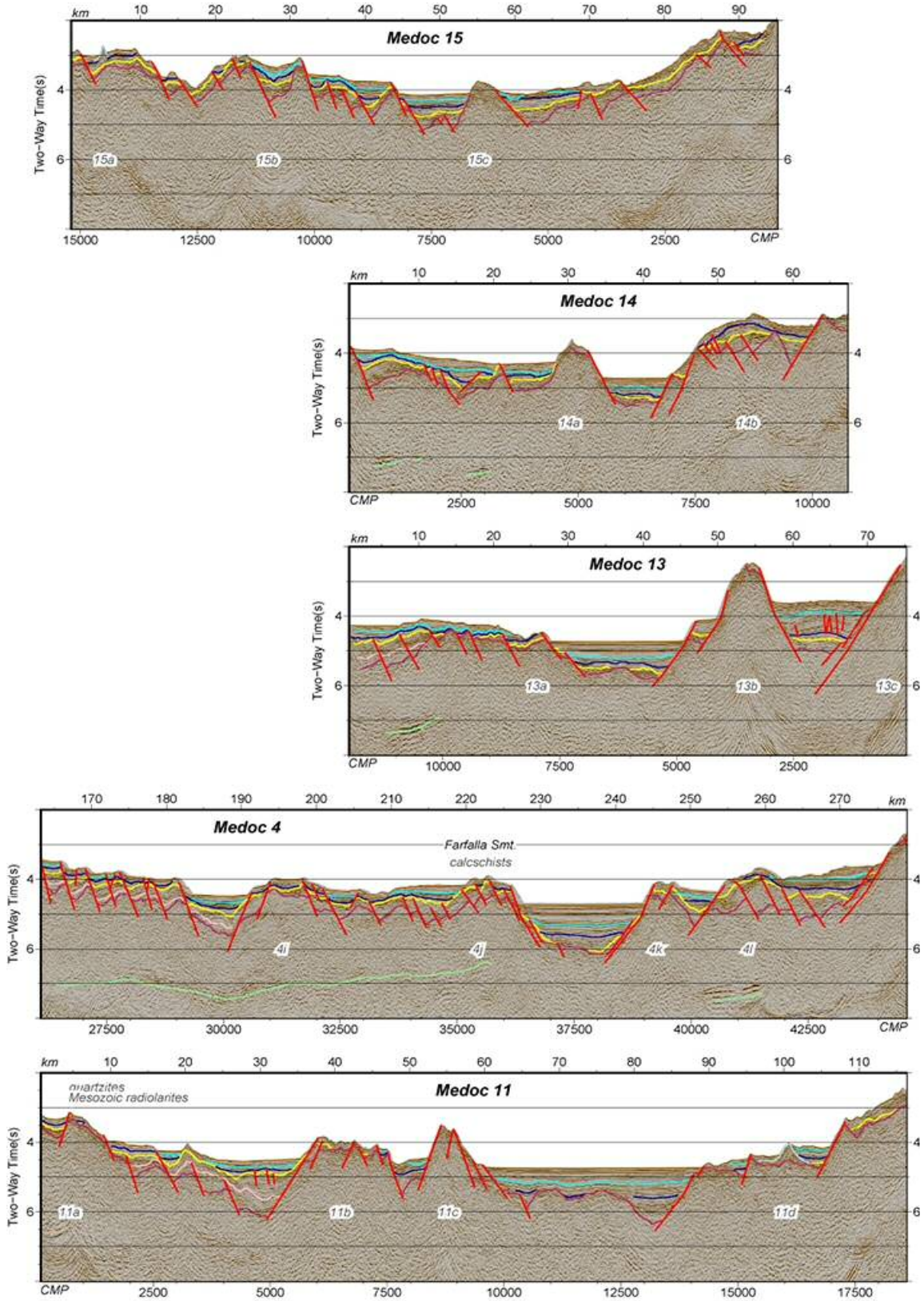

Figure 5.5-b: MCS sections crossing the Vavilov and Magnaghi basins northern area. At the places were dredging data were available, it has been pointed out (Colantoni et al., 1981).

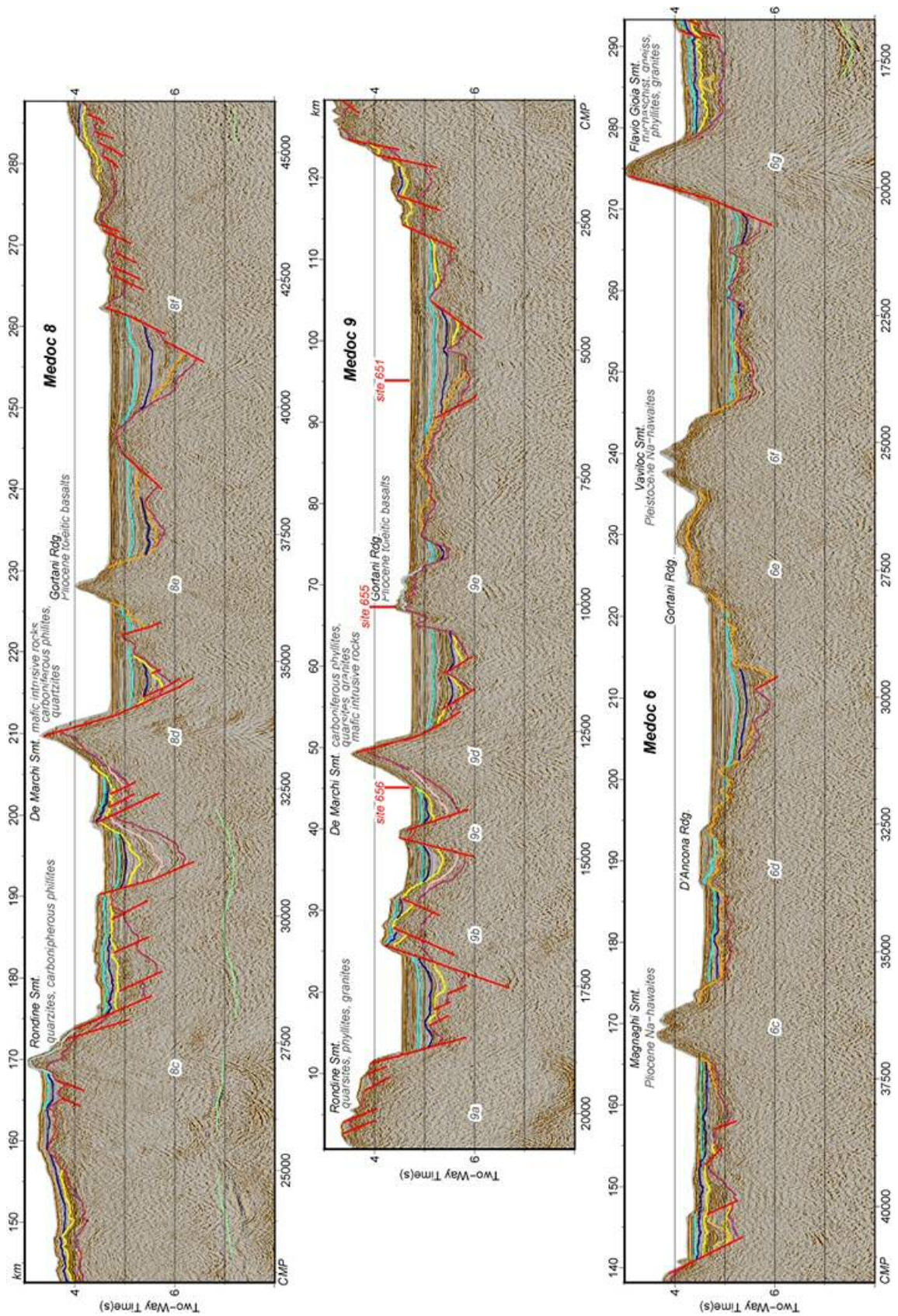

Figure 5.5-c: MCS sections crossing the Vavilov and Magnaghi basins southern area. At the places were dredging data were available, it has been pointed out (Colantoni et al., 1981). Also the ODP sites 651 and 655 location have been plotted (see explanation on stratigraphy chapter).

The northernmost sections crossing this region are lines MEDOC-14, 13, 4, and 11 (fig. 5.5-a). These four sections image the narrowest part of this region, at the northern part of the Vavilov Basin, and they show similar characteristics. First, the faulting is concentrated at the domains edges, while towards the center no basement faulting is observed. These structures display important fault offsets with a vertical throw of at least 1 second TWT (roughly 1 km). In addition, no clear syn-rift deposits associated to them have been observed. These sections confirm the lack of Moho reflections beneath the domain, while at the surrounding areas it is well imaged (e.g. MEDOC-13, CMPs 10,000 to 11,000, or MEDOC-4, CMPs 40,300 to 41,500, fig. 5.5-b), with the exception of MEDOC-11, where the multiple noise masks any possible Moho reflector (MEDOC-11, fig. 5.5-b).

The MEDOC-8 and MEDOC-9 lines, located to the south, cross the Vavilov Basin (fig. 5.5-c) and the apex of the Magnaghi Basin. In the Vavilov Basin sector, the structure is similar to the northern sections with higher fault density at the basin flanks, but here some faults have been identified within the central basin area (e.g. MEDOC-8, around CMP 35,700, fig. 5.5-c). However, these structures are not necessarily related to extension, but perhaps to volcanism. For example, this could be the origin of the small fault-bounded highs interpreted in the vicinity of the Gortani Ridge (MEDOC-9, CMPs 11,000 to 12,000, fig. 5.5-c), which is a well-known fissural basaltic structure.

The MEDOC-9 profile runs over three ODP leg 107 sites. The westernmost site 656 drilled the de Marchi seamount finding continental-type crustal rocks (Kastens et al., 1988; Kastens & Mascle, 1990). This ridge helps to delimit the boundary between the continental North Tyrrhenian domain and the Magnaghi-Vavilov exhumed mantle region. Faults related with this continental crust rupture can be observed at both sides of the sub-basin, and are similar to those described in the previous seismic sections to the north, with important fault offset and associated Messinian pre-rift sediments, and absence of syn-rift deposits. Therefore it has been assigned a lower Pliocene age, too. Site 651 in the center of Vavilov Basin found serpentinized mantle as main basement rock (Kastens et al., 1988; Kastens & Mascle, 1990; Bonatti et al., 1990). It is the only ground-truthing evidence for exhumed mantle in this region, but as mentioned above it is supported by results obtained by wide-angle data at the E-F and H-G MEDOC sections (Prada et al., 2014; 2015).

The southernmost profile crossing this region is MEDOC-6. It crosses two of the most important volcanic buildings in the Tyrrhenian: the Magnaghi and the Vavilov Seamounts, aside from the Gortani Ridge. Similar to the north, large faults have been imaged at both sides of the basin, while in the center fault density decreases. Messinian sediments have been imaged at the Magnaghi Basin, possibly with a pre-rift configuration, while no clear syn-rift sediment wedge is observed. However, in the Vavilov Basin some deposits appear to form small wedges

with fan-like strata configuration (e.g. MEDOC-6, CMPs 25,000 to 21,200 and 29,400 to 30,000, fig. 5.5-c). These deposits are interpreted as lowermost Pliocene sediments, and may indicate the age of opening of this area.

5.6. Campania Terrace region

Like the rest of the tectonic regions, the boundaries of the Campania Terrace are well defined in the structures that are visible in the bathymetry because they coincide with an evident change in the tectonic style. It lays between the Italian continental margin to the northeast, the Vavilov basin to the west, and the Issel ridge to the south (fig. 5.1). However, only MEDOC-6 was acquired across the area, therefore its interpretation should be extrapolated to the entire region with caution.

A first view of the bathymetric data indicates a homogeneous character for the entire region. It presents a gentle slope dipping towards the center of the Tyrrhenian with any important relief, with the exception of the Issel Seamount at the eastern side of the domain (fig. 5.6-a). The seafloor depth is rather uniform suggesting small changes in crustal thickness. In addition, the Moho reflector observed in line MEDOC-6 is almost horizontal with high amplitude, supporting this interpretation. The seismic image also displays a highly reflective crust (MEDOC-6, CMPs 10,500 to 18,000, fig. 5.6-b). All those features recall the structure of Cornaglia Terrace discussed above. Like in the Cornaglia Terrace, the wide-angle seismic models also support the presence of a magmatic back-arc crust type (Prada et al., 2014; 2015). But in the Campania Terrace, the tectonic region defined in this work doesn't coincide exactly with the crustal domain defined by Prada et al., (2014; 2015), which expands towards the north into the Italian continental margin domain, as will be detailed below.

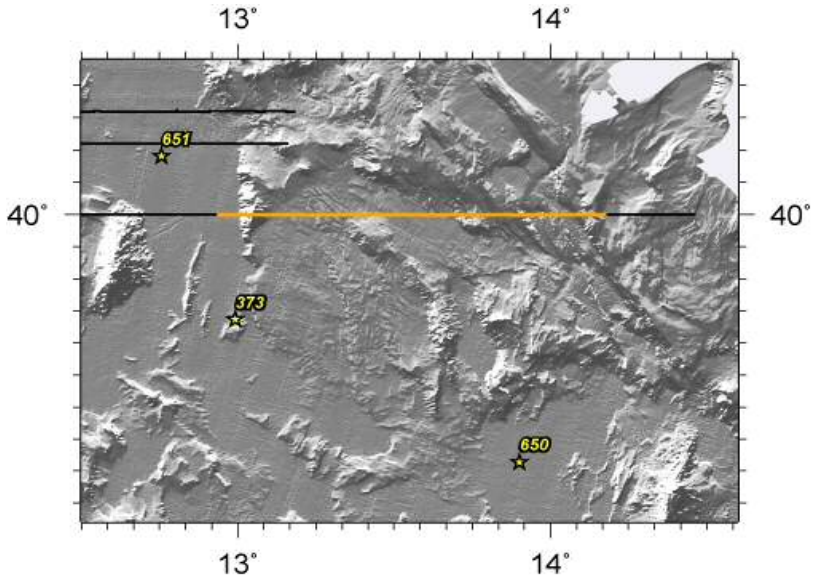

Figure 5.6-a: Local map of the Campania Terrace domain. Location of the segments used to work this domain (see figure 5.6-b) are highlighted in orange.

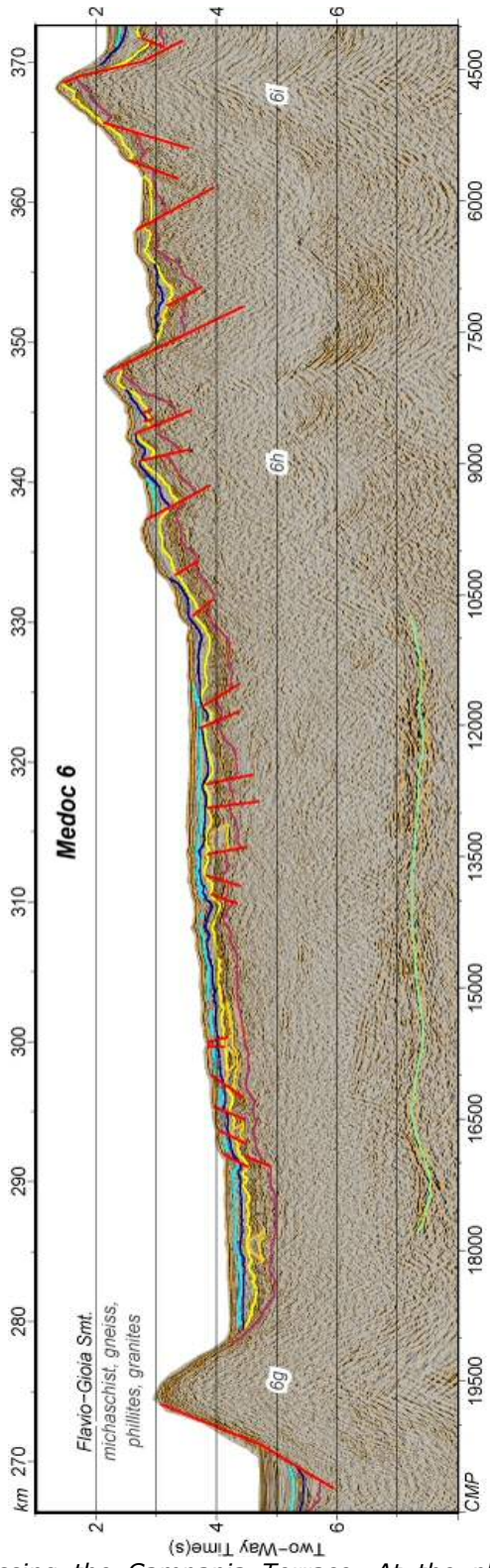

Figure 5.6-b: MCS section crossing the Campania Terrace. At the places were dredging data were available, it has been pointed out (Colantoni et al., 1981).

In general, fault density is high in comparison with the nearby Central Abyssal Plain domain or even the Cornaglia Terrace. However all these faults display comparatively very small offsets (fig. 5.6-b). In addition, a few possibly syn-rift sediment wedges are too thin to

identify well the activity period for these faults, and in most of the faults, no sedimentary wedge can be observed.

In fact, the deformation of the sediment column seems to be related with salt tectonics more than with extensional stresses, like in the southern Cornaglia Terrace. But here, the Messinian deposits are comparatively very thin, resembling the northernmost Cornaglia Terrace domain. Therefore, taking into account the sediments affected by the faults, and the similarities that the region shares with the Cornaglia Terrace, an age of (at least) Messinian to lower Pliocene is inferred for this deformation.

5.7. Italian Margin region

This region is located in the easternmost part of the study area, between the Italian Peninsula to the northeast, the North Tyrrhenian region to the west, and the Campania Terrace together with the Marsili basin to the southwest (fig. 5.1).

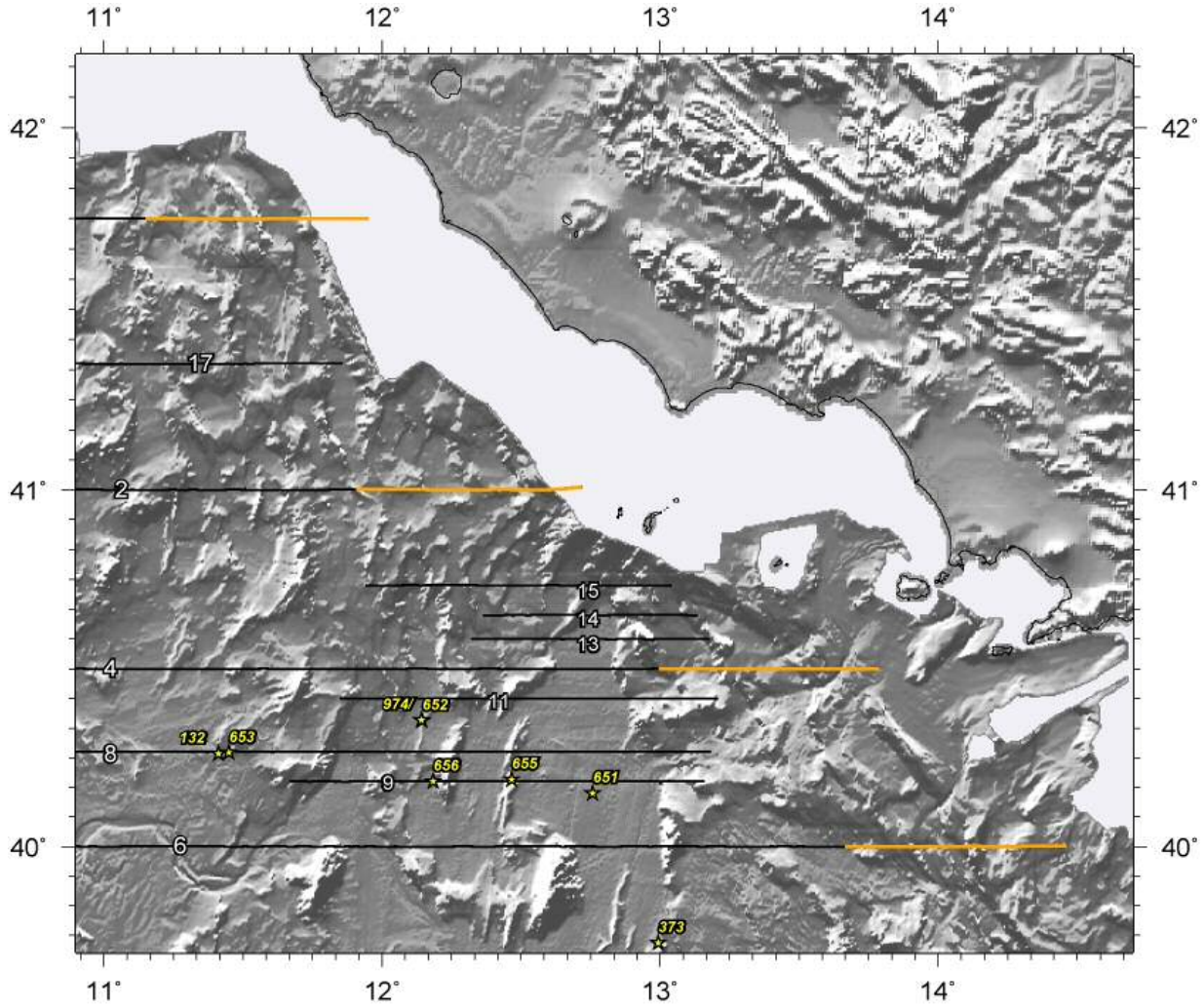

Figure 5.7-a: Local map of the Italian margin domain. Location of the segments used to work this domain (see figure 5.7-b) are highlighted in orange.

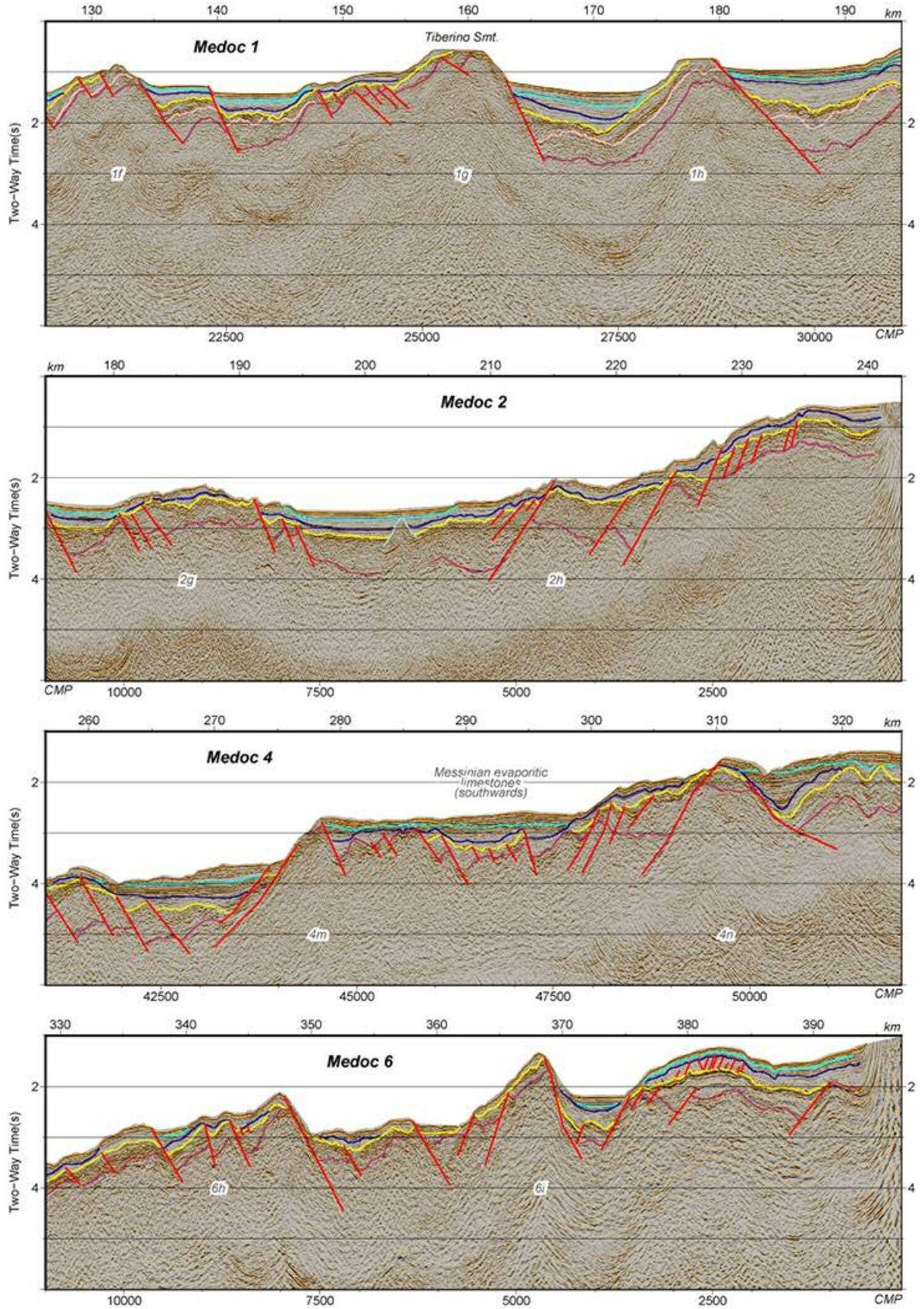

Figure 5.7-b: MCS section crossing the Italian margin. At the places were dredging data were available, it has been pointed out (Colantoni et al., 1981).

Along the margin, elongated faulted blocks run parallel to the coastline, with a broadly NW-SE strike, as it is well displayed in the bathymetric map (fig. 5.7-a). The abundance of these blocks is higher in comparison with the conjugate margin of Sardinia, although the relief and associated fault offset is smaller as observed in the seismic images (fig. 5.7-b).

The bathymetry shows a marked lateral variability along the margin, with these fault blocks changing from ridge to fault-bounded depressed areas along the same fault system, indicating a transpressional-transtensional fault zone roughly parallel to the coast. This structural style has not been observed anywhere else in the Tyrrhenian basin, being characteristic of this domain.

In this region, the seafloor rises towards the coast suggesting a thicker crust in comparison with the neighbouring areas. Here again, the bathymetry provides an overview of the main structural features of the region (fig. 5.7-a). Although this area should be the conjugated margin of the Sardinia continental margin, both regions share few common structural characteristics. The differences include a different structural style and dissimilar sedimentary thickness of the units.

However, the Campania margin (fig. 5.1) does share common features with the easternmost sector of the North Tyrrhenian region. It shows rugged relief, and wide-angle data support that the basement is composed of stretched continental crust (Moeller et al., 2013; 2014; Prada et al., 2014; 2015). This is supported by dredge samples of basement outcrops (Colantoni et al, 1981) from faulted blocks of continental crust. However, there is a narrow zone to the west, in the deepest seafloor of the region, where wide-angle velocity models support that vigorous magmatic activity has modified the continental crust (Prada et al., 2015). Here again, the tectonic region doesn't coincide exactly with the crustal-type domain.

In general, in this region there are few Messinian deposits in comparison with other domains, and no Tortonian sediments have been observed as discussed in the stratigraphy chapter number 4.

Seafloor relief together with seismic images indicate a wide structural variability along the margin. Starting from the north, lines MEDOC-1 and 2 display a tectonic structure resembling the nearby North Tyrrhenian domain. But here, sedimentary layers dip at unusually high angles (e.g. MEDOC-1, CMPs 26,000 to 29,000, fig. 5.7-b), and antiformal structures have been observed locally (e.g. the easternmost side of MEDOC-2, fig. 5.7-b), supporting that these layers were deformed after deposition. This deformation makes difficult to image well syn-rift structures like sediment wedges. In some locations, it appears that the uppermost rifting event occurs within the lower Pliocene (e.g. MEDOC-4, near CMP 44,500, fig. 5.7-b), and in other places, close to top Messinian (e.g. MEDOC-6, near CMP 7,000, fig. 5.7-b). The

base could not be determined well due to imaging issues and/or the younger deformation experienced in the area.

Southwards, the line MEDOC-15 (fig. 5.5-b) shows widely spaced faults with small offsets, which in some cases affect the entire sedimentary column. This tectonic characteristic occurs in seismic sections to the south, although in these cases, faulting density increases considerably. Here, the sedimentary layers have been uplifted an even folded in some points, as can be clearly appreciated in MEDOC-14 (CMPs 7,500 to 9,500, fig. 5.5-b) and MEDOC-13 (CMPs, 1,000 to 2,500, fig. 5.5-b). These structures can be followed until line MEDOC-4, where deformation and fault offset decrease, and fault density increases (fig. 5.7-b).

Towards the south, sections MEDOC-11, MEDOC-8 and MEDOC-9 do not provide representative images of this domain because they don't go far enough into it. However, the bathymetry of this area shows noticeable lateral variability of the structures along the margin. In line MEDOC-11 (fig. 5.5-b), faults are widely spaced and fault offset is larger. In addition, a volcanic layer with high reflectivity has been imaged within these grabens that could be partially obscuring the original structure. In contrast, in lines MEDOC-8 and MEDOC-9, faults are more frequent, and fault offset decreases again (fig. 5.5-c).

The southernmost profile crossing the area is line MEDOC-6. It presents some similarities with previously described sections, with many small faults fairly homogeneously distributed. However, in the eastern end, sedimentary deposits appear folded like in MEDOC-13. Another structural feature shared with MEDOC-13 is the presence of a family of small, densely spaced faults (or merely fractures) affecting only the Pliocene sediments. These structures are probably related with the folding processes (MEDOC-13, CMPs, 1,000 to 2,500, fig. 5.5-b).

This unusual tilting and folding of the sediments indicates contractional deformation. Unlike extensional normal faults, it seems to affect until the Pleistocene strata, supporting a recent period of tectonic activity. In addition, this phase of deformation has reactivated previous normal faults, reinforcing the inference of a recent tectonic reactivation of the region. These contractional structures, caused by compressional efforts, can be related with the transpressional/transtensional deformation inferred from bathymetry as discussed previously.

5.8. North Sicily Margin domain

This region lies to the south of the Tyrrhenian basin, and is bounded by the Cornaglia Terrace to the west and the Calabrian arc to the east. Its southern edge is delimited by the Sicily Island (fig. 5.1). from the thesis dataset, only the re-processed seismic section M28-b images the western part of this domain.

Compared to other regions, the bathymetry displays a rough seafloor with a great variety

of linear and irregular structures (fig. 5.8-a). The linear ones present a range of orientations, suggesting different origins for them. But within the area considered in this work, the main orientation of these structures is NE-SW.

It is worth noting that considering the seafloor depth observed at the bathymetry map, the crust should be thicker here than the surrounding areas to the north and west, and although Moho reflection depth is fairly constant in the MCS sections, and similar to the nearby Cornaglia Terrace (6-7 s TWT), basement thickness is larger (CMPs 10,500 to 15,000, fig. 5.8-b). The wide-angle velocity model of MN section shows that crustal thickness increases little with respect to the nearby Cornaglia Terrace (see the 3rd chapter).

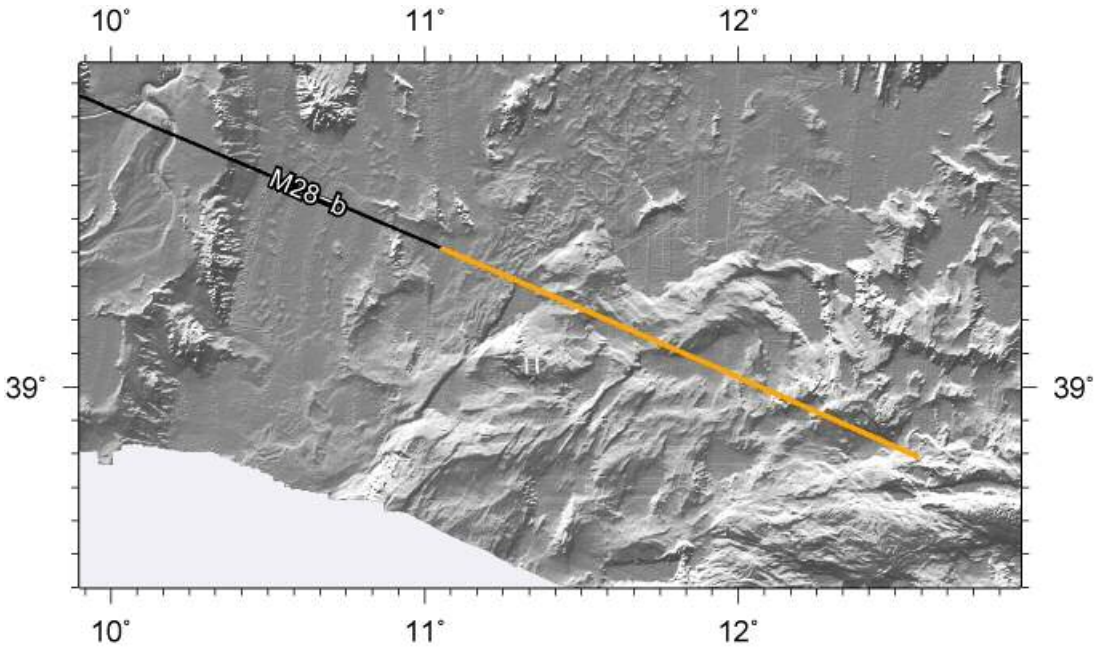

Figure 5.8-a: Local map of the North Sicily margin domain. Location of the segments used to work this domain (see figure 5.6-b) are highlighted in orange.

Faulting observed in section M28-b (fig. 5.5-b) across this domain can be related to the rough topography observed in the bathymetry (fig. 5.5-a). Most of these faults are east-verging structures, with the exception of the faults between CMPs 15,000 to 16,000 (fig. 5.5-b). Their syn-rift sediment wedges display highly variable thickness, but in general suggest an age between upper Tortonian to Messinian for these structures. Broadly, the faults have an heterogeneous distribution along the profile, and their offsets are quite variable. This feature resembles partially the Sardinia continental margin arrangement, supporting that both margins are conjugated, as can be inferred from the bathymetric map trend of structures.

The correlation between bathymetry and seismic data makes evident that the observed faulting processes are not enough to explain the irregular basement topography. We suggest that the rough relief may be partially explained by volcanic constructions, because there is a documented presence of volcanic edifices in this area (Cella et al, 1998; Lustrino et al., 2011;

Trua et al, 2007). At the eastern part of the seismic profile M28-B some layering with high reflectivity can be interpreted as lava flows (CMPs 16,000 to 17,000 and 18,000 to the end of the profile, fig. 5.5-b), supporting the inference of the presence of an old volcanic arc in this area, which became inactive as the migration of the subduction front evolved towards the current Calabrian arc.

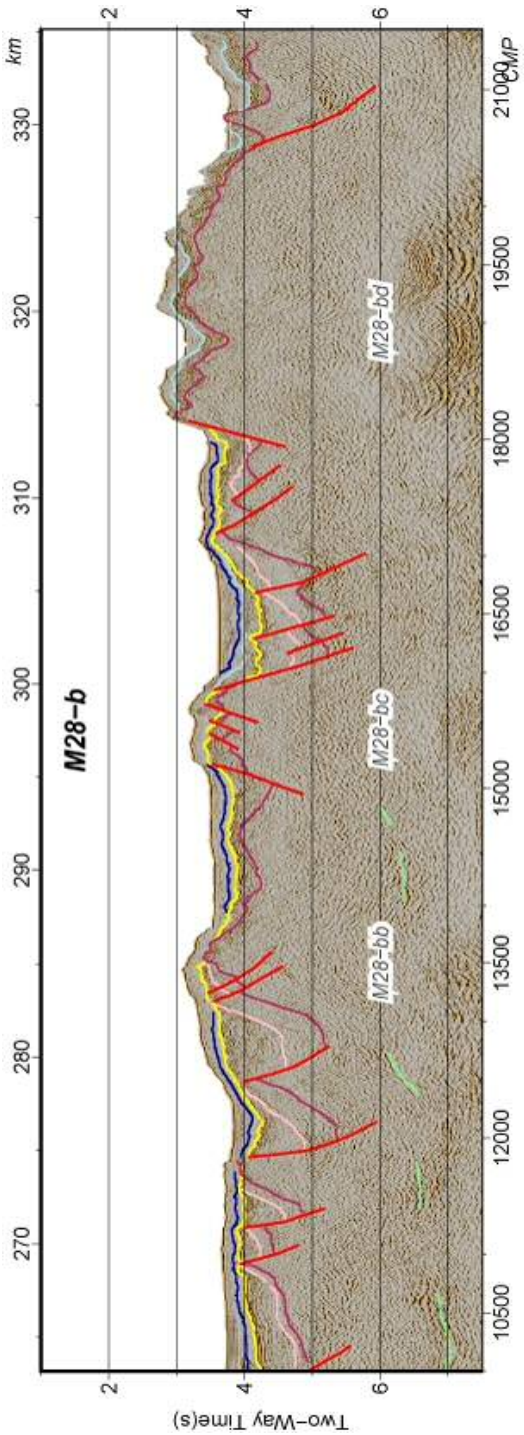

Figure 5.8-b: MCS section crossing the North Sicily margin. At the places were dredging data were available, it has been pointed out (Colantoni et al., 1981).

5.9. Discussion

Broadly speaking, two tectonic styles have been observed within the working area. The first one is the extensional structures related with the opening of the basin, which are well imaged all along the MEDOC lines. The second style is characterized by transpressional structures running along the eastern side of the basin, forming a shear zone near the shelf edge, and parallel to the Italian coast. The area affected by these structures does not display well-defined boundaries. It rather appears that deformation intensity increases towards the Italian peninsula. Most of these structures appear to reactivate the former extensional faults indicating that they belong to a posterior younger tectonic phase.

Extensional deformation has been observed all along the entire Tyrrhenian Sea, although its style changes throughout the basin varying for each tectonic domain.

In general, at the continental domains (North Tyrrhenian, Corsica-Sardinia basins and the Italian margin), extensional faulting is the only opening mechanism. Conversely, at the domains identified as magmatic crustal regions (the Campania and Cornaglia Terraces), magmatism also takes part of the opening. And at the North Sicily margin domain, which has been identified as near-arc region, volcanism was active during opening. Finally, in the central domain of the Magnaghi and Vavilov basins, extension occurred fundamentally by crustal break-up and mantle exhumation.

Faulting age varies depending on the domain. At the Sardinia and Corsica basins extension started during the lower Miocene and lasted until the Messinian. At the North Tyrrhenian domain and Cornaglia and Campania Terraces, syn-rift sediment wedges indicate an age ranging from Tortonian to lower Pliocene. The Italian continental margin domain opened from Messinian to lower Pliocene, although in the literature there are references to younger extensional events, but we interpret that they are related to the later transpressional/transtensional strike or oblique slip fault activity. In the North Sicily margin extension started during the Tortonian, and lasted until the Pliocene. Finally, in the Vavilov and Magnaghi basins, opening concentrated in a short time lapse during the lowermost Pliocene.

In contrast with the extensional tectonics, transpression/transtension has only been observed at the eastern side of the basin, along a shear zone parallel to the Italian coast. Therefore, those structures have only been observed in the Italian margin and at the easternmost sector of the North Tyrrhenian and Campania Terrace domains. Most of these structures probably reactivate inherited extensional structures within a new kinematic configuration caused by recent changes in the stress field. Previous work suggests an age ranging between Pleistocene (Casciello et al., 2006) and late Pliocene/Quaternary (Bartole et al., 1984) for this region.

5.9.1. Corsica-Sardinia Margin domain

The entire basement of the region is consist in continental crust, although the tomographic data obtained during the MEDOC survey suggest striking differences in the Moho depth, varying from around 15 km at the Corsica Basin (Moeller et al., 2013; 2014), to 25 km at the Sardinia basin (Prada et al., 2014), which implies the presence of thinned continental crust. Dredge samples include Variscan and Alpine basement rocks (Collantoni et al., 1981) all along the margin, indicating also a stretched continental crust type. The velocity models obtained by wide-angle data (Prada et al., 2014; 2015 and Moeller et al., 2013; 2014) agree with this hypothesis.

All tectonic structures observed in both basins are extensional, with the exception of a sub-vertical fault imaged at the MEDOC-8 near Baronie seamount and under the Orosey Canyon. Previous interpretations propose a transpressional lineament located in this region (Sartori et al., 2001), that might have been active during Neogene and could explain the different extension rates between the central and the southwest Tyrrhenian. However, our profiles do not show any evidence of deformation caused by this structure, which is relatively small compared to other faults in the region.

The rest of the structures show clear extensional kinematics, with well-developed syn-rift deposits associated to them at half-grabens. With the exception of the Orosey Canyon zone, the major faults are west-dipping structures at the flanks of the Mt. Etruschi in the Corsica Basin and of the Baronie Seamount in the Sardinia Basin. Locally, antithetic faults related to the major west-dipping structures have been observed (e.g. at MEDOC-4, near CMP 2,000, fig. 5.2-b). Previous works based on older seismic images (Sartori et al., 2001; Carrara, 2002) proposed also that the opening of the Sardinia basin is linked to a series of west-dipping main faults.

The age of the deformation in this area is given by the syn-rift sediment wedges, with strata showing a fan-shaped geometry towards the fault planes. However, the base of the syn-rift packages remains unidentified. Previous works suggests a Burdigalian age for the start of the opening at the Corsica Basin (Mauffret et al., 1999; Mauffret & Contrucci, 1999), and that rifting started somewhat later during the Serravalian at the Sardinia Basin (Sartori et al., 2001; Sartori et al., 2004). The end of the rifting processes has been interpreted as Messinian, or in some places during the lower Pliocene, as discussed above. However, the main activity phase ended during the Tortonian.

5.9.2. North Tyrrhenian region

As discussed previously in this chapter, the bathymetry map shows a similar seafloor

depth for the North Tyrrhenian domain and for the nearby Corsica-Sardinia margin, so crustal thickness across the entire domain should be similar. This is supported by the wide-angle seismic models that give a crustal thickness of ~15 km in this area. Moreover, velocity gradients obtained from this data support a continental crust nature for the basement in the whole domain (Moeller et al., 2013; 2014).

The main characteristic of this tectonic domain is a series of large, faulted blocks with north-south trending observed all along the area (fig. 5.1, 5.3-a). These blocks are bounded by normal faults related to the rifting processes. The sediments on syn-rift wedges provide an age of Tortonian to lower Pliocene for the extensional phase. According to literature, the basal discontinuity marking beginning of the syn-rift phase falls within the upper Tortonian (Trincardi & Zitellini, 1987; Moeller et al., 2013; and references therein), but at the MEDOC sections no clear structure has been observed allowing to locate accurately this limit. The top of syn-rift corresponds to the lower Pliocene, like in the Corsica sub-basin, as has also been observed by other authors (Moeller et al., 2013; and references therein). However, it must be noted that the main activity period probably occurred from Tortonian to early Messinian.

These faults display offsets in the seismic images that are considerably larger than those inferred from the bathymetry chart alone (fig. 5.3-a, b and c). Across the entire region, fault offsets are highly variable, but in general offsets become smaller approaching the Italian margin and towards the south, especially at the Sechi-Farfalla region. This fault-controlled block size difference outlines the boundary between the northern and the Sechi-Farfalla sub-domains.

The different tectonic style in the southern Sechi-Farfalla region can be explained by the different tectonic stresses that acted in each region, although all of them show a clear east-west component. In the north, the tectonic style is more heterogeneous while at the south the pattern is more homogeneous. Furthermore, the deformation in the North Tyrrhenian lasted until the lower Pliocene. And this may have had an impact on the final tectonic structure. It is also known that faulting of a thinner plate is resolved by closer spacing of faults that individually have comparatively smaller offsets (Gawthorpe et al, 2003; Soliva et al., 2006).

As mentioned above, the differences in the bathymetric relief compared to the southern domains (Cornaglia Terrace and Vavilov-Magnaghi area) have been taken as a natural boundary by several authors (Bartole et al., 1984) known as the “41º parallel lineation”, and has been described as a transfer zone. Although our data does not provide any evidence of this structure, the bathymetry map shows faulted blocks stop near this latitude (approximately around 40º30' to 41º). However, this change appears gradual and not an abrupt termination or truncation and can also be related with the different activity during the period of deformation between these two sub-domains.

5.9.3. Cornaglia Terrace domain

Faulting style changes along the region, and variation does not seem to be gradual. In this domain, like in the previous one, only extensional deformation structures have been observed.

In the whole region, seafloor is deeper than in the surrounding areas, showing a fairly constant depth, with the exception of the nearby Magnaghi Basin (fig. 5.4-a). As discussed previously, this characteristic indicates a fairly uniform crustal thickness. In addition, multichannel profiles show clear Moho reflections with a fairly constant depth beneath the top of the basement, supporting this interpretation (fig. 5.4-b). Moreover, faulting in the region is smaller compared to the amount of opening to create the terrace domain: in a general comparison with continental domains, faulting is scarce in the whole area, and cannot explain the observed structure. The seismic/crystalline basement displays a comparatively complex internal reflectivity. Furthermore, the wide-angle seismic models (Prada et al., 2014; 2015) support the presence of a magmatic basement. These characteristics together are typical of oceanic-type magmatic crust, and support an origin at a (back-arc) spreading center for the basement across much of the Terrace. Finally, the lack of clear pre-rift sediments is consistent with an opening driven to a large degree by the formation of a magmatic crust rather than continental crust extension and thinning.

Therefore, a complex spreading geometry interacting with continental rifting to the north along the area could have caused the variability in extensional style. However, due to the changes in kinematics, the timing of deformation for this area remains uncertain. The absence of clear pre- and syn-rift sediments in the whole area does not allow to date the start of the opening properly, but it is clear that some tectonic activity occurred during the Messinian. Most faults seem to have ended its activity during the lower Pliocene, although some others ended earlier, during Messinian times.

Although only Messinian and lower Pliocene sediments have been observed as syn-rift deposits, some indicators suggest that rifting in the area may have started during Tortonian. Because of the effect of the evaporitic salts obscuring the image of the underling sediments, the base of the syn-rift sediment package cannot be properly constrained, so that the presence of poorly constrained Tortonian sediments at the base is possible. This assumption is supported by the fact that it is difficult that the total amount of stretching observed (about 100 km at the MEDOC-6 and 8, fig. 5.4-b) was attained only during early Messinian times. Therefore, even if no clear sediment packages have been identified, it is possible that the region was fundamentally formed during Tortonian to earliest Messinian time, so that the main rifting phase could have perhaps happened during Tortonian times.

5.9.4. Vavilov and Magnaghi Basins region

The Vavilov and Magnaghi Basin domain is the area with the best coverage of MCS profiles shot during the MEDOC survey (fig. 5.5-a). These sections were acquired at different latitudes to image the crustal rupture at different locations, in order to get a time evolution of the process.

From north to south, crustal break-up becomes progressively more complex. At the northern sections faulting has only been observed at the basin flanks, while towards the south, especially at MEDOC-6 (fig. 5.5-c), several fault blocks and volcanic bodies have been observed along the area. In seismic images, the offset of these faults is smaller than that observed in previous domains.

In bathymetry, in spite of these local fault blocks and volcanic edifices, the area generally shows a smooth flat topography. In the central region, where the seafloor is consistently smooth (fig. 5.5-a), peridotites were drilled at ODP site 651 (Kastens & Mascle, 1990; Bonatti et al., 1990). This fact, together with the fairly constant depth in most of the area, the lack of Moho reflection in the MCS images and the WAS data, as well as the strong vertical velocity gradient in the seismic velocity models (Prada et al. 2014; 2015) have been interpreted as indicative of large-scale mantle exhumation in this domain. Considering the smooth seafloor relief, has been proposed that the entire domain shares a common origin. Wide-angle seismic velocity models by Prada et al. (2014; 2015) are consistent with a basement made fundamentally of altered mantle rocks.

In addition, in some locations volcanism seems to have taken advantage of inherited weak lineaments or fractures to rise up, but interestingly, the main faulting is restricted to the basin flanks and not to the area of exhumation.

Therefore, faulting at the domain's flanks is probably related to the final continental crust break up leading to mantle exhumation. These bounding faults present large fault slips, and most of them don't seem to present any related syn-rift sedimentation. The absence of syn-rift wedges suggest a fast velocity for the faulting or alternatively low sedimentation rates during its activity. Taking into account the notable thickness of the sedimentary deposits in these basins (fig. 5.5-b and 5.5-c), the latter option appears unlikely. In addition, this area is the deepest region of the entire basin and at least pelagic sedimentation should have occurred simultaneous with faulting, thus the rupture appears to have been an abrupt event. The small, potentially syn-tectonic rift-related sediment wedges observed in line MEDOC-6 (around CMP 29,500, fig. 5.5-c), support an early Pliocene age for the opening of these faults. However, dating from these syn-rift sediment wedges have to be taken with caution because later episodes of volcanism could have tilted and or intruded the sediments. Thus, this entire region

appears to have formed during a short time lapse, supporting the hypothesis of a high faulting velocity, rather than a low sedimentation rate, during its formation.

5.9.5. Campania Terrace region

The Campania Terrace boundaries are clear in the seafloor relief shown in the bathymetric map (fig. 5.1 and 5.6-a), because of its uniform tectonic character and the contrast in relief with the surrounding areas.

This region coincides approximately with the Campania Terrace domain defined by Prada et al. (2014; 2015), which has been identified as a magmatic crustal domain based on the seismic velocity models. But in fact, this crustal domain extends towards the north, into the Italian continental margin region where important magmatism has heavily intruded the extended continental crust (Prada et al., 2015).

Within the Campania Terrace no clear syn-rift sedimentary deposit has been observed in the seismic images, and apparently the faults identified accommodate very limited extension. Indeed there are two fault families. The first one seems to be related with salt tectonics, rather than with extensional activity. Therefore, they were probably generated after the salt sedimentation, and probably acted during the Messinian-Pliocene period (MEDOC-6, CMPs 15,000 to 17,000; fig. 5.6-b). The second group cut the basement and the sedimentary column until the top of the Messinian or even the intra-Pliocene discontinuity. However, the total amount of fault displacement is not enough to explain the extension in the area.

Therefore, as in the conjugate Cornaglia Terrace, there are few extensional structures along this domain, and opening of the area must have been accommodated by magmatism forming new crust. The calibration of the age of these processes is difficult, but the magmatic activity is pre-salt deposition. Hence the age is possibly uppermost Tortonian to earliest Messinian so that the evolution of this region resembles the Cornaglia Terrace one.

5.9.6. Italian Margin region

Seafloor depth of this region indicates a crust that is generally thicker than the nearby Campania Terrace and North Tyrrhenian domain (fig. 5.7-a). The wide-angle seismic velocity models display a crustal thickness of ~15 km (Prada et al., 2014; Moeller et al., 2013), and indicate a continental nature for the basement in this domain. The exception is a small region at the western part of the central area, where abundant magmatic intrusions or magmatic underplating of the continental crust, gives a different crustal nature than the rest of the region. It has described in the previous section as the northern extension of the Campania Terrace crustal domain (Prada et al., 2015).

The MCS sections covering this region show at least two distinct deformation phases (fig. 5.7-b). The first phase is related with extensional processes, while the second suggest compression or strike-slip tectonism, and appears to act mainly reactivating inherited structures. It has to be taken into account that the area has developed in the vicinity of the Apenninic chain, and thus near that subduction-related structural arc. So that the stress field operating here may have been different from that acting in the rest of the basin.

In this area sedimentary deposits are thin in comparison with the other regions. No Tortonian sedimentation has been interpreted, and Messinian deposits are thinner than at the rest of the basin (fig. 5.7-b). Because of this limited information, it is difficult to define the deformation phases and the age of their activity period, although some information from previous studies helps to define it.

According to Bartole et al. (1984), compressional deformation related to the Apennine orogenesis ended in the uppermost Messinian in this area, and until the lower Pliocene the area was affected by subsidence after the end of orogenic process. It corresponds to the first extensional phase developed on this area (Bartole et al, 1984), and poorly developed syn-rift sediment wedges on our sections indicate an age between Messinian and lower Pliocene, in agreement with previous work. This tectonic phase is more clearly observed in the western sector of the domain, where the younger deformation phase is weaker than in the rest of the domain, and does not overprints the structure.

A subsequent tectonic phase deformed the region, but during this phase, no extensional tectonics took place, rather folding and strong tilting of sediment deposits occurred. Because of this deformation, topographic highs change laterally along the margin, and sedimentary layers are tilted with a geometry that indicates uplift and folding due to the locally compressional stresses, like those observed at the eastern side of line MEDOC-15 (CMPs 1,000 to 4,000, fig. 5.5-b) or MEDOC-17 (CMPs 500 to 2,000, fig. 5.3-b). The deformation results in elongated structures roughly parallel to the coastline, well displayed in the bathymetry data. These structures change in tectonic style abruptly laterally along the margin, from compressional to extensional type, forming along the same fault system graben-like depressions, also clearly visible in the bathymetric map. Thus the deformation patterns appear to indicate a tectonic regime of transpression grading laterally into transtension in a broad strike-slip fault zone system.

Apparently, this tectonic stage has lasted from lower Pliocene to recent times. Previous work has interpreted it in two different deformation phases. The first one corresponds to extensional processes that occurred from lower Pliocene to middle Pleistocene, which progressed in an approximate NW-SE direction leading to the opening of the nearby Marsilli basin (Bartole et al, 1984). The structures generated during this extensional phase were

interpreted to run oblique (NE-SW oriented) to the strike of our profile, but no clear evidence has been observed in our seismic images or bathymetry maps. Based on land fieldwork, it is proposed another deformation phase that started during middle Pleistocene and lasted until recent times (Casciello et al., 2006). It consists of an - at least locally - transpressive phase. This stage, which has been described onshore, could be the deformation associated to the elongated structures parallel to the coastline observed in our data along the entire domain. These structures reactivate previous normal faults, changing its kinematics and deforming older syn-rift sediment wedges.

5.9.7. North Sicily Margin domain

In the North Sicily Margin domain the observed tectonic structure resembles the Sardinian margin one. This fact supports that both margins are probably conjugated, although opening in between is probably limited to the region of the intervening Cornaglia Terrace (fig. 5.8-a).

Extension in this area occurred through large-scale normal faulting, with km-scale offset, which are similar to faults described in the Sardinia margin. However, the lack of major faults towards the easternmost sector imaged on the M28-b section (fig. 5.8-b), and the presence of the volcanic deposits, may indicate that in this area extension took place thanks to a combination of processes, or that volcanic activity has obliterated the structures related to faulting. In fact, this domain has been interpreted as a continental crust intruded by limited arc volcanism based on the WAS modelling results along the MN line (see chapter 3).

In this domain, syn-rift sedimentary wedges clearly support a Tortonian to Messinian age for the extension, although the base of these deposits is poorly imaged and the beginning of extension might be older. The age of the volcanic activity is given by the presence of Tortonian and Messinian deposits below the lava flows (CMPs 18,000 to the end of the section, fig. 5.8-b), which suggest that these deposits were emplaced in a formerly stretched continental-type crust, later than Messinian times. The structure observed in wide-angle seismic velocity models support this interpretation.

5.10. Kinematic evolution

The MEDOC data analysed here provide a detailed coverage to produce a novel overview of the formation of the Tyrrhenian Basin through the time. Its evolution has been divided into three main geodynamical stages (fig. 5.9).

The first stage corresponds to the formation of the Corsica and Sardinia basins. The main faults opening this area are large-scale, west-dipping structures with synthetic faults related to them, and in some cases with antithetic faults slipping for long offsets and making very large

half grabens.

According to published work, the opening of these two basins began during the Burdigalian in the Corsica basin (Mauffret et al., 1999; Mauffret & Contrucci, 1999), and during the Serravalian in the Sardinia basin (Sartori et al., 2001). Although in both cases some minor fault activity lasted until lower Pliocene, according to MEDOC data, the main activity phase ended during the Tortonian, and most of the faults ceased its activity at that time.

However, it is also discussed if the Corsica basin formation might have started even earlier, during the Oligocene, within a different kinematic context (Mauffret et al., 1999; and references therein). In this context, the basin began as a piggy-back basin related to the subduction front, while the opening was focused in the Liguro-Provençal basin (fig. 5.9). Later on, during Burdigalian time, the eastward migration of the Corsica-Sardinia block ended, and the locus of extension jumped towards the east, towards the Corsica basin. Therefore, the stress distribution changed to an extensional setting (Faccenna, 2001), and in this moment the extensional tectonics observed in the Corsica basin started.

In addition, within such a model the Italian and Sicilian margins should be the conjugated to the Corsica and Sardinia basins according to their geographic distribution. Therefore, they should have formed simultaneously. However, in the Italian margin, the scarce pre-Messinian sedimentation makes the correlation difficult. This absence of pre-Messinian sediment can be explained by two different reasons. The first one is that they actually exist, but have not been identified because of the lack of dredging data and/or drills to suitably calibrate the sediment ages. Alternatively, the proximity of the area to the subduction front can imply a different stress field than its conjugated, so sedimentation of these deposits could be somehow different or even absent. The two possibilities are potentially plausible and fit the context. Bartole et al. (1984) argues about a compressional context until the Messinian.

However, the MEDOC images are of sufficient quality to demonstrate that the pre-Messinian, if present at all in the Italian margin, can hardly extend back in time to the early opening of the Corsica Basins and thus that phase must be independent of the extensional phase that opened the Italian margin.

The images in the Sicily margin show that the syn-rift sedimentation is dominantly Tortonian to Messinian, but could extend back as much as Serravalian in the deeper part of the un-calibrated column and thus it might be of similar age or somewhat younger of the Sardinia basin, and there is a clear similarity between both margins in the bathymetric data. Thus, in conclusion, correlation between both sides of the Tyrrhenian basin but should be considered with caution.

The second stage started during the Tortonian, when the locus of extension migrated

eastwards. This shift has been related with a migration of the subducting slab towards the east (Faccenna et al., 2001; Faccenna et al., 2007). At this time the main rifting phase left the Corsica and Sardinia basins, and extensional processes started to open the North Tyrrhenian domain and the Campania and Cornaglia Terraces, although some faults still remained active in the Corsica and Sardinia margin at that time, but with minor activity. Extension in the North Tyrrhenian and the Campania and Cornaglia Terraces lasted until the lower Pliocene, although several major normal faults worked only until upper Messinian.

It should be noted that, in spite of this trench migration, the North Tyrrhenian basins support a quite similar stress distribution compared to the neighbouring areas of the Corsica and Sardina basins. They show a similar structural arrangement (north-south trending) and shapes (elongated depocenters), but with smaller sizes. This is an indication that the driving forces of the opening changed locus but their direction remained the same, because the orientation of the structure remained roughly north-South.

Looking at the seafloor relief, it becomes evident that the North Tyrrhenian domain suffered less extension than the southwards Campania and Cornaglia Terraces (fig. 5.1). However, extension timing for both areas is similar, so that the extension velocity should be higher towards the south.

This effect may explain the different mechanisms working on each area. In the North Tyrrhenian only extensional faults have been imaged, suggesting that only rifting processes took place there, while in the Cornaglia and Campania Terraces, the high reflectivity of the crust and the Moho reflector, together with wide-angle seismic velocity models (Prada et al., 2014; 2015) suggest a combination of faulting and magmatic processes. Thus, the new magmatic crust formed in the area provides a mechanism to account for the different extensional rates.

Finally, the third stage started during the lower Pliocene, when the extensional efforts changed again with the locus of extension migrating area one more time.

As discussed previously, this migration resulted in an abrupt displacement of the rift axis, as suggested by the scarcity of syn-rift sediment wedges and the important thickness of the lower Pliocene, which based on geometry has been identified mostly as a post-rift sedimentary unit. This assumption is supported by Faccena et al. (2007) argument that relates the fast displacement occurred with the rupture of the slab beneath the Sicily Channel region. As a result of this tear, the slab retreated rapidly to a steeper angle dragging the upper plate towards the SE. This process made the opening rate faster, and that produced a crustal rupture that splitted the Cornaglia and Campania Terraces area, which formed a single unit together until this moment.

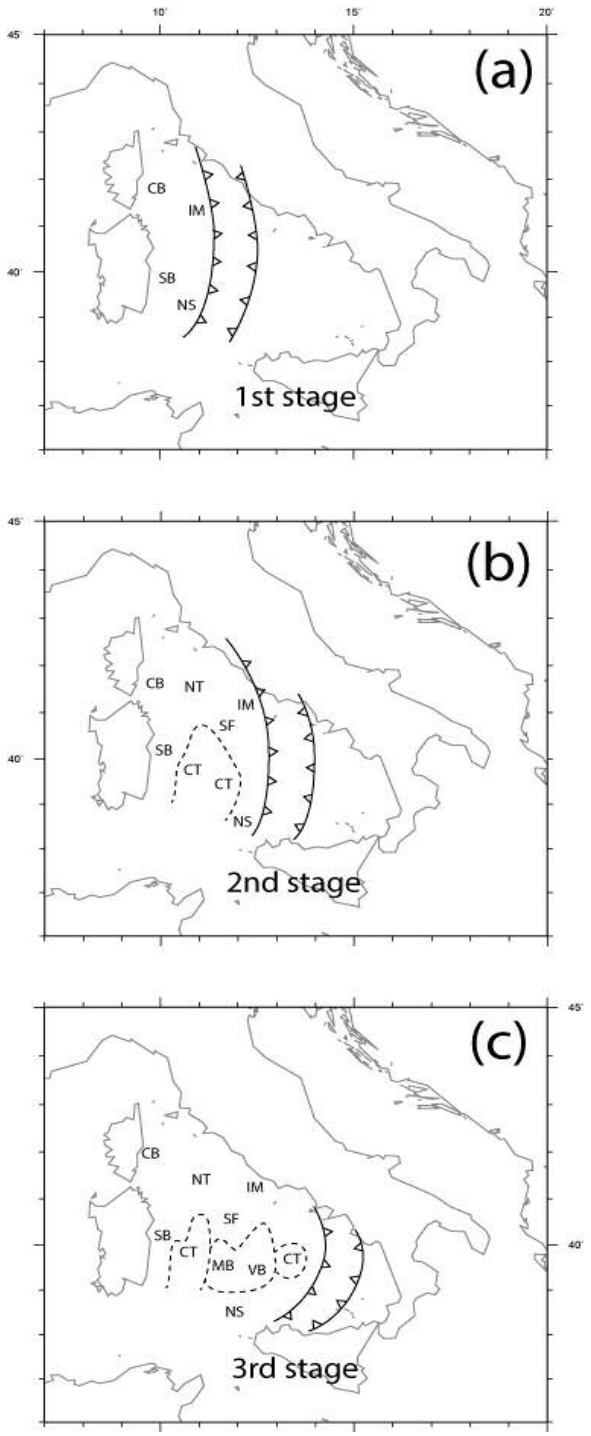

Figure 5.9: The three main stages of the evolution of the basin described in thee text. Notation of the areas: CB:Corsica Basin, SB: Sardinia Basin, NT: North Tyrrhenian, SF: Sechi-Farfalle region, IM: Italian Margin, NS: North Sicily margin, CT: Cornaglia Terrace, CT: Campania Terrace, MB: Magnaghi Basin, VB: Vavilob Basin, MB: Marsili Basin.

This event triggered the opening of the Magnaghi and Vavilov basins. Across this domain ODP drill data (Kastens & Mascle, 1990; Bonatti et al., 1990), and the MEDOC WAS velocity models support that opening caused widespread mantle exhumation (Prada et al., 2014; 2015). Therefore, unlike during the former stage, no initial magmatism associated to the opening is observed in this second stage. However, mounting evidence shows that magmatism

occurred mostly after mantle exhumation in the area (e.g. Vavilov and Magnaghi Seamounts), as indicated by the widespread presence of basaltic ridges and intraplate volcanic edifices (Sartori et al., 2004; Lustrino et al., 2011). However it remains a question whether they are directly related with the opening. This opening system (crustal break-up and posterior volcanism) may have been very recently repeated at the Marsili basin.

At last, another point to be considered is the roughly triangular shape of these basins. Like for the former opening stage, we can presume that it reflects different extensional rates at different latitudes.

In conclusion, the locus of the opening and deformation migrated towards the east in abrupt jumps. This migration was directly controlled by the slab evolution, which rolled back episodically (Faccenna et al., 2001; Faccenna et al., 2007). Each change in the stress frame led to a new stage, and the rifting locus migrated to a new location starting the formation of new domains. The stretching velocities of the upper plate probably determined the mechanisms working on each region.

6.CONCLUSIONS AND OUTLOOK

6.1. Crustal domains from the Sardinia to the NW Sicily margins

- Four crustal domains have been characterized along the south-west of the Tyrrhenian basin based on geomorphological, Vp structure, gravity data and tectonic structure. The model obtained from Vp data show minor lateral changes along the section. In contrast, there are important crustal thickness and tectonic fabric variations. At the Sardinia continental margin, the crust is 22 km thick, thinning to 7 km thick next to the Cornaglia Terrace, where a thin basement is overlaid by a comparatively thick Messinian evaporitic package. Towards the east, at the northwest Sicily Margin, crust thickens to ~12 km thick.
- Basement nature has been assessed integrating the velocity model and gravity data together, and combining it with information from limited available ground sampling. Results support a basement mainly constituted of continental crust, which has been locally intruded by subduction-related magmatism. The geophysical results support that a minor amount of magmatic intrusions may have locally occurred in the lower crust, linked to back-arc extension.
- The seismic tomography results support that the basement beneath the southern Cornaglia Terrace is made of continental-type rocks. These results contrast with the tomographic analysis along lines the E-F and G-H MEDOC transects acquired across the north segment of the Cornaglia Terrace, were magmatic crust formed by back-arc spreading had been previously interpreted (Prada et al., 2014, 2015).
- According to the geodynamic evolution of the Tyrrhenian subduction system, the lateral interaction of landmasses (Italian Peninsula and the Sicily Island) with the trench reduces the width of the subducting oceanic slab, therefore it results in turn in variations on the style of back arc extension and consequently in spatial variations of back-arc magmatism. This way, we suggest that subduction of continental blocks slowed down slab roll back and progressively stopped. Hence back arc extension in the northern and southern Cornaglia slowed, while in the central area extension continued due to the uninterrupted retreat of the slab towards the E-SE, which potentially triggered the production of partial decompression melting in the area.

6.2. Basin-scale stratigraphy

- The unit mapped as the uppermost basement in seismic images has no petrological significance. Its composition is possibly heterogeneous across the area of study, which is supported by previous works and available sampling. This seismic basement may contain pre-rift sediments, previously described at the Corsica and Sardinia basins. They consist in pre-Tortonian Miocene sediments, while no evidence of them exist at the rest of the study area. Thus, can be deduced that the rest of the basin should have formed in younger times.

- The onset of rifting occurred within the Tortonian time. This unit is imaged only in continental domains in local depocenters, typically half-grabens, with the exception of the Italian continental margin region. Although in this case, the absence of this unit should be taken with caution, because it can be related with imaging issues in shallower areas, or even with the recent transpression/transtension deformation suffered in the area. During the Tortonian occurred the main rifting pulse, in spite of the apparent scarce presence of this unit everywhere.
- The Messinian unit has a widespread distribution across the basin, acquiring its maximum thickness at the Cornaglia Terrace. In contrast it is not present at the nearby Vavilov and Magnaghi Basin area pointing out that they are younger. The unit has been divided into three sub-units. The basal one - M1 -is poorly defined almost everywhere, and seems scarcer than the upper sub-units. Possibly, not all depocenters and faults observed currently existed during early Messinian. Next, the M2 sub-unit corresponds to the evaporitic deposits with diapiric behaviour. It has only been described at the back-arc magmatic-type basement regions, indicating that they were the flooded areas during the Messinian crisis. Finally, the M3 sub-unit corresponds to the latermost Messinian, and its uniform well-layered reflective character is easy to identify marking the top of the Messinian across much of the basin.
- At last, both Pliocene sub-units and the Pleistocene are ubiquitous across all the study area, including the Vavilov and Magnaghi basin. Opening of these two basin occurred in a short time lapse during the uppermost Messinian (Magnaghi Basin) to the lowermost Pliocene (Vavilov Basin).
- The basement nature can be taken as a proxy of the tectonic processes that worked on the area. If Moho has been imaged, some type of crust should be present. Continental crust stretched by rifting displays typically faint, discontinuous Moho, while back-arc areas formed by magmatic oceanic-like crust accretion display strong and continuous Moho reflection. Finally, where no Moho reflector has been imaged, crustal break up and the resulting mantle exhumation occurred. All these mechanisms did not work at the same time; they rather evolved stepwise throughout the time.
- Within the sedimentary record, several stratigraphic discontinuities are directly related with changes occurring during basin evolution. The first is the one corresponding to the onset of the rifting due to the displacement of the stress field, described in the literature as the "L" discontinuity. It belongs to the Tortonian time, probably to the upper Tortonian. The end of the rifting is marked by the middle-Pliocene discontinuity – the "X" unconformity -, which coincides with another jump of the extension locus towards the east. This change leaded to the end of rifting processes and the beginning of magmatic – back-arc - crust formation at the Cornaglia and Campania Terraces. At last, there is another tectonic discontinuity occurring at the Pliocene-Pleistocene limit,

which responds to the jump of the extension from the Vavilov Basin to the Marsili Basin, to the southeast Tyrrhenian.

- Finally, there is a fourth stratigraphic discontinuity not related with the tectonic evolution of the basin but it is a well-known marker all along the Mediterranean. It is the Messinian Crisis horizon, which belongs to the uppermost Messinian. In the literature it is also known as "Y" discontinuity (or "M" according to some authors).

6.3. Tectonic framework

The interpretation of the tectonic structures provides a novel overview of the basin evolution throughout the time. Its evolution has been divided into three main geodynamical stages.

1. The first stage corresponds to the formation of the Corsica and the Sardinia Basins. Their opening occurred during the Burdigalian in the Corsica Basin, and during the Serravalian in the Sardinia Basin. In both basins the main activity phase ended during the Tortonian and most of the faults ceased its activity at that time, although few faults worked until lower Pliocene.
    - During this stage, the Italian and Sicilian margins should be the conjugated to the Corsica and Sardinia basins according to their geographic distribution. Therefore they should have been formed during the same period.
    - However, scarce pre-Messinian sediments have been observed in the Italian Margin. Thus, the margin correlation become difficult. This lack of pre-Messinian strata could be explained by two possibilities. The first one is that these sediments actually exist, but they have not been properly identified because to the lack of dredging and/or drilling data to suitably calibrate them. Alternatively, the short distance between the margin and the subduction front could make that the stress field in this part of the margin differ from that acting in its conjugated margin. Therefore sedimentation of these deposits could be somehow different or even absent. Both possibilities are potentially plausible and fit the context. Therefore, both margins could have likely suffered different tectonic processes during this period.
    - Meanwhile at the northwest Sicily Margin, the syn-rift sedimentation is predominantly Tortonian to Messinian, but rifting probably started earlier as much as Serravalian, thus it might be similar in age as the Sardinia Basin region. In this case the margin correlation is clearer than with the Italian Margin.
2. The second stage corresponds to the opening of the North Tyrrhenian region and the Cornaglia and Campania Terraces. It started during the Tortonian when the extension locus migrated eastwards from the Corsica and Sardinia Basins. Extension lasted until

the lower Pliocene, although several major normal faults worked only until upper Messinian.

- Tectonic structures in the bathymetry suggest a quite similar stress field distribution in the North Tyrrhenian region compared to the neighbouring areas of the Corsica and Sardina basins, in spite of the trench migration: there are similar structural arrangement (north-south trending) and shapes (elongated depocenters), but with comparatively smaller sizes. This fact could be interpreted as an indicator that the driving forces of the opening displaced their locus but their direction remained the same.
- The seafloor relief also shows that the North Tyrrhenian region suffered less extension than the southwards Campania and Cornaglia Terraces. However, extension timing for both areas is similar, so that the extension velocity should be higher towards the south.
- This last observation can explain the different mechanisms working on each region. In the North Tyrrhenian only extension during rifting processes occurred, while southwards, in the Cornaglia and Campania Terraces a combination of faulting and magmatic processes accounted for the opening. Thus, the new magmatic crust formed in the area provided the mechanism to account for the different extensional rates.

3. Finally, the third stage corresponds to the Magnaghi and Vavilov Basins formation. It started at the lower Pliocene with a new jump of the locus of extensional efforts towards the east, and lasted until the Piocene-Pleistocene boundary.

    - The scarce syn-rift sedimentation points out to an abrupt displacement of the extensional locus, and the considerable thickness of the lower Pliocene deposits, which have been identified mostly as a post-rift sedimentary unit. This hypothesis agrees well with Faccena et al. (2007) argument that relates the fast displacement to a slab tearing beneath the Sicily Channel region. This would have lead to an abnormally abrupt retreat of the slab that drag in turn the upper plate towards the south-east abruptly.
    - From this last point it can be proposed that an acceleration of the opening rate occurred, and produced a crustal rupture that split the Cornaglia and Campania Terraces area, which was one unit together until this moment. This event triggered the opening of the Magnaghi and Vavilov basins.
    - Crustal rupture led to widespread mantle exhumation. This interpretation is strongly supported by the core data of ODP site 651, and the WAS results from the MEDOC survey.
    - Therefore, unlike the former stage, no initial magmatism related to the opening has

been observed. But some evidences indicate that local magmatic intrusions occurred overlapping with or following mantle exhumation in the area (e.g. Vavilov and Magnaghi Seamounts) generating basaltic ridges and intraplate volcanic edifices. However it remains a question whether they are directly related with the opening.

- Finally, the roughly triangular shape of these basins is probably related with different extensional rates at different latitudes.
- At the Pliocene-Pleistocene boundary, the extensional locus migrated again related to another change in slab subduction dynamics, and started the formation of the Marsili Basin southeastwards of the study area. This opening system (crustal break-up, mantle-exhumation and further volcanism) may have been very recently repeated there.

6.4. Summary of basin formation evolution

The figure 6.1 is a schematic representation of the evolution of the basin formation. As mentioned previously, the Tyrrhenian back-arc system formed within a context of slab roll-back, which started during the lower Oligocene with the formation of the Liguro-Provençal Basin. But during the late Oligocene – early Miocene, the subducting slab retreat came to a halt. This pause has been related with the arrival of the slab at the 660 km transition zone (upper-lower mantle transition). During a time interval the slab was hold back in this interface while subduction continued slowing down. In this context, the Tyrrhenian Basin formation started during the early Miocene with the formation of two epi-sutural basins: the Corsica and the Sardinia Basins (fig. 6.1-a), although it could be possible that that early phases of this first stage started during the uppermost Oligocene in the Corsica Basin area. Also during this phase, the conjugate Italy and North Sicily Margins underwent compressional efforts related with the subduction processes.

Figure 6.1: Schematic evolution of the basin. Orange areas represent continental extension by rifting. Blue areas correspond to oceanic-like crust formation. Green areas represent exhumation of the mantle. Finally, purple ones represent areas affected by transpressional/transtensional deformation. The areas that remain blank are the inactive areas. Areas with striped pattern represent almost inactive processes or where two processes work at the same time. The magmatic events marked at the figure are those described at the chapter 4 (section 4.2.6), that could be related with magmatism observed at our sections. They are represented by red dots (squares for intraplate volcanism, triangles for MOR basalts, and circles for subduction-related volcanism). 1:Cornacya Seamount, 2: Vercelli Seamount, 3: Elba-Pianosa Ridge, 4: Ancheste Seamount, 5: Anchise Seamount, 6:Pontine Islands, 7: Quirra Seamount, 8: Gortani Ridge, 9: Magnaghi Seamount, 10: Vavilov Seamount, 11: Marsili Seamount. Notation of the areas: CB:Corsica Basin, SB: Sardinia Basin, NT: North Tyrrhenian, SF: Sechi-Farfalle region, IM: Italian Margin, NS: North Sicily margin, CT: Cornaglia Terrace, CT: Campania Terrace, MB: Magnaghi Basin, VB: Vavilob Basin, MB: Marsili Basin.

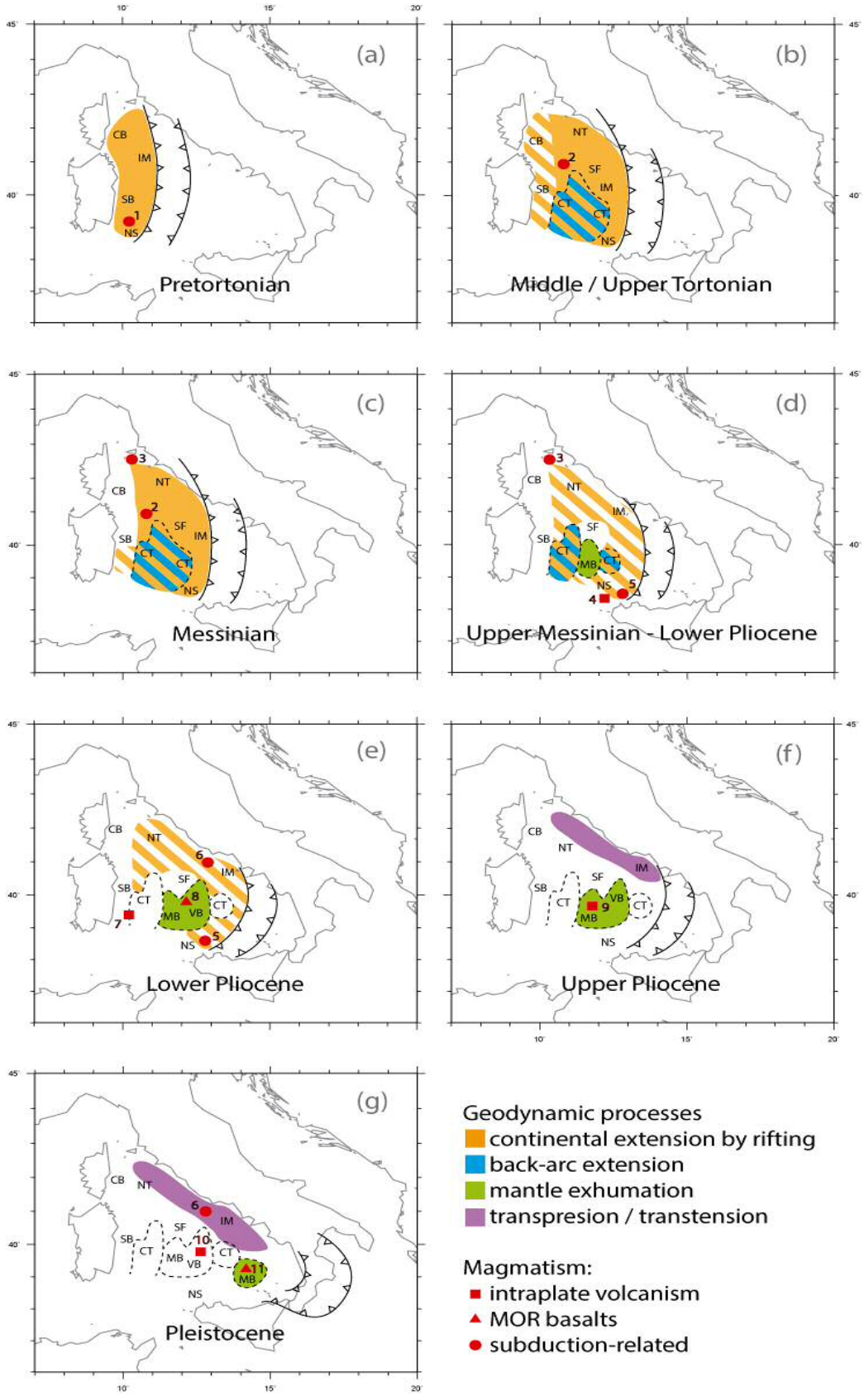
(a)
Pretortonian
(b)
Middle / Upper Tortonian
(c)
Messinian
(d)
Upper Messinian - Lower Pliocene
(e)
Lower Pliocene
(f)
Upper Pliocene
(g)
Pleistocene
CB
IM
SB
NS
NT
SF
CT
MB
VB
Geodynamic processes
continental extension by rifting
back-arc extension
mantle exhumation
transpresion / transtension
Magmatism:
intraplate volcanism
MOR basalts
subduction-related

Based on Faccenna et al., (2004; 2007), during the Tortonian, the slab rearranged itself at the upper-lower mantle discontinuity and acquired a steeper dip. Hence, the slab roll-back resumed and the trench migration changed to higher velocities in comparison with the Oligocene ones. In addition, Africa-Europe convergence direction changed becoming more parallel to slab subduction direction. This fact also contributed to the fastening of the slab roll-back.

Hence, rift axis migrated and extension started at the actual North Tyrrhenian region, and at the Cornaglia and Campania Terraces (fig. 6.1-b). Although at the Corsica and Sardinia Basins some extensional processes remain still active, but in these cases the geodynamic context changed to compressional related to the subduction front, to extensional on the back-arc context. This change in the extensional setting was recorded by the stratigraphyc "L" discontinuity which marks the beginning of the rift.

At the North Tyrrhenian, rifting processes led to extended continental crust with rotated blocks with a north-south trend, pointing an E-W extension direction. While southwards, at the Cornaglia and Campania Terraces extensional processes appear to be more complex, with continental extension in the south of the Cornaglia, while at the center, at the north and at the Campania Terrace back-arc magmatic crustal accretion took place. Instead, in the southern Cornaglia Terrace a limited amount of magmatic crustal accretion might have happened. This north-south variability of the extensional processes has been related with the interaction of landmasses with the subduction front, reducing the width of subducting slab. This fact triggered in variations on the style of back arc extension and consequently in spatial variations of back-arc magmatism.

This situation lasted until the upper Messinian (fig. 6.1-c), although at the Corsica and Sardina Basins extension ceased almost everywhere during the Tortonian, with the exception of some location in the southern Sardinia Basin.

During the uppermost Messinian a change in the tectonic frame happened. Extensional processes slowed down everywhere, and even in the continental regions of Sechi-Farfalle and the Sardinia Basin stopped completely (fig. 6.1-d). This change has been related with the tearing of the subducting plate below the Sicily Channel region, which triggered a sudden retreat of the slab towards the east, giving a migration of the extensional locus and a crustal break-up of the overriding plate, which subsequently leads to the formation of the Vavilov and Magnaghi Basins.

The Magnaghi Basin may have started its opening at the uppermost Messinian, as suggested by the pre-rift Messinian evaporites observed at the western half of this basin (fig. 6.1-d). In a short time lapse, migration extension evolved towards the east and the Vavilov

basin opened at the lower Pliocene (fig. 6.1-e). At the same time, extensional processes at the continental and back-arc regions ceased completely, while the crustal break-up in the Vavilov and Magnaghi Basins led to widespread mantle exhumation. It implies that the former magmatic extensional regime changed to an essentially amagmatic extension.

This tectonic rearrangement has been recorded at the sedimentary column by the so-called "X" discontinuity. It is a basin-scale regional discontinuity, which marks the end of the syn-rift sequence at the continental areas during the lower Pliocene.

Later, at some point during the upper Pliocene transpression-transtensional tectonics started along the Italian Margin region (fig.6.1-g). There, some former extensional structures were reactivated as compressional structures. Finally, at the Pliocene-Pleistocene transition another abrupt change in the tectonic setting occurred. In this case, it was related with a slab tearing below the Italian Peninsula, which again caused a fast retreat of the slab and a new jump in the extensional locus of extension, leaving behind the magmatic arc formed during the previous stage, which stood at the Issel Bridge region (Malinverno, 2012). As in the former case, a new basin opened: the Marsili Basin (fig. 6.1-g). In this episode, the direction of extension changed from E-W to fairly NW-SE related with this slab tearing. Therefore, it become more parallel to the slab subduction direction and thus roll-back fastened. Like in the former cases, this evolution is recorded by a stratigraphic discontinuity across the basin.

In summary, the Tyrrhenian opened stepwise with the extension locus moving towards the east and later on towards the south-east. This migration was directly controlled by the slab evolution, which rolled back episodically dredging and stretching the overriding plate. Each change in the stress field led to a new tectonic stage and the rifting locus migrated to a new location starting the formation of new domains. The stretching velocities of the upper plate – controlled by the slab retreat - probably determined the mechanisms working on each region.

6.5. Outlook

Data obtained during the MEDOC survey provide novel information about tectonic and sedimentary processes as well as the geodynamic evolution of the Tyrrhenian Basin. However, the findings have opened new questions. In this section some new petrological and geophysical information that would help to advance in the understanding of a number of these open questions is sketched.

Drilling and dredging

In the back-arc magmatic domains there is scarce seafloor sampling in contrast with the surrounding continental areas, where a significant number of dredging samples exist (Colantoni et al., 1981). In addition, the available sampling only includes the sedimentary

cover, and does not reach the basement. Thus, although the MEDOC data strongly suggest that the Cornaglia and Campania Terraces are magmatic crustal domains, there is a need of petrological evidence to corroborate this hypothesis and further advance in understanding of the magmatic processes in this setting.

Therefore it would be interesting to drill in this domain in order to constrain the magmatic nature of its basement and the actual stratigraphic position of its top in order to correlate well with the seismic data, since evaporitic deposits presence in these regions obscures its seismic imaging. Next, three drill sites were proposed to tackle these questions (fig. 6.2):

- D1: The first proposed site to drill is in the southern Cornaglia Terrace, in the vicinity of line M28-b CROP (fig. 6.2). In this region there is the thickest syn-rift sequence, probably ranging from Tortonian to lower Pliocene. This borehole would go across the entire evaporitic sequence in the area (although in the flank where it is thinnest) and would reach the basement. The interest of this drilling site is on one hand the calibration of the basement top, while on the other hand to determine the basement nature (that in this region should be continental). In addition this site would provide invaluable information about the entire syn-rift sedimentary sequence and thus the evolution of one of the major extensional stages in the Tyrrhenian evolution.

- D2: Another proposed drilling site would be in the vicinity of MEDOC 8, also in the Cornaglia Terrace (fig. 6.2). In this area the sedimentary sequence and evaporitic deposits are comparatively thinner. Therefore the basement top is more easily accessible, and the thin evaporites would not be an impediment to drill as important as in other areas. According to Prada et al. (2014; 2015) results, basement on this area consist in back-arc magmatic crust, thus it would be interesting to assess its magmatic nature as well as drill the continental-ocean transition - COT -.

- D3: Finally, a third drilling site would be the Campania Terrace (fig. 6.2), with the aim to locate better the basement top and to identify the basement nature. As in the D2 case, the proposed drilling site is located at a inferred back-arc crust area (Prada et al., 2014). This drilling would provide information about the composition of the basement nature as well as on the evaporitic and older sequence (like in the former D2 site).

- Although those proposed drilling sites are located on the track of yet acquired MCS sections, it would be provably necessary to acquire some further 2D and/or 3D MCS data to explore better the sites to drill. These sections should also be used to calibrate and extrapolate the drilling data.

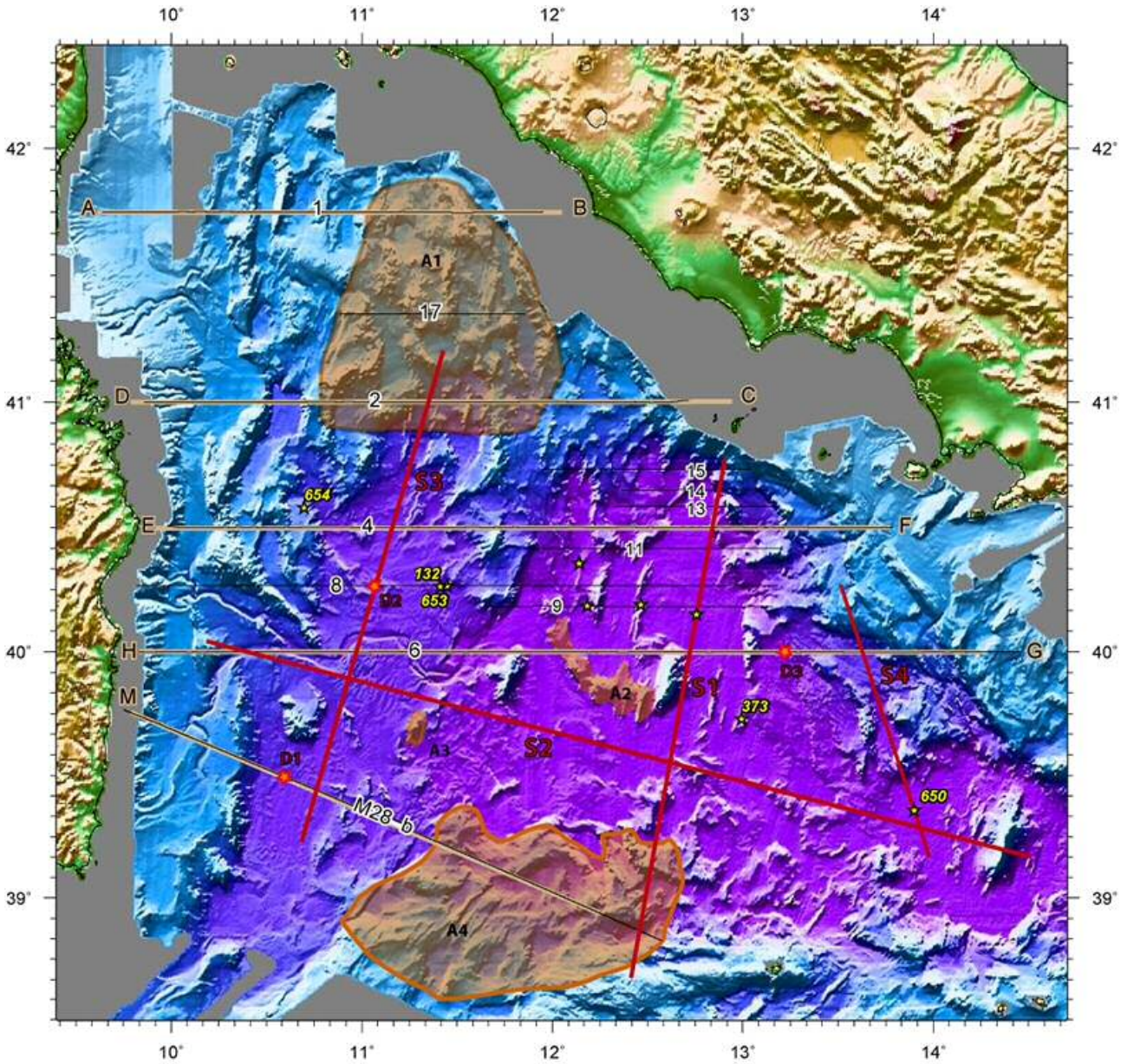

Figure 6.2: Map showing the available MEDOC data (grey lines for WAS sections and black lines for MCS sections) and the available drilling data (yelow stars), together with the proposals done in this outlook section (red lines for WAS/MCS transects, orange stars for proposed drillings and orange-shaded areas for dredging areas).

Dredges are another method to obtain physical samples of the subsoil, with the advantage that costs are much lower in comparison with drilling. Although the dredging data coverage at the Tyrrhenian Basin is good, there are still several locations with where there is a lack of information. With the aim to get some representative bedrock samples, dredging should be carried out at the seamounts to avoid unconsolidated materials. Therefore, on figure 6.2 some potential dredging sites have been shaded.

- A1 and A4: The eastern side of the North Tyrrhenian region and the North Sicily margin have a scarce coverage of sampling records. Thus it would be interesting to acquire some sample rocks at the faulted ridges, to unravel the nature of this areas.

- A2: The d'Ancona Ridge is a poorly-known structure where no sampling data exist. Petrological information would shed some light about its nature and origin.

- A3: The nature of this small seamount between the Cornaglia Terrace and the Magnaghi Basin has an unknown origin, and because of its location – between a back-arc region and an exhumed mantle region – it is difficult to conjecture its origin. Dredging would provide some data to answer this question.

Seismic sections

The MEDOC seismic profiles were shot considering the orientation of the main structural features that are visible in the bathymetry, with the aim to cut them perpendicular and to provide a real representation of their dips. This is the reason why all of them have a similar E-W orientation. But the distance between the profiles does not allow to correlate the information between them. In addition, they are not planned to delineate the along-strike changes in nature of the different domains. Consequently, most of the boundaries between the crustal domains remain poorly constrained. Therefore to get extensive information on the Tyrrhenian it is necessary to collect some additional geophysical transects (MCS and/or WAS) across the basin (fig. 6.2).

- S1: A first section would cross the basin north-south from the Italian Continental Margin to the North Sicily Margin going across the Vavilov Basin. Wide-angle data would provide the transition from the continental Italian domain to the exhumed mantle at the Vavilov Basin, and in addition the nature of the Sicilian Margin. If the section is acquired over the ODP site 651, MCS data would provide a tool to correlate the actual E-W MEDOC sections, and in addition would support the information of the WAS section.

- S2: A second WAS/MCS transect would be acquired perpendicular to the former S1, and parallel to the direction of extension. It will go fairly east-west through the Cornaglia terrace, the Magnaghi and Vavilov Basins, the Issel Bridge and the Marsili Basin. It will provide information on the transition between these domains and about the nature of the Issel Bridge, and the Marsili Basin basement.

- S3 and S4: Finally, it would be interesting two additional WAS/MCS sections crossing the back-arc areas of Cornaglia and Campania Terrace with a north-south direction to define well the transition between the different domains. In the Cornaglia Terrace, they would limit the boundaries between the ultra-thin extended continental crust in the south, the back-arc area, and the continental crust of the North Tyrrhenian. While in the Campania Terrace, would be interesting to see the transition between the Italian continental margin, the back-arc area and the – arguably – exhumed mantle of the Marsili Basin.

Bibliography

Bartole, R., Savelli, D., Tramontana, M., Wezel, F., 1984. Structural and sedimentary features in the Tyrrhenian margin of Campania, southern Italy. Marine Geology, 55, 163-180.

Bartole, R., 1995 . The North Tyrrhenian-Northern Apennines post-collisional system: constraints for a geodynamic model, Terra Nova, 7, 7-30.

Beccaluva, L., Bonatti, E., Dupuy, C., Ferrara, G., Innocenti, F., Lucchini, F., Macera, P., Petrini, R., Rossi, P.L., Serri, G., Seyler, M., Siena, F., 1990. Geochemistry and mineralogy of volcanic rocks from the ODP Sites 650, 651, 655 and 654 in the Tyrrhenian Sea. In: Kastens, K.A., Mascle, J. (eds.). Proceedings of the Ocean Drilling Program, Scientific Results, 107, 49–74. doi:10.2973/odp.proc.sr.107.140.1990

Bertelli, L., Mazzotti, A., Persoglias, S., 2003. Planning, acquisition and processing of the CROP seismic data: a few comments. Memorie Descrittive della Carta geologica d'Italia, LXII, 47-54.

Bertrand, H., Boivin, P., Robin, C., 1990. Petrology and Geochemistry of Basalts from the Vavilov Basin (Tyrrhenian Sea), Ocean Drilling Program Leg 107, holes 651A and 655B. In: Kastens, K.A., Mascle, J. (eds.). Proceedings of the Ocean Drilling Program, Scientific Results, Vol. 107. 75-92.

Bonatti, E., Seyler, M., Channell, J., Giraudeau, J., Mascle, G., 1990. Peridotites drilled from the Tyrrhenian Sea. In Kastens, K.A., Mascle, J., et al. (Eds.), Proceedings of the Ocean Drilling Program, Scientific Results 107, pp. 37– 48, doi:10.2973/odp.proc.sr.107.141.1990

Borsetti, A.M., Curzi, P.V., Landuzzi V., Mutti, M., Ricci Lucchi, F., Sartori, R., Tomadin, L., Zuffa, G.G., 1990. Messinian and Pre-Messinian sediments from ODP leg 107 sites 652 and 654 in the Tyrrhenian Sea: Sedimentologic and Petrographic study and possible comparisons with Italian sequences. In: Kastens, K.A., Mascle, J. (eds.). Proceedings of the Ocean Drilling Program, Scientific Results, Vol. 107, 169-186.

Carlson, R.L., Miller, D.J., 2003. Mantle wedge water contents estimated from seismic velocities in partially serpentinized peridotites, Geophysical Research Leters, 30 (5), doi: 10.1029/2002GL016600.

Carrara, G., 2002. Neogenic tectonic evolution of the Tyrrhenian western margin (Central Mediterranean). PhD Thesis. Parma University (Italy), 160p.

Casciello, E., Cesarano, M., Pappone, G., 2006. Extensional detachment faulting on the

Tyrrhenian margin of the southern Apennines contractional belt (Italy). Journal of Geological Society, London. 163, 617-629.

Cella, F., Fedi, M., Florio, G., Rapolla, A., 1998. Boundaries of magnetic anomaly sources in the Tyrrhenian region. Annali di geofisica, 41 (3), 433-447

Cella, F., F. Maurizio, G. Florio, V. Paoletti, and A. Rapolla (2008), A review of the gravity and magnetic studies in the Tyrrhenian Basin and its volcanic districts, Ann. Geophys., vol. 51, N. 1

Cherchi, A., and L. Montadert (1982), Oligo-Miocene rift of Sardinia and the early history of the western Mediterranean basin, Nature, 298, 736–739.

Chiarabba, C.; De Gori, P.; Speranza, F.; 2008. The southern Tyrrhenian subduction zone: Deep geometry, magmatism and Plio-Pleistocene evolution. Earth and Planetary Science Letters 268 (2008) 408–423.

Christensen, N., and W. Mooney (1995), Seismic velocity structure and composition of the continental crust: a global view, J. Geophys. Res, 100 (B7), doi:10.1029/95JB00259.

Chun, J.H. and Jacewitz, C., 1981. Fundamentals of frequency-domain migration. Geophysics, 46, 717-732.

Cifelli, F.; Mattei, M.; Rossetti, F., 2007. Tectonic evolution of arcuate mountain belts on top of a retreating subduction slab: The example of the Calabrian Arc. Journal of Geophysical Research, 112.

Colantoni, P., Fabbri, A., Gallignani, P., Sartori, R. Lithologic and Statigraphic map of the Italian Seas [map]. 1:1,500,000. 1981.

Compagnoni, R., E. Morlotti, and L. Torelli (1989) Crystalline and sedimentary rocks from the scarps of the Sicily-Sardinia Trough and Cornaglia Terrace (southwestern Tyrrhenian Sea, Italy): Paleogeographic and geodynamic implications. Chemical Geology, 77, 375-398.

Dietrich, V., R. Emmermann, J. Keller, and H. Puchelt (1977), Tholeitic basalts from the Tyrrhenian sea floor, Earth Planet. Sci. Let., 36, 285-296.

Dunn, R.A., and F. Martinez (2011), Contrasting crustal production and rapid mantle transitions beneath back-arc ridges, Nature, 469, 198-202, doi: 10.1038/nature09690.

Duschenes, J., M.C. Sinha, and K.E. Louden (1986), A seismic refraction experiment in the Tyrrhenian Sea, Geophys. J. R. Astron. Soc. 85, 139–160.

Fabretti, P., R. Sartori, L. Torelli, N. Zitellini, and G. Brancolini, (1995), La struttura profonda del margine orientale della Sardegna dall'interpretazione di sismica a riflessione e a rifrazione. Studi Geologivi Camerti, Volume Speciale 1995/2, 239-246

Fabri, A., and Curzi, P.V., (1979) The Messinian of the Tyrrhenian Sea: seismic evidence and dynamic implications. Giornale di Geologia 43 (2), 215-248.

Faccenna, C., Funiciello, F., Giardini, D., Lucente, P., 2001. Episodic back-arc extension during restricted mantle convection in the Central Mediterranean. Earth and Planetary Science Letters, 5796, 1-12.

Faccena, C., T.W. Becker, F. P. Lucente, L. Jolivet, and F. Rossetti, 2001. History of subduction and back-arc extension in the Central Mediterranean, Gophys. J. Int., 145, 809-820.

Faccenna, C.; Piromallo, C.; Crespo-Blanc, A.; Jolivet, L.; Rossetti, F.; 2004. Lateral slab deformation and the origin of the western Mediterranean arcs. Tectonics, 23. TC1012, doi:10.1029/2002TC001488

Faccenna, C., Funiciello, F., Civetta, L., D'Antonio, M., Moroni, M., Piromallo, C., 2007. Slab disruption, mantle circulation, and the opening of the Tyrrhenian basins. Geological Society of America Special Papers, 418, 153-169.

Gailler, A., F. Klingelhoefer, J.-L. Olivet, and D. Aslanian (2009), Crustal structure of a young margin pair: New results across the Liguro-Provencçal Basin from wide-angle seismic tomography, Earth Planet. Sci. Let., 289, 333-345. doi: 10.1016/j.epsl.2009.07.001.

Gasparon, M., G. Rosenbaum, J. Wijbrans, P. Manetti (2009), The transition from subduction arc to slab tearing: Evidence from Capraia Island, northern Tyrrhenian Sea, Journal of Geodynamics, 47, 30-38, doi: 10.1016/j.jog.2008.06.004

Gattacceca, J., A. Deino, R. Rizzo, D.S. Jones, B. Henry, B. Beaudoin, and F. Vadeboin (2007), Miocene rotation of Sardinia: New paleomagnetic and geochronological constraints and geodynamic implications, Earth Planet. Sci. Let., 258, 359-377, doi: 10.1016/j.epsl.2007.02.003.

Gawthorpe, R.L., Jackson, C.A.L., Young, M.I., Sharp, I.R., Moustafa, A.R., Leppard, C.W., 2003. Normal fault growth, displacement localisation and the evolution of normal fault populations: the Hamman Faraun fault block, Suez Rift, Egypt. J. Struct. Geol., 25, 1347-1348, 2003.

Gueguen, E., Doglioni, C., Fernandez, M., 1998. On the post-25 Ma geodynamic evolution

of the western Mediterranean. Tectonophysics, 298, 259–269.

Hamilton, E.L., (1978), Sound velocity-density relations in sea-floor sediments and rocks, J. Acoust. Soc. Am., 63, 366-377.

Hsü. K.J., Montadert, L., Bernoulli, D., Bizon, G., Cita, M., Erickson, A., Fabricius, F., Garrison, R.E., Kidd, R.B., Mélières, F., Müller, C., Wright, R.C., 1978. Site 373: Tyrrhenian Basin, In Hsü, K., Montadert, L., et al. , 1978. Initial reports of the Deep Sea Drilling Project, Volume 42, Part 1: Washington (U.S. Government Printing Office).

Kastens, K., Mascle, J., Christian, A., Bonatti, E., Broglia, C., Channell, J., Curzi, P., Emeis, K.C., Glacon, G., Hasegawa, S., Hieke, W., Mascle, G., McCoy, F., McKenzie, J., Mendelson, J., Mueller, C., Rehault, J.P., Robertson, A., Sartori, R., Sprovieri, R., Torii, M.; 1988. ODP Leg 107 in the Tyrrhenian Sea: Insights into passive margin and back-arc basin evolution. Geological Society of America Bulletin, 100, 1140-1156.

Kastens, K., Mascle, J., 1990. The geological evolution of the Tyrrhenian Sea: an introduction to the scientific results of ODP leg 107. Proceedings of the Ocean Drilling Program, Scientific Results, Vol. 107.

Kastens, K.A., Mascle, J., Auroux, C.A., 1985. Ocean Drilling Program Leg 107 Scientific Prospectus Tyrrhenian Sea. Scientific Prospectus, 7.

Kastens, K.A., Mascle, J., Auroux, C.A., 1986. Ocean Drilling Program Leg 107 Preliminary Report Tyrrhenian Sea. Preliminary Report.

Kern, H., Tubia, J.M. (1993) Pressure and temperature dependence of P- and S-wave velocities, seismic anisotropy and density of sheared rocks from the Sierra Alpujata massif (Ronda peridotites, Southern Spain), Earth & Planet. Sci. Lett.

Korenaga, J., P. B. Kelemen, R. S. Detrick, H.-C. Larsen, J. R. Hopper, and T. Dahl-Jensen (2000), Crustal structure of the southeast Greenland margin from joint refraction and reflection seismic tomography, J. Geophys. Res., 105(B9), 21, 591–21, 614, doi:10.1029/2000JB900188.

Korenaga, J., W. S. Holbrook, G. M. Kent, P. B. Kelemen, R. S. Detrick, H.-C. Larsen, J. R. Hopper, and T. Dahl-Jensen, 2000. Crustal structure of the southeast Greenland margin from joint refraction and reflection seismic tomography, J. Geophys. Res., 105(B9), 21, 591–21, 614, doi:10.1029/2000JB900188.

Korenaga, J., W.S. Holbrook, R.S. Detrick, and P.B. Kelemen (2001), Gravity anomalies and crustal structure at the southeast Greenland margin, J. Gophys. Res., 106 (B5), 8853-

8870.

Lowrie, W.,2007. Fundamental of Geophysics, Cambridge University Press, New York, pp. 374.

Lustrino, M., Duggen, S., Rosenberg, C.L., 2011. The Central-Western Mediterranean: anomalous igneous activity in anomalous collisional tectonic setting. Earth-Science Reviews, 104, 1–40.

Malinverno, A., 2012. Evolution of the Tyrrhenian Sea – Calabrian Arc system: the past and the present. 86º Congresso Società Geologica Italiana. 18-20 Settembre 2012.

Malinverno, A., Ryan, W.B.F., 1986. Extension in the Tyrrhenian Sea and shortening in the Apennines as result of arc migration driven by sinking of the lithosphere. Tectonics, 5, 2, 227-245, doi:10.1029/TC005i002p00227.

Martinez, F., Okino, K., Ohara, Y., Reysenback, A., Goffredi, S. K., 2007. Back-arc basins. Oceanography, 20 (1), 116-127.

Mauffret, A., Contrucci, I., 1999. crustal structure of the North Tyrrhenian Sea: first result of the multichannel seismic LISA cruise. In: Durand, B., Jolivet, L., Horvath, F., Seranne, M. (eds), The Mediterranean Basins: Tertiary Extension within the Alpine Orogen. Geological Society, London, Special Publications, 156, 169-193.

Mauffret, A., Contrucci, I., Brunet, C., 1999. Structural evolution of the Northern Tyrrhenian Sea from new seismic data. Marine and Petroleum Geology, 16, 381-407.

Manzi, V.; Gennari, R.; Hilgen, F; Krijgsman, W; Lugli, S; Roveri, R; Sierro, F.J., 2013. Age refinement of the Messinian salinity crisis onset in the Mediterranean. Terranova, 25 (4), 315-322.

Marani, M.P., Gamberi, F., 2004. Structural framework of the Tyrrhenian Sea unveiled by seafloor morphology, in Marani, P., F. Gamberi, and E. Bonatti (Eds.). From seafloor to deep mantle: Architecture of the Tyrrhenian back-arc basin (Memorie Descrittive della carta Geologica d'Itlaia, Vol. LXIV), pp 97-108.

Martinez, F., Okino, K., Ohara, Y., Reysenback, A., Goffredi, S. K., 2007. Back-arc basins. Oceanography, 20 (1), 116-127.

Mascle, G. H., P. Tricart, L. Torelli, J-P.Bouillin, F. Rolfo, H. Lapierre, P. Monié, S. Depardon, J. Mascle, and D. Peis (2001), Evolution of the Sardinia Channel (Western Mediterranean): new constraints from a diving survey on Cornacya seamount off SE Sardinia,

Marine Geology, 139, 179-202

Mascle, J., Rehault, J.P., 1990. A revised seismic stratigraphy of the Tyrrhenian Sea: Implications for the basin evolution. In Kastens, K.A., Mascle, J. (eds.), Proceedings of the Ocean Drilling Program, Scientific Results 107, pp. 617-636.

Michaud, F., A. Chabert, J.-Y. Collot, V. Sallares, E.R. Flueh, Ph. Charvis, D. Graiindorge, M.-A. Gutscher, J. Bialas (2005), Fields of multi-kilometer scale sub-circular depressions in the Carnegie Ridge sedimentary blanket: Effect of underwater carbonate dissolution?, Marine Geology, 216 (4), 205-219, doi:10.1016/j.margeo.2005.01.003

Moeller, S., Grevemeyer, I., Ranero, C.R., Berndt, C., Klaeschen, D., Sallares, V., Zitellini, N. and de Franco, R. (2013). Early-stage rifting of the northern Tyrrhenian Sea Basin: Results from a combined wide-angle and multichannel seismic study. Geochemistry Geophysics Geosystems, 14 (8), 3032-3052. DOI: 10.1002/ggge.20180.

Moeller, S. I. Grevemeyer, C. R. Ranero, C. Berndt , D. Klaeschen V. Sallares, N. Zitellini, and R. de Franco. Crustal thinning in the northern Tyrrhenian Rift: Insights from multichannel and wide-angle seismic data across the basin. doi:10.1002/ 2013JB010431 J. Geophys. Res. Solid Earth. (2014)

Moser, T.J., 1991. Shortest path calculation of seismic rays, Geophysics, 56, 59-67.

Moser, T.J., G. Nolet, and R. Snieder, 1992. Ray bending revisted, Bull. Seismol. Soc. Am., 82, 259-288.

Mutter, C. Z. & Mutter, J. C. Variations in thickness of layer 3 dominate oceanic crustal structure. Earth Planet. Sci. Let. 117, 295-317 (1993).

Newman, P., 1973. Divergence effects in a layered earth. Geophysics 38, 481-8.

Parker, R.L. (1972), The rapid calculation of potential anomalies, Geophys. J. R. Astron. Soc., 31, 447-455.

Paige, C.C., and Saunders, M.A., 1982. LSQR: An algorithm for sparse linear equation and sparse least squares, Trans. Math. Software, 8, 43-71.

Peacock, K.L. & Treitel, S.; 1969. Predictive Deconvolution: Theory and Practice, Geophysics, Vol. 34, No.2, pp. 155-169.

Pérez-Gussinyé, M., and Reston, T. (2001), Rheological evolution during extension at nonvolcanic rifted margins: Onset of serpentinization and development of detacgments leading to continental breakup, J. Geophys. Res., vol. 106, no B3, pp 3961-3975.

Pérez-Gussinyé, M., Phipps Morgan, J., Reston, T, & Ranero, C. R., (2006) From rifting to spreading at non-volcanic margins: insights from numerical modelling, Earth & Planet. Sci. Lett. 244, 458-473

Prada, M., V. Sallares, C. R. Ranero, M. G. Vendrell, I. Grevemeyer, N. Zitellini, and R. de Franco, Seismic structure of the Central Tyrrhenian basin: Geophysical constraints on the nature of the main crustal domains, J. Geophys. Res. Solid Earth, 119, doi:10.1002/2013JB010527. (2014)

Prada, M., V. Sallares, C. R. Ranero, M. G. Vendrell, I. Grevemeyer, N. Zitellini, and R. de Franco, 2015. The complex 3D transition from continental crust to back-arc magmatism and exhumed mantle in the Central Tyrrhenian rifted basin. Geophys. J. International 203 (1), 63-78, doi:10.1093/gji/ggv271

Ranero, C.R., J. P. Morgan, K. McIntosh, and C. Reichert, (2003) Bending-related faulting and mantle serpentinization at the Middle America trench, Nature, 425, 367-373.

Ranero, C. R. & Sallares, V., Geophysical evidence for alteration of the crust and mantle of the Nazca Plate during bending at the north Chile trench. Geology 32, 549–552; (2004).

Ryan, W.B.F., Hsü, K.J., Cita, M.B., Dumitrica, P., Lort, J., Maync, W., Nesteroff, W.D., Pautot, G., Stradner. H., Wezel, F.C., 1973. Site 132: Tyrrhenian Basin, Initial reports of the Deep Sea Drilling Project, Volume 13.

Rosenbaum, G., Lister, G.S., 2004. Neogene and Quaternary rollback evolution of the Tyrrhenian Sea, the Apennines, and the Sicilian Maghrebides. Tectonics, 23.

Rosenbaum, G., Lister, G. S. and Duboz, C. 2002. Reconstruction of the tectonic evolution of the western Mediterranean since the Oligocene. In:Rosenbaum, G. and Lister, G. S. 2002. Reconstruction of the evolution of the Alpine-Himalayan Orogen. Journal of the Virtual Explorer, 8, 107 - 130.

Sallarès, V., J.J: Dañobeitia, E.R. Flueh (2000), Seismic tomography with local earthquakes in Costa Rica, Tectonophysics, 329 (1), pp.61-78.

Sallarès, V., Gailler, A., Gutscher, M. A., Graindorge, D., Bartolomé, R., Gràcia, E., Diaz, J., Zitellini, N. (2011). Seismic evidence for the presence of jurassic oceanic crust in the central gulf of cadiz (SW iberian margin). Earth Planet. Sci. Lett., 311(1-2), 112-123.

Sallarès, V., S. Martinez-Loriente, M. Prada, E. Gràcia, C. Ranero, M.-A. Gutscher, R. Bartolomé, A. Gailler, J.J. Dañobeitia, and N. Zitellini (2013a), Seismic evidence of exhumed mantle rock basement at the Gorringe Bank and the adjacent Horseshoe and Tagus abyssal

plains (SW Iberia), Earth Planet. Sci. Let., 365, 120-131, doi: 10.1016/j.epsl.2013.01.021.

Sallarès, V., A. Meléndez, M. Prada, C. R. Ranero, K. McIntosh, and I. Grevemeyer (2013b), Overriding plate of the Nicaragua convergent margin: Relationship to the seismogenic zone of the 1992 tsunami earthquake, Geochem. Geophys. Geosyst., doi: 10.1002/ggge20214.

Sartori, R. (1990), The main results of ODP Leg 107 in the frame of Neogene to Recent geology of perityrrhenian areas, in Kastens, K.A., Mascle, J., et al. (Eds.), Proceedings of the Ocean Drilling Program. Scientific Results 107, pp. 715– 730.

Sartori, R., Carrara, C., Torelli, L., Zitellini, N., 2001. Neogene evolution of the southwestern Tyrrhenian Sea (Sardinia Basin and western Bathyal plain). Marine Geology, 175, 47-66.

Sartori, R., Torelli, L., Zitellini, N., Carrara, G., Magaldi, M., Mussoni, P., 2004. Crustal features along a W–E Tyrrhenian transect from Sardinia to Campania margins (Central Mediterranean). Tectonophysics 383, 171–192.

Savelli, C. (1988) Late Oligocene to Recent episodes of magmatism in and around the Tyrrhenian Sea: implications for the processes of opening in a young inter-arc basin of intra-orogenic (Mediterranean) type, Tectonophysics, 146, 163-181

Savelli, C. (2002), Time-space distribution of magmatic activity in the western Mediterranean and peripheral orogens during the past 30 Ma (a stimulus to geodynamic considerations), J. Geodyn., 34, 99-126.

Shawn Wei, S., Douglas A. Wiens, Yang Zha, Terry Plank, Spahr C. Webb, Donna K. Blackman, Robert A. Dunn, and James A. Conder (2015), Seismic evidence of effects of water on melt transport in the Lau back-arc mantle, Nature letters, doi:10.1038/nature14113

Soliva, R., Benedicto, A., Maerten, L., 2006. Spacing and linkage of confined normal faults: Importance of mechanical thickness, J. Geophys. Res., doi:10.1029/2004JB003507, 2006.

Tarantola, A., and Valette, B., 1982. Inverse Problems=Quest for Information, J. Geophys., 50, 159-170.

Tarantola, A., 1987. Inverse Problem Theory: Methods for Data Fitting and Model Parameter Estimation, Elsevier Science, New York. 613 pp.

Taylor, B., A. Goodliffe, F. Martinez, and R. Hey (1995), Continental rifting and initial seafloor spreading in the Woodlark basin, Nature, 374, 534 – 537

Thybo, H., and Artemieva, I.M. (2013), Moho and magmatic underplating in continental lithosphere, Tectonophysics, http://dx.doi.org/10.1016/j.tecto.2013.05.032

Toomey, D.R., and G.R. Foulger, 1989. Tomographic inversion of local earthquake data from Hengill-Grensdalur central volcano complex, Iceland, J. Geophys. Res., 94, 17497-17510.

Toomey, D.R., S.C. Solomon, and G.M. Purdy, 1994. Tomographic imaging of the shallow crustal structure of the East Pacific Rise at 9º30'N, J. Geophys. Res., 99, 24.135-24.157.

Trorey, A.W., 1977. Diffraction for arbitrary source receiver location, Geophysics, 42, 1177-1182.

Trincardi, R., Zitellini, N., 1987. The rifting of the Tyrrhenian Basin. Geo-Marine Letters, 7, 1-6.

Trorey, A.W., 1977. Diffraction for arbitrary source receiver location, Geophysics, 42, 1177-1182.

Trua, T., Serri., G., 2007. Geochemical features and geodynamic significance of the southern Tyrrhenian back-arc basin. Geological Society of America, Special Paper, 418, 221-233.

Vignaroli, G., C. Faccena, F. Rossetti, and L. Jolivet (2009), Insights from the Apennines metamorphic complexes and their bearing on the kinematics evolution of the orogen, in VAN HINSBERGEN, D. J. J., M. A. EDWARDS, and R. GOVERS (Eds), Collision and Collapse at the Africa-Arabia-Eurasia Subduction Zone. The Geological Society, London, Special Publications, 311, 235–256.

Viti, M., Mantovani, E., Babbucci, D., Tamburelli, C., 2009. Generation of Trench-Arc-Back Arc Systems in The Western Mediterranean Region driven by plate convergence. Italian journal of geosciences, 128 (1). pp. 89-106.

White, R.S., D. McKenzie, and R.K. O'Nions (1992), Oceanic crustal thickness from seismic measurements and rare earth element inversions. J. Geophys. Res. 97, 19683–19715.

White, R.S., L.K. Smith, A.W. Roberts, P.A.F. Christie, N.J. Kusznir, and the rest of the iSIMM Team (2008) lower crustal intrusion on the North Atlantic continental margin, Nature Letters, 452, doi:10.1038/nature06687

Yilmaz, Ö., 2001. Seismic data analysis: processing, inversion, and interpretation of seismic data, Society of Exploration Geophysics, Tulsa, USA.

Zelt, C.A., and Smith, R.B., 1992. Seismic traveltime inversion for 2-D crustal velocity

structure, Geophysical Journal International, 108, 16-34.

Zitellini N., F. Trincardi, M. Marani, and A Fabbri (1986), Neogene tectonics of the northern Tyrrhenian Sea, Giorn. Geol, 48, 1, 2.

Annexes

Figure index

Figures

Figure 1.1: Regional bathymetric map of the Western Mediterranean domain, with the working area – the Tyrrhenian Sea – framed in the red rectangle, and enlarged next. Also the major topographic features mentioned at the text have been labelled. 16
Figure 1.2: Models for back arc basin opening. Left panels show the evolution of a basin with a slab roll-back as a dredging mechanism, while right panels show the evolution of a basin with the slab acting as a mantle anchor (from Martinez et al., 2007)....18
Figure 1.3: Schematic diagram showing the evolution of the Tyrrhenian Basin from the early/middle Miocene until present day (modified from Cifelli et al., 2007)....22
Figure 2.1: Bathymetric map showing the dataset used in this thesis. The data acquired during the MEDOC survey are the red lines (wide-angle data), and the black lines (multichannel data). Also the CROP profile (M28-b) given by the Italian CNR is plotted in black. The ST lines are the orange lines, and were acquired during the preparation of the ODP Leg 107 survey. The OBSs from the line M-N analysed in this thesis are plotted with yellow circles. Finally, the ODP and DSDP sites that were used to calibrate the horizons are the yellow stars....29
Figure 2.2: When a seismic wave reaches the interface between two strata, it scatters due to the reflection and refraction phenomena. Those phenomena can be described by Huygen's principle (a) and the Snell's law (b)....31
Figure 2.3: Definition of the inner Fresnel zone. Modified from Yilmaz, 2001....32
Figure 2.4: Diffractions are seismic energy scattered in all directions when the interface which separates two geologic layers with different seismic proprieties ends in a discontinuity. Reflections are a special case of diffraction where the angle of reflection equals or is close to the angle of the incident wave....33
Figure 2.5:Acquisition diagram for the multichannel sections....35
Figure 2.6: Within a shot gather can be identified the characteristic patterns of direct waves, primary and multiple reflections, refracted waves and diffracted waves....36
Figure 2.7: Example raypaths of some multiple noise arrivals. The minimum time for this arrivals is, at least, the double than the primay signal (left seabed multiple). A pegleg (right case) is a special type of multiple where the ray bounce more than one time within a layer. 37
Figure 2.8: Processing flow followed for the MEDOC and M28-b MCS profiles....40
Figure 2.9: (a) Example of some shots from MEDOC 8 with no processing applied. This display allow to detect traces (or even entire shots) with incoherent noise. (b) A near-trace display consist in plot the first trace of each shot to test the lateral coherency of the data. Like in the shots case, these data have no processing applied. 41
Figure 2.10: (a) The rays from a single shot travel across the subsoil and are reflected by the different layers. (b) Shot-gather concept: each shot covers a section of the profile track, which is recorded by each of the channels on the streamer. (c) CMP (common-mid point) gather concept: rays reflected in the same point in depth, coming from different shots can be gathered together in to CMPs. (d) each shot covers a section of the profile through several traces. When the vessel advances, the section covered by the new shot overlaps partially the former section. This allows a multi-coverage of several shots of a single point in depth. 44
Figure 2.11: Graphical representation of a seismic trace in terms of the convolution model explained by equation 5 (without the noise term), being x(t) the recorded trace, w(t) the source wavelet and

e(t) the Earth's impulse response. After Yilamz [2001].....45
Figure 2.12: (a) Frequency spectrum of the seismogram Ax(μ) as a result of the multiplication of the seismic wavelet Aw(μ), and the Earth's impulse response Ae(μ). (b) Autocorrelation functions of the three seismograms shown in figure 2.11. The registered seismogram (left) gets the first peak from the Earth's impulse response, and the rest come from the font. After Yilamz [2001].....46
Figure 2.13: Example of a single CMP before (a) and after (c) NMO correction. The central panel (b) is the corresponding velocity function, where the black line is the velocity function and the blue steped line is the calculated (by the software) interval velocity between the picked points.....49
Figure 2.14: Ilustration of the PRT filtering. In the tau-p domain, straight arrivals become punctual at the tau-p domain, while hiperbolic events become parabolic. From http://www.xsgeo.com/course/basic.htm#tp.....51
Figure 2.15: Figure caption of the mutes picked on a CMP. Blue line: external mute; green line: internal mute.....53
Figure 2.16: Conceptual model of a CMP stack: (left) Seismic traces of a CMP gather. (mid) Traces of a CDP gather with NMO applied. (right) Stacked trace result of the sum of all traces. From http://www.glossary.oilfield.slb.com/en/Terms/s/stack.aspx.....54
Figure 2.17: Quantitative analysis of migration process (from Yilmaz, 2001), where points C and D are moved to C' and D' after migration. The final amount of horizontal and vertical displacement (dx and dt) are calculated with equations 14 and 15.....56
Figure 2.18: Section of the M28-b profile showing the effects of the overmigration in deep reflectors. This overmigration produces "smiles" ("u" shaped artifacts) that hide the real structure. 58
Figure 2.19: Pictures of the air-gun array (a) and the OBSs (b) used during the survey. In there, main components are tagged.....61
Figure 2.20: Schematic diagram of the wide-angle acquisition system, and the propagation of the different seismic phases refracted through the sediments (PsP), crust (Pg), and mantle (Pn); and reflected at the sediment-basement boundary (PsP), and at the crust-mantle boundary (PmP).....63
Figure 2.21: Diagram showing path of the rays through the surface and the evolution of the reflections and refractions as the source-receiver distance increases. Note that after a certain point, the ray of the seismic wave incides with the critical angle ic and critically refracts through the top of the lower layer. Reflections that occur after the critical distance are known as wide-angle reflections.....64
Figure 2.22: Record section blank (a), and with the identified seismic phases picked (b): the refracted through the crust (Pg: in red) and mantle (Pn: in green), and reflected at the Moho (PmP: in blue). Cyan is for the wather wave. Note that the relation between the refracted Pg and the reflected PmP is asymptotic.....65
Figure 2.23: Flow diagram of the joint refraction and reflection travel-time inversion method applied with TOMO2D code [Korenaga et al., 2000].....67
Figure 2.24: Derivative weight sum for the velocity model obtained. The higher is the DWS, the higher is the ray coverage.....69
Figure 3.1: Upper image shows the bathymetric and topographic map of the Tyrrhenian basin. The MEDOC Wide-Angle seismic (WAS) and Multichannel seismic (MCS) lines are represented with black and red lines, respectively. The data from line M28-b and the coincident WAS MEDOC transect M-N are used in this thesis to infer the crustal structure of the southwestern region of the Tyrrhenian basin. Middle image displays a close up of the study area with the location of MCS line M28-b (red line) and WAS Line M-N (thick black line), as well as the location of the Ocean Bottom Seismometers (OBS) and Land stations (LS) deployed along Line M-N (yellow circles). WAS transect G-H (thick grey line) and MCS line MEDOC 6 (thin black line) are also shown in the figure. Ground truthing in the area is depicted by colored triangles, yellow stars, and red and black dots (Dietrich et al., 1977; Colantoni et al., 1981; Campagnoni et al., 1989; Kastens and Mascle,

1990; Mascle et al., 2001). Numbers are 1: Sardinia basin, 2:Quirra volcano, 3: Cornacya volcano, 4: Baronie seamount, 5: Cornaglia seamount, 6: Magnaghi seamount, 7: Vavilov seamount, 8: Drepano seamount, 9: Anchise seamount, 10: Ustica Island, 11: Marsili seamount. CT: Cornaglia Terrace, MB: Magnaghi basin, VB: Vavilov basin, MaB: Marsili basin, AI: Aeolian Islands. Lower panel depicts the topographic and bathymetric profile together with the LS and OBS locations along WAS transect M-N. 75
Figure 3.2: From top to bottom: record section, travel time fits and ray-tracing representation of OBSs 96 (a), 101 (b), and 108 (c). Seismic phases of interest are shown in the upper record sections, while white and black dots in the middle sections depict the calculated and observed travel times, respectively. Black thick line in the lower image represents the PmP-inverted Moho. 76
Figure 3.3: Upper profile is the 2D P-wave velocity model of the crust and uppermost mantle, and geometry of the PmP-derived Moho boundary (blue line) along transect M-N. LS and OBS are depicted by yellow circles. Lower profile represents the derivative weight sum (DWS) which is used as a proxy of ray density along the profile. 77
Figure 3.4: a) RMS (left) and $\chi 2$ (right) values of each Monte Carlo realization before (upper) and after (lower) the uncertainty assessment. The figure shows the initial random distributions of models and the good convergence after inversion. b) Average crustal tomographic model of the 500 Monte Carlo realizations. Moho geometry is represented by the blue line. The velocity structure and Moho geometry reported by the average tomographic model shows important similarities with the model presented in figure 3.3a, indicating that most features observed in the model of figure 3.3a are not artifacts from inversion but real crustal features explained by Pg and PmP travel times. c) Uncertainty values for the crustal velocity field and the depth of the Moho reflector (black band). 79
Figure 3.5: 1D Vp-z profiles of each zone along the profile (black band) compared to the Vp-z reference of continental crust (yellow band) (Christensen and Mooney, 1995), transitional continental crust (orange band) (Prada et al., in prep), and 0-7 Ma Atlantic oceanic crust (blue band) (White et al., 1992). The gray bands represent the lateral variability of Vp along each zone, while the colored bands depict the standard deviation of each Vp-z measurement.....81
Figure 3.6: Upper panel shows the Vp-derived density model along transect M-N. Blue line and yellow circles depict the Moho geometry and the OBS location along the profile. The gravity response of this model is shown in the lower panel (red band) compared to the observed gravity response (white circles). The misfit is rather good with a RMS of 9.6 mGal.....83
Figure 3.7: Post-stack time migration image of CROP profile M28B overlaid with the tectonic interpretation (red lines). The location of the top of basement is depicted by pointing hands, while Moho reflections are indicated by dashed black lines. The TWT-converted PmP-derived Moho boundary is represented by the blue line along the profile.....84
Figure 3.8: MCS profile M28B overlaid by the velocities of the tomographic model and the Moho geometry (blue line) converted from depth to TWT assuming near-vertical propagation. Yellow circles represent the OBS/H location. 85
Figure 3.9: Left panel shows the bathymetric map of the Cornaglia Terrace and the location of the WAS MEDOC transects E-F (Prada et al., 215), G-H (Prada et al., 2014), and M-N (this study), as well as the corresponding OBS/H location (yellow circles). Colored sections along each line depict the selected portions of each tomographic model along which mean lower crustal Vp (right upper panel) and basement thickness variation (right lower panel) have been extracted. The Vp of 6.0 km/s has been taken from each model as the top of the lower-crust to extract velocity values in the right upper panel, whereas Vp of 5 km/s has been taken as the top of the basement to calculate basement thickness.....88
Figure 4.1: General map of the working area, showing the profile tracks used to get the interpretation: the MEDOC lines (from MEDOC survey, 2010), the ST (from ODP leg 107 survey), and the M28-b line (form CROP survey, 1994). Also ODP leg 107, used to calibrate the horizons, were plotted. Black lines are the lines processed (or reprocessed in the M28-b case) by me, while

the orange ones were got already processed, and only were used to calibrate the horizons.....93
Figure 4.2-a: Topographic map of the Tyrrhenian with analysed MCS sections. Location of the segments used to work the Corsica-Sardinia continental margin (see figure 4.2-b) are highlighted in orange.....96
Figure 4.2-b: MCS sections crossing the Corsica-Sardinia continental margin. At the places were dredging data were available, it has been pointed out (Colantoni et al., 1981). Also the ODP site 654 location has been plotted (see figure 4.2-c).....97
Figure 4.2-c: Stratigraphic column of ODP site 654 (modified from Kastens & Mascle, 1988), and its position at the ST 6 section. ST sections were used to bring the horizon location from ODP 654 to the MEDOC survey (and M28-b) profiles. Red vertical lines show the places were these sections cross with each others. 98
Figure 4.3-a: Topographic map of the Tyrrhenian with analysed MCS sections. Location of the segments used to work the North Tyrrhenian (see figure 4.3-b) are highlighted in orange.....100
Figure 4.3-b: MCS sections crossing the North Tyrrhenian. At the places were dredging data were available, it has been pointed out (Colantoni et al., 1981).....101
Figure 4.4-a: Topographic map of the Tyrrhenian with analysed MCS sections. Location of the segments used to work the Sechi-Farfalle region (see figure 4.4-b) are highlighted in orange.....102
Figure 4.4-b: MCS sections crossing the Sechi-Farfalle region. At the places were dredging data were available, it has been pointed out (Colantoni et al., 1981). Also the ODP sites 652 and 656 location have been plotted (see figure 4.4-c and 4.4-d).....103
Figure 4.4-c: Stratigraphic column of ODP site 656 (modified from Kastens & Mascle, 1988), and its position at the MEDOC 9 section. 104
Figure 4.4-d: Stratigraphic column of ODP site 652 (modified from Kastens & Mascle, 1988), and its position at the ST 1 section. ST sections were used to bring the horizon location from ODP 652 to the MEDOC survey (and M28-b) profiles. Red vertical lines show the places were these sections cross with each others. 105
Figure 4.5-a: Topographic map of the Tyrrhenian with analysed MCS sections. Location of the segments used to work the Vavilov and Magnaghi basins (see figure 4.5-b) northern area are highlighted in orange.....106
Figure 4.5-b: MCS sections crossing the Vavilov and Magnaghi basins northern area. At the places were dredging data were available, it has been pointed out (Colantoni et al., 1981).....107
Figure 4.6-a: Topographic map of the Tyrrhenian with analysed MCS sections. Location of the segments used to work the Cornaglia Terrace (see figure 4.6-b) are highlighted in orange.....112
Figure 4.6-b: MCS sections crossing the Cornaglia Terrace. At the places were dredging data were available, it has been pointed out (Colantoni et al., 1981). Also the ODP site 653 location has been plotted (see figure 4.6-c).....113
Figure 4.6-c: Stratigraphic column of ODP site 653 (modified from Kastens & Mascle, 1988), and its position at the MEDOC 8 section. 114
Figure 4.7-a: Topographic map of the Tyrrhenian with analysed MCS sections. Location of the segments used to work the Campania Terrace (see figure 4.7-b) are highlighted in orange.....115
Figure 4.7-b: MCS section crossing the Campania Terrace. At the places were dredging data were available, it has been pointed out (Colantoni et al., 1981).....116
Figure 4.8-a: Topographic map of the Tyrrhenian with analysed MCS sections. Location of the segments used to work the Italian continental margin (see figure 4.8-b) are highlighted in orange. 122
Figure 4.8-b: MCS sections crossing the Italian continental margin. At the places were dredging data were available, it has been pointed out (Colantoni et al., 1981).....123
Figure 4.9-a: Topographic map of the Tyrrhenian with analysed MCS sections. Location of the segments used to work the Vavilov and Magnaghi basins southern area (see figure 4.9-b) are highlighted in orange.....126

Figure 4.9-b: MCS section crossing the Vavilov and Magnaghi basins southern area. At the places were dredging data were available, it has been pointed out (Colantoni et al., 1981). Also the ODP sites 651 and 655 location have been plotted (see figure 4.9-c and 4.9-d).....127
Figure 4.9-c: Stratigraphic column of ODP site 651 (modified from Kastens & Mascle, 1988), and its position at the MEDOC 9 section. 128
Figure 4.9-d: Stratigraphic column of ODP site 655 (modified from Kastens & Mascle, 1988), and its position at the MEDOC 9 section. 129
Figure 4.10-a: Topographic map of the Tyrrhenian with analysed MCS sections. Location of the segments used to work the North Sicily margin (see figure 4.10-b) are highlighted in orange.....130
Figure 4.10-b: MCS section crossing the North Sicily margin. At the places were dredging data were available, it has been pointed out (Colantoni et al., 1981).....131
Figure 4.11: Magmatic events (effusive and intrusive) described at the text are marked with red dots. Circles for subduction-related magmatism, squares correspond to intraplate volcanism and triangles are MOR-type basalts). Places: 1: Elba-Pianosa Ridge, 2: Vercelli Seamount, 3: Cornacya Seamount, 4: Ancheste Seamount, 5: Anchise Seamount, 6:Pontine Islands, 7: Quirra Seamount, 8: Gortani Ridge, 9: Magnaghi Seamount, 10: Vavilov Seamount, 11: DSDP drilling site 373.....144
Figure 4.12: Sedimentary distribution for most important units worked at the text. “Basement” refers to the seismic basement identified as crustal basement, regardless of its continental or oceanic nature. While “peridotite” location is mostly based on tomographic work from MEDOC survey (Prada et al., 2014). Also the M2 Messinian sub-unit is important because of its relation with submerged areas during the Messinian Salinity crisis. Finally, Pleistocene has been ignored in this figure because is the youngest unit and its presence is widespread, giving any relevant information (and in addition, its distribution coincides pretty well with the Pliocene one).....147
Figure 5.1: General map of the working area, showing the profile tracks used to get the interpretation: the MEDOC lines (from MEDOC survey, 2010), the ST (from ODP leg 107 survey), and the M28-b line (form CROP survey, 1994). Also ODP leg 107, used to calibrate the horizons, were plotted (see stratigraphy chapter for more information). Black lines are the lines processed (or reprocessed in the M28-b case) by me, while the orange ones were got already processed, and only were used to calibrate the horizons. Also domain names were plotted, and the colour code correspond to the that were working during their formation. At the yellow shaded areas only rifting processes worked. At the green shaded areas the magmatism was the main extensional mechanism. The red area correspond to a mix of rifting and volcanism. And finally, at the blue area exhumed mantle have been found. 153
Figure 5.2-a: Local map of the Corsica-Sardinia margin domain. Location of the segments used to work this domain (see figure 4.2-b) are highlighted in orange.....154
Figure 5.2-b: MCS sections crossing the Corsica-Sardinia continental margin. At the places were dredging data were available, it has been pointed out (Colantoni et al., 1981). Also the ODP site 654 location has been plotted (see explanation on stratigraphy chapter).....155
Figure 5.3-a: Local map of the North Tyrrhenian domain. Location of the segments used to work this domain (see figure 4.3-b and 4.3-c) are highlighted in orange.....158
Figure 5.3-b: MCS sections crossing the North Tyrrhenian. At the places were dredging data were available, it has been pointed out (Colantoni et al., 1981).....159
Figure 5.3-c: MCS sections crossing the Sechi-Farfalla region. At the places were dredging data were available, it has been pointed out (Colantoni et al., 1981).....160
Figure 5.4-a: Local map of the Cornaglia Terrace domain. Location of the segments used to work this domain (see figure 5.4-b) are highlighted in orange.....162
Figure 5.4-b: MCS sections crossing the Cornaglia Terrace domain. At the places were dredging data were available, it has been pointed out (Colantoni et al., 1981). Also the ODP sites 652 and 656 location have been plotted (see explanation on stratigraphy chapter).....163
Figure 5.5-a: Local map of the Vavilov and Magnaghi basins domain. Location of the segments

used to work this domain (see figure 5.5-b) are highlighted in orange.....165
Figure 5.5-b: MCS sections crossing the Vavilov and Magnaghi basins northern area. At the places were dredging data were available, it has been pointed out (Colantoni et al., 1981). 166
Figure 5.5-c: MCS sections crossing the Vavilov and Magnaghi basins southern area. At the places were dredging data were available, it has been pointed out (Colantoni et al., 1981). Also the ODP sites 651 and 655 location have been plotted (see explanation on stratigraphy chapter).....167
Figure 5.6-a: Local map of the Campania Terrace domain. Location of the segments used to work this domain (see figure 5.6-b) are highlighted in orange.....169
Figure 5.6-b: MCS section crossing the Campania Terrace. At the places were dredging data were available, it has been pointed out (Colantoni et al., 1981).....170
Figure 5.7-a: Local map of the Italian margin domain. Location of the segments used to work this domain (see figure 5.7-b) are highlighted in orange.....172
Figure 5.7-b: MCS section crossing the Italian margin. At the places were dredging data were available, it has been pointed out (Colantoni et al., 1981).....173
Figure 5.8-a: Local map of the North Sicily margin domain. Location of the segments used to work this domain (see figure 5.6-b) are highlighted in orange.....175
Figure 5.8-b: MCS section crossing the North Sicily margin. At the places were dredging data were available, it has been pointed out (Colantoni et al., 1981).....176
Figure 5.9: The three main stages of the evolution of the basin described in thee text. Notation of the areas: CB:Corsica Basin, SB: Sardinia Basin, NT: North Tyrrhenian, SF: Sechi-Farfalle region, IM: Italian Margin, NS: North Sicily margin, CT: Cornaglia Terrace, CT: Campania Terrace, MB: Magnaghi Basin, VB: Vavilob Basin, MB: Marsili Basin. 187
Schematic evolution of the basin. Orange areas represent continental extension by rifting. Blue areas correspond to oceanic-like crust formation. Green areas represent exhumation of the mantle. Finally, purple ones represent areas affected by transpressional/transtensional deformation. The areas that remain blank are the inactive areas. Areas with striped pattern represent almost inactive processes or where two processes work at the same time. The magmatic events marked at the figure are those described at the chapter 4 (section 4.2.6), that could be related with magmatism observed at our sections. They are represented by red dots (squares for intraplate volcanism, triangles for MOR basalts, and circles for subduction-related volcanism). 1:Cornacya Seamount, 2: Vercelli Seamount, 3: Elba-Pianosa Ridge, 4: Ancheste Seamount, 5: Anchise Seamount, 6:Pontine Islands, 7: Quirra Seamount, 8: Gortani Ridge, 9: Magnaghi Seamount, 10: Vavilov Seamount, 11: Marsili Seamount. Notation of the areas: CB:Corsica Basin, SB: Sardinia Basin, NT: North Tyrrhenian, SF: Sechi-Farfalle region, IM: Italian Margin, NS: North Sicily margin, CT: Cornaglia Terrace, CT: Campania Terrace, MB: Magnaghi Basin, VB: Vavilob Basin, MB: Marsili Basin. 196
Fig. 6.2: Map showing the available MEDOC data (grey lines for WAS sections and black lines for MCS sections) and the available drilling data (yelow stars), together with the proposals done in this outlook section (red lines for WAS/MCS transects, orange stars for proposed drillings and orange-shaded areas for dredging areas).....201

Acquisition parameters of the multichannel profiles

	Shot		CMP		Length (km)
	First	Final	First	Final	
MEDOC 1	101	3,950	100	31,167	257.17
MEDOC 2	98	4,921	100	38,935	255.68
MEDOC 4	105	6,556	100	52,015	422.74
MEDOC 6	109	8,011	100	62,988	514.19
MEDOC 8	102	5,825	100	46,159	374.01
MEDOC 9	101	2,647	100	20,743	166.04
MEDOC 11	101	2,387	100	18,663	151.00
MEDOC 13	101	1,557	100	12,023	95.47
MEDOC 14	101	1,405	100	10,807	85.74
MEDOC 15	101	1,962	100	15,163	122.54
MEDOC 17	107	1,899	100	14,711	119.11

Table showing the initial and final shot and CMP for each of the sections worked in this thesis. Also the profile length is given.

Wide-angle seismic record sections

First panel correspond to the record section from each of OBS. Second panel are the data fit with black circles (picked data) and white circles (calculated data). Finally, the third panel is the ray tracing used to get the 2D P-wave velocity model. In there, the black line represents the inverted Moho geometry, and the white circle is the receiver location.

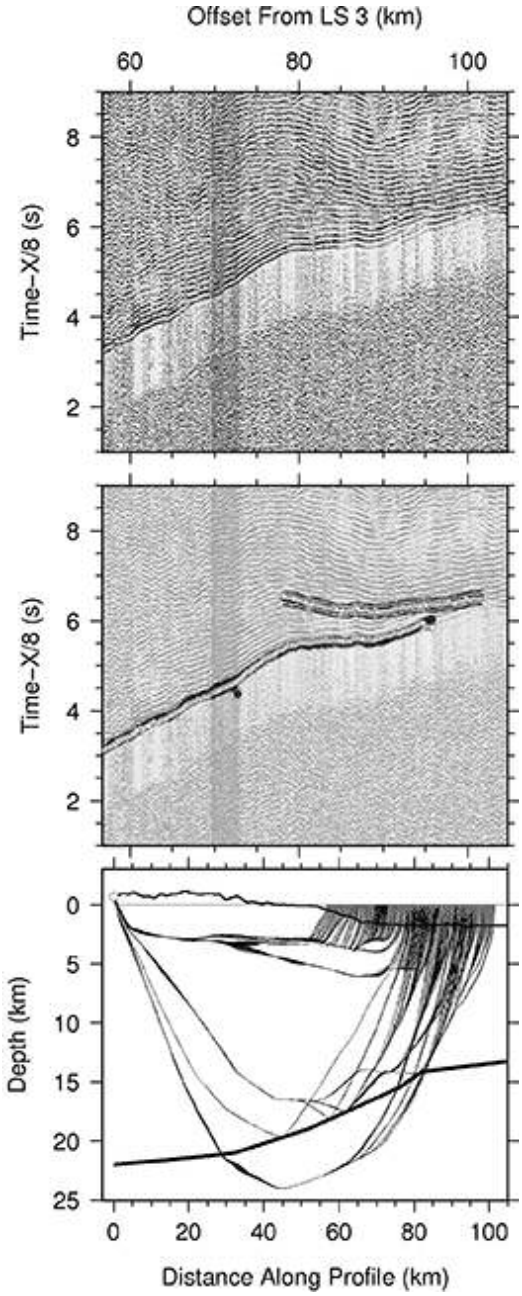

Landstation MN-3

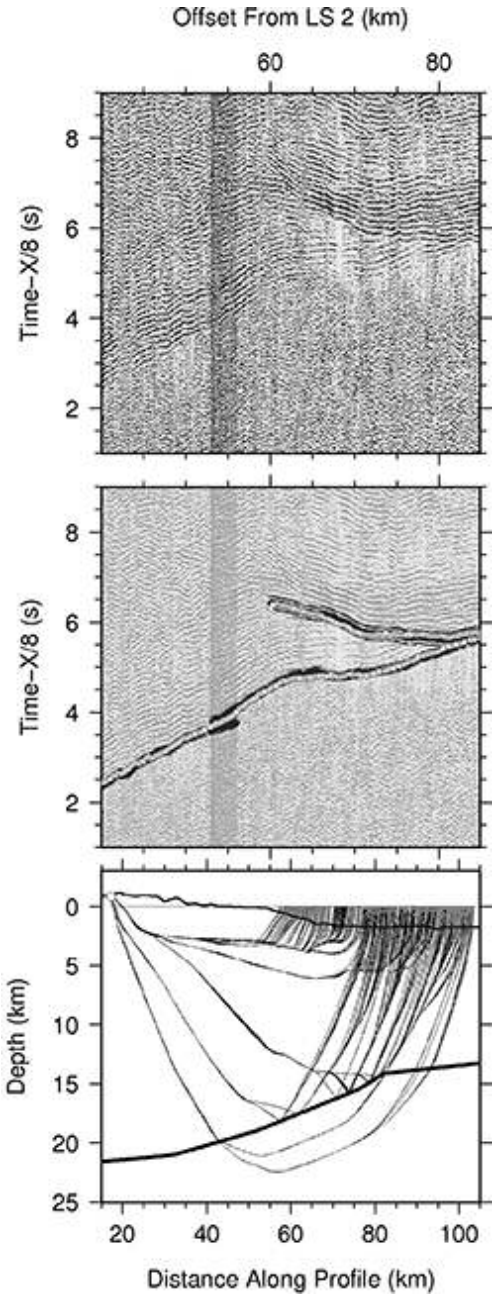

Landstation MN-2

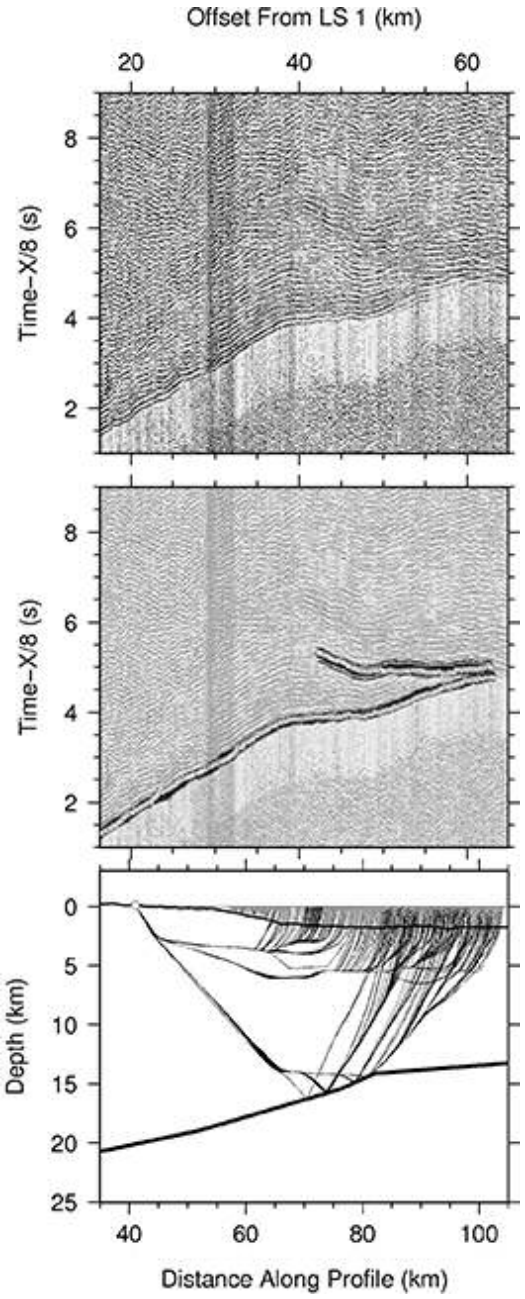

Landstation MN-1

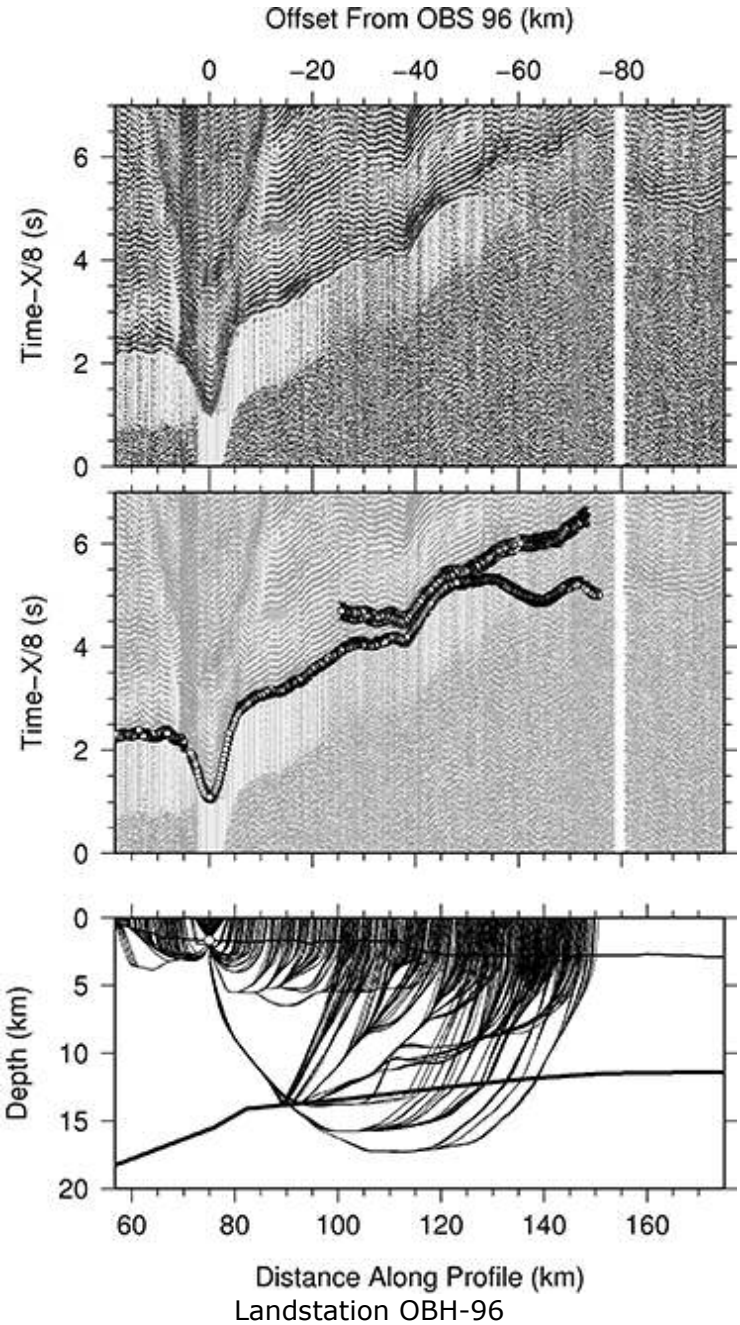

Landstation OBH-96

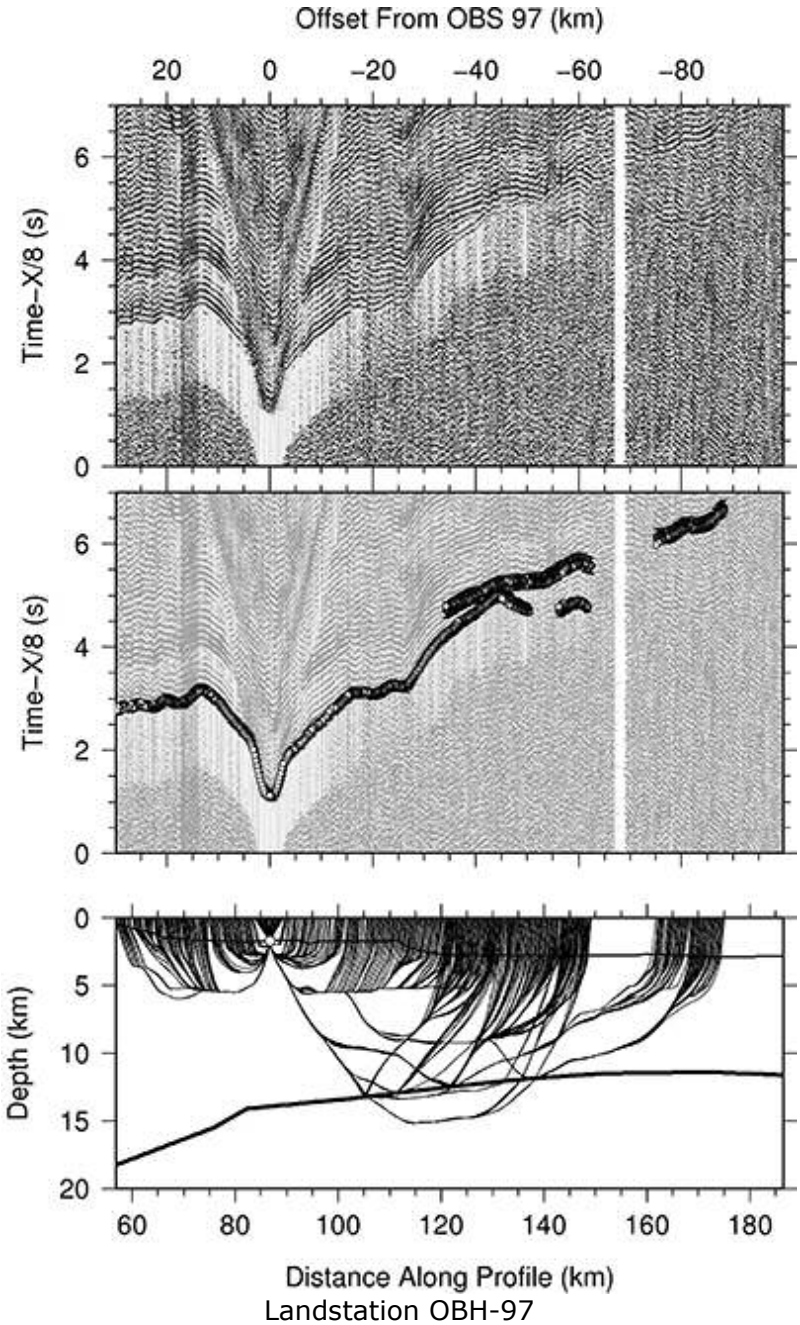

Landstation OBH-97

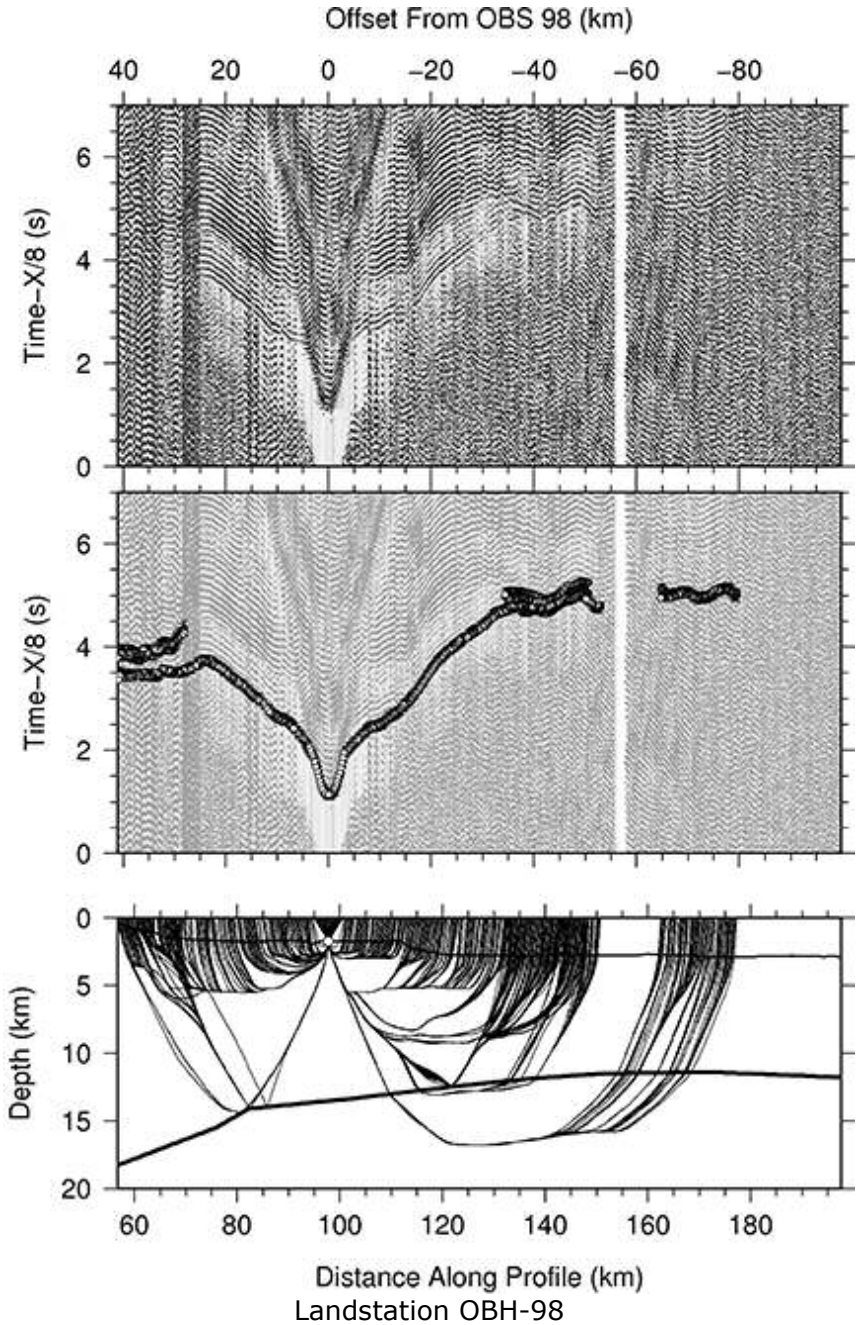

Landstation OBH-98

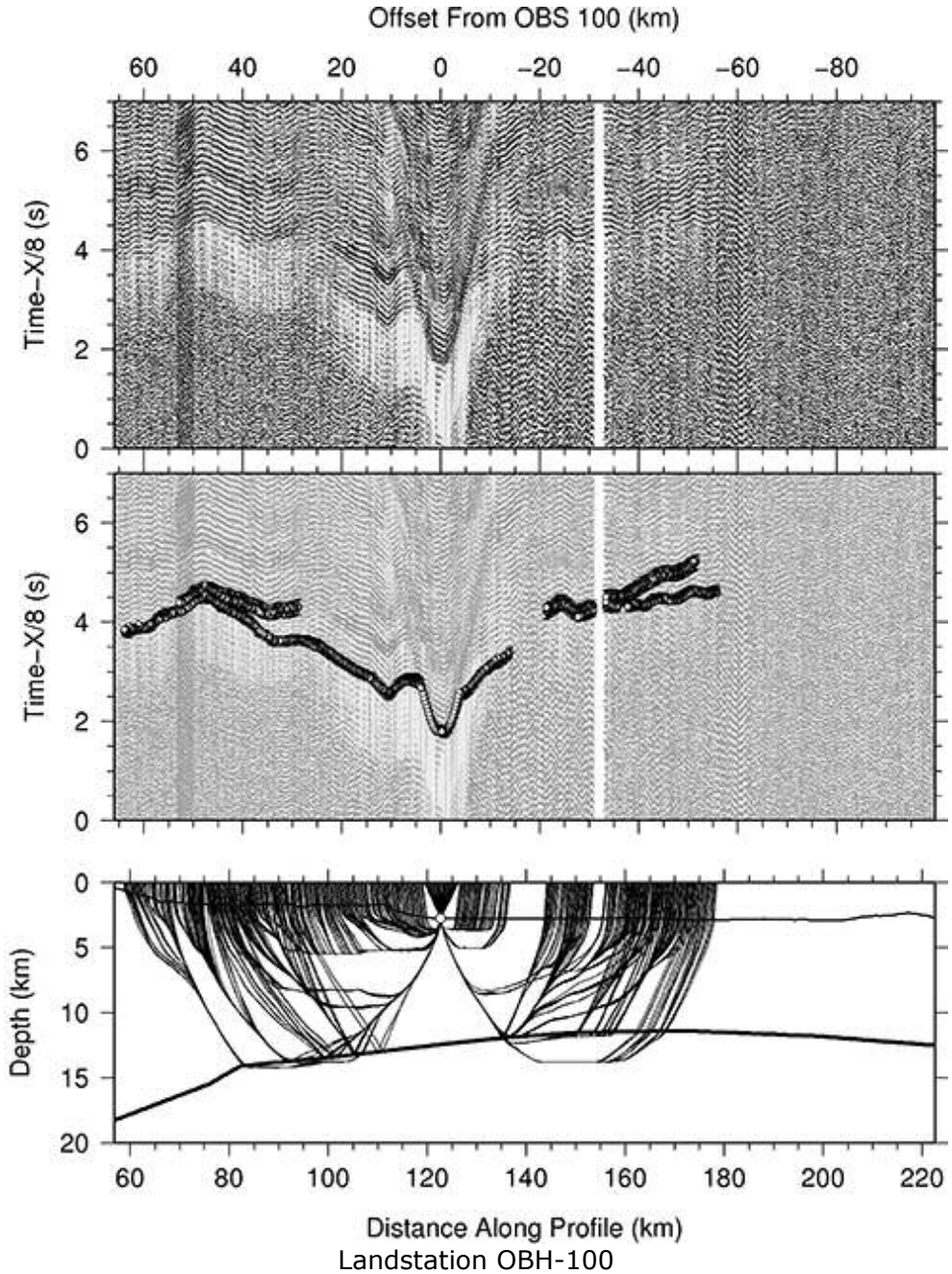

Landstation OBH-100

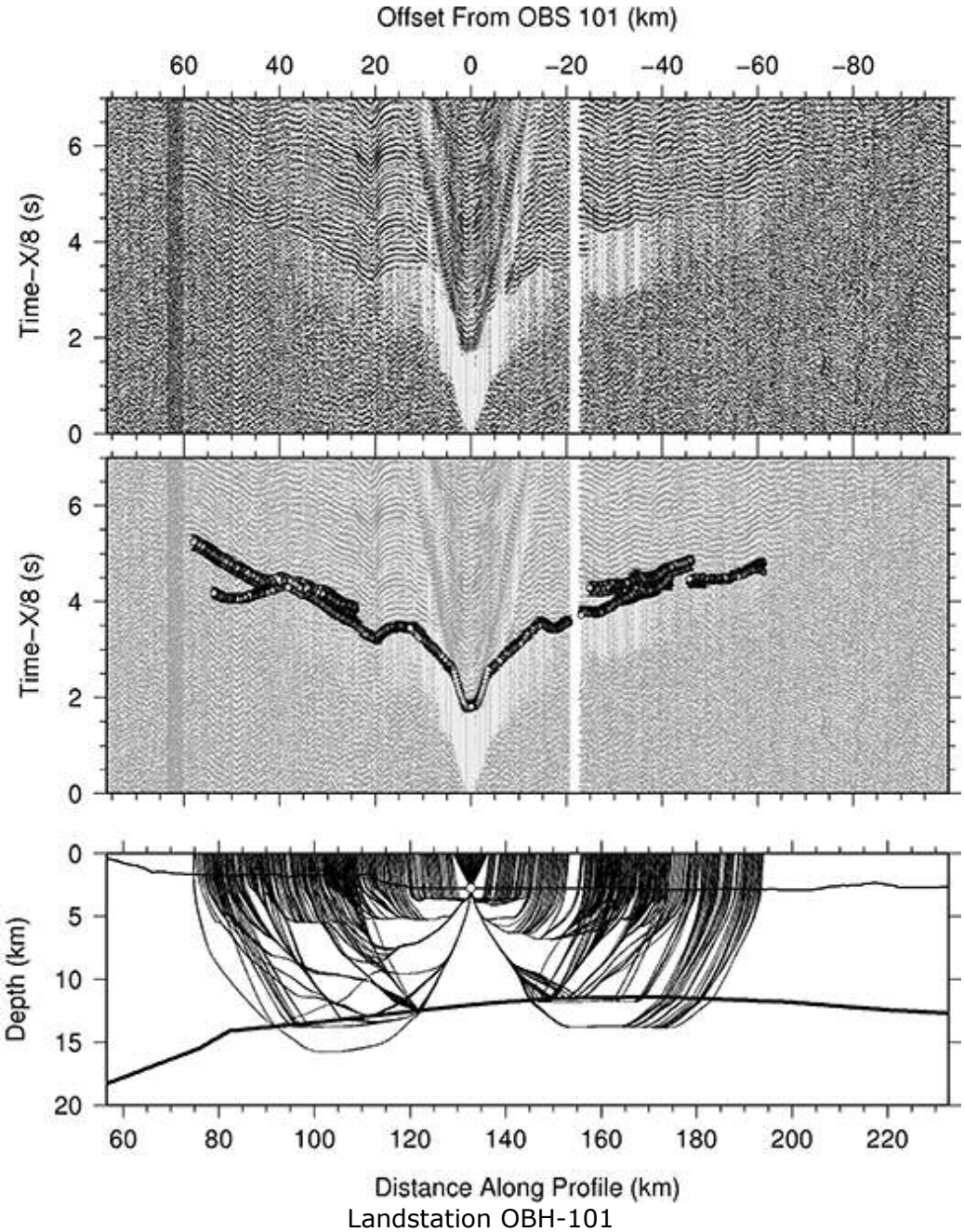

Landstation OBH-101

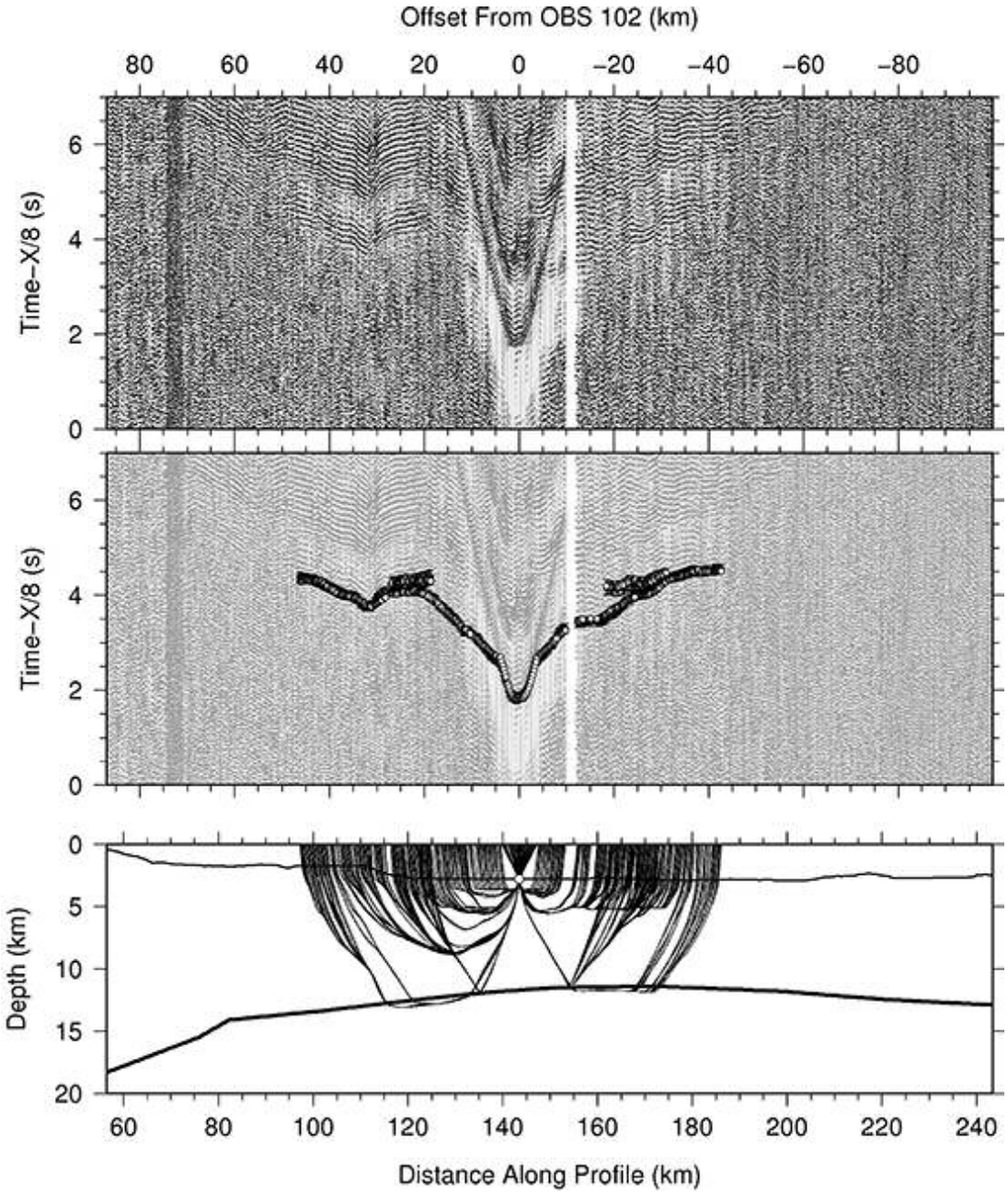

Landstation OBH-102

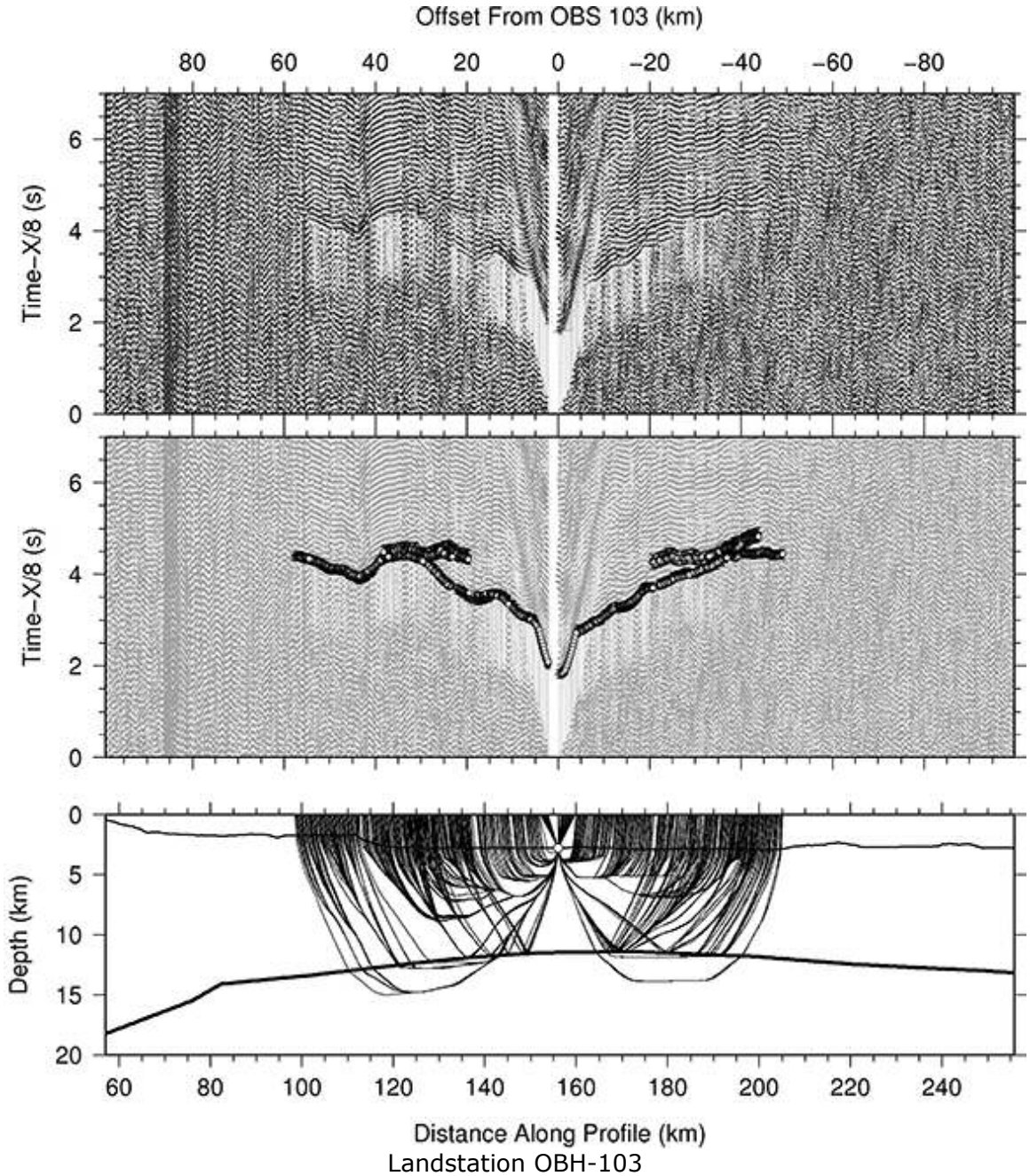

Landstation OBH-103

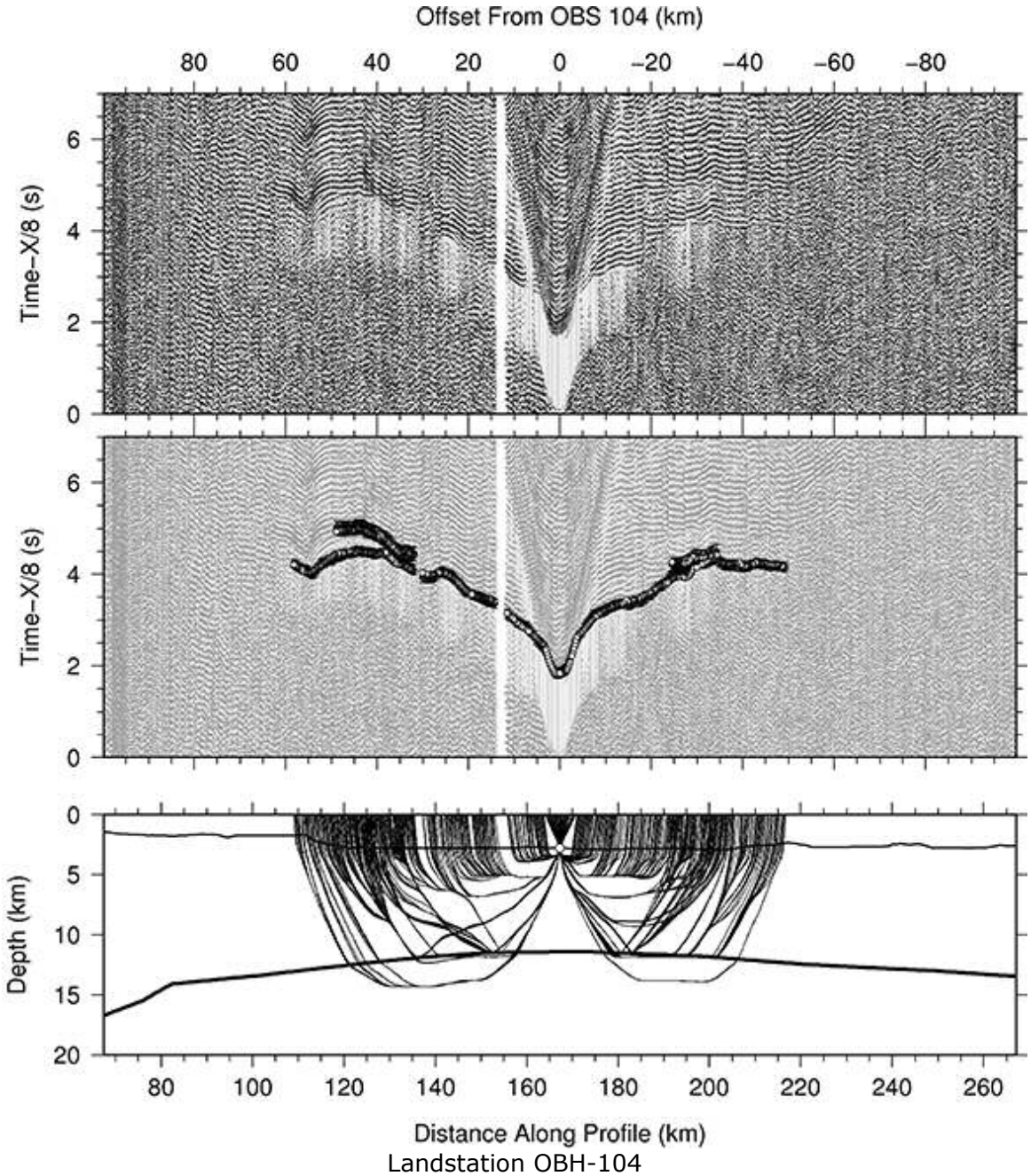

Landstation OBH-104

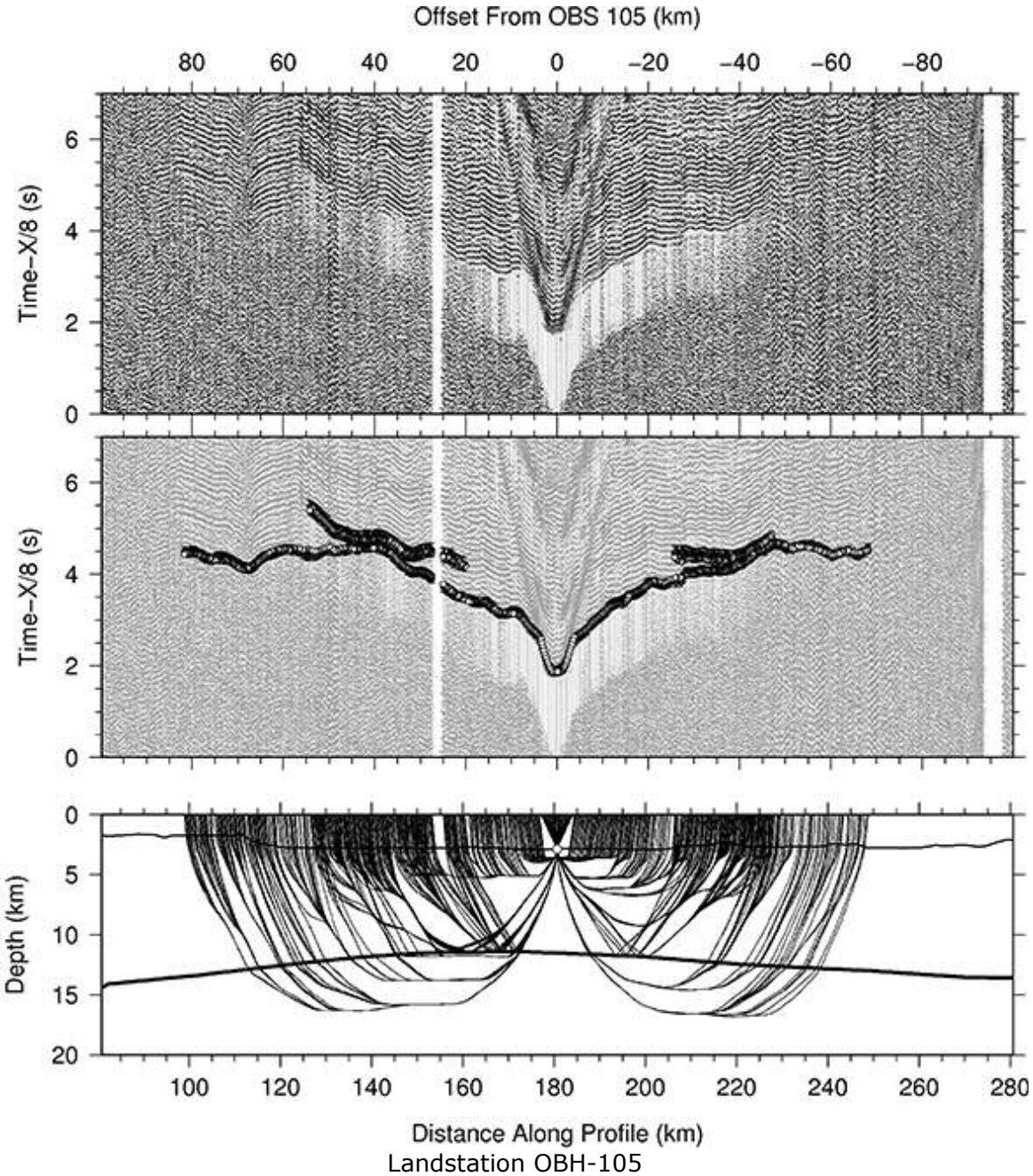

Landstation OBH-105

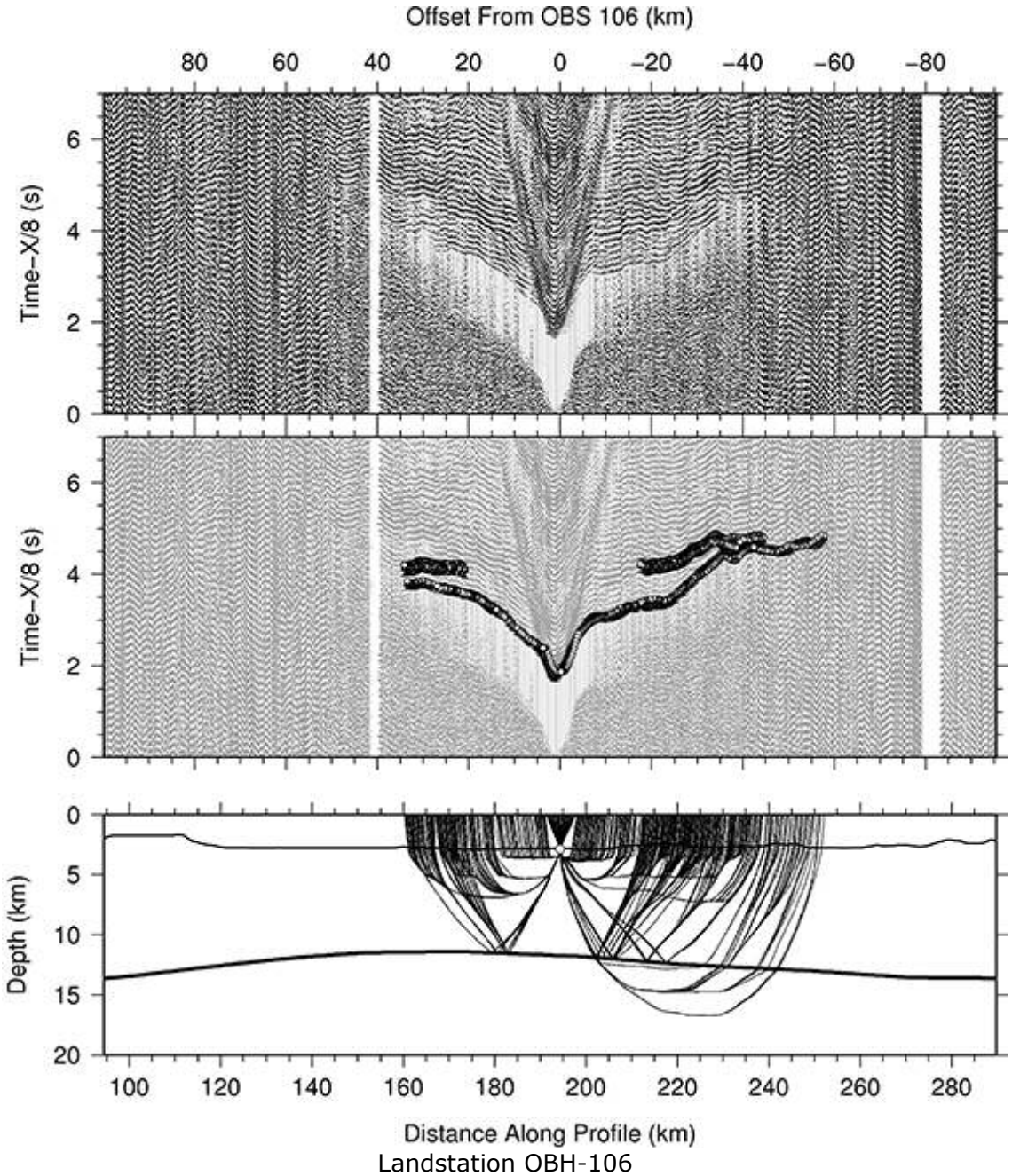

Landstation OBH-106

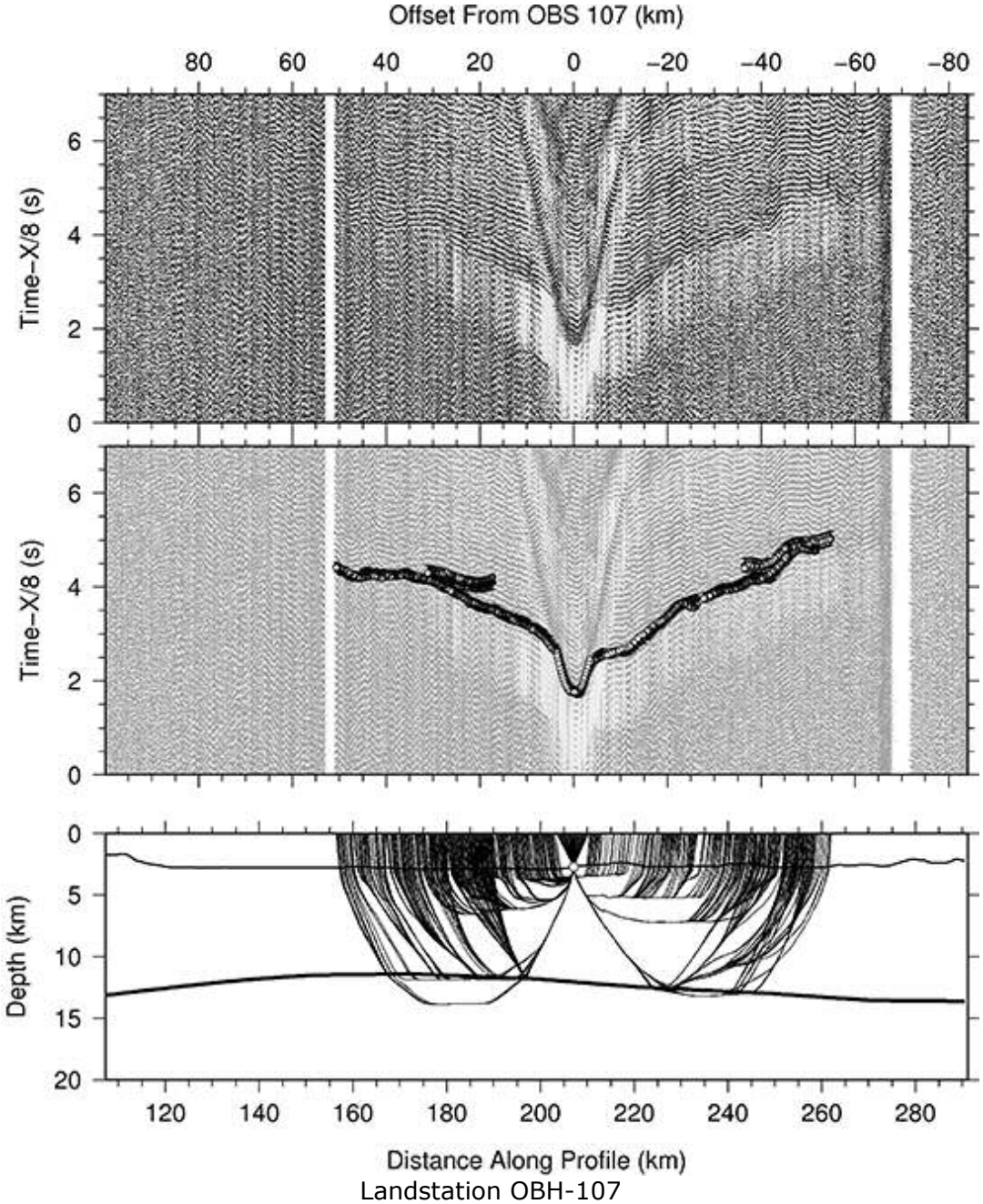

Landstation OBH-107

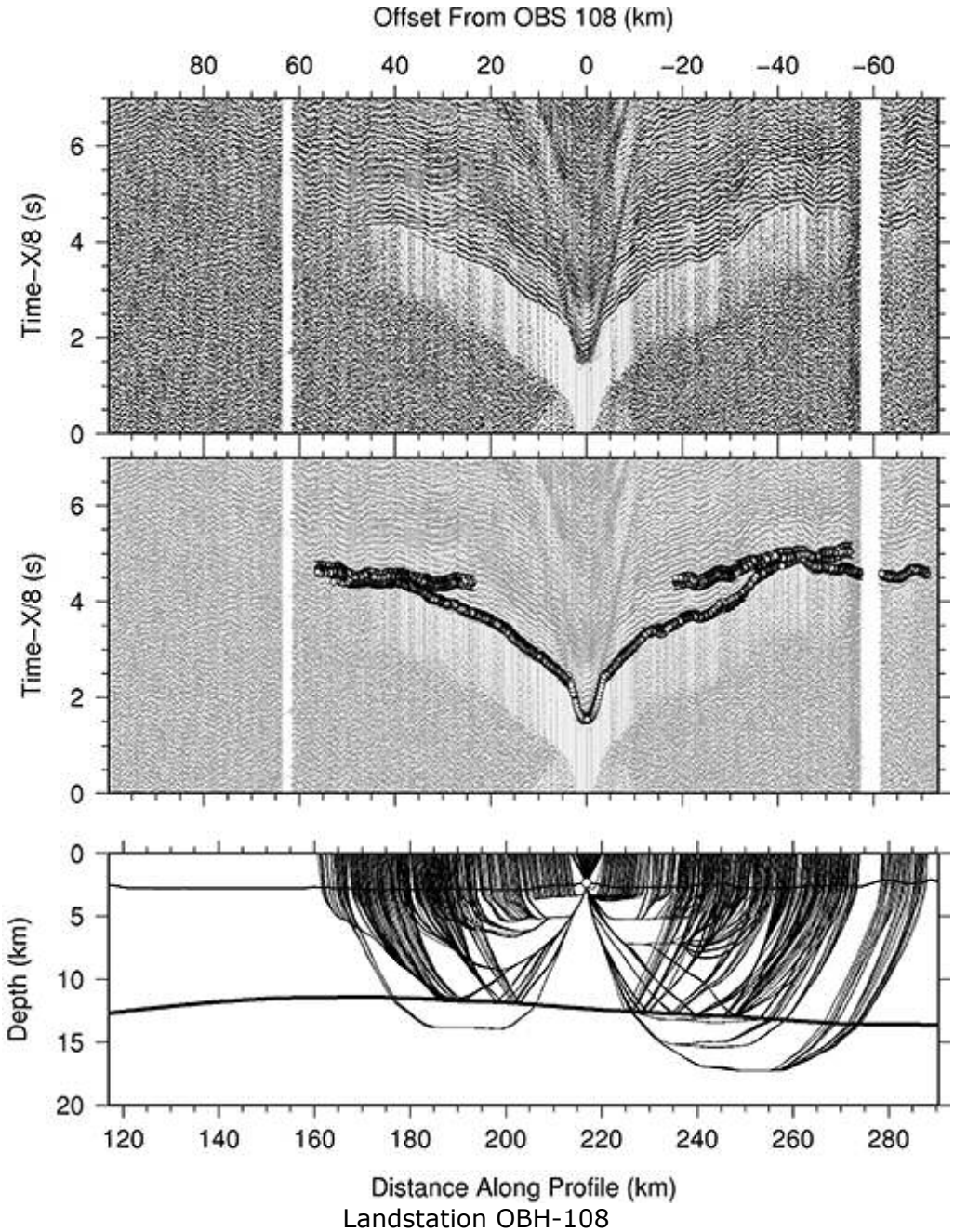

Landstation OBH-108

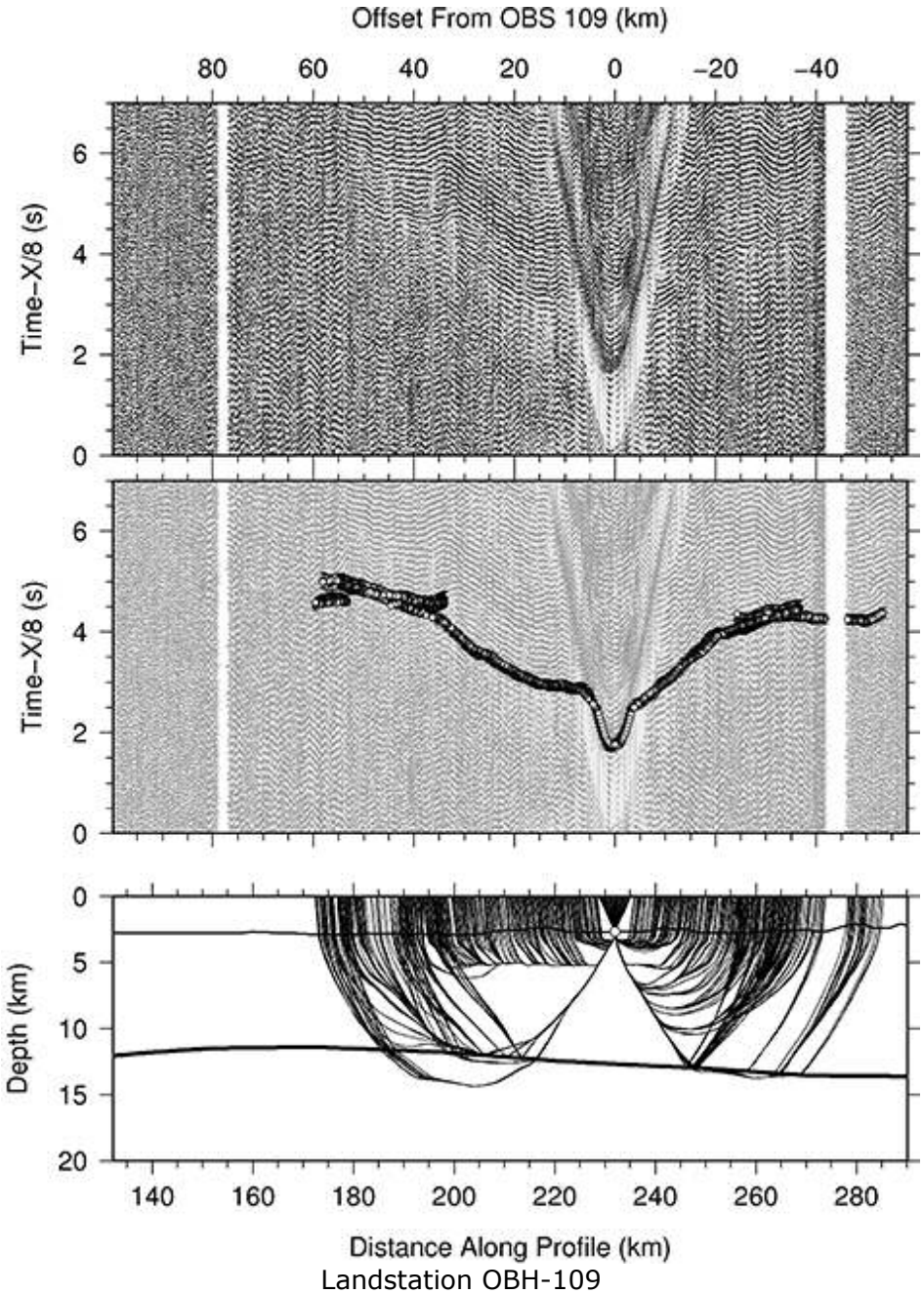

Landstation OBH-109

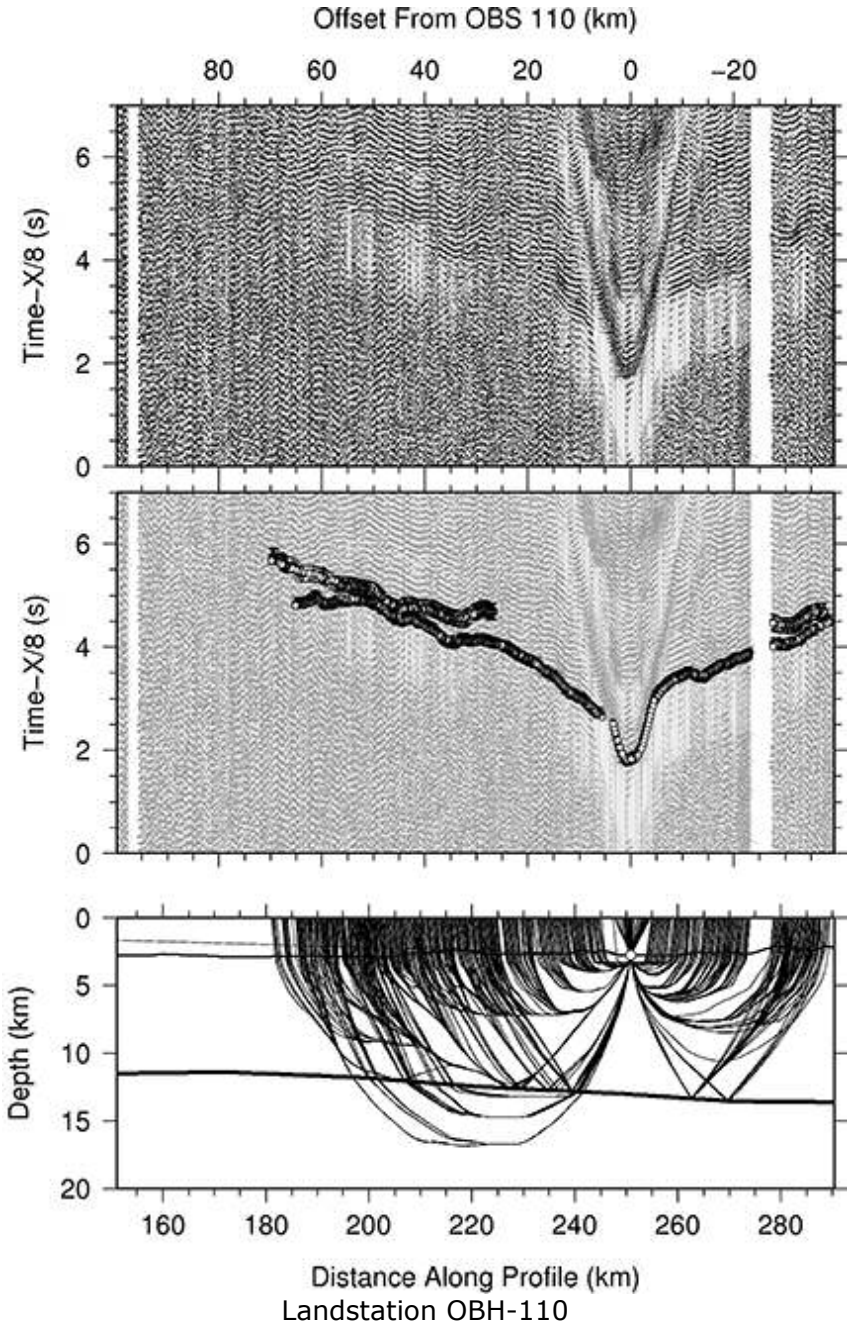

Landstation OBH-110